Projections of Future Physical and Biogeochemical Conditions in Hudson and Baffin Bays from CMIP5 Global Climate Models

Lavoie, D., N. Lambert and A. van der Baaren

Fisheries and Oceans Canada
Pelagic and Ecosystem Science Branch
Maurice Lamontagne Institute
C.P. 1000, 850 route de la mer
Mont-Joli (Québec)
G5H 3Z4

2013

Canadian Technical Report of
Hydrography and Ocean Sciences 289

Fisheries and Oceans Canada Pêches et Océans Canada

Canada

Canadian Technical Report of Hydrography and Ocean Sciences

Technical reports contain scientific and technical information of a type that represents a contribution to existing knowledge but which is not normally found in the primary literature. The subject matter is generally related to programs and interests of the Oceans and Science sectors of Fisheries and Oceans Canada.

Technical reports may be cited as full publications. The correct citation appears above the abstract of each report. Each report is abstracted in the data base *Aquatic Sciences and Fisheries Abstracts.*

Technical reports are produced regionally but are numbered nationally. Requests for individual reports will be filled by the issuing establishment listed on the front cover and title page.

Regional and headquarters establishments of Ocean Science and Surveys ceased publication of their various report series as of December 1981. A complete listing of these publications and the last number issued under each title are published in the *Canadian Journal of Fisheries and Aquatic Sciences*, Volume 38: Index to Publications 1981. The current series began with Report Number 1 in January 1982.

Rapport technique canadien sur l'hydrographie et les sciences océaniques

Les rapports techniques contiennent des renseignements scientifiques et techniques qui constituent une contribution aux connaissances actuelles mais que l'on ne trouve pas normalement dans les revues scientifiques. Le sujet est généralement rattaché aux programmes et intérêts des secteurs des Océans et des Sciences de Pêches et Océans Canada.

Les rapports techniques peuvent être cités comme des publications à part entière. Le titre exact figure au-dessus du résumé de chaque rapport. Les rapports techniques sont résumés dans la base de données *Résumés des sciences aquatiques et halieutiques*.

Les rapports techniques sont produits à l'échelon régional, mais numérotés à l'échelon national. Les demandes de rapports seront satisfaites par l'établissement auteur dont le nom figure sur la couverture et la page de titre.

Les établissements de l'ancien secteur des Sciences et Levés océaniques dans les régions et à l'administration centrale ont cessé de publier leurs diverses séries de rapports en décembre 1981. Vous trouverez dans l'index des publications du volume 38 du *Journal canadien des sciences halieutiques et aquatiques*, la liste de ces publications ainsi que le dernier numéro paru dans chaque catégorie. La nouvelle série a commencé avec la publication du rapport numéro 1 en janvier 1982.

Canadian Technical Report of
Hydrography and Ocean Sciences 289

2013

Projections of future physical and biogeochemical conditions in Hudson and Baffin bays from CMIP5 Global Climate Models

by

Diane Lavoie, Nicolas Lambert and Augustine van der Baaren

Fisheries and Oceans Canada
Pelagic and Ecosystem Science Branch
Maurice Lamontagne Institute
C.P. 1000, 850 route de la mer
Mont-Joli (Québec)
G5H 3Z4

Cat. No. Fs 97-18/289E-PDF ISNN 1488-5417 (on-line version)

Correct citation for this publication:

Lavoie, D., N. Lambert and A. van der Baaren. 2013. Projections of future physical and biogeochemical conditions in Hudson and Baffin bays from CMIP5 Global Climate Models, Can. Tech. Rep. Hydrogr. Ocean Sci. 289: xiii + 129 pp.

TABLE OF CONTENTS

LIST OF TABLES

LIST OF FIGURES

LIST OF APPENDICES

ABSTRACT

Lavoie, D., N. Lambert and A. van der Baaren. 2013. Projections of future physical and biogeochemical conditions in Hudson and Baffin bays from CMIP5 Global Climate Models, Can. Tech. Rep. Hydrogr. Ocean Sci. 289: xiii + 129 pp.

Results from the new generation of global climate models were made available for the Fifth Assessment Report (AR5) of the Intergovernmental Panel on Climate Change (IPCC) through the Coupled Model Intercomparison Project Phase 5 (CMIP5) archive. The outputs from five of these models were analyzed as a contribution to the climate change risk assessment analysis for the Atlantic Large Aquatic Basin (LAB) as part of the Aquatic Climate Change Adaptation Services Program (ACCASP). Simulated and observed trends were compared for the historical period (between 1960 and 2005) when possible for sea-surface temperature, sea-surface salinity, mixed layer depth, sea-ice concentration, nitrate concentration, primary production, chlorophyll *a*, dissolved oxygen, dissolved inorganic carbon, pH, and aragonite and calcite saturation horizon depths. Multi-model ensemble mean projections were calculated for the next 50 years using two different scenarios (RCP 4.5 and RCP 8.5). The models present consistent future trends in both regions for sea-surface temperature (increase), sea-ice concentration, pH, and calcium carbonate saturation horizon depths (decrease). The models also show consistent trends in Hudson Bay for nitrate concentration in the upper layers (decrease) and primary production (increase), but not in Baffin Bay (large differences in the trends among models).

RÉSUMÉ

Lavoie, D., N. Lambert and A. van der Baaren. 2013. Projections of future physical and biogeochemical conditions in Hudson and Baffin bays from CMIP5 Global Climate Models, Can. Tech. Rep. Hydrogr. Ocean Sci. 289: xiii + 129 pp.

Les résultats de la nouvelle génération de modèles climatiques globaux, utilisés pour la préparation du Cinquième Rapport d'Évaluation (AR5) du Groupe d'experts Intergouvernemental sur l'Évolution du Climat (GIEC), sont disponibles sur le site de la phase 5 du Projet d'Inter-Comparaison de Modèles Couplés (CMIP5). Les simulations de cinq modèles ont été analysées en vue de contribuer à l'évaluation des risques liés aux changements climatiques dans le bassin Arctique pour le Programme sur les Sciences Aquatiques en lien avec l'Adaptation aux Changements Climatiques (PSAACC) de Pêches et Océans Canada. Une comparaison de l'évolution de différentes variables océanographiques simulées et observées a été faite sur la période historique de 1960 à 2005 (lorsque possible), notamment pour la salinité de surface, la température de surface, la profondeur de la couche de mélange, les concentrations de glace de mer, les concentrations de nitrate, d'oxygène dissous, et de carbone inorganique dissous, la production primaire et la chlorophylle *a*, le pH, et les profondeurs de la lysocline de l'aragonite et de la calcite. Les projections moyennes obtenues à partir de l'ensemble des cinq modèles climatiques ont étés calculés pour les 50 prochaines années avec deux des nouveaux scénarios de forçage du GIEC (RCP 4.5 et RCP 8.5). Les résultats des modèles montrent des tendances futures évidentes pour la température de l'eau à la surface (hausse), la concentration de glace de mer, le pH et les profondeurs de la lysocline de l'aragonite et de la calcite (diminution). De plus, les modèles indiquent une hausse de la production primaire et une baisse des concentrations de nitrate en surface dans la Baie d'Hudson. Par contre, dans la Baie de Baffin, de larges différences dans les tendances de nitrate et de production primaire ont été observées d'un modèle à un autre, nous empêchant de poser un diagnostic fiable.

1 INTRODUCTION

This report is a contribution to the climate change risk assessment analysis for the Canadian Arctic Large Aquatic Basin (DFO, 2013) requested by Fisheries and Oceans Canada as part of the Aquatic Climate Change Adaptation Services Program (ACCASP). It also provides information on future trends for a larger summary report of five sub-regions of the Canadian Arctic (Steiner et al., 2013).

Numerical models are an essential tool to obtain projections of future physical and biochemical conditions in the ocean. Regional climate models are not available yet for Hudson and Baffin bays, and although Global Climate Models (GCMs) have a coarse resolution, we need to rely on them to obtain projections of ocean biogeochemical and physical variables. GCM projections have formed the basis of the Intergovernmental Panel on Climate Change Fourth Assessment Report (IPCC AR4) and are archived as part of Phase 3 of the Coupled Model Intercomparison Project (CMIP3). Hundreds of scientific papers have been written using the output of these models (see http://www-pcmdi.llnl.gov/ipcc/subproject_publications.php); however, the simulations produced for IPCC AR4 do not include biogeochemical components. Simulations from coupled physical–biogeochemical models are now available for the IPCC Fifth Assessment Report (AR5) and are archived as part of CMIP5. While these climate models are bigger and more sophisticated than versions used for AR4, no major changes in output were detected when compared to AR4 results, only slightly better agreement with observations (e.g., Sakaguchi et al., 2012; Zhang and Jin, 2012; Knutti et al., 2013). When we undertook this assessment, the outputs of five GCMs that include a biochemical component were available. We have attempted to determine if one or more of these models perform better than others in the different regions under study by comparing their output over the historical period with available observations. In a second step, we calculated the multi-model ensemble mean projections of physical and biochemical oceanographic variables for the next 50 years. A similar report produced for the Atlantic Large Aquatic Basin is available (Lavoie et al., 2013). More information on AR5 projections of atmospheric and oceanographic variables can also be found in Loder and van der Baaren (2013) and Chassé et al. (2013).

1.1 DESCRIPTIONS OF MODELS AND EXPERIMENTS

We used the CMIP5 multi-model ensemble (http://www-pcmdi.llnl.gov/) that had biochemical components and that were available in spring 2012 (see Table 1). Two types of experiments are available under CMIP5: 1) near-term simulations (10- to 30-years), some of which were initialized with observed ocean state and sea-ice data, and 2) long-term (through 2100 and beyond) simulations initialized from the end of freely evolving simulations of the historical period (1850–2005) (Taylor et al., 2012). We use the long-term simulations (2006–2100) of the ensemble member r1i1p1 forced with specified concentrations consistent with a high emissions scenario (RCP 8.5) and a medium mitigation scenario (RCP 4.5). In the RCP 4.5 scenario, radiative forcing stabilizes at

~4.5 W m^{-2} after 2100, while it reaches ~8.5W m^{-2} in 2100 but stabilizes later (around 2250) in the RCP8.5 scenario. In the remainder of the text, the following short names will be used to identify the models: CanESM2, GFDL, HadGEM2, IPSL, and MPI.

Table 1. Identification of the models and institutions that supplied the output data used in this study.

Modeling Center (or Group)	Model Name
Canadian Centre for Climate Modelling and Analysis	CanESM2
NOAA Geophysical Fluid Dynamics Laboratory	GFDL-ESM2M
Met Office Hadley Centre	HadGEM2-ES
Institut Pierre-Simon Laplace	IPSL-CM5A-LR
Max Planck Institute for Meteorology	MPI-ESM-LR

1.1.1 CanESM2

The physical ocean component of CanESM2 has 40 levels with approximately 10 m resolution in the upper ocean (Arora et al., 2011). The horizontal resolution of the physical ocean is approximately 1.41° (longitude) × 0.94° (latitude) in CanESM2, compared to 1.87° × 1.87° in CanESM1. Hudson Bay is isolated (not connected to the Arctic or Atlantic), and Baffin Bay is not connected to the Arctic Ocean. The K-profile parameterization of Large et al. (1994) and a tidally driven mixing parameterization are used. Horizontal friction is represented by the anisotropic viscosity of Large et al. (2001). The sea-ice component of CanESM2 uses the atmospheric horizontal grid with a resolution of 2.81°. The sea ice is divided in two vertical layers, one layer of ice and one layer of snow. The growth and melt of the ice is governed by the thermodynamic energy balance (Flato et al., 2000). The Canadian Model of Ocean Carbon (CMOC), the ocean carbon cycle component of CanESM2, incorporates an inorganic chemistry module (solubility pump) and a simple NPZD ecosystem model (organic and carbonate pumps) for simulating the ocean–atmosphere exchange of CO_2 (Zahariev et al., 2008; Christian et al., 2010). Dissolved inorganic carbon (DIC) and total alkalinity are prognostic variables while chlorophyll is semi-prognostic.

1.1.2 GFDL-ESM2M

The physical climate formulation and simulation characteristics of the GFDL-ESM2M global climate model are described by Dunne et al. (2012). This GCM includes different components for each major system (land, atmosphere, ocean, sea ice, iceberg, and ocean). The ocean component of GFDL-ESM2M uses a 1° horizontal grid and a tripolar grid above 65°N, with 50 vertical levels and a surface layer of 10 m (Griffies et al., 2005). Hudson Bay is isolated (not connected to the Arctic or Atlantic Oceans), while Baffin Bay is connected to the Arctic through Parry Channel and Nares Strait. The model use a K-profile parameterization based on Danabasoglu et al. (2006). GFDL-ESM2M was updated from the previous version by using an isotropic Laplacian friction instead of a horizontal anisotropic friction scheme (Large et al., 2001). The sea-ice component of GFDL-ESM2M uses the same horizontal grid as the ocean component with three vertical layers (two ice and one snow layer; Winton, 2000). The ocean biogeochemical

component is TOPAZ2 (Tracers of Ocean Phytoplankton with Allometric Zooplankton): a detailed description was made by Dunne et al. (2013). TOPAZ2 simulates the biogeochemical cycle (carbon, nitrogen, phosphorus, silicon, iron, oxygen, and alkalinity) using 30 prognostic tracers. Three phytoplankton groups are used to define primary production with their own growth functions and limiting factors: small (prokaryotic picoplankton and nanoplankton), large (diatoms) and diazotrophic (nitrogen fixers). Finally, calcite and aragonite formation in TOPAZ2 are diagnostic variables.

1.1.3 HadGEM2-ES

The different components of the HadGEM2-ES model (troposphere, land surface and hydrology, aerosols, ocean and sea ice, terrestrial carbon cycle, and ocean biogeochemistry) are described by Johns et al. (2006) and Martin et al. (2011). The ocean component of HadGEM2-ES uses a latitude–longitude grid with a zonal resolution of 1° everywhere and meridional resolution of 1° between the poles and 30° of latitude, after which it increases smoothly to 1⁄3° at the equator. Hudson Bay is connected to the Atlantic but not to the Arctic Ocean (Fury and Hecla Straits are blocked), while Baffin Bay is connected to the Arctic Ocean through Parry Channel and Nares Strait. There are 40 vertical layers with thicknesses of 10 m near the surface. An anisotropic Laplacian viscosity is used (Large et al., 2001). The sea-ice model component of HadGEM2-ES uses the same grid as the ocean component, and the sea ice is divided into five thickness categories (Hunke and Lipscomb, 2004). The carbon cycle model used by HadGEM2-ES is Diat-HadOCC (Collins et al., 2011). This model is similar to the model described by Palmer and Totterdell (2001) except for the phytoplankton component which was divided into two compartments: diatoms and other phytoplankton. Phytoplankton growth is simulated by an NPZD model that uses nitrogen, iron and silicon (diatoms) as the limiting nutrients. Finally, the aragonite and calcite saturation states are diagnostic variables.

1.1.4 IPSL-CM5A-LR

The different components of the IPSL-CM5A-LR global climate model are described by Dufresne *et al.* (2013): atmosphere (LMDZ), ocean (NEMO/OPA), sea-ice (NEMO/LIM2), land (ORCHIDEE), chemistry and aerosol (INCA), and stratospheric chemistry (REPROBUS). The OASIS coupler is used to exchange fields between the different components of the model. The ocean model uses a tri-polar global grid (Madec and Imbard, 1996) with a resolution of 2° for most of the grid (a latitudinal grid refinement of 0.5° is used in the tropics) and 31 vertical levels (with thicknesses of 10 m near the surface to 500 m at 5000 m depth). Hudson Bay is connected to the Atlantic but not to the Arctic Ocean, while Baffin Bay is connected to Arctic Ocean through a fictive channel (between Parry Channel and Nares Strait). The sea-ice model uses the same horizontal grid as the ocean model with three vertical layers. The biogeochemistry of the ocean is simulated by the PISCES model (Pelagic Interaction Scheme for Carbon and Ecosystem Studies; Aumont and Bopp, 2006). It has 24 compartments, including two phytoplankton groups (nanophytoplankton and diatoms) and five nutrients (nitrate, ammonium, phosphate, silicate, and iron).

1.1.5 MPI-ESM-LR

The MPI-ESM-LR climate model uses different components to simulate the atmosphere (ECHAM6), the ocean (MPIOM; Marsland et al., 2003), the land surface (JSBACH), and the oceanic biogeochemistry processes (HAMOCC). These components are coupled using the OASIS3 coupling program. The ocean model horizontal grid is an orthogonal curvilinear grid with an arbitrary placement of the grid poles (the North Pole shifted to Greenland and the South Pole moved toward the centre of the Antarctic continent). The grid spacing is 15 km (0.14°) at minimum around Greenland, and 184 km (1.65°) at maximum in the Pacific (Jungclaus et al., 2006). There are 40 unevenly spaced vertical levels, with thicknesses between 10 m and 600 m. Hudson Bay is connected to the Atlantic but not to the Arctic Ocean, while Baffin Bay is connected to Arctic Ocean through Parry Channel and Nares Strait. The sea-ice model uses the same horizontal grid as the ocean model and the effect of snow accumulation on sea ice is included. The HAMOCC global ocean biogeochemistry model (Hamburg Ocean Carbon Cycle Model) is part of the MPI-ESM-LR global model (Ilyina et al., 2013). HAMOCC uses 17 state variables in the water column (including only one group of phytoplankton and three nutrients (phosphate, nitrate and iron) and 12 variables in the sediment.

1.2 Methods

Two different regions (Hudson Bay and Baffin Bay) were selected for trend analysis (Figure 1) due to the different hydrodynamic conditions prevailing in each area. We first looked at how representative different simulated physical (temperature, salinity, sea ice, mixed layer depth) and biochemical (nitrate, chlorophyll *a* [Chl *a*], primary production, oxygen, DIC, pH, aragonite and calcite saturation horizon depths) variables are in each region by comparing them with observed values (range of values and distribution). We also compared the trends simulated over the historical period (1960–2005) with available observed trends. The period over which the trend was calculated was sometimes shortened to better compare with available observations. Next, we calculated future trends over a 50-year period (2012–2062) for each model as well as the mean trends of the multi-model ensemble. The mean trend over each region was calculated as well as the trend over each grid cell within each region to analyze spatial variability in the trends. The trends were calculated for the surface layer, for the 50–100 m layer, and for the 100–400 m layer as in Lavoie et al. (2013). In Hudson Bay, bottom depths are shallower than 400 m and the 100–400 m layer rather represents the >100 m layer. Past and future bi-decadal distributions, from 1966–1985 to 2066–2085, were also calculated for each variable for the RCP 4.5 and 8.5 scenarios, at the surface and along some transects (vertical distribution, see Figure 1). Figures of these results are available on demand, and some of these can also be found in Appendix II.

2 RESULTS

2.1 HUDSON BAY

Hudson Bay is a large (0.8×10^6 km^2), fairly shallow (mean depth of approximately 150 m), inland sea that is relatively isolated from the Arctic and Atlantic oceans. It receives large amounts of freshwater and the mean circulation in the bay is cyclonic. The bay has been the subject of renewed scientific attention recently, with the MERICA (Harvey et al., 2006) and ArcticNet (ArcticNet, 2012) programs. Descriptions of the Hudson Bay characteristics can be found in Stewart and Lockhart (2005), Steiner et al. (2013) and ArcticNet (2012) and references therein. The bathymetry of the region is shown in Figure 2.

2.1.1 Historical trends

2.1.1.1 Sea-surface salinity:

In Hudson Bay, the lowest surface salinities in summer and early fall are found in the southeastern area, particularly in James Bay (e.g., Lapoussiere et al., 2009). This is also the region of lowest mean annual salinities found in the models (Figure 3). Hudson Bay receives a large amount of freshwater from its drainage basin, which covers more than a third of Canada's land mass (Déry et al., 2011), as well as relatively fresh water from the Arctic. Freshening of the cold, saline surface water entering Hudson Bay from the north occurs as these waters circulate cyclonically around Hudson Bay due to river runoff (Prinsenberg, 1986; St-Laurent et al., 2012). Average annual sea-surface salinities given in the World Ocean Atlas (Antonov et al., 2010; bottom rigth panel in Figure 3) are around 27 in Hudson Bay. CanESM2, IPSL, and MPI represent the surface salinity well, while GFDL and HadGEM2 surface salinities are too low. Bottom salinities should be greater than 32.8 (Prinsenberg, 1984). MPI and IPSL best reproduce these subsurface conditions, while, as is the case at the surface, GFDL and HadGEM2 salinities are too low (Figure II- 1).

We know of no available trends of observed surface salinity for Hudson Bay. The simulated sea-surface salinity trends over the historical period are very low and of varying signs: GFDL and MPI show negative trends while the others show positive trends (Figure 4). The multi-model ensemble mean displays no trend (0.0 ± 0.06 per decade). There are also regional differences in the trends, with GFDL showing a decreasing trend over the whole region, HadGEM2 showing an increasing trend over the whole region, and the three other models showing both increasing and decreasing trends (Figure 5).

2.1.1.2 Sea-surface temperature:

Average annual sea-surface temperatures (SST) given by the World Ocean Atlas (Figure 6, bottom right panel) are warmer in the northwestern area (4–5°C) and colder in the southwest (around 0.5^{o}C). The IPSL model best represents these conditions. CanESM2, MPI, and GFDL have cooler conditions and generally display warmer SST along the

coast while SST from HadGEM2 is too cold over the whole bay. Temporal trends calculated from satellite data were computed for the warmest week of the year (in August or September) between 1985 and 2009 (Galbraith and Larouche, 2011), indicating an SST increase between 0.8 and 1.4°C depending the on region within the bay. The average simulated SST increase for August over the 1985–2005 period ranges between 0.4 and 1.2°C, with an ensemble mean of 0.87°C (0.44±0.21°C per decade; Figure 7). GFDL and MPI show the lowest August SST trends. The difference in SST between cold and warm periods originates from changes in the southwest area (Galbraith and Larouche, 2011), which is the last region to experience sea-ice breakup (Stewart and Lockhart, 2005). Although all models show an increase in SST over the region, MPI and to a lesser degree HadGEM2 are the models that best capture this regional pattern (Figure 8). The annual mean trend of the multi-model ensemble for the 1960–2005 period is 0.13±0.05°C per decade (not shown).

2.1.1.3 Sea ice

Sea ice starts to disappear in June in the northwestern and eastern parts of the bay. The bay is ice free in summer (CIS, 2002; Tivy et al., 2011). Sea ice begins to form in northwestern Hudson Bay in October. In November the ice cover spreads southward along the western coast of Hudson Bay and then eastward (Stewart and Lockhart, 2005). By mid-December, most of the region is ice covered. Maximum ice thickness occurs between late February and early June and ranges between 70 cm and 285 cm (Stewart and Lockhart, 2005). Many studies have demonstrated a large reduction in sea-ice cover in recent decades in Hudson Bay; this reduction is among the largest in the circumpolar Arctic (Tivy et al., 2011). Between 1979 and 2006, Parkinson and Cavalieri (2008) reported a decrease in sea-ice extent of 19.5% per decade in Hudson Bay. Tivy et al. (2011) reported a sea-ice coverage decrease of 7.5% to 13.6% per decade for Hudson Bay (depending on the region within the bays) for the 1968–2008 period, while Galbraith and Larouche (2011) reported an earlier trend in sea-ice break-up of 3.2 days per decade since 1971. Earlier breakup was also observed by Gagnon and Gough (2005).

The HadGEM2 model has a good representation of the sea-ice fraction in Hudson Bay (Figure 9) but the bay does not get completely ice free in summer. IPSL is good in the fall and winter, but the ice melts too early in spring. MPI is good also, although it gives a sea ice formation that is a little late in the fall and a melt that is a little early in spring. The other two models (CanESM2 and GFDL) both show later formation and earlier melt than observed and GFDL displays relatively thin ice compared to the other models. Figure 10 shows the sea-ice fraction trends for the months of November, March, and June over the historical period. Most models show a trend towards later sea-ice formation and earlier sea-ice melt, as observed (e.g., Gagnon and Gough, 2005; Galbraith and Larouche, 2011). The mean sea-ice thicknesses in April (month when sea-ice thickness maxima occurs) for the 1986-2005 period are 66 cm, 111 cm, 115 cm, 137 cm, and 175 cm for GFDL, CanESM2, IPSL, MPI, and HadGEM2, respectively.

2.1.1.4 Mixed layer depth

Hudson Bay is characterized by strong vertical stratification. During summer, there is a sharp pycnocline at 15 to 25 m that prevents vertical mixing between surface and deep waters. In the winter, salt rejection from sea-ice formation tends to reduce stratification, and mixing can reach 90 m in the central part of the bay (Prinsenberg, 1986; Ferland et al., 2011). In the GCMs, the mixed layer depth is given by two different but similar variables. The mixed layer depth (MLD) is defined by the water density and the maximum mixed layer depth (MMLD) is based on the mixing scheme of the GCMs. The MLD and MMLD are available for CanESM2, GFDL, and MPI while only the MMLD is available for IPSL. GFDL seems to have a better representation of the MLD, with an annual average (over the bay) varying between 18 and 50 m and with greater MLD in the central part of the Hudson Bay (Figure 11). Mixed layer depths from MPI and CanESM2 appear too shallow, with monthly areal average MLDs varying between 8 and 30 m and 8 and 40 m, respectively (Figure 12). There are no significant changes in average simulated MLDs over the historical period (Figure 12). However, there are spatial differences in the trends, with, in general, a reduction of the MLD on the western side of Hudson Bay and an increase on the eastern side (Figure 13). There are no observed trends to compare with.

2.1.1.5 Nitrate

Nitrogen is the nutrient which limits primary production in Hudson Bay (e.g., Drinkwater and Jones, 1987; Ferland et al., 2011). The strong haline stratification inhibits mixing and thus the transport of nutrients from the bottom to the surface. In summer and early fall, nitrate concentrations above the Chl *a* maximum are typically low (usually <1 mmol m−3, Ferland et al., 2011; Lapoussiere et al., 2013). No measurements of nitrate concentrations are available for spring, but they should be close to what is observed/modelled on the Mackenzie Shelf in the Beaufort Sea; around 3–4 mmol m^{-3} (Lavoie et al., 2009 and references therein) and as simulated by Sibert et al. (2011) with a regional model. The annual mean surface concentration should thus be below 4 mmol m^{-3}. Nitrate concentrations at the surface in the World Ocean Atlas vary from 1 mmol m^{-3} in the southern area to 7 mmol m^{-3} in the northern area, but these high values are most likely the result of sparse data and an interpolation effect over a larger area including the Labrador Sea (Figure 14, bottom right panel). Simulated nitrate concentrations in CanESM2 and HadGEM2 are higher both at the surface (Figure 14 and Figure 15) and at depth (Figure II- 5), with an average of around 35 and 25 mmol m^{-3} in the 50–100 m layer for these models (Figure 16). These values are high compared to observed values of around 10 mmol m^{-3} (Ferland et al., 2011). On the other hand, the sub-surface nutrient inventory in GFDL is too low (~ 1 mmol m^{-3}), and this is also reflected in the surface layer. Overall, nitrate concentrations appear to be best represented by MPI and IPSL, although it is difficult to judge from the sparse observations and from the interpolated World Ocean Atlas data.

Sparse observations between 1961 and 2006 show a decreasing trend in nitrate concentration (-0.81 mmol m^{-3} per decade) in the centre of the bay in the 0–30 m layer (M. Starr and J.-Y. Couture, Maurice Lamontagne Institute, DFO, unpublished data). At

depths greater than 100 m, nitrate concentrations exhibited an increasing trend of 1.7 mmol m^{-3} per decade. However, at the scale of the whole bay, no trends were detected by Starr and Couture. Except for CanESM2, which shows a clear decreasing trend, the models show either no trend or a small decreasing trend for nitrate concentration at the surface, with a multi-model ensemble mean of -0.13±0.19 mmol m^{-3} per decade over the historical period (Figure 15). Below 100 m, three of the models show an overall increasing trend (Figure 17), with a multi-model ensemble mean trend of 0.13±24 mmol m^{-3} per decade. Due to the scarcity of observations and variability in the simulated trends, it is difficult to conclude that one of the models better represents the trends or if there is a trend.

2.1.1.6 Primary production

Hudson Bay is not a productive ecosystem due to low nutrient concentrations in the surface layer. Ferland et al. (2011) estimated the daily primary production in summer at 0.32 g C m^{-2}. Assuming a growth season of 120 days, this gives a total seasonal production of 38.4 g C m^{-2} or 3.2 mol C m^{-2}. Figure 18 and Figure 19 show that most models overestimate primary production in Hudson Bay. MPI gives the best average primary production, ranging between 3 and 4 mol C m^{-2}, followed by IPSL, which shows high primary production values due to high production near river mouths (Figure 18). CanESM2 displays very high primary production values, especially in the northwest, where observed primary production is low.

Larouche (Maurice Lamontagne Institute, DFO, unpublished data) calculated primary production trends from three different satellites over the 1998–2010 period at stations corresponding to MERICA stations (along an east–west transect across the middle of the bay; Harvey et al., 2006; see Figure 1) and generally found small increasing trends with higher trends closer to the shores (0.287–0.537 mg C m^{-2} d^{-1} per decade). However, results from paleoceanographic studies of the sediments suggest a decreasing primary production trend since the late 1980s (Ladouceur, 2007). These differences could be explained by changes in primary production taking place in the subsurface Chl *a* maximum (e.g., Martin et al., 2010), although the lengthening of the growth season resulting from earlier sea-ice breakup (see section 2.1.1.3) should favour higher primary production in the subsurface Chl *a* maximum (Lavoie et al., 2010). A tendency towards earlier Chl *a* maxima was indeed observed by Kahru et al. (2011). The SeaWiFS period is too short to allow comparison of trends with the GCMs, but over the 1960–2005 period, most models show increasing trends in annual primary production, with an ensemble mean of 0.075±0.062 mol C m^{-2} $year^{-1}$ per decade (Figure 19 and Figure 20).

2.1.1.7 Chl *a*

A composite image of annual mean surface Chl *a* for the SeaWiFS record (January 1998 to December 2010) shows that surface Chl *a* concentrations are very low in the centre of the bay (0.02 mg m^{-3}) and vary between 0.4 and 1 mg m^{-3} except for a narrow band along the coast (Figure 21, bottom right panel). However, these high concentrations along the coast are a result of contamination by high chromophoric dissolved organic matter

(CDOM) content and do not represent Chl *a* concentrations only (Granskog et al., 2007). Even though it displays high vertically integrated primary production values, CanESM2 has very low surface Chl *a* concentrations (Figure 21). HadGEM2 represents well the surface Chl *a* pattern, although values are a little high. IPSL and MPI are the models with the best range of surface Chl *a* concentrations (if we assume high CDOM content along the shores).

Larouche's results (unpublished data, see previous section) showed a Chl *a* increase of 0.024 to 0.120 mg m^{-3} per decade over the 1998–2010 period. Vantrepotte and Mélin (2011) also observed a significant increase in Chl *a* along the eastern side of the bay. As mentioned above, the SeaWiFS record is too short to allow a comparison of trends with the GCMs, so we display the trends obtained over the historical period. The trends are variable at the surface (Figure 22) and increasing in 50–100 m layer (Figure 23). However, the multi-model ensemble mean trends are small and not significant.

2.1.1.8 Oxygen

Dissolved oxygen (O_2) concentration in the ocean is affected by salinity and temperature, as well as by primary production and remineralization of organic matter. Colder water can hold higher concentrations of oxygen. The World Ocean Atlas gives dissolved oxygen concentrations at the surface between 0.34 and 0.38 mol m^{-3} (using a conversion factor of 22.392 L mol^{-1} O_2; Hofmann et al., 2011) for Hudson Bay (Figure 24, bottom right panel). Oxygen is not available in CanESM2, so only the output of four models is compared. HadGEM2 displays the highest O_2 concentration in Hudson Bay due to its corresponding estimation of very cold sea-surface temperature (Figure 24). GFDL also shows high O_2 concentrations, but these result from the low sea-surface salinity it reports. IPSL, which has the best representation of sea-surface temperature, displays O_2 concentrations that are closer to the observations, although it does not match the spatial pattern seen in the World Ocean Atlas data. All the models show a weak decreasing oxygen concentration at the surface linked to surface warming (not shown) but little changes took place in the different layers over the historical period (Figure 25 and Figure 26).

2.1.1.9 Ocean acidification

Oceans have taken up a large part (~ 40%) of anthropogenic CO_2 emissions, thereby reducing climate warming caused by greenhouse gas (Zeebe et al., 2008). However, the increase of CO_2 in the oceans alters its chemistry, which can have potentially serious consequences for marine life, especially calcifying species. When CO_2 gas enters the ocean, it decreases the seawater pH as well as the concentration of the carbonate ion [CO_3^{2-}], which lowers the saturation state of calcium carbonates ($CaCO_3$) such as calcite and aragonite. This process is called ocean acidification. The saturation state is defined as the product of [CO_3^{2-}] and the concentration of calcium ion [Ca^{2+}] divided by the stoichiometric solubility product (K_{sp}) (Azetsu-Scott et al., 2010 and references therein). The latter differs for calcite and aragonite and is influenced by water temperature (solubility product increases as the temperature decreases). The calcium concentration is

estimated from the salinity (the lower the salinity the less calcium). Thus, fresher and colder waters such as in Arctic seas are more susceptible to low saturation states.

2.1.1.9.1 DIC

Few DIC measurements are available in Hudson Bay. DIC values measured in the ice-free surface waters of the Canada Basin by Cai et al. (2010) ranged between 1700 and 1900 µmol kg^{-1} while values measured in the Arctic outflow in the Canadian Arctic Archipelago by Azetsu- Scott et al. (2010) ranged between 1960 and 2056 µmol kg^{-1}. Surface DIC concentrations measured in 2004, 2005, and 2006 along the MERICA transect (see Figure 1) were within these two ranges (1847 to 2029 µmol kg^{-1}, Azetsu-Scott, Bedford Institute of Oceanography, DFO, unpublished data). Converting to mol m^{-3} (1.8 and 1.98 mol m^{-3}), we see that the DIC values from GFDL and HadGEM2 are too low, while the other GCMs (CanESM2, IPSL, and especially MPI) have better representations of surface DIC (Figure 27). Except for MPI, all models show an increasing surface DIC trend on average, with a multi-model ensemble mean trend of 0.003±0.004 mol m^{-3} per decade (Figure 28 and Figure 29). The mean trend is smaller than in the Northwest Atlantic region (including the Labrador Sea; see Lavoie et al., 2013) and the standard deviation higher than the mean. The significance of these changes for ocean acidification depends on the Revelle factor, which is relatively high in polar and sub-polar waters (Sabine et al., 2004; Bates et al., 2006).

2.1.1.9.2 pH

According to measurements made in the 2000s, surface pH in Hudson Bay varies between 7.9 and 8.1 (Azetsu-Scott, Bedford Institute of Oceanography, DFO, unpublished data). These values are lower than those reported outside of Hudson Bay (Azetsu-Scott et al., 2010). Although pH values differ among models, all the GCMs simulated lower pH values in Hudson Bay than in Baffin Bay or the Labrador Sea (see Figures II-26 to II-30 in Lavoie et al., 2013). Three GCMs appear to have a good representation of surface pH: CanESM2, GFDL, and IPSL (Figure 30). HadGEM2 surface pH values are too low, while MPI values are high (compared to the recent observations of Azetsu-Scott). The surface pH trends are very similar among models, with a significant pH decrease ranging between -0.05 and -0.08 over the 1960–2005 period (Figure 31), as observed in other parts of the world (e.g., Feely et al., 2009 and references therein).

2.1.1.9.3 Calcium carbonate saturation horizons

In southern Hudson Strait (outflow region for Hudson Bay water) water is saturated with respect to aragonite down to a depth of 200 m while for calcite, water is saturated down to the bottom (350 m; Azetsu-Scott et al., 2010). In Hudson Bay, Azetsu-Scott et al. (2008) report the shallowest saturation horizon for aragonite at depths of around 100 m, at the western side of the MERICA section. Among the GCMs analyzed, three simulated both the calcite and aragonite saturation horizon depths (CanESM2, GFDL, and HadGEM2), while one simulated the calcite saturation horizon depth only (MPI). Of

these models, only CanESM2 appears to simulate valid saturation horizons, although too shallow (mean horizon depths < 11 m for aragonite and < 40 m for calcite) compared to the result of Azetsu-Scott et al. (2008).

2.1.2 Future trends (next 50 years)

There are substantial similarities between the changes projected by the two scenarios analyzed in this study (RCP 4.5 and RCP 8.5), with those from RCP 8.5 generally having a larger magnitude.

- **Salinity**: Three models out of five show a freshening of the sea surface for the next 50 years with the RCP 4.5 scenario (Figure 32). The freshening trend is more important with the RCP 8.5 scenario, and there is even a trend reversal with CanESM2 (from positive to negative). The multi-model ensemble mean trends are -0.10±0.19 and -0.15±0.18 units per decade for RCP 4.5 and 8.5, respectively, so there are no clear trend from the multi-model ensemble (variable trends and standard deviation higher than the mean).

- **Temperature**: All models show an increasing trend for SST that ranges between +0.16 and +0.36°C per decade for RCP 4.5 and +0.2 and +0.38°C per decade for RCP 8.5 over the next 50 years, with a multi-model ensemble mean trend of +0.22±0.08 and +0.31±0.07°C per decade, respectively (Figure 33). These trends are about two times greater than the trend calculated over the historical period (+0.13±0.05^{o}C per decade; section 2.1.1.2).

- **Sea Ice:** A diminution of sea-ice thickness is predicted in all the GCMs and with both emission scenarios. The mean sea-ice thicknesses in April for the 2046-2065 period are 34 cm, 56 cm, 85 cm, 110 cm, and 133 cm for GFDL, CanESM2, IPSL, MPI, and HadGEM2, respectively, for RCP 4.5. With the RCP 8.5 scenario, the corresponding sea-ice thicknesses are 22 cm, 52 cm, 70 cm, 93 cm, and 117 cm. These reductions in sea-ice thickness, compared to the 1986-2005 period, correspond to multi-model ensemble mean trends of -6.2 and -8.3 cm per decade for RCP 4.5 and RCP 8.5, respectively. Sea ice is also projected to form later in the fall (by up to one month with RCP 8.5) and to melt earlier in spring (by one to two months with RCP 4.5 and RCP 8.5, respectively). Figure 34 and Figure 35 show the corresponding sea-ice fraction trends for the months of November, March, and June for RCP 4.5 and RCP 8.5.

- **Mixed layer depth**: There are basically no trends for the mixed layer depth (Figure 36). CanESM2 has a decreasing MMLD for both RCP 4.5 and 8.5 (-0.15 and -0.42 m per decade, respectively), IPSL shows no trends (very low values), while GFDL and MPI show increasing trends (0.17 m per decade on average). Trends for MLD are also of opposite signs or very low. Therefore, no firm conclusions can be drawn on future MMLD and MLD in Hudson Bay.

- **Nitrate**: Most models show decreasing nitrate concentration at the surface and in the 50–100 m depth range for both RCP 4.5 and 8.5: the exception is IPSL, which shows an increasing trend in the 50–100 m layer for RCP 4.5 (Figure 37 and Figure 38). The smallest trend is obtained with GFDL, which has very low nitrate concentrations at all depths. The multi-model ensemble mean trends are -0.19±0.17 and -0.23±0.18 mmol m^{-3} per decade at the surface for RCP 4.5 and 8.5, respectively (around one unit over the next 50 years), and -0.11±0.15 and -0.24±0.17 mmol m^{-3} per decade in the 50–100 m layer for RCPs 4.5 and 8.5, respectively. A nitrate concentration decrease thus appears likely, especially at the surface.

- **Primary production**: The vertically integrated primary production increases in all models over the next 50 years, except for IPSL in the RCP 4.5 simulation. The multi-model ensemble mean trends are 0.14±0.16 and 0.14±0.11 mol C m^{-2} $year^{-1}$ per decade for RCPs 4.5 and 8.5, representing a 9.4 and 9.5% increase over 50 years, respectively (Figure 39). Most models show a greater increase in the southern part of the bay (Figure 40).

- **Chlorophyll *a***: Trends in Chl *a* concentration at the surface are disparate, with two models displaying positive trends (CanESM2 and GFDL) and three models displaying negative trends (IPSL, MPI, and HadGEM2). The multi-model ensemble mean trends show no changes in surface Chl *a* over the next decade, with -0.0008±0.0098 and -0.004±0.012 mg Chl *a* m^{-3} per decade for RCP 4.5 and RCP 8.5, respectively (Figure 41). However, subsurface Chl *a* is predicted to increase marginally (see Figure 42, Appendix I-1, and Figure II- 7).

- **Oxygen:** All models show low decreasing dissolved oxygen concentration trends at the surface, with multi-model ensemble mean trends of -0.8±0.4 and -1.3±0.5 mmol m^{-3} per decade for RCPs 4.5 and 8.5, respectively (Figure 43). However, in the deeper layers, the trends are low and variable (e.g., Figure 44), so no firm conclusions can be drawn on future dissolved oxygen concentration.

- **DIC:** Dissolved inorganic carbon concentration trends are weak and variable in all layers for both scenarios (e.g., Figure 45), and thus no firm conclusions can be drawn on future DIC concentration in these layers.

- **pH:** All models show similar negative trends for pH at the surface (Figure 46). The multi-model ensemble mean trends at the surface are -0.022±0.003 and -0.036±0.003 unit per decade for RCPs 4.5 and 8.5, respectively, representing a pH decrease of -0.11 and -0.20 units over the next 50 years.

- **Calcium carbonate saturation horizons:** In Hudson Bay, the mean aragonite saturation horizon depths provided by CanESM2 decrease at a rate of -69.5 cm and -116 cm per decade to reach the surface around 2065 and 2055 for RCP 4.5 and RCP 8.5, respectively (Figure 47). However, the saturation horizon depths simulated by CanESM2 are initially too shallow and thus might not reach the surface as early as

2065 and 2055. The mean calcite saturation horizon depths decrease at a faster rate, -1.5 and -4.4 m per decade, but do not reach the surface.

2.2 BAFFIN BAY

Baffin Bay serves as a pathway for the fresh and cold Arctic water and sea ice flowing through Nares Strait and the straits and channels of the Canadian Arctic Archipelago towards the Labrador Sea. The mean circulation pattern is cyclonic. A review of the physical environment of Baffin Bay and Davis Strait is given by Hamilton and Wu (2013) and will not be repeated here. The region retained here for the trend analysis excludes the Baffin Bay polynya located north of 75°N (Figure 1). The bathymetry of the region is shown in Figure 51.

2.2.1 Historical trends

2.2.1.1 Sea-surface salinity

Average annual sea-surface salinities given by the World Ocean Atlas range between 31 and 34, with higher salinities on the eastern side and lower salinities on the western side of the bay (Figure 49, bottom right panel). CanESM2 and GFDL have a good representation of the average sea-surface salinities in the bay but do not reproduce the east–west gradient in the south of the bay. On the other hand, MPI and HadGEM2 have a good representation of the east–west salinity gradient, but the salinity is too low on the east side of the bay. All models show decreasing sea-surface salinity over the 1960–2005 period, with an ensemble mean of -0.07± 0.03 per decade (Figure 50), although some spatial variability is present (Figure 51). Hamilton and Wu (2013) observed similar freshening in the 50–200 m interval on the Baffin Island Shelf over this same period.

2.2.1.2 Sea-surface temperature

The World Ocean Atlas shows annual average surface temperatures ranging between -1 and 2.5ºC, with higher temperatures on the eastern side of the bay (Figure 52, bottom right panel). The source of this warmer and saltier water is the Irminger Sea inflow which flows northward along the eastern side of the Labrador Sea. Most models have SST within the World Ocean Atlas temperature range, with better representation by IPSL and MPI. GFDL, HadGEM2, and CanESM2 display cooler temperatures, especially on the western side of the Bay (Figure 52).

All models show increasing sea-surface temperature over the 1960–2005 period, with a multi-model ensemble mean of +0.09±0.05°C per decade (Figure 53 and Figure 54). However, Hamilton and Wu (2013) analyzed the average temperature in the upper 50 m of the bay and did not observe any trend over the last 50 years. Over a longer period (1940–2003), Zweng and Münchow (2006) found no significant trend for the surface water of Baffin Bay. Moreover, when looking at central Baffin Bay only (0–50 m interval), Hamilton and Wu (2013) detected a cooling trend of -0.16°C per decade.

2.2.1.3 Sea ice

The cycle of sea-ice formation and melt in Baffin Bay resembles that of Hudson Bay (see Tang et al., 2004; Tivy et al., 2011). Baffin Bay is free of sea ice in summer. Sea ice starts to form (and is advected into the bay; Kwok, 2007) in October in the northwestern part of the bay, covers most of the bay by December, reaches its maximum thickness in March, and starts to recede in June in the northwest (due to the polynya) and in its eastern part (due to the warmer Atlantic water advected along the Greenland coast by the West Greenland Current). Tivy *et al.* (2011) showed that the ice coverage has decreased by 9.5% to 11.1% per decade in Baffin Bay (depending on the region within the bay) over the 1971–2000 period, while Parkinson and Cavalieri (2008) reported a decrease in sea-ice extent of 16% per decade in Baffin Bay/Labrador Sea between 1979 and 2006. Among the five GCMs analyzed, GFDL appears to best represent the historical sea-ice concentrations (Figure 55), but it displays a trend for increasing concentration in spring, unlike all the other models (Figure 56). HadGEM2 has thicker sea ice than the other models and the bay does not get ice-free in summer. The mean simulated sea-ice thicknesses in April (month when sea-ice thickness maxima occurs in most models) for the 1986-2005 period are 93 cm, 99 cm, 110 cm, 129 cm, and 167 cm for CanESM2, MPI, GFDL, IPSL and HadGEM2, respectively.

2.2.1.4 Mixed layer depth

Baffin Bay is characterized by a strong pycnocline near the surface (10–30 m) in summer (e.g., Harrison et al., 1982; Jensen et al., 1999) that deepens in winter (80–100 m; Melling et al., 2001). In the GCMs, the MLD obtained with CanESM2 was anomalous (greater than the MMLD), so we decided to concentrate on MMLD (Figure 57 and Figure 58). The mean simulated MMLD varies between 30 and 60 m, or between 30 and 45 m if we exclude CanESM2 (Figure 58). As expected with the decreasing surface salinity and increasing surface temperature the model predicts, simulated MLD and MMLD are decreasing over the historical period (1960–2005), with multi-model ensemble mean trends of -3.8±6.7 and -1.1±0.8 m per decade, respectively.

2.2.1.5 Nitrate

The World Ocean Atlas shows annual average surface nitrate concentrations of about 1 mmol m^{-3} in the northern area and concentrations of 3–4 mmol m^{-3} in the southern part of the bay (Figure 60). Harrison et al. (1982) found consistently low mixed layer nitrate concentrations (0.15 mmol m^{-3}) at all the stations they visited in Baffin Bay in summer 1978. Jensen et al. (1999) reported that nitrate was below the detection limit in the upper 10 m of the water column in the eastern part of the bay. These concentrations are similar to concentrations found in other Arctic seas with high water-column stability (see section 2.1.1.5). Below the pycnocline (or the subsurface Chl *a* layer, depending on its depth), nitrate concentrations range between 10 and 18 mmol N m^{-3} (see Carmack and McLaughlin, 2011). The mean simulated surface nitrate concentrations with GFDL and MPI are much higher than the observed values (as much as 8 to 10 times higher in some

parts of the bay; Figure 60). Most models show a decreasing trend in surface nitrate concentration over the 1960–2005 period (except for HadGEM2; Figure 61 and Figure 62), while the trends in the 100–400 m layer are more variable (Figure 63 and Figure 64). The multi-model ensemble mean trends for the 1960–2005 period are -0.11± 0.15 mmol m^{-3} per decade at the surface and +0.034± 0.217 mmol m^{-3} per decade for the 100–400 m layer.

2.2.1.6 Primary Production

Except in the West Greenland Current, primary production in Baffin Bay is low, with values comparable to Hudson Bay. Harrison et al. (1982) reported primary production values of 227 mg C m^{-2} d^{-1} in late summer, while Jensen et al. (1999) reported primary production values between 67 and 318 mg C m^{-2} d^{-1} in the eastern part of the bay (when excluding one site with particularly high primary production). Assuming an average of 225 mg C m^{-2} d^{-1} and a 120 day growing season, we get a total annual production of 27 g C m^{-2} or 2.25 mol C m^{-2}. All the models display higher primary production in the West Greenland Current, but the values are generally too high (except for IPSL; Figure 65). Trends over the historical period are divergent (Figure 66 and Figure 67), which results in a null multi-model ensemble mean trend (0.00±0.12 mol C m^{-2} $year^{-1}$ per decade).

2.2.1.7 Chl *a*

Figure 68 (bottom right panel) shows that the annual mean surface Chl *a* concentrations are low in Baffin Bay except for a region in the southeast corresponding to the inflow of the warm West Greenland Current. Most values range between 0.4 and 0.7 mg Chl *a* m^{-3}, while higher values, between 0.7 and 2.5 mg Chl *a* m^{-3}, can be found along Greenland and in the northwest corner of the bay. HadGEM2 best represents the observed Chl *a* values and distribution, followed by MPI (Figure 68). The values displayed by the other models are low. Both Vantrepotte and Mélin (2011) and Li et al. (2006) noted an increase in Chl *a* around the southern tip of Greenland in the last decade or so. The models show weak variable trends, both at the surface and in the 50–100 m layer, over the historical period (Figure 69 and Figure 70), and no firm conclusion can be drawn on historical trends.

2.2.1.8 Oxygen

The World Ocean Atlas gives dissolved oxygen concentrations at the surface of Baffin Bay between 0.35 and 0.39 mol m^{-3} (Figure 71, bottom right panel). IPSL, MPI, and HadGEM2 values are within this range, although they display higher dissolved oxygen concentrations on the northwestern side of the region (Figure 71). GFDL, on the other hand, displays generally low values. Three models (out of four) show a decreasing trend in dissolved oxygen concentration at the surface (Figure 72), while all models show consistent decreasing trends at the 100–400 m depth range for the historical period (Figure 73) with a multi-model ensemble mean of -1.8±0.6 mmol m^{-3} per decade.

2.2.1.9 Ocean acidification

See section 2.1.1.9 for a description of ocean acidification.

The surface properties of Baffin Bay are affected by the Arctic outflow in the west and by Atlantic inflow in the east. The deeper waters of Baffin Bay are relatively isolated, leading to high DIC content from remineralization of organic matter, which in turns leads to low pH and low saturation states (Azetsu-Scott et al., 2010).

2.2.1.9.1 DIC

Azetsu-Scott et al. (2010) report an average DIC concentration of 2.10 mol m^{-3} for the upper layer (0–500m) and an average DIC concentration of 2.20 mol m^{-3} in the deep layer (1000–2400 m). Because there are very few measurements, it is difficult to say which model best represents surface DIC concentrations (Figure 74), but at depth (Figure II-19), HadGEM2 and IPSL values are higher than those reported by Azetsu-Scott et al. (2010). Most models show an increasing trend in surface DIC concentration (except for GFDL; Figure 75). The ensemble mean trend is 0.0012±0.0014 mol m^{-3} per decade for the historical period (1960–2005). This trend is less than half the trend calculated for Hudson Bay (see section 2.1.1.9.1).

2.2.1.9.2 pH

Surface pH in Baffin Bay appears to range between 8.1 and 8.2 (Azetsu-Scott et al., 2010), and surface pH values from all models are within this range. However, from samples taken across Baffin Bay and Davis Strait (Azetsu-Scott et al., 2010), it appears that pH is lower along Baffin Island (Arctic outflow) than along the Greenland Shelf (West Greenland Current). All GCMs have surface pH values within the observed range, but MPI has a better spatial representation, with higher values along the Greenland Shelf (Figure 76). All models show a decreasing trend in surface pH over the historical period, with CanESM2 having the smallest trend and MPI the largest trend (Figure 77). The ensemble mean trend is -0.015 ± 0.003 units per decade.

2.2.1.9.3 Calcium carbonate saturation horizons

The low saturation state of Arctic waters flowing through the Canadian Arctic Archipelago can be traced along western Baffin Bay down to Davis Strait (Azetsu-Scott et al., 2010). In Baffin Bay, the aragonite and calcite saturation horizons vary from 200–500 m and 1000–1500 m, respectively, with shallower depths on the western side of the bay (Azetsu-Scott et al., 2010). The saturation horizon depths obtained with CanESM2 are close to the observed ones for aragonite, while calcite is saturated at all depths.

2.2.2 Future trends (next 50 years)

There are substantial similarities between the changes projected by the two scenarios analyzed in this study (RCP 4.5 and RCP 8.5), with those for RCP 8.5 generally having a larger magnitude.

- **Salinity**: All models show a freshening of the sea surface for the next 50 years for both scenarios (Figure 78), although the freshening trend is stronger with RCP 8.5. The multi-model ensemble mean trends are -0.12±0.12 and -0.19± 0.12 per decade for RCPs 4.5 and 8.5, respectively (slightly higher than in Hudson Bay).

- **Temperature:** All models show an increasing trend for SST, with multi-model ensemble mean trends of 0.12±0.07 and 0.21± 0.09°C per decade for RCPs 4.5 and 8.5, respectively (Figure 79). This corresponds to an increase of 0.6–1.1°C over the next 50 years. The SST increase was observed over the whole bay with all the models (i.e., the trend was variable but always greater than or equal to zero in the different grid cells).

- **Sea Ice:** A diminution of sea-ice thickness is predicted in all the GCMs and with both emission scenarios. The mean sea-ice thicknesses in April for the 2046-2065 period are 79 cm, 79 cm, 87 cm, 94 cm, and 141 cm for CanESM2, MPI, GFDL, IPSL, and HadGEM2, respectively, for RCP 4.5. With the RCP 8.5 scenario, the corresponding sea-ice thicknesses are 79 cm, 73 cm, 79 cm, 87 cm, and 128 cm. These reductions in sea-ice thickness, compared to the 1986-2005 period, correspond to multi-model ensemble mean trends of -3.9 and -5.1 cm per decade for RCP 4.5 and RCP 8.5, respectively. Sea ice is also projected to form later in the fall and to melt earlier in spring (by a few weeks to one month in both cases, which is a little less than in Hudson Bay for the melt period). Figure 80 and Figure 81 show the corresponding sea-ice fraction trends for the months of November, March, and June for RCP 4.5 and RCP 8.5.

- **Mixed layer depth**: All four models that provided MMLD show a decreasing trend. The trends are very similar with RCP 8.5, except for CanESM2, which displays a higher (negative) trend (Figure 82). The multi-model ensemble mean trends for MMLD are -0.7±0.6 and -1.0±0.6 m per decade for RCPs 4.5 and RCP 8.5, respectively, while the trends for MLD (from three models) are -1.8±2.4 and -1.6±1.8 m per decade for RCP 4.5 and RCP 8.5, respectively. If we exclude CanESM2, the resulting MLD trends would be 0.4 m and 0.6 m per decade, for a change of only 2–3 m over the next 50 years.

- **Nitrate**: The models show trends of opposite signs for nitrate concentration at the surface and in the 100–400 m layer for both RCPs 4.5 and 8.5 (Figure 83 to Figure 85). The multi-model ensemble mean trends are -0.09±0.18 and -0.16±0.15 mmol m^{-3} per decade at the surface for RCPs 4.5 and 8.5, respectively, and 0.18±0.37 and 0.08±0.55 mmol m^{-3} per decade in the 100–400 m layer for RCPs 4.5 and 8.5, respectively. Therefore, no firm conclusions can be drawn on the future direction of nitrate concentration changes in Baffin Bay.

- **Primary production**: As was the case for nitrate, the models show divergent trends for primary production with multi-model ensemble mean trends of -0.02±0.20 mol C m^{-2} $year^{-1}$ per decade for both RCP 4.5 and RCP 8.5 (Figure 86). Therefore, no

firm conclusions can be drawn on the future direction of changes in primary production in Baffin Bay.

- **Chlorophyll *a*:** Trends in Chl *a* concentration at the surface and in the 50–100 m layer are variable with the RCP 4.5 scenario but are more consistent among models with the RCP 8.5 scenario, with four out of five models displaying a same sign trend (Figure 87 and Figure 88). The multi-model ensemble mean trends are 0.001±0.019 and -0.01±0.02 mg m^{-3} per decade at the surface and -0.004± 0.012 and 0.0003± 0.005 mg m^{-3} per decade in the 50–100 m layer for RCPs 4.5 and 8.5, respectively. Similar to the situation for nitrate and primary production, no firm conclusions can be drawn on the future direction of Chl *a* changes in Baffin Bay.

- **Oxygen:** Consistent with the predicted sea-surface warming in Baffin Bay, all models show decreasing oxygen concentration at the surface (Figure 89). The multi-model ensemble mean trends at the surface are -0.0009±0.0010 and -0.0013±0.0011 mol m^{-3} per decade for RCP 4.5 and RCP 8.5, respectively. These trends are very similar to the Hudson Bay trends even though surface warming is smaller. In the 100–400 m layer, all models show a decreasing trend except for one with the RCP 8.5 scenario (HadGEM2; Figure 90). The multi-model ensemble mean trends at 100–400 m are -0.003±0.001 and -0.002±0.002 mol m^{-3} per decade for RCP 4.5 and RCP 8.5, respectively. Therefore a small decrease in oxygen concentration is likely.

- **DIC:** Dissolved inorganic carbon concentration trends at the surface are variable, leading to non-significant trends (Figure 91). However, all models show a positive trend in the 100–400 m layer (Figure 92), with multi-model ensemble mean trend of 0.006±0.003 mol m^{-3} per decade for both RCPs 4.5 and 8.5.

- **pH:** All models show similar negative trends for pH at the surface (Figure 93). The multi-model ensemble mean trends are -0.028± 0.004 and -0.043±0.004 units per decade for RCPs 4.5 and 8.5, respectively, representing a pH decrease of 0.14 and 0.22 units over the next 50 years. In the 100–400 m layer, the trend is similar to that at the surface for RCP 4.5 and slightly lower for RCP 8.5 (-0.034±0.006 units per decade).

- **Calcium carbonate saturation horizons:** In Baffin Bay, CanESM2 displays a rather linear trend for aragonite saturation horizon depths, with values of -41 m and -60 m per decade for RCP 4.5 and RCP 8.5, respectively (Figure 94). CanESM2 predicts that the mean aragonite saturation horizon depth in Baffin Bay 50 years from now will be less than 100 m with RCP 4.5, while it would be close to the surface with RCP 8.5. On the other hand, GFDL and HadGEM2 display a rapid shoaling of the saturation horizon until about 2017 with a smoother decrease afterward. The aragonite saturation horizon simulated by HadGEM2 reaches the surface as early as 2032 with the RCP 8.5 scenario (Figure 94).

3 DISCUSSION AND CONCLUSION

We used results from the new generation of climate models with enhanced complexity (CMIP5 intercomparison project) to obtain projections of physical and biogeochemical conditions in Hudson and Baffin bays. One may think that increased complexity could increase uncertainty and not necessarily lead to better results, but recent studies using the output from these models tend to show similar or improved performance. The climate sensitivity (expected warming given a doubling of preindustrial atmospheric carbon dioxide levels) of this new generation of models is similar to the previous generation (Andrews et al., 2012). Moreover, Sillmann et al. (2013) found that the CMIP5 models better represent climate extremes related to temperature and Knutti et al. (2013) found better agreement with observations in general. However, these results concerned only the physics of the models. This is the first generation that includes biogeochemistry, and the results are often quite different among models, especially in Baffin Bay. Hudson Bay is relatively small (from the perspective of global climate models) and more or less isolated from the Arctic and Atlantic Oceans. It is thus surprising that some of the models (MPI and IPSL) have a good representation of the environmental conditions in general (both physical and chemical). However, none of the models stands out as giving a good representation of the environmental conditions in Baffin Bay, although GFDL and MPI were better for about three of the variables analyzed.

It is not possible to predict which model better represents future trends. However, we can safely conclude that sea-surface temperature will increase, that sea-ice concentration, pH, and calcium carbonate saturation horizon will decrease (general model agreement on the direction of change). While no firm conclusions can be reached for Baffin Bay for nitrate concentration, primary production, and Chl *a*, for Hudson Bay there is a possible decrease in nitrate concentration in the upper layers and an increase in integrated primary production with an increase of Chl *a* in the subsurface layer. We have not yet analyzed the reasons for lower model performance in Baffin Bay. However, the different ways in which this bay is connected to the Arctic Ocean add to the differences in the physical structure and circulation of the ocean engine and to the large differences in the number of state variables and parameterization of the biochemical components in the different models (see section 1.1). The characteristics of Arctic waters indeed differ depending on the path taken to reach Baffin Bay (Azetsu-Scott et al., 2010; Torres-Valdés et al., 2013). Moreover, global models generally disagree on what factor, nutrients or light, limits primary production in the Arctic (Steinacher et al., 2010; Popova et al., 2012). Nevertheless, there is a general agreement that the western Arctic and its subarctic seas will be the first, and most strongly, impacted by ocean acidification (Steinacher et al., 2009; Denman et al., 2011). Results from the present exercise show that surface water will likely become undersaturated with respect to calcium carbonate, which may have a strong impact on many marine calcifying organisms (e.g., Doney et al., 2009 and references therein).

GCMs are built to represent climate change at a global scale and in general have difficulties in reproducing the observed sea-ice cover in the Arctic (Parkinson et al., 2006b; a). Regional downscaling systems need to be developed to project future changes

at the regional scale, in order to better reproduce sea ice and mixed layer properties. The biochemical components of the coupled models also need to be improved (e.g., improve nitrate concentrations, include the microbial loop, etc.). This is necessary to better represent the complex dynamics of the regions under study in this document, and the interactions between the physical environment and the biogeochemical variables (e.g. changes in seasonality of the spring bloom associated with sea-ice retreat, changes in total primary production and in the contribution of small/large phytoplankton cells to primary production, expansion of low pH water, and shoaling of the calcium carbonate saturation horizons). With this more detailed knowledge, it will be possible to evaluate the impact on higher trophic levels to determine potential habitat changes, movements of marine organisms, and species shifts.

ACKNOWLEDGEMENTS

We acknowledge the World Climate Research Programme's Working Group on Coupled Modelling, which is responsible for CMIP, and we thank the climate modeling groups (listed in Table 1 of this paper) for producing and making available their model output. For CMIP the U.S. Department of Energy's Program for Climate Model Diagnosis and Intercomparison provided coordinating support and led development of software infrastructure in partnership with the Global Organization for Earth System Science Portals.

We also thank Jim Hamilton, Michael Scarratt, and Laure Devine for their careful review of the report.

REFERENCES

Andrews, T., Gregory, J.M., Webb, M.J., and Taylor, K.E. 2012. Forcing, feedbacks and climate sensitivity in CMIP5 coupled atmosphere-ocean climate models. Geophys. Res. Lett. 39(9): L09712, doi: 10.1029/2012gl051607.

Antonov, J.I., Seidov, D., Boyer, T.P., et al. 2010. World Ocean Atlas 2009 Volume 2: Salinity, *Edited by* S. Levitus, NOAA Atlas NESDIS 69. U. S. G. P. Office, Washington, D.C., 184 pp.

ArcticNet 2012. *Impacts of Environmental Change in the Canadian Coastal Arctic: A Compendium of Research Conducted During ArcticNet Phase I (2004-2008), Volume 2*, *Edited by* R. Pienitz, et al., 256 pp., ArcticNet Inc., Quebec City, Quebec, Canada.

Arora, V.K., Scinocca, J.F., Boer, G.J., et al. 2011. Carbon emission limits required to satisfy future representative concentration pathways of greenhouse gases. Geophys. Res. Lett. 38: L05805, doi: 10.1029/2010gl046270.

Aumont, O., and Bopp, L. 2006. Globalizing results from ocean in situ iron fertilization studies. Global Biogeochem. Cycles 20: GB2017, doi: 10.1029/2005gb002591.

Azetsu-Scott, K., Clarke, A., Falkner, K., et al. 2010. Calcium carbonate saturation states in the waters of the Canadian Arctic Archipelago and the Labrador Sea. J. Geophys. Res. 115(C11): C11021, doi: 10.1029/2009jc005917.

Azetsu-Scott, K., Slauenwhite, D., and Starr, M. (2008), Freshwater and carbon dynamics in Hudson Bay: results from MERICA 2003-2006, paper presented at ArcticNet Science Meeting, Quebec. http://caid.ca/ArtCha2008.pdf.

Bates, N.R., Moran, S.B., Hansell, D.A., and Mathis, J.T. 2006. An increasing CO_2 sink in the Arctic Ocean due to sea-ice loss. Geophys. Res. Lett. 33(23): L23609, doi: 10.1029/2006gl027028.

Cai, W.-J., Chen, L., Chen, B., et al. 2010. Decrease in the CO_2 uptake capacity in an ice-free Arctic Ocean basin. Science **329**(5991): 556-559.

Carmack, E., and McLaughlin, F. 2011. Towards recognition of physical and geochemical change in Subarctic and Arctic Seas. Prog. Oceanogr. **90**(1-4): 90-104.

Chassé, J., Lambert, N., and Lavoie, D. 2013. Precipitation, evaporation and freshwater flux over Canada from six global climate models. Can. Tech. Rep. Hydrog. Ocean. Sci. **287**: xiii + 47 pp.

Christian, J.R., Arora, V.K., Boer, G.J., et al. 2010. The global carbon cycle in the Canadian earth system model (CanESM1): Preindustrial control simulation. J. Geophys. Res. 115(G3): G03014, doi: 10.1029/2008jg000920.

CIS. 2002. Sea ice climatic atlas: Northern Canadian waters 1971-2000. Canadian Ice Services. Ottawa, ON. En56-173/2002, 249 pp.

Collins, W.J., Bellouin, N., Doutriaux-Boucher, M., et al. 2011. Development and evaluation of an earth-system model-HadGEM2. Geosci. Model Dev. **4**(4): 1051-1075.

Danabasoglu, G., Large, W.G., Tribbia, J.J., Gent, P.R., Briegleb, B.P., and McWilliams, J.C. 2006. Diurnal coupling in the tropical oceans of CCSM3. J. Clim. **19**(11): 2347-2365.

Denman, K., Christian, J.R., Steiner, N., Portner, H.O., and Nojiri, Y. 2011. Potential impacts of future ocean acidification on marine ecosystems and fisheries: current knowledge and recommendations for future research. ICES J. Mar. Sci. **68**(6): 1019-1029.

Déry, S.J., Mlynowski, T.J., Hernandez-Henriquez, M.A., and Straneo, F. 2011. Interannual variability and interdecadal trends in Hudson Bay streamflow. J. Mar. Syst. **88**(3): 341-351.

DFO. 2013. Risk-based assessment of climate change impacts and risks on the biological systems and infrastructure within Fisheries and Oceans Canada's mandate - Arctic Large Aquatic Basin. DFO Can. Sci. Advis. Sec. Sci. Resp. **2012/042**.

Doney, S.C., Fabry, V.J., Feely, R.A., and Kleypas, J.A. 2009. Ocean acidification: The other CO_2 problem. Annu. Rev. Mar. Sci. **1**(1): 169-192.

Drinkwater, K.F., and Jones, E.P. 1987. Density stratification, nutrient and chlorophyll distributions in the Hudson Strait region during summer and their relation to tidal mixing. Cont. Shelf Res. **7**(6): 599-607.

Dufresne, J.L., Foujols, M.A., Denvil, S., et al. 2013. Climate change projections using the IPSL-CM5 Earth System Model: from CMIP3 to CMIP5. Clim. Dyn. **40**(9-10): 2123-2165.

Dunne, J.P., John, J.G., Adcroft, A.J., et al. 2012. GFDL's ESM2 global coupled climate-carbon earth system models. Part I: physical formulation and baseline simulation characteristics. J. Clim. **25**(19): 6646-6665.

Dunne, J.P., John, J.G., Shevliakova, E., et al. 2013. GFDL's ESM2 global coupled climate-carbon earth system models. Part II: carbon system formulation and baseline simulation characteristics. J. Clim. **26**(7): 2247-2267.

Feely, R.A., Doney, S.C., and Cooley, S.R. 2009. Ocean acidification: present conditions and future changes in a high-CO_2 world. Oceanography **22**(4): 36-47.

Ferland, J., Gosselin, M., and Starr, M. 2011. Environmental control of summer primary production in the Hudson Bay system: The role of stratification. J. Mar. Syst. **88**(3): 385-400.

Fetterer, F., Knowles, K., Meier, W., and Savoie, M. 2009. Sea ice index. National Snow and Ice Data Center. Boulder, Colorado USA.

Flato, G.M., Boer, G.J., Lee, W.G., McFarlane, N.A., Ramsden, D., Reader, M.C., and Weaver, A.J. 2000. The Canadian centre for climate modelling and analysis global coupled model and its climate. Clim. Dyn. **16**: 451-467.

Gagnon, A.S., and Gough, W.A. 2005. Trends in the dates of ice freeze-up and breakup over Hudson Bay, Canada. Arctic **58**(4): 370-382.

Galbraith, P.S., and Larouche, P. 2011. Sea-surface temperature in Hudson Bay and Hudson Strait in relation to air temperature and ice cover breakup, 1985-2009. J. Mar. Syst. **87**: 66-78.

Garcia, H.E., Locarnini, R.A., Boyer, T.P., Antonov, J.I., Baranova, O.K., Zweng, M.M., and Johnson, D.R. 2010a. World Ocean Atlas 2009, Volume 3: Dissolved Oxygen, Apparent Oxygen Utilization, and Oxygen Saturation, *Edited by* S. Levitus, NOAA Atlas NESDIS 70. U. S. G. P. Office, Washington, D.C., 344 pp.

Garcia, H.E., Locarnini, R.A., Boyer, T.P., Antonov, J.I., Zweng, M.M., Baranova, O.K., and Johnson, D.R. 2010b. World Ocean Atlas 2009, Volume 4: Nutrients (phosphate,

nitrate, silicate), *Edited by* S. Levitus, NOAA Atlas NESDIS 71. U. S. G. P. Office, Washington, D.C., 398 pp.

Granskog, M.A., Macdonald, R.W., Mundy, C.J., and Barber, D.G. 2007. Distribution, characteristics and potential impacts of chromophoric dissolved organic matter (CDOM) in Hudson Strait and Hudson Bay, Canada. Cont. Shelf Res. **27**(15): 2032-2050.

Griffies, S.M., Gnanadesikan, A., Dixon, K.W., et al. 2005. Formulation of an ocean model for global climate simulations. Ocean Science **1**(1): 45-79.

Hamilton, J.M., and Wu, Y. 2013. Synopsis and trends in the physical environment of Baffin Bay and Davis Strait. Can. Tech. Rep. Hydrogr. Ocean Sci. **282**: vi + 39 pp.

Harrison, W.G., Platt, T., and Irwin, B. 1982. Primary production and nutrient assimilation by natural phytoplankton populations of the eastern Canadian Arctic. Can. J. Fish. Aquat. Sci. **39**(2): 335-345.

Harvey, M., Starr, M., Therriault, J.-C., Saucier, F., and Gosselin, M. 2006. MERICA-Nord Program: Monitoring and research in the Hudson Bay complex. AZMP Bulletin PMZA **5**: 27-32.

Hofmann, A.F., Peltzer, E.T., Walz, P.M., and Brewer, P.G. 2011. Hypoxia by degrees: Establishing definitions for a changing ocean. Deep-Sea Res. I **58**(12): 1212-1226.

Hunke, E., and Lipscomb, W.H. 2004. CICE: The Los Alamos Sea Ice Model, documentation and software, Version 3.1. Los Alamos National Laboratory. Los Alamos, NM. Tech. Rep. LA-CC-98-16, 56 pp.

Ilyina, T., Six, K.D., Segschneider, J., Maier-Reimer, E., Li, H., and Nunez-Riboni, I. 2013. The global ocean biogeochemistry model HAMOCC: Model architecture and performance as component of the MPI-Earth System Model in different CMIP5 experimental realizations. J. Adv. Model. Earth Syst. **5**: 287-315.

Jensen, H.M., Pedersen, L., Burmeister, A., and Hansen, B.W. 1999. Pelagic primary production during summer along 65 to 72 degrees N off West Greenland. Polar Biol. **21**(5): 269-278.

Johns, T.C., Durman, C.F., Banks, H.T., et al. 2006. The new Hadley Centre Climate Model (HadGEM1): Evaluation of coupled simulations. J. Clim. **19**(7): 1327-1353.

Jungclaus, J.H., Keenlyside, N., Botzet, M., et al. 2006. Ocean circulation and tropical variability in the coupled model ECHAM5/MPI-OM. J. Clim. **19**(16): 3952-3972.

Kahru, M., Brotas, V., Manzano-Sarabia, M., and Mitchell, B.G. 2011. Are phytoplankton blooms occurring earlier in the Arctic? Global Change Biology **17**(4): 1733-1739.

Knutti, R., Masson, D., and Gettelman, A. 2013. Climate model genealogy: Generation CMIP5 and how we got there. Geophys. Res. Lett. **40**(6): 1194-1199.

Kwok, R. 2007. Baffin Bay ice drift and export: 2002-2007. Geophys. Res. Lett. 34(19), doi: 10.1029/2007gl031204.

Ladouceur, S. 2007. Évaluation des changements hydrographiques de la Baie d'Hudson et du Bassin de Foxe au cours des derniers siècles à partir de traceurs palynologiques et micropaléontologiques, MSc thesis, 78 pp, Université du Québec à Montréal, Montreal, QC.

Lapoussiere, A., Michel, C., Gosselin, M., and Poulin, M. 2009. Spatial variability in organic material sinking export in the Hudson Bay system, Canada, during fall. Cont. Shelf Res. **29**(9): 1276-1288.

Lapoussiere, A., Michel, C., Gosselin, M., Poulin, M., Martin, J., and Tremblay, J.E. 2013. Primary production and sinking export during fall in the Hudson Bay system, Canada. Cont. Shelf Res. **52**: 62-72.

Large, W.G., Danabasoglu, G., McWilliams, J.C., Gent, P.R., and Bryan, F.O. 2001. Equatorial circulation of a global ocean climate model with anisotropic horizontal viscosity. J. Phys. Oceanogr. **31**(2): 518-536.

Large, W.G., McWilliams, J.C., and Doney, S.C. 1994. Oceanic vertical mixing - a review and a model with a nonlocal boundary-layer parameterization. Rev. Geophys. **32**(4): 363-403.

Lavoie, D., Denman, K.L., and Macdonald, R.W. 2010. Effects of future climate change on primary productivity and export fluxes in the Beaufort Sea. J. Geophys. Res. 115, doi: 10.1029/2009jc005493.

Lavoie, D., Lambert, N., Ben Mustapha, S., and van der Baaren, A. 2013. Projections of future physical and biogeochemical conditions in the Northwest Atlantic from CMIP5 Global Climate Models. Can. Tech. Rep. Hydrogr. Ocean. Sci. **285**: xiv + 156 pp.

Lavoie, D., Macdonald, R.W., and Denman, K.L. 2009. Primary productivity and export fluxes on the Canadian shelf of the Beaufort Sea: A modelling study. J. Mar. Syst. **75**: 17-32.

Li, W.K.W., Harrison, W.G., and Head, E.J.H. 2006. Coherent sign switching in multiyear trends of microbial plankton. Science **311**(5764): 1157-1160.

Locarnini, R.A., Mishonov, A.V., Antonov, J.I., Boyer, T.P., Garcia, H.E., Baranova, O.K., Zweng, M.M., and Johnson, D.R. 2010. World Ocean Atlas 2009, Volume 1: Temperature, *Edited by* S. Levitus, NOAA Atlas NESDIS 68. U. S. G. P. Office, Washington, D.C., 184 pp.

Loder, J.W., and van der Baaren, A. 2013. Climate change projections for the Northwest Atlantic from six CMIP5 Earth System Models. Can. Tech.. Rep. Hydrogr. Ocean. Sci. **286**: xiv + 112 pp.

Madec, G., and Imbard, M. 1996. A global ocean mesh to overcome the North Pole singularity. Clim. Dyn. **12**(6): 381-388.

Marsland, S.J., Haak, H., Jungclaus, J.H., Latif, M., and Roske, F. 2003. The Max-Planck-Institute global ocean/sea ice model with orthogonal curvilinear coordinates. Ocean Modelling **5**(2): 91-127.

Martin, G.M., Bellouin, N., Collins, W.J., et al. 2011. The HadGEM2 family of Met Office Unified Model climate configurations. Geosci. Model Dev. **4**(3): 723-757.

Martin, J., Tremblay, J.É., Gagnon, J., et al. 2010. Prevalence, structure and properties of subsurface chlorophyll maxima in Canadian Arctic waters. Mar. Ecol. Prog. Ser. **412**: 69-84.

Melling, H., Gratton, Y., and Ingram, G. 2001. Ocean circulation within the North Water Polynya of Baffin Bay. Atmosphere-Ocean **39**(3): 301-325.

Palmer, J.R., and Totterdell, I.J. 2001. Production and export in a global ocean ecosystem model. Deep-Sea Res. I **48**(5): 1169-1198.

Parkinson, C.L., and Cavalieri, D.J. 2008. Arctic sea ice variability and trends, 1979 - 2006. J. Geophys. Res. 113: C07003, doi: 10.1029/2007jc004558.

Parkinson, C.L., Vinnikov, K.Y., and Cavalieri, D.J. 2006a. Correction to 'Evaluation of the simulation of the annual cycle of Arctic and Antarctic sea ice coverages by 11 major global climate models'. J. Geophys. Res. 111: C12009, doi: 10.1029/2006jc003949.

Parkinson, C.L., Vinnikov, K.Y., and Cavalieri, D.J. 2006b. Evaluation of the simulation of the annual cycle of Arctic and Antarctic sea ice coverages by 11 major global climate models. J. Geophys. Res. 111: C07012, doi: 10.1029/2005jc003408.

Popova, E.E., Yool, A., Coward, A.C., et al. 2012. What controls primary production in the Arctic Ocean? Results from an intercomparison of five general circulation models with biogeochemistry. J. Geophys. Res. 117: C00D12, doi: 10.1029/2011jc007112.

Prinsenberg, S.J. 1984. Freshwater contents and heat budgets of James Bay and Hudson-Bay. Cont. Shelf Res. **3**(2): 191-200.

Prinsenberg, S.J. 1986. Salinity and temperature distributions of Hudson Bay and James Bay. *In Canadian Inland Seas*. *Edited by* I. P. Martini. Elsevier Science Publishers, Amsterdam. pp. 163-186.

Sabine, C.L., Feely, R.A., Gruber, N., et al. 2004. The oceanic sink for anthropogenic CO_2. Science **305**(5682): 367-371.

Sakaguchi, K., Zeng, X., and Brunke, M.A. 2012. The hindcast skill of the CMIP ensembles for the surface air temperature trend. J. Geophys. Res. 117(D16): D16113, doi: 10.1029/2012jd017765.

Sibert, V., Zakardjian, B., Gosselin, M., Starr, M., Senneville, S., and LeClainche, Y. 2011. 3D bio-physical model of the sympagic and planktonic productions in the Hudson Bay system. J. Mar. Syst. **88**(3): 401-422.

Sillmann, J., Kharin, V.V., Zhang, X., Zwiers, F.W., and Bronaugh, D. 2013. Climate extremes indices in the CMIP5 multimodel ensemble: Part 1. Model evaluation in the present climate. J. Geophys. Res. **118**(4): 1716-1733.

St-Laurent, P., Straneo, F., and Barber, D.G. 2012. A conceptual model of an Arctic sea. J. Geophys. Res. 117(C6): C06010, doi: 10.1029/2011jc007652.

Steinacher, M., Joos, F., Frölicher, T.L., et al. 2010. Projected 21st century decrease in marine productivity: a multi-model analysis. Biogeosciences **7**(3): 979-1005.

Steinacher, M., Joos, F., Frolicher, T.L., Plattner, G.K., and Doney, S.C. 2009. Imminent ocean acidification in the Arctic projected with the NCAR global coupled carbon cycle-climate model. Biogeosciences **6**(4): 515-533.

Steiner, N., Galbraith, P., Hamilton, J., et al. 2013. Climate change assessment in the Arctic Basin Part 1: Trends and projections - A contribution to the Aquatic Climate Change Adaptation Services Program. Can. Tech. Rep. Fish. Aquat. Sci. **3042**: xv + 163 pp.

Stewart, D.B., and Lockhart, W.L. 2005. An overview of the Hudson Bay marine ecosystem. Can. Tech. Rep. Fish. Aquat. Sci. **2586**: i+487 pp.

Tang, C.C.L., Ross, C.K., Yao, T., Petrie, B., DeTracey, B.M., and Dunlap, E. 2004. The circulation, water masses and sea-ice of Baffin Bay. Prog. Oceanogr. **63**(4): 183-228.

Taylor, K.E., Stouffer, R.J., and Meehl, G.A. 2012. An overview of CMIP5 and the experiment design. Bull. Am. Meteorol. Soc. **93**(4): 485-498.

Tivy, A., Howell, S.E.L., Alt, B., McCourt, S., Chagnon, R., Crocker, G., Carrieres, T., and Yackel, J.J. 2011. Trends and variability in summer sea ice cover in the Canadian Arctic based on the Canadian Ice Service Digital Archive, 1960-2008 and 1968-2008. J. Geophys. Res. 116(C3): C03007, doi: 10.1029/2009jc005855.

Torres-Valdés, S., Tsubouchi, T., Bacon, S., et al. 2013. Export of nutrients from the Arctic Ocean. J. Geophys. Res. 118, doi: 10.1002/jgrc.20063.

Vantrepotte, V., and Mélin, F. 2011. Inter-annual variations in the SeaWiFS global chlorophyll a concentration (1997-2007). Deep-Sea Res. I **58**(4): 429-441.

Winton, M. 2000. A reformulated three-layer sea ice model. J. Atmos. Ocean. Technol. **17**(4): 525-531.

Zahariev, K., Christian, J.R., and Denman, K.L. 2008. Preindustrial, historical, and fertilization simulations using a global ocean carbon model with new parameterizations of iron limitation, calcification, and N_2 fixation. Prog. Oceanogr. **77**(1): 56-82.

Zeebe, R.E., Zachos, J.C., Caldeira, K., and Tyrrell, T. 2008. Oceans: Carbon emissions and acidification. Science **321**(5885): 51-52.

Zhang, W., and Jin, F.-F. 2012. Improvements in the CMIP5 simulations of ENSO-SSTA meridional width. Geophys. Res. Lett. 39(23): L23704, doi: 10.1029/2012gl053588.

Zweng, M.M., and Münchow, A. 2006. Warming and freshening of Baffin Bay, 1916-2003. J. Geophys. Res. 111: C07016, doi: 10.1029/2005JC003093.

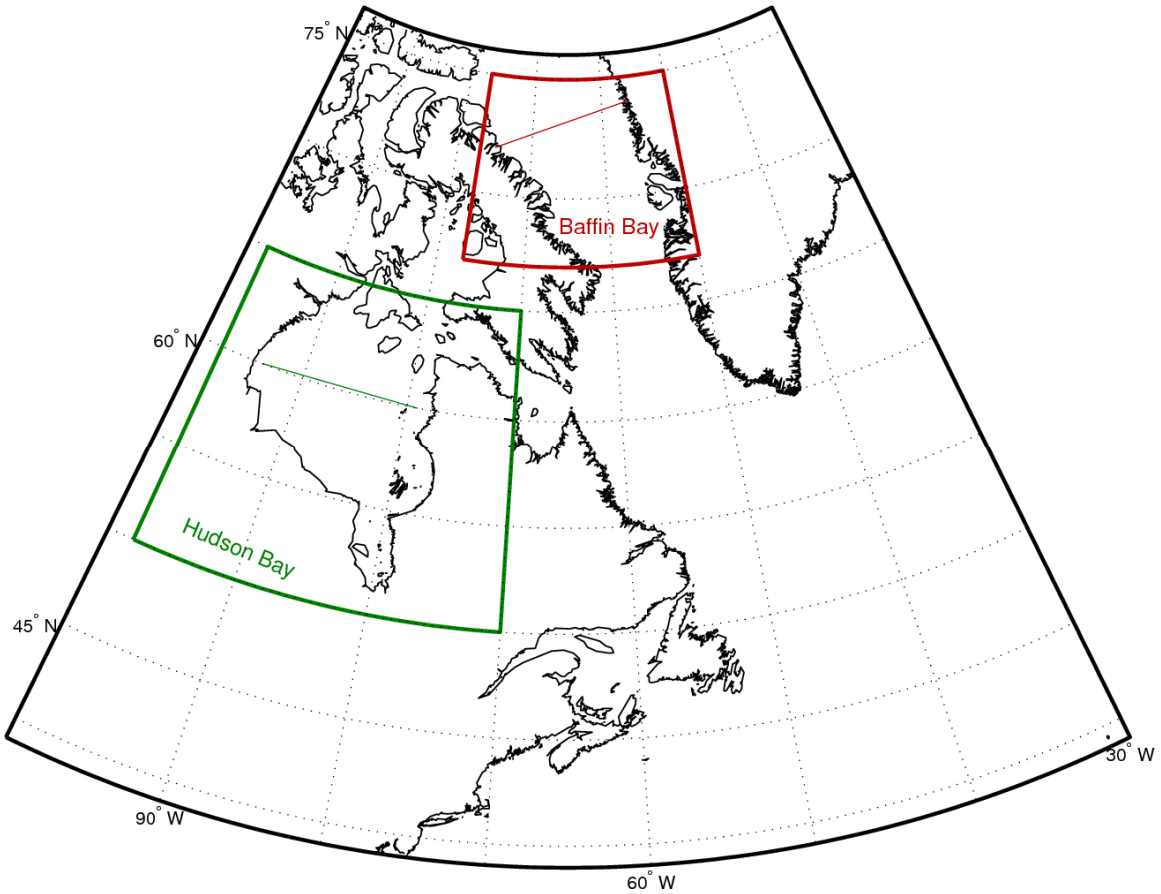

Figure 1. Regions selected for trend analysis with transect positions shown. The transect in Hudson Bay corresponds to that of MERICA (Harvey et al., 2006).

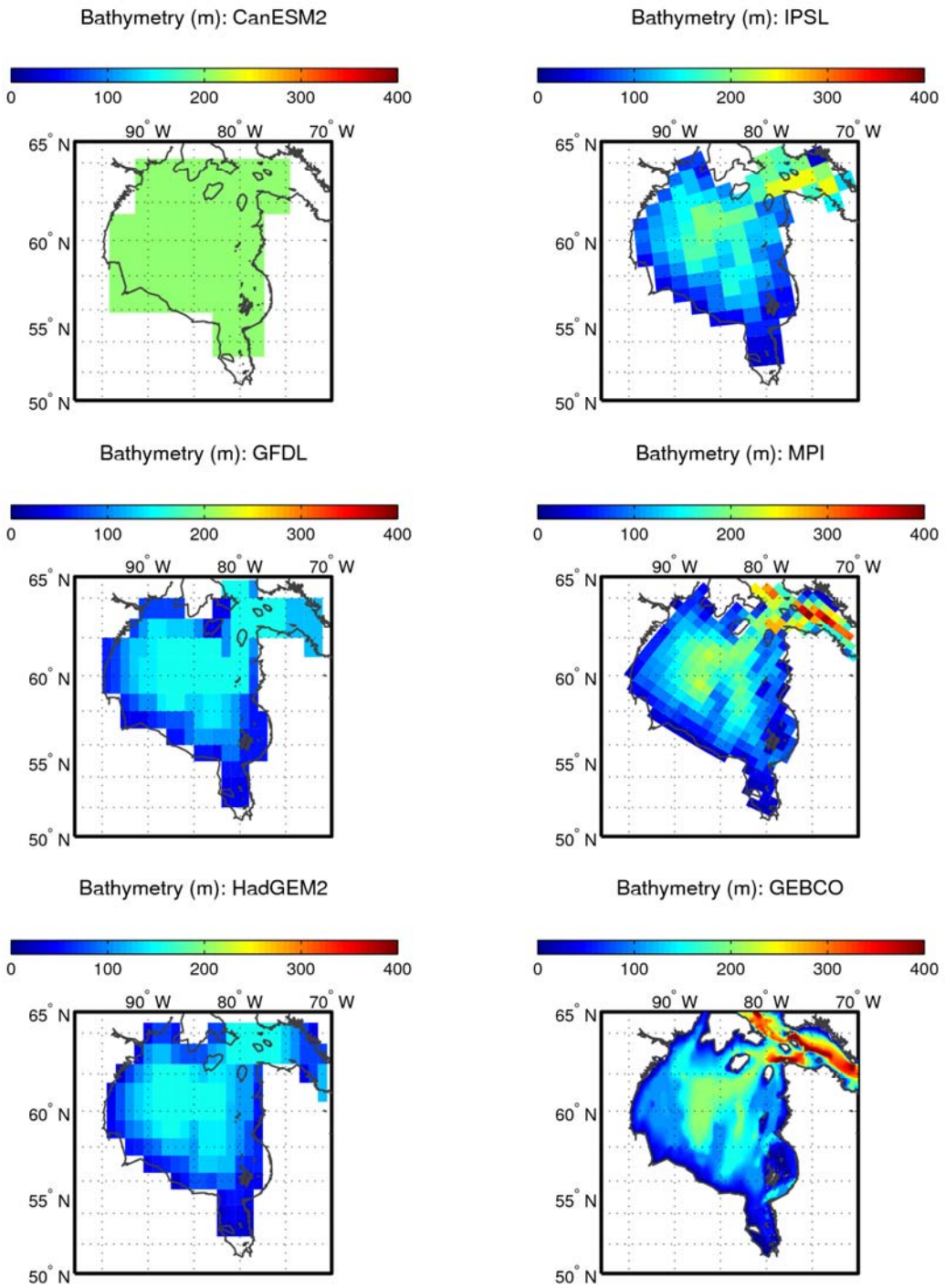

Figure 2. **Bathymetry of Hudson Bay in the different models and bathymetry from the General Bathymetric Chart of the Oceans (GEBCO, www.gebco.net).**

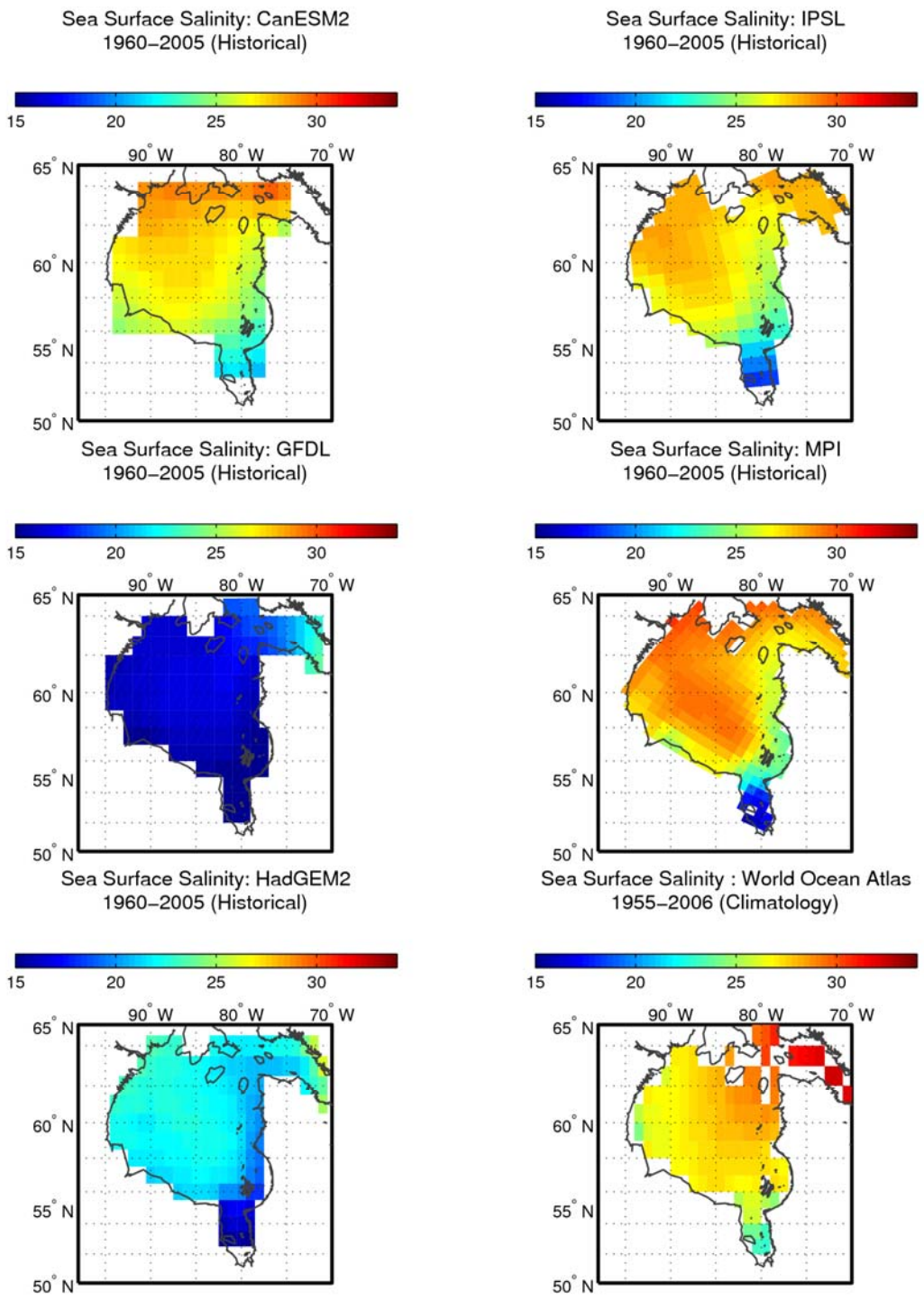

Figure 3. Mean simulated sea-surface salinity in Hudson Bay for the historical period (1960–2005) and mean annual sea-surface salinity from the World Ocean Atlas (Antonov et al., 2010).

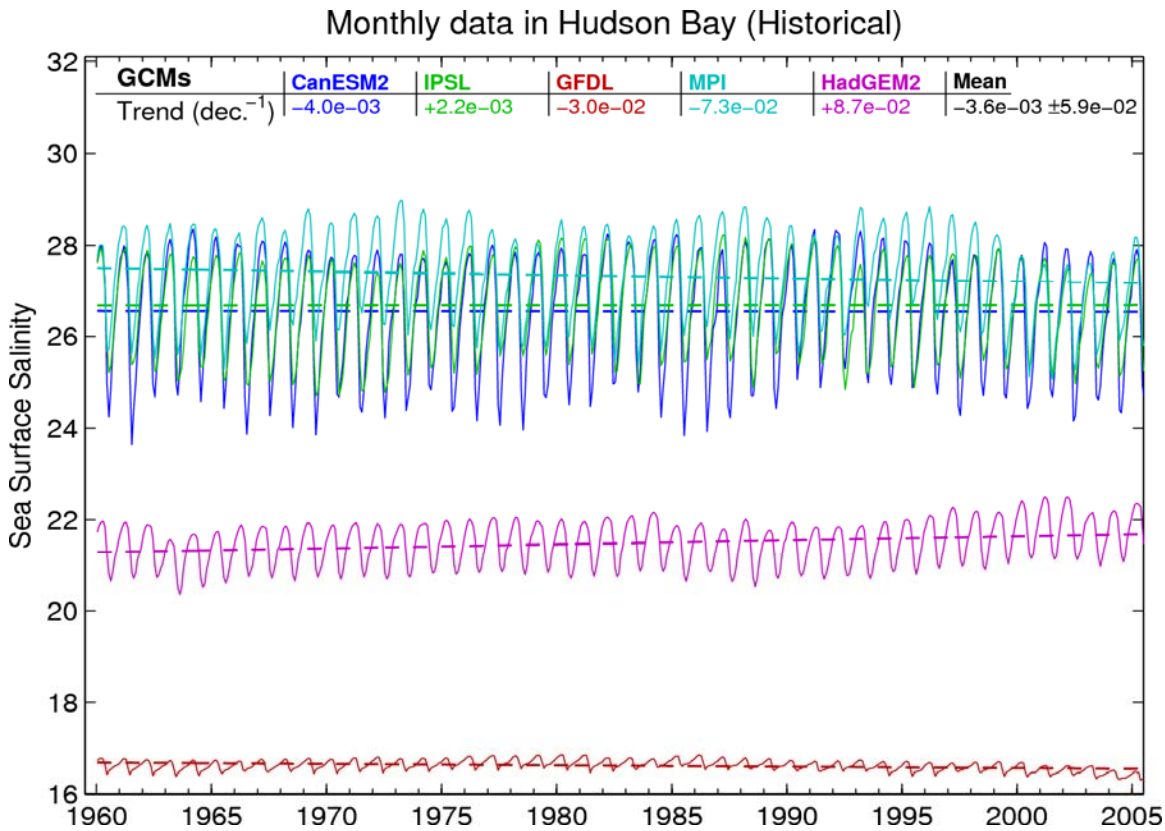

Figure 4. Average sea-surface salinity trends (per decade) over Hudson Bay (see Figure 1) for the historical period (1960–2005).

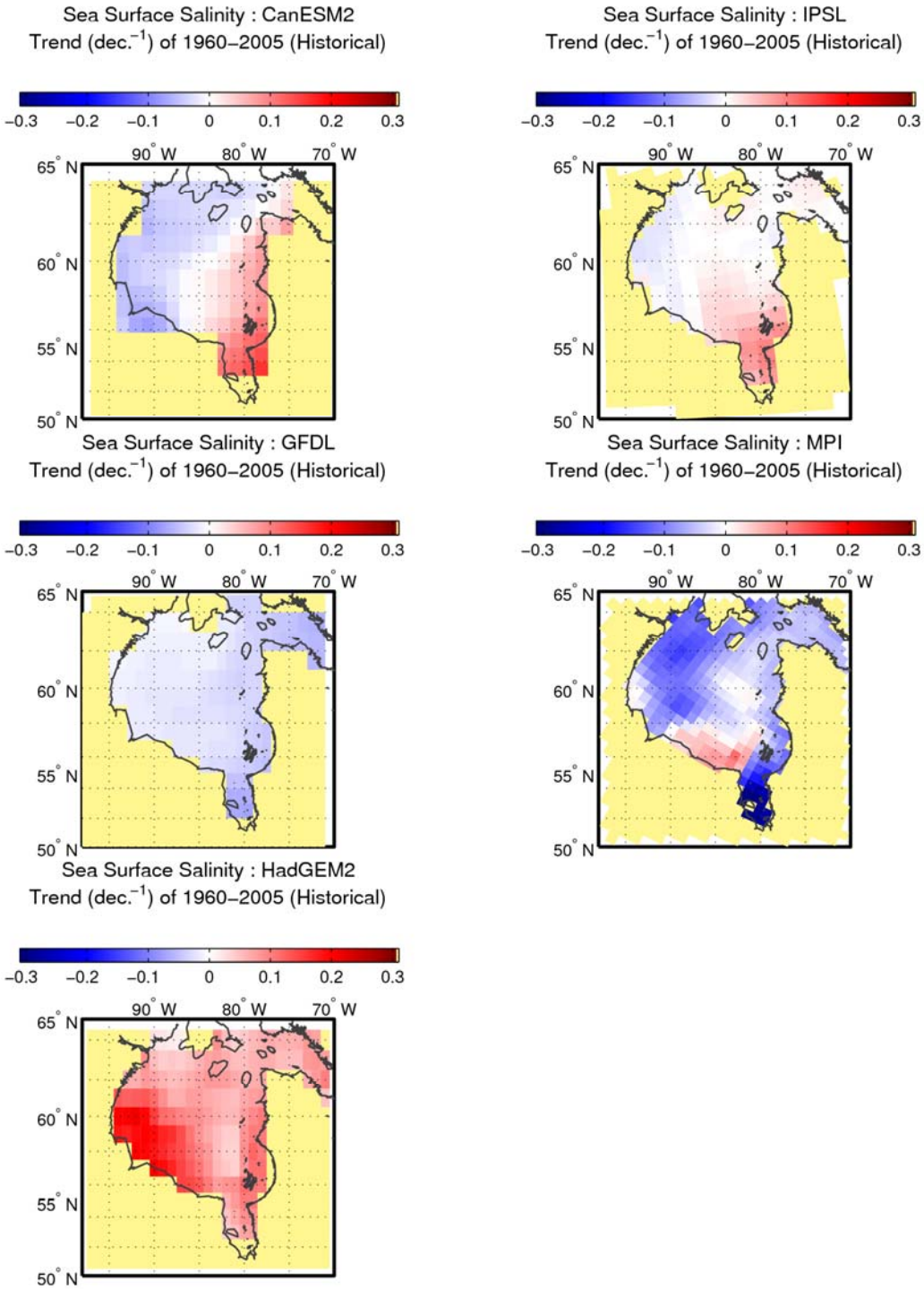

Figure 5. Sea-surface salinity trends (per decade) in each grid cell in Hudson Bay for the historical period (1960–2005).

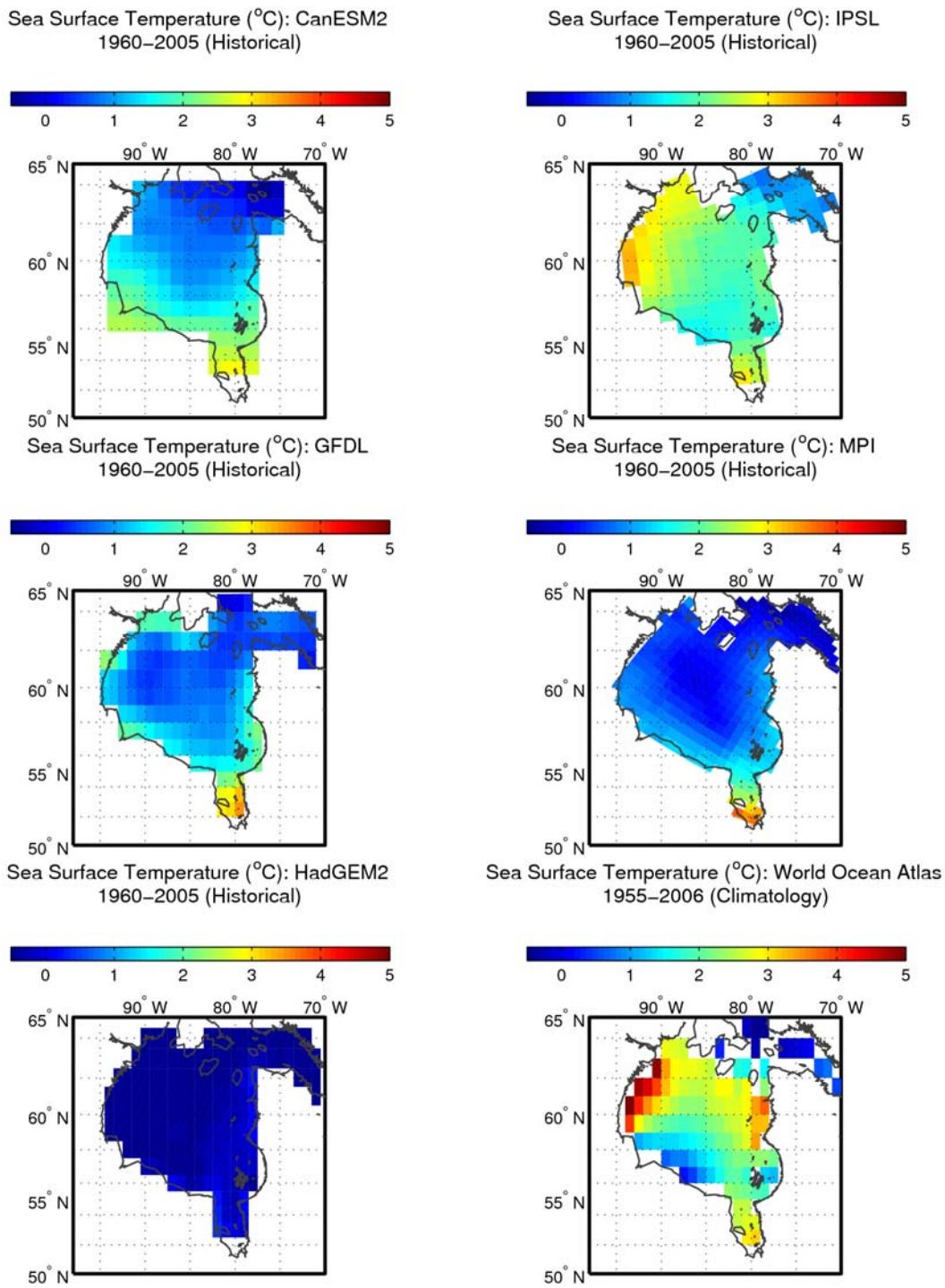

Figure 6. Mean simulated sea-surface temperature for the historical period (1960–2005) and annual sea-surface temperature from the World Ocean Atlas (Locarnini et al., 2010).

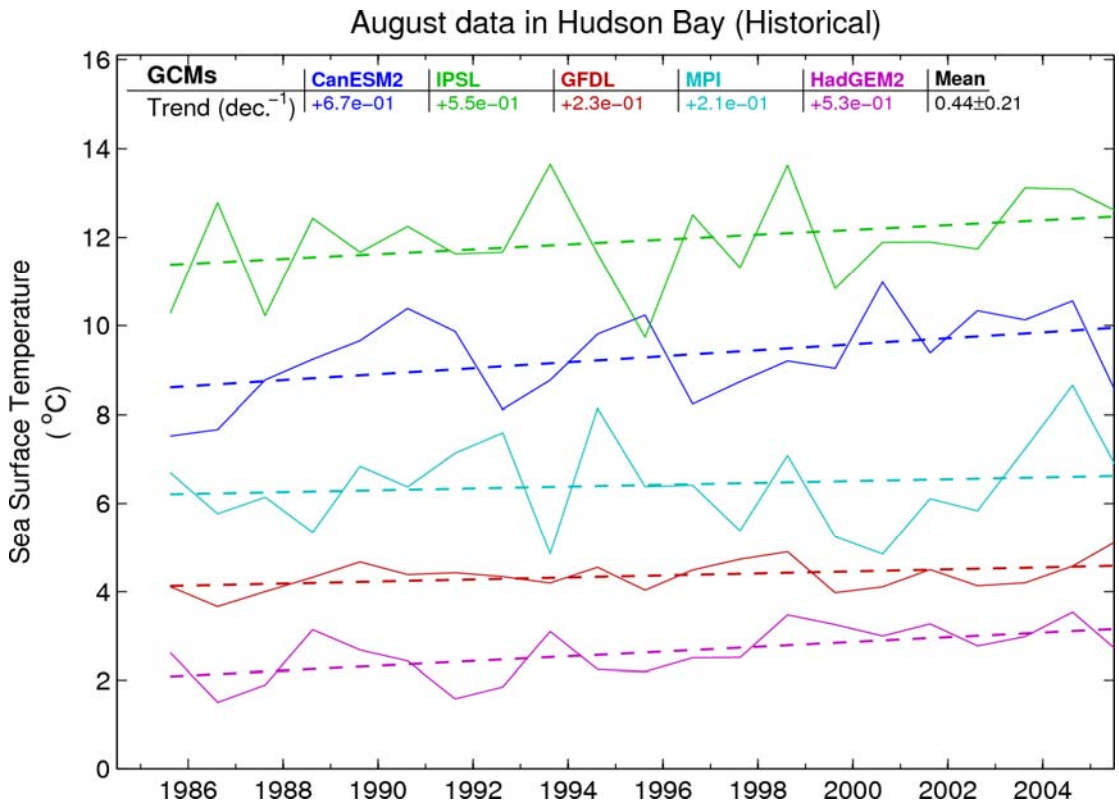

Figure 7. Simulated August sea-surface temperature trends (°C/decade) in Hudson Bay for the historical period between 1985 and 2005.

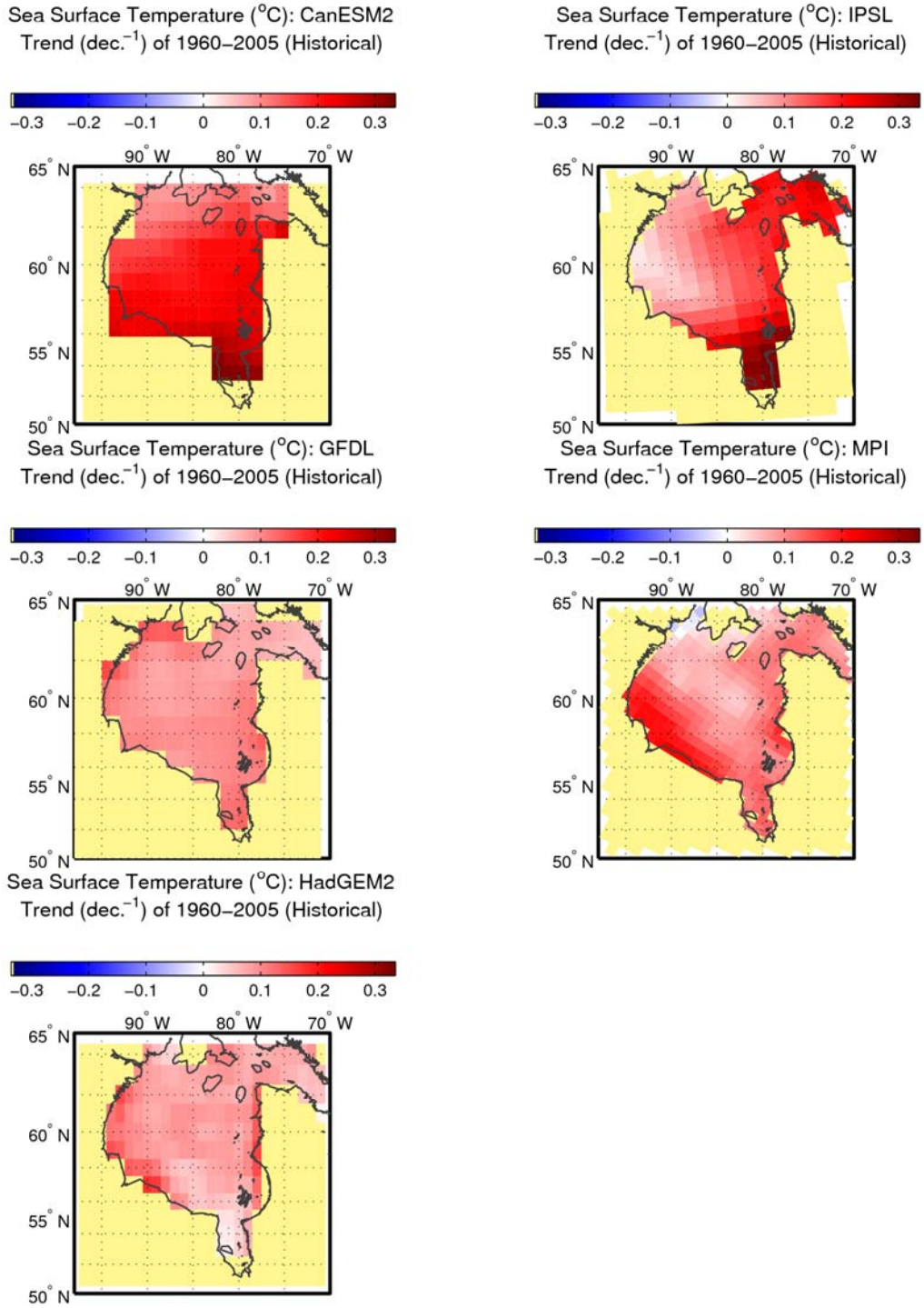

Figure 8. Sea-surface temperature trends (°C/decade) in each grid cell from the historical simulations (1960–2005).

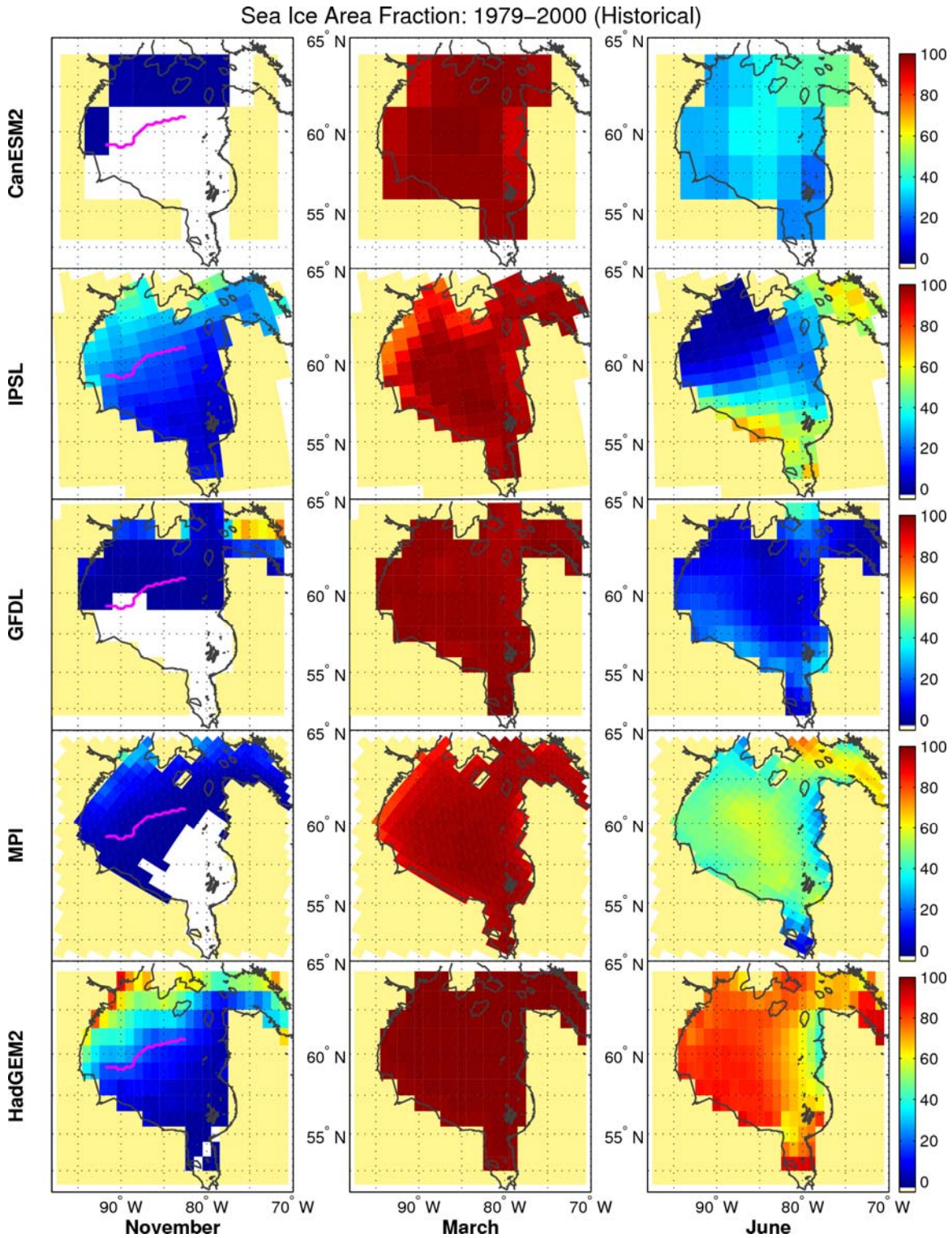

Figure 9. Average sea-ice concentration in Hudson Bay for November, March, and June for the historical period (1979–2000) and with the five GCMs. The magenta line represents the median extent (15% limit) measured by Fetterer et al. (2009) for the same period.

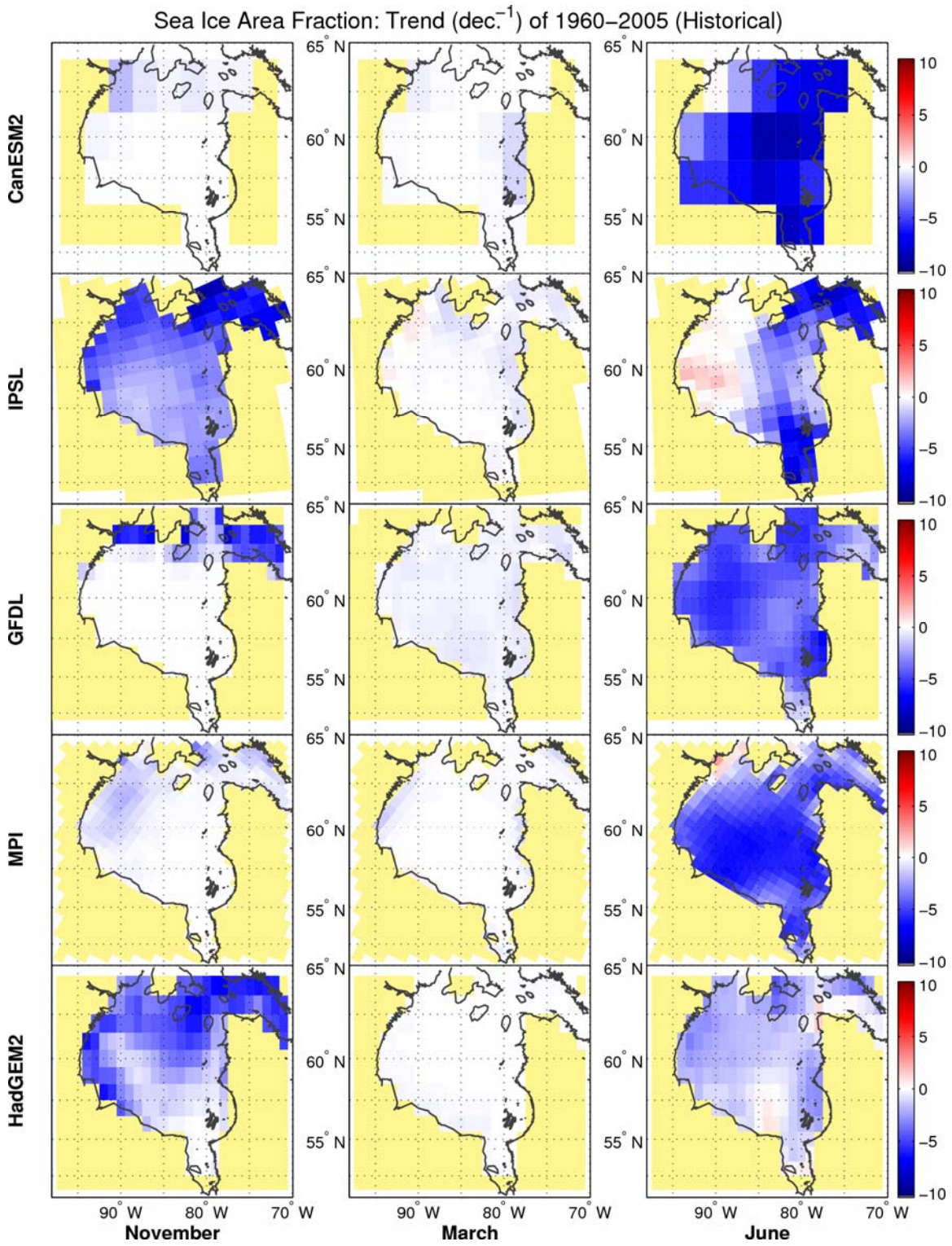

Figure 10. Sea-ice concentration trends (%/decade) in each grid cell in Hudson Bay for November, March, and June for the historical period (1960–2005) and with the 5 GCMs.

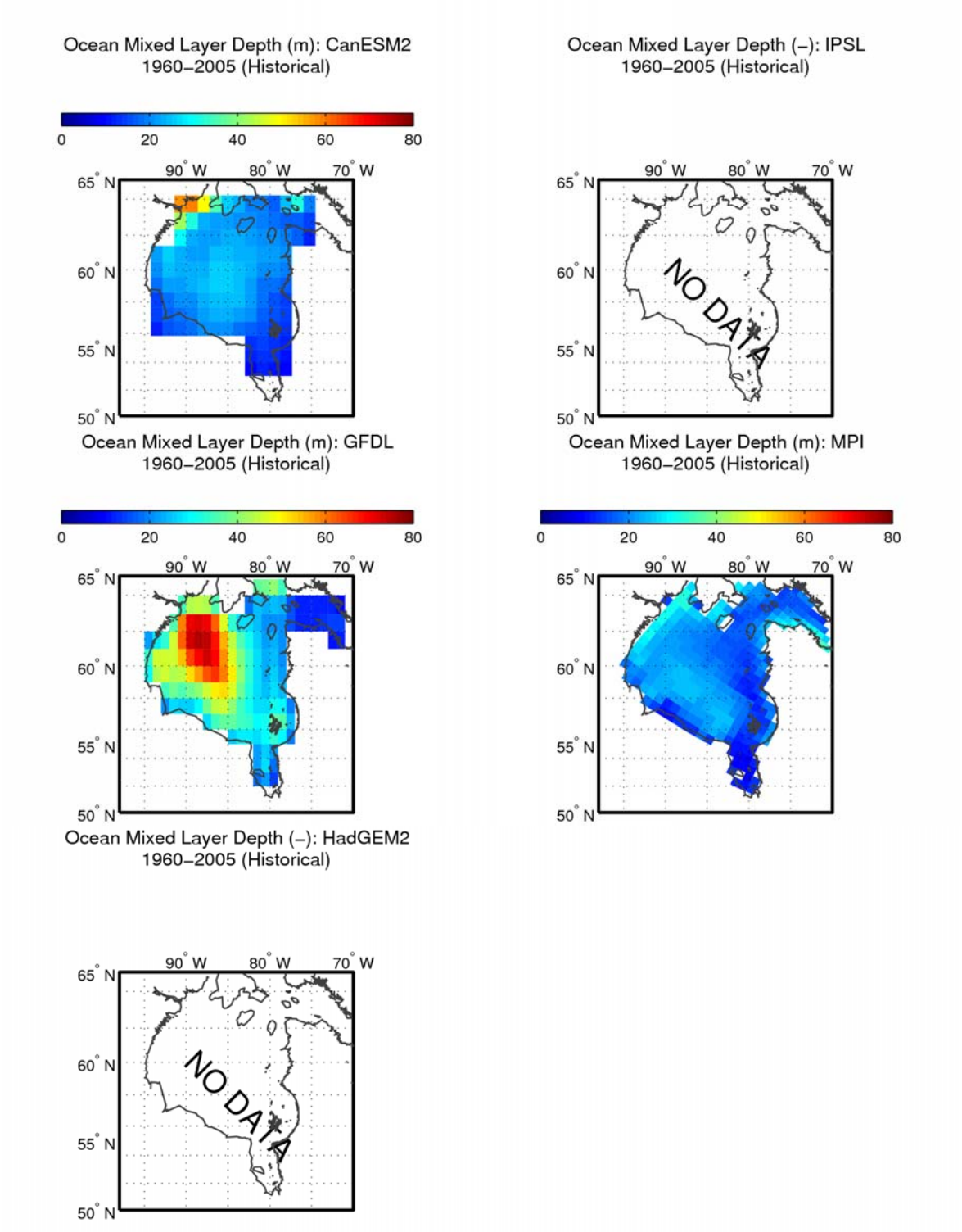

Figure 11. Average mixed layer depth in Hudson Bay for the historical period (1960–2005).

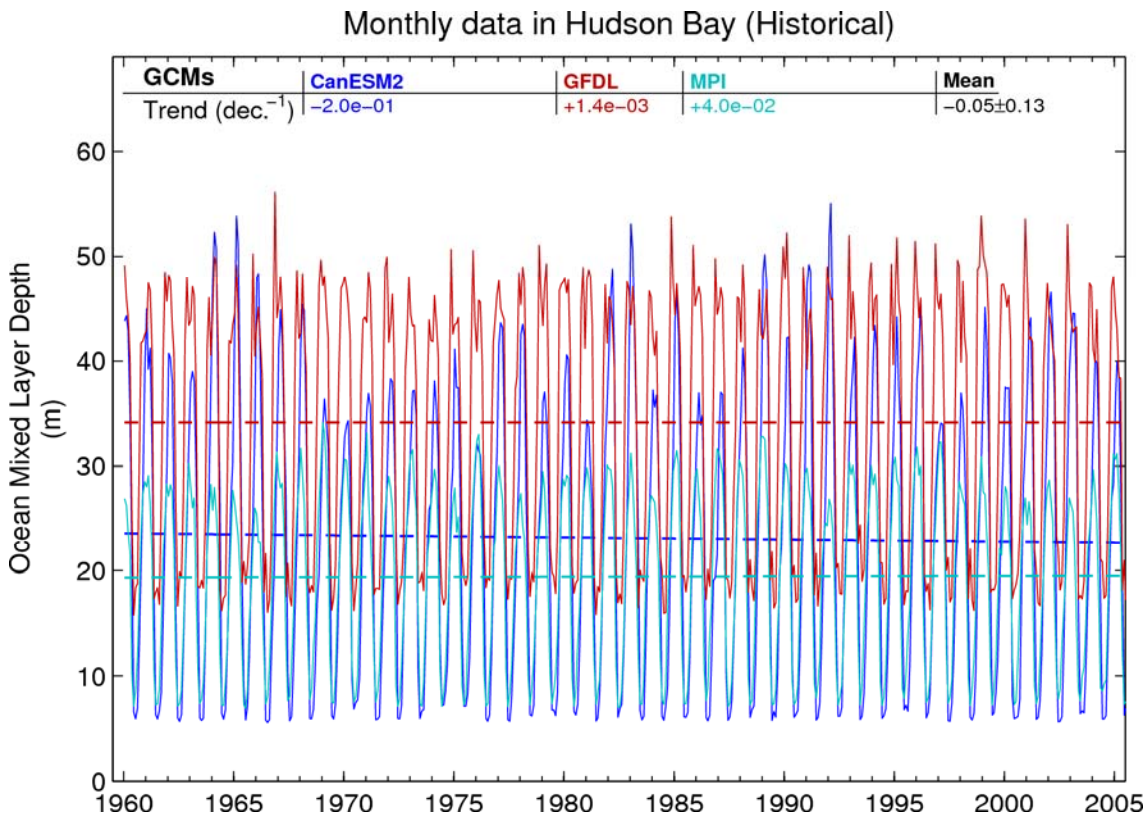

Figure 12. Ocean mixed layer depth trends (m/decade) in Hudson Bay for the historical period (1960–2005).

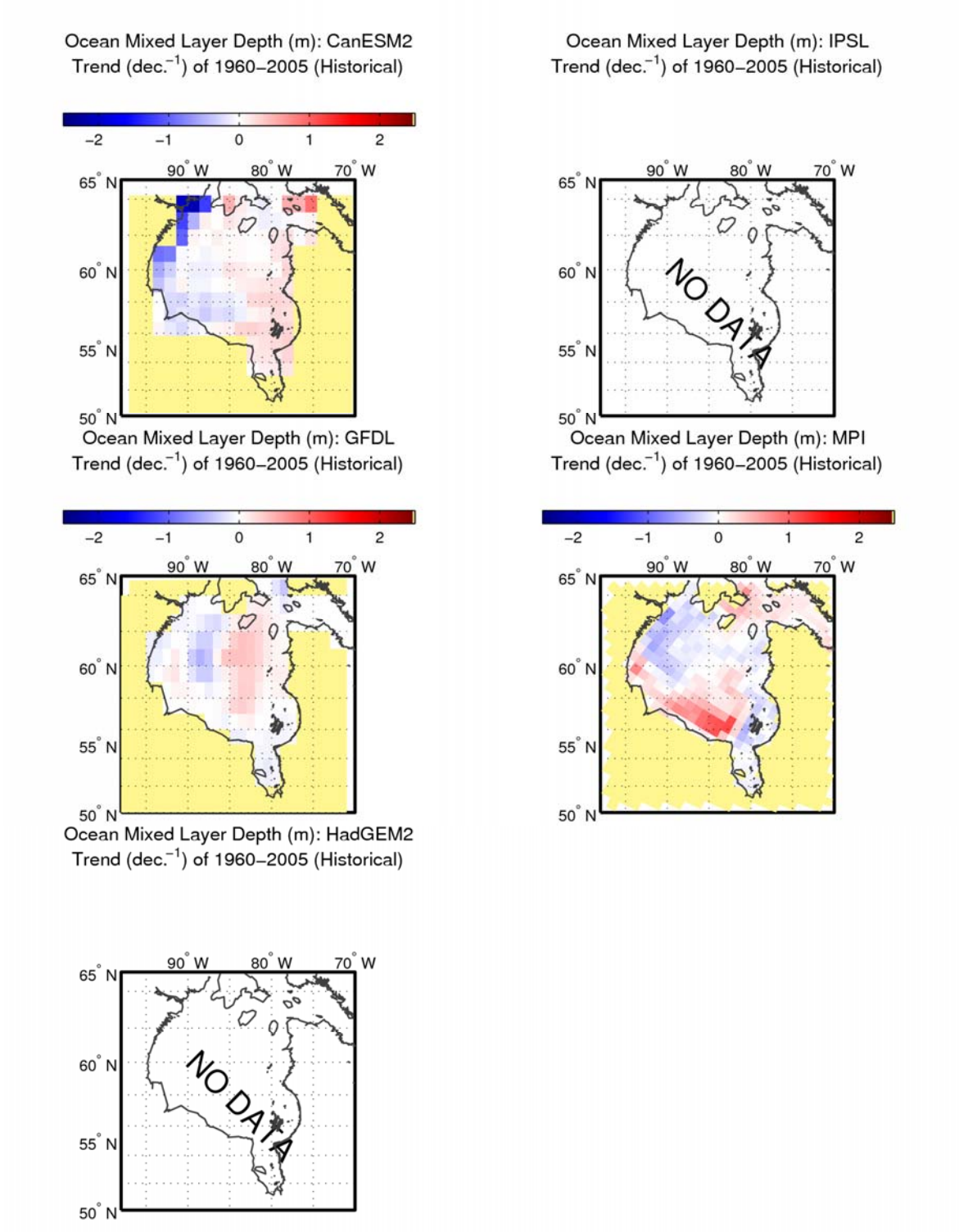

Figure 13. Ocean mixed layer depth trends (m/decade) in Hudson Bay for the historical period (1960–2005).

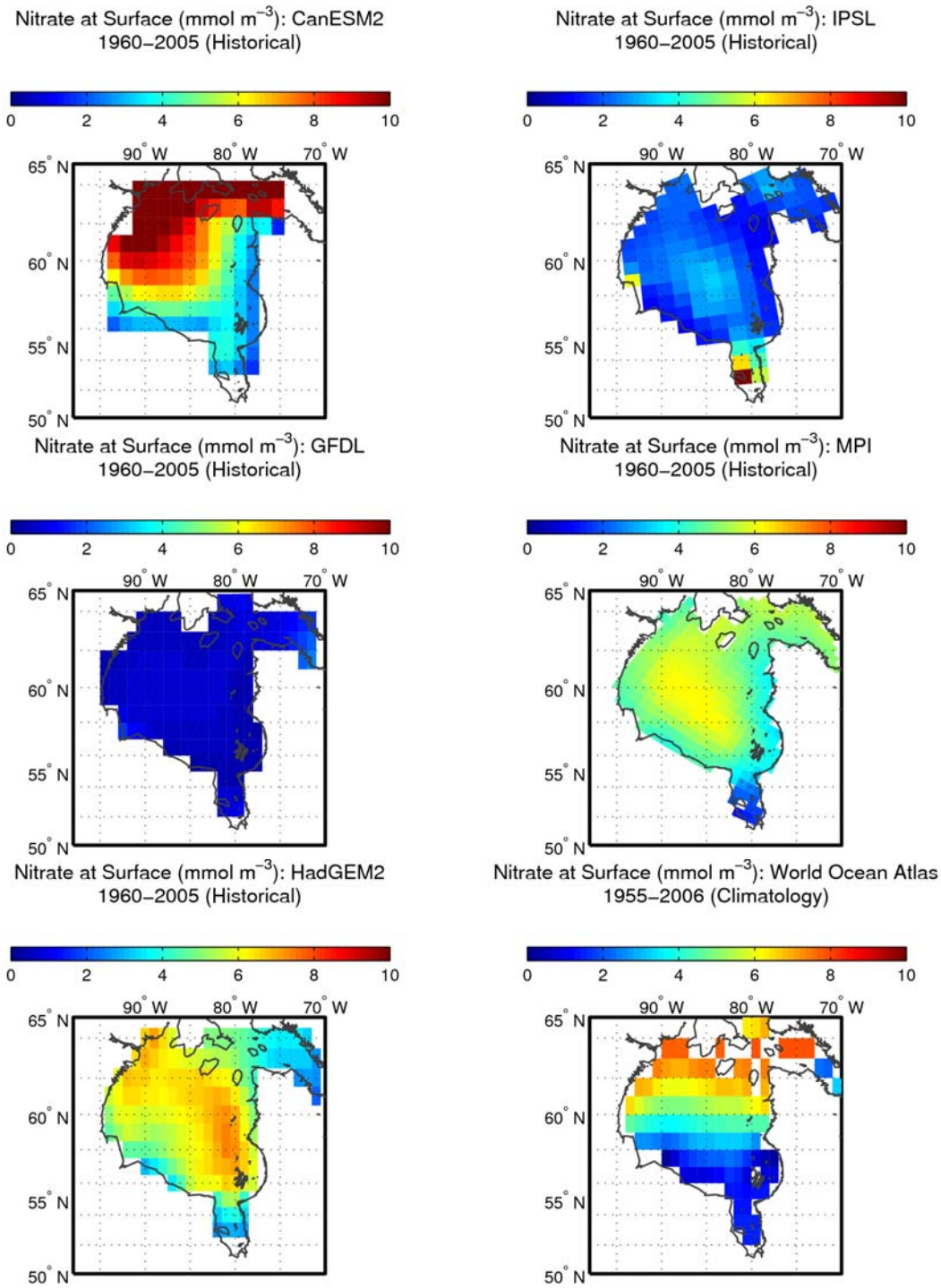

Figure 14. Mean simulated surface nitrate concentration in Hudson Bay for the historical period (1960–2005) and surface nitrate from the World Ocean Atlas (Garcia et al., 2010b).

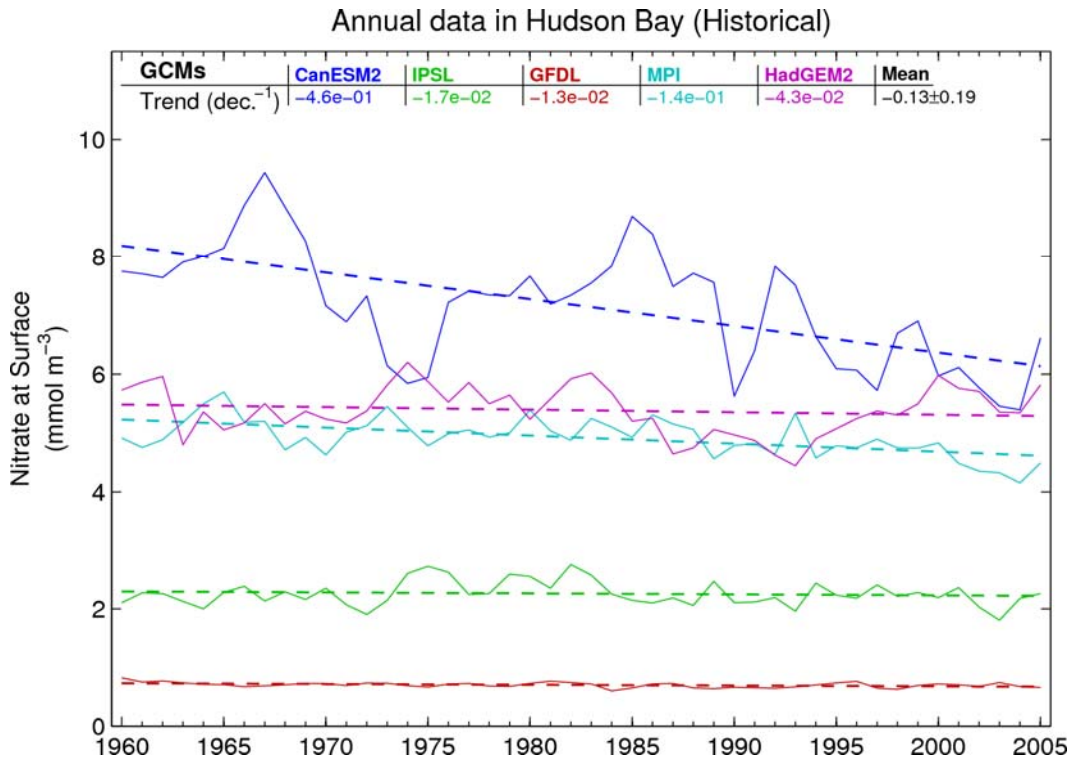

Figure 15. Surface nitrate concentration trends (mmol m^{-3}/decade) in Hudson Bay for the historical period (1960–2005).

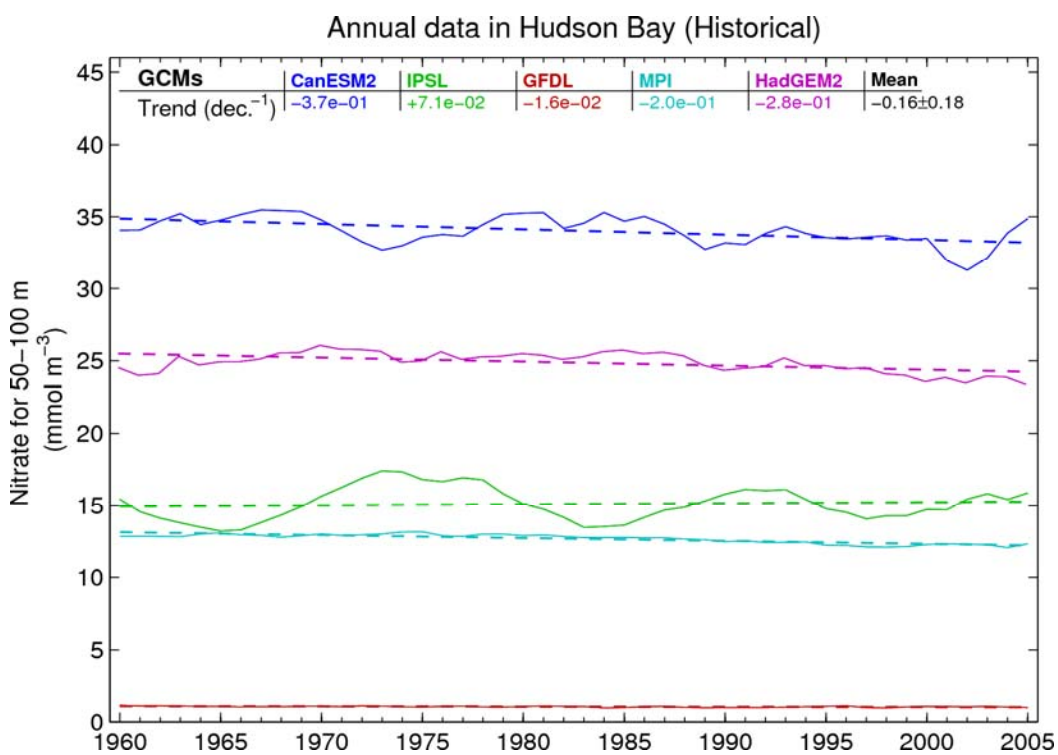

Figure 16. Average nitrate concentration trends (mmol m^{-3}/decade) at 50–100 m in Hudson Bay for the historical period (1960–2005).

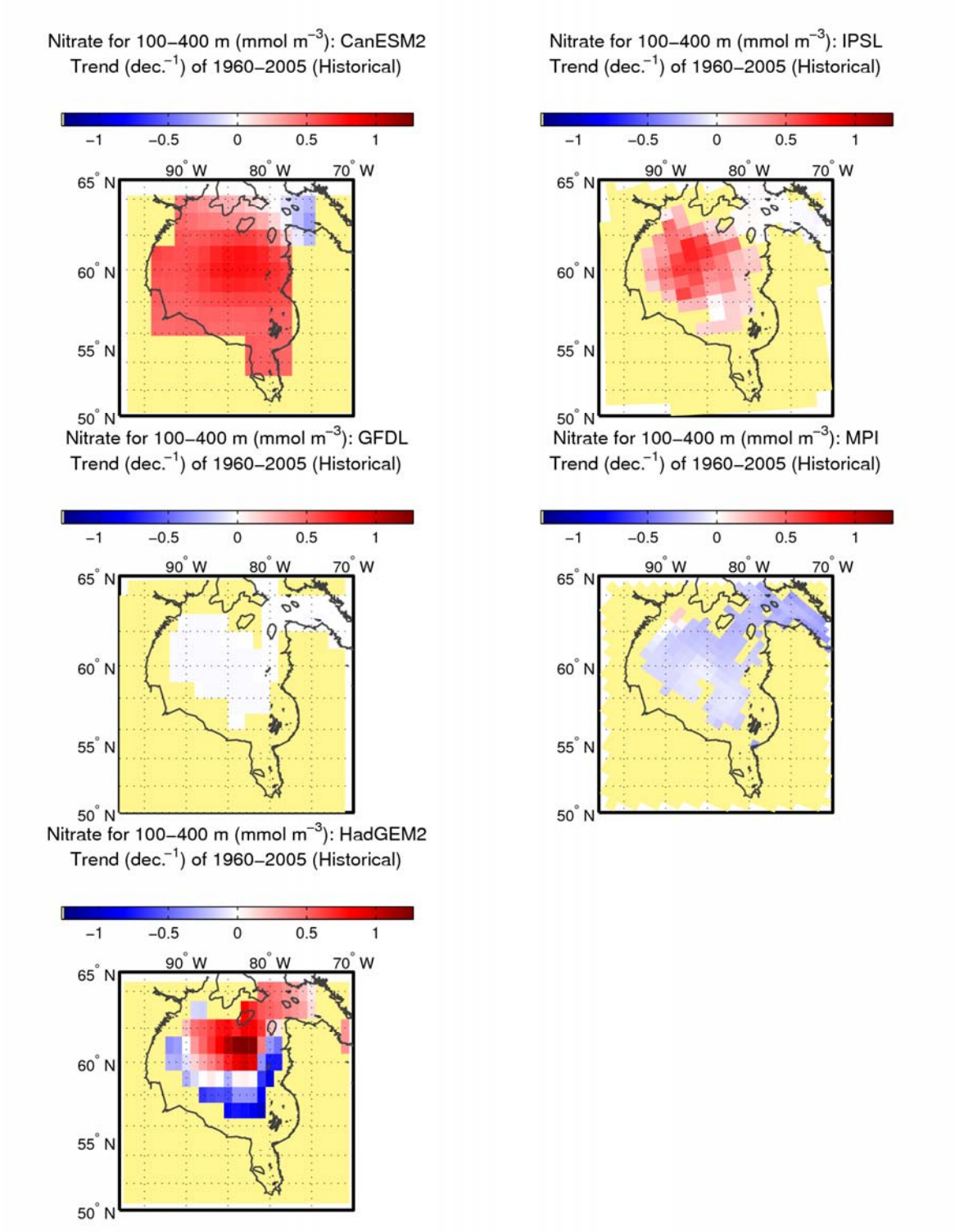

Figure 17. Nitrate concentration trends (mmol m^{-3}/decade) at 100–400 m in each grid cell in Hudson Bay for the historical simulations (1960–2005).

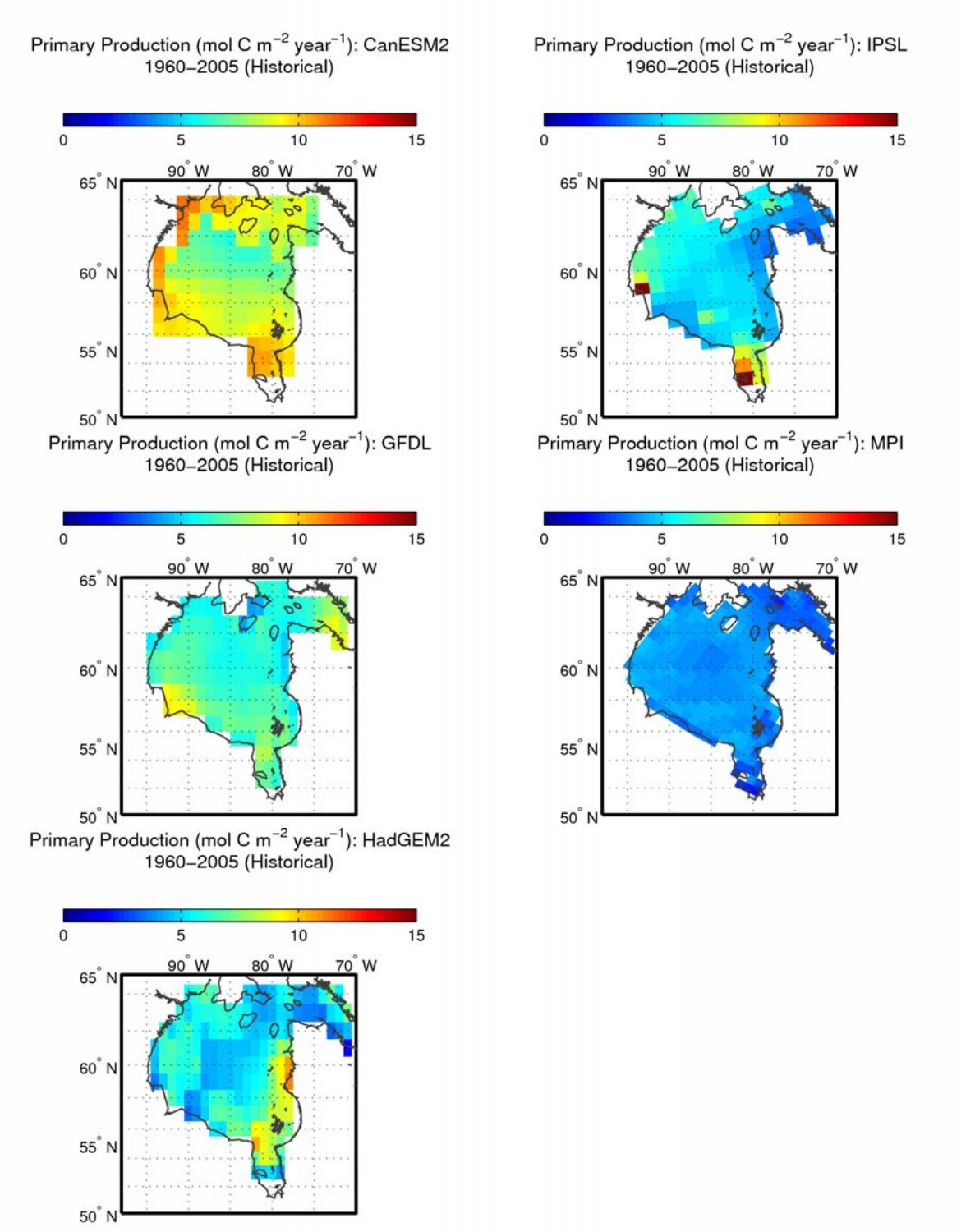

Figure 18. Mean simulated vertically integrated primary production (mol C m^{-2} year^{-1}) in Hudson Bay for the historical period (1960–2005).

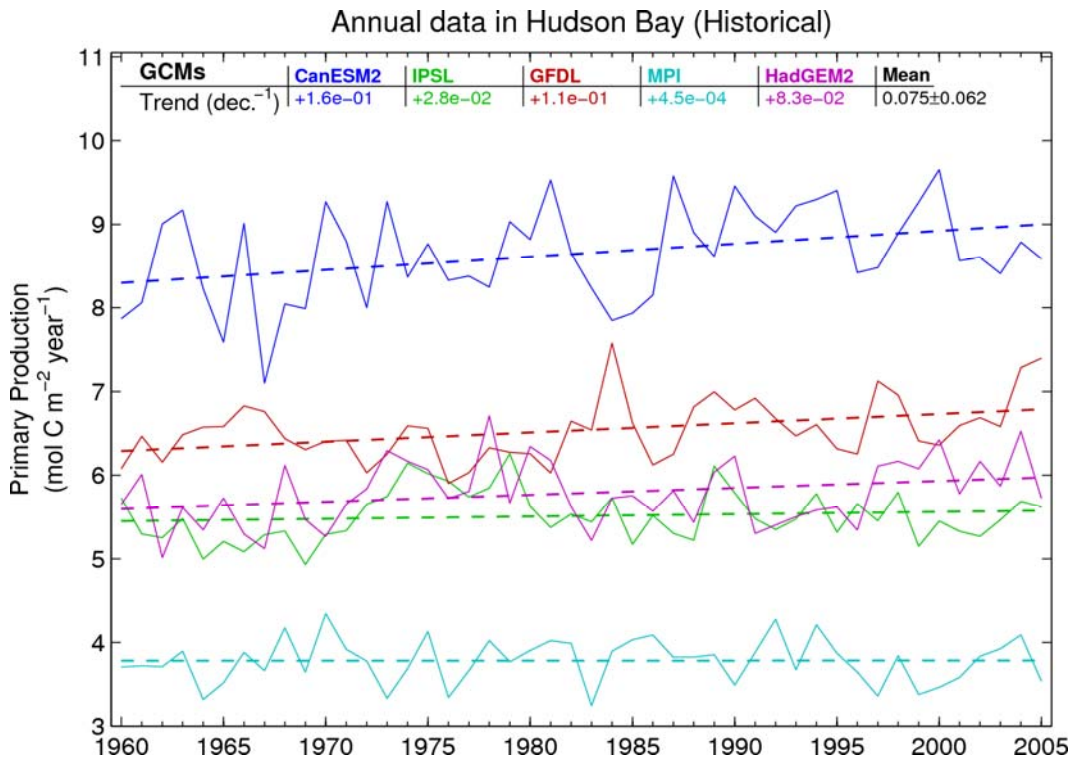

Figure 19. Simulated vertically integrated primary production trends (mol C m^{-2} year^{-1} per decade) in Hudson Bay for the historical period (1960–2005).

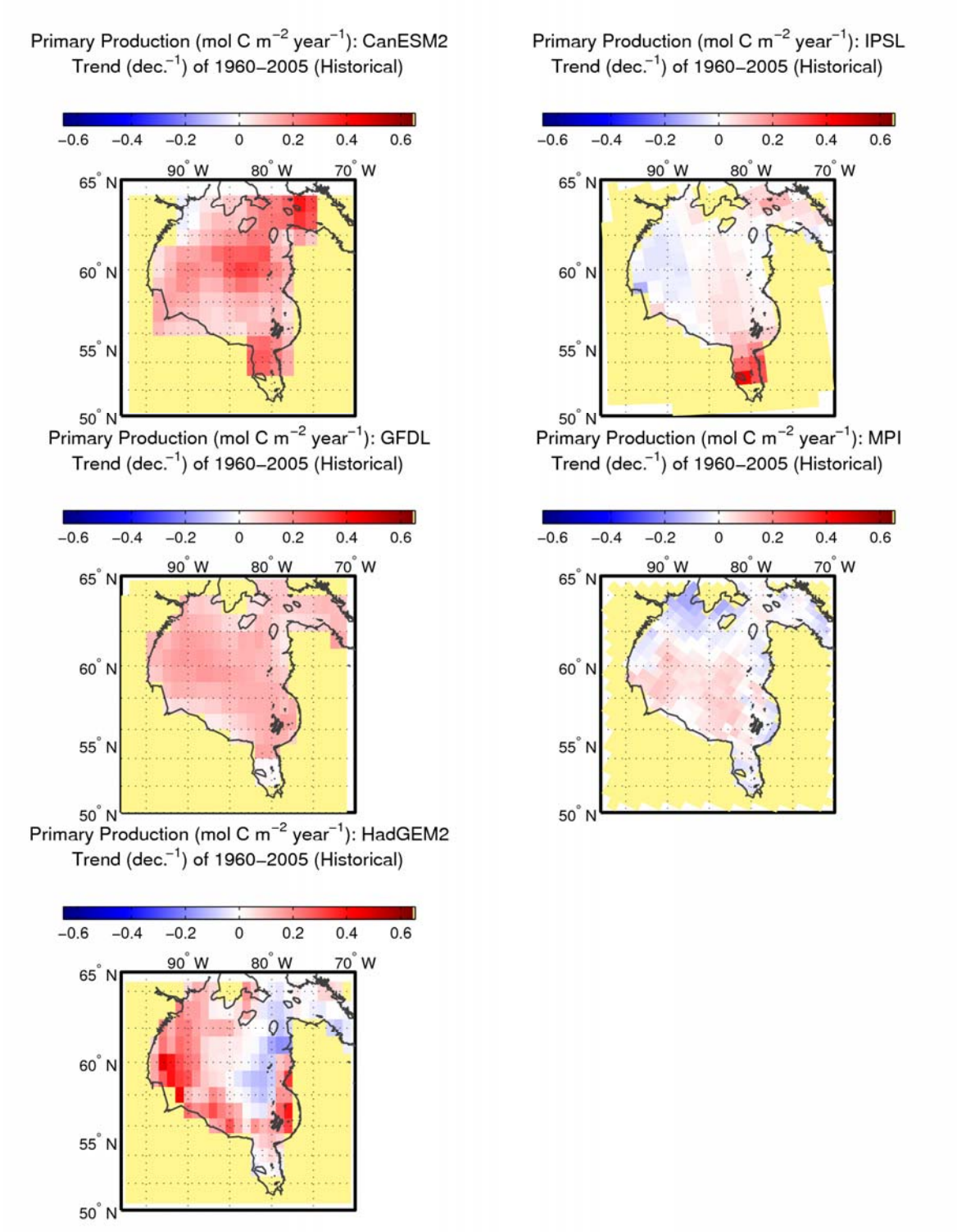

Figure 20. Vertically integrated primary production trends (mol C m^{-2} year^{-1} per decade) in each grid cell in Hudson Bay for the SeaWiFS record period (1960–2005).

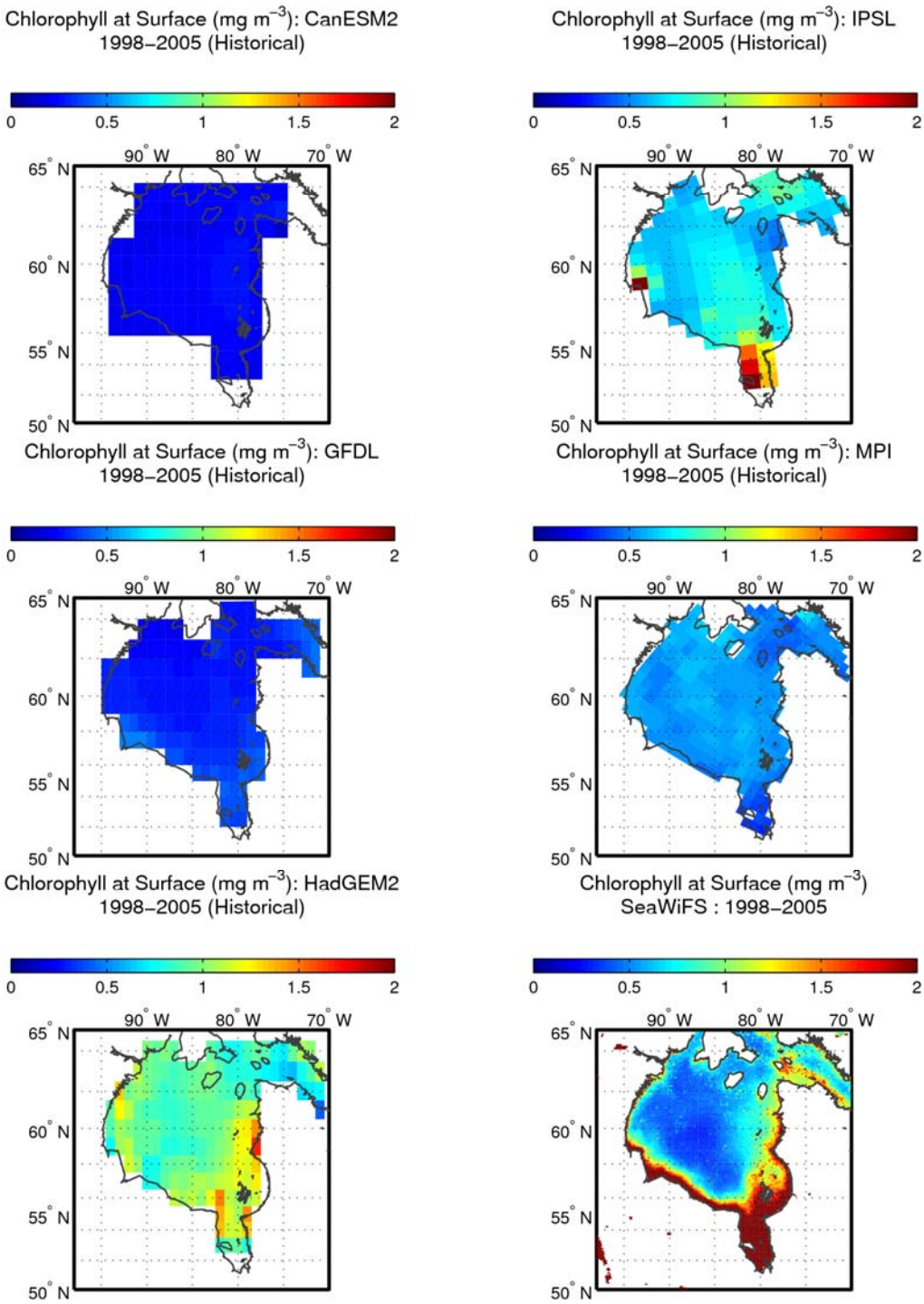

Figure 21. Mean simulated surface Chl *a* concentration and Chl *a* data from SeaWiFS in Hudson Bay over the 1998–2005 period.

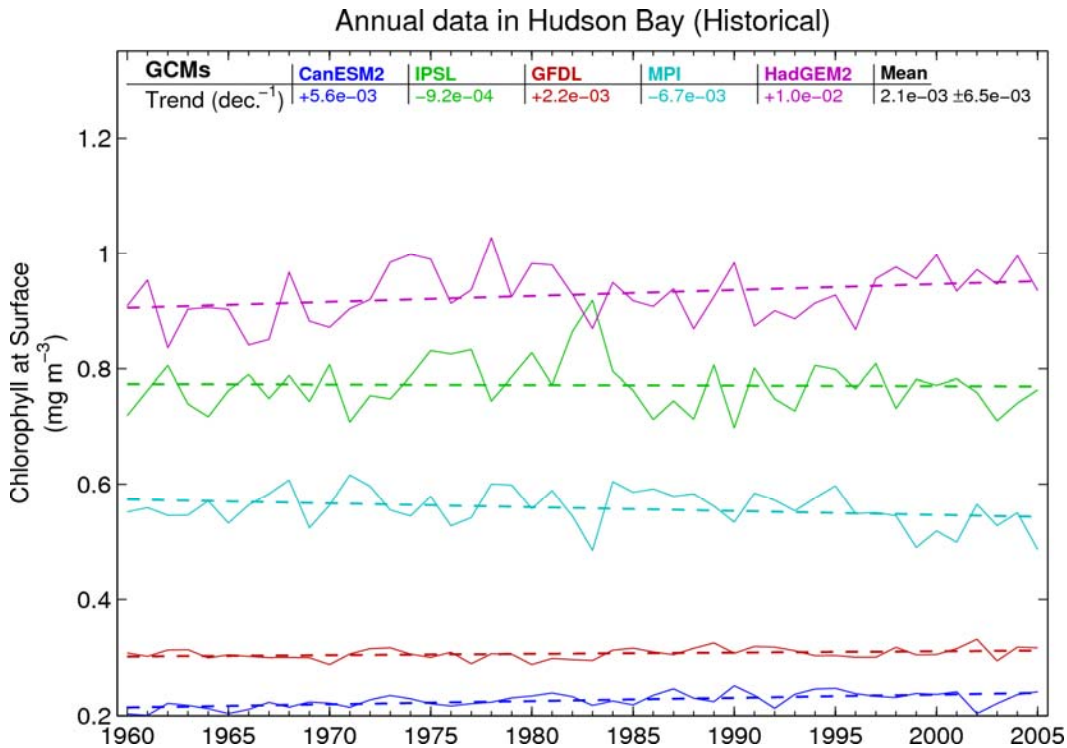

Figure 22. Average Chl *a* concentration trends (mg m^{-3}/decade) at the surface in Hudson Bay for the historical period (1960–2005).

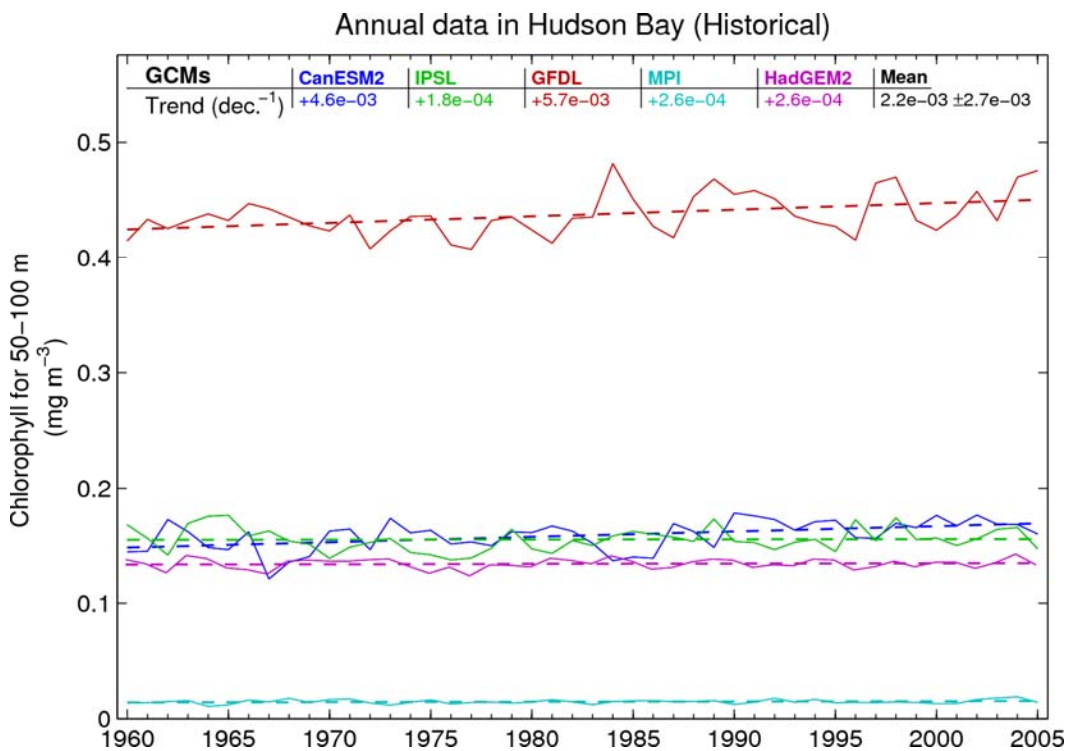

Figure 23. Average Chl *a* concentration trends (mg m^{-3}/decade) at 50–100 m for the historical period (1960–2005).

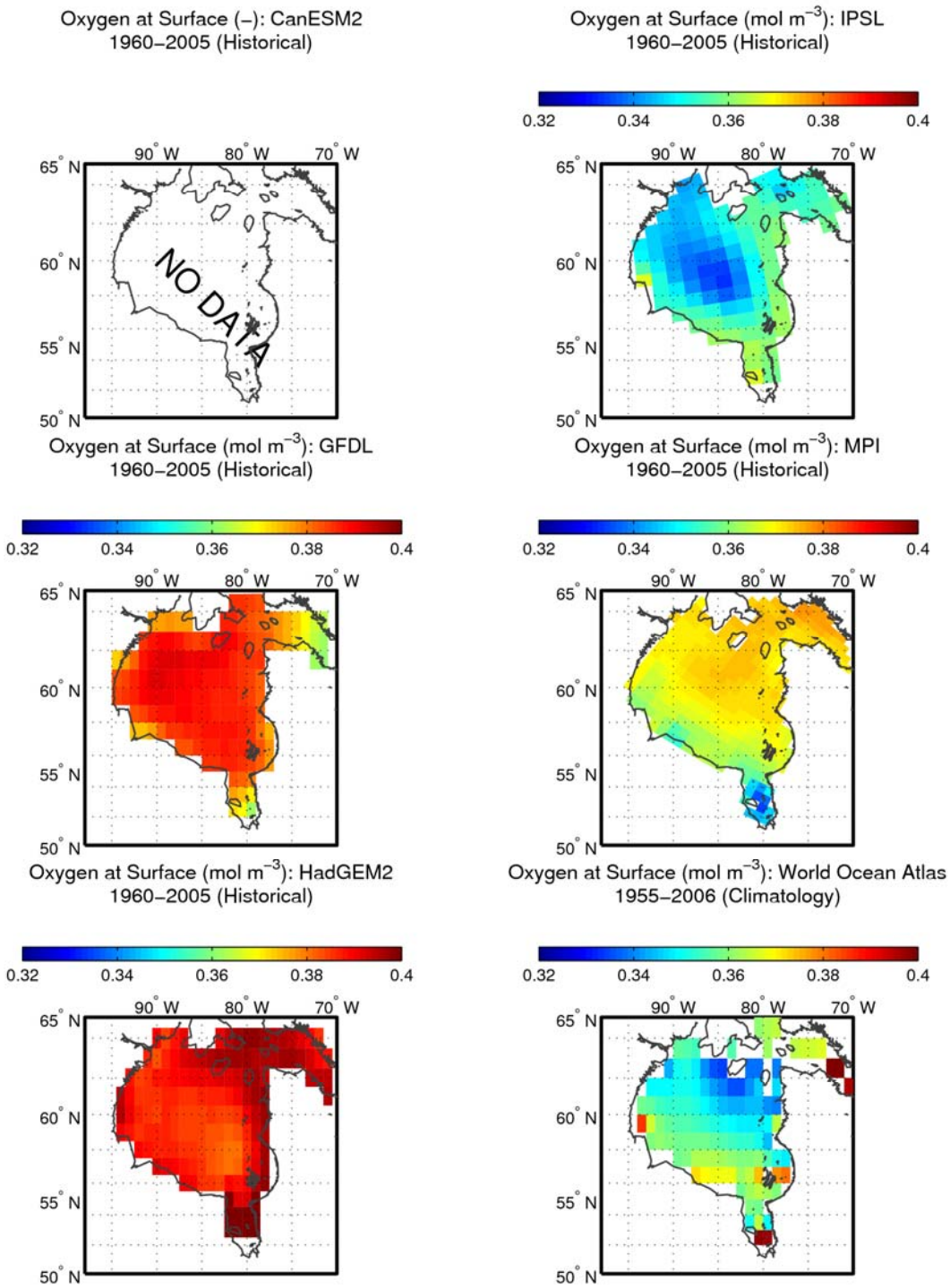

Figure 24. Mean simulated surface dissolved oxygen concentration in Hudson Bay for the historical period (1960–2005) and dissolved oxygen at surface from the World Ocean Atlas (Garcia et al., 2010a).

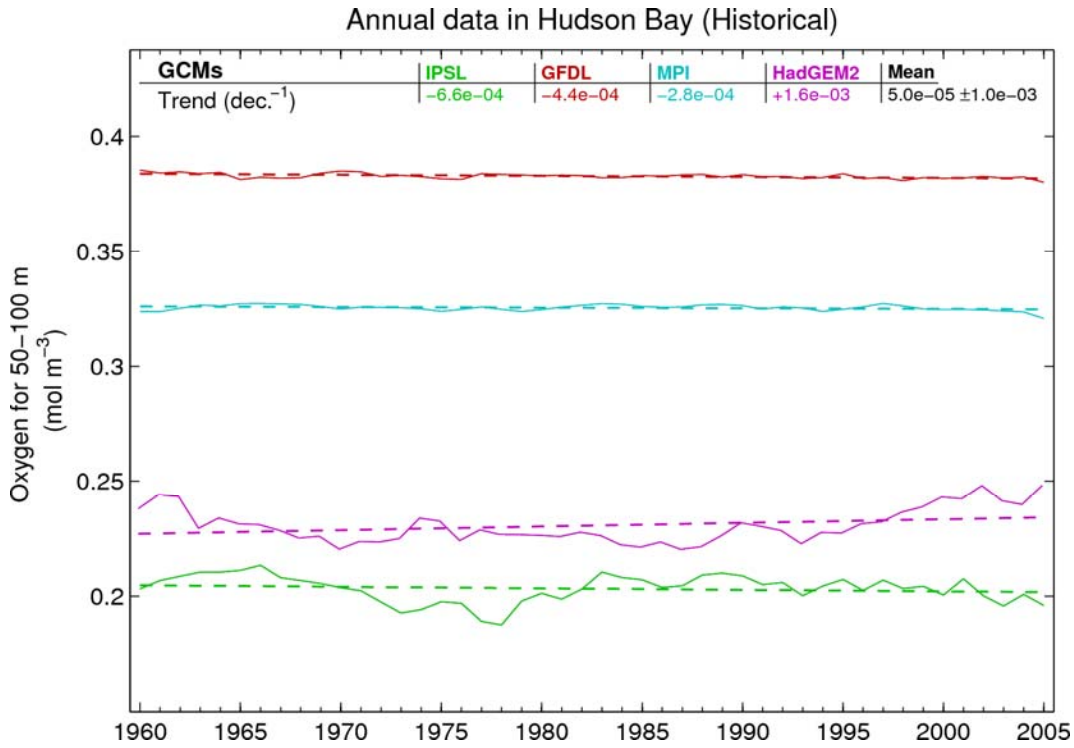

Figure 25. Simulated dissolved oxygen concentration trends (mol m^{-3}/decade) at 50-100 m in Hudson Bay for the historical period (1960–2005).

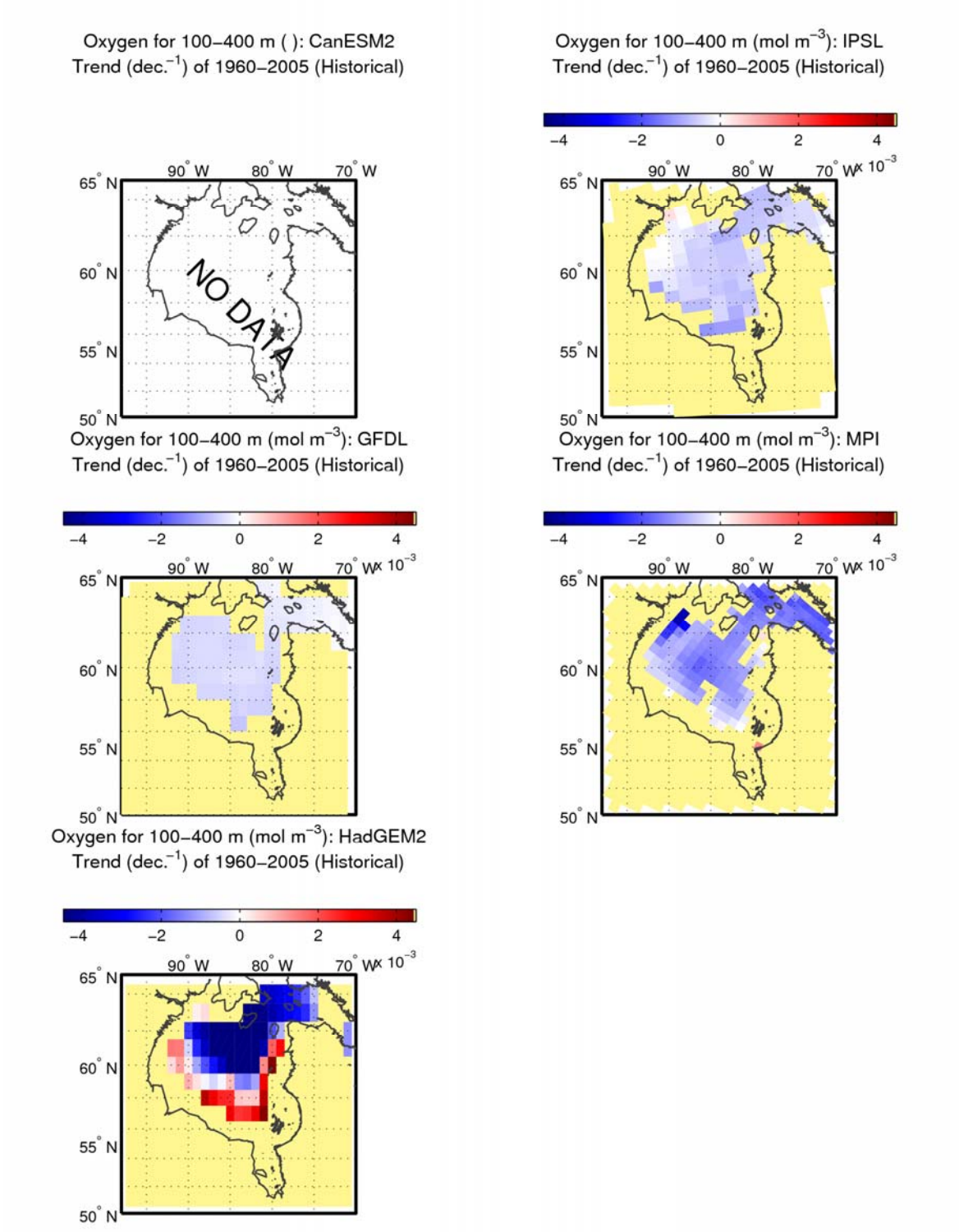

Figure 26. Dissolved oxygen concentration trends (mol m^{-3}/decade) at 100-400 m in each grid cell in Hudson Bay for the historical simulations (1960–2005).

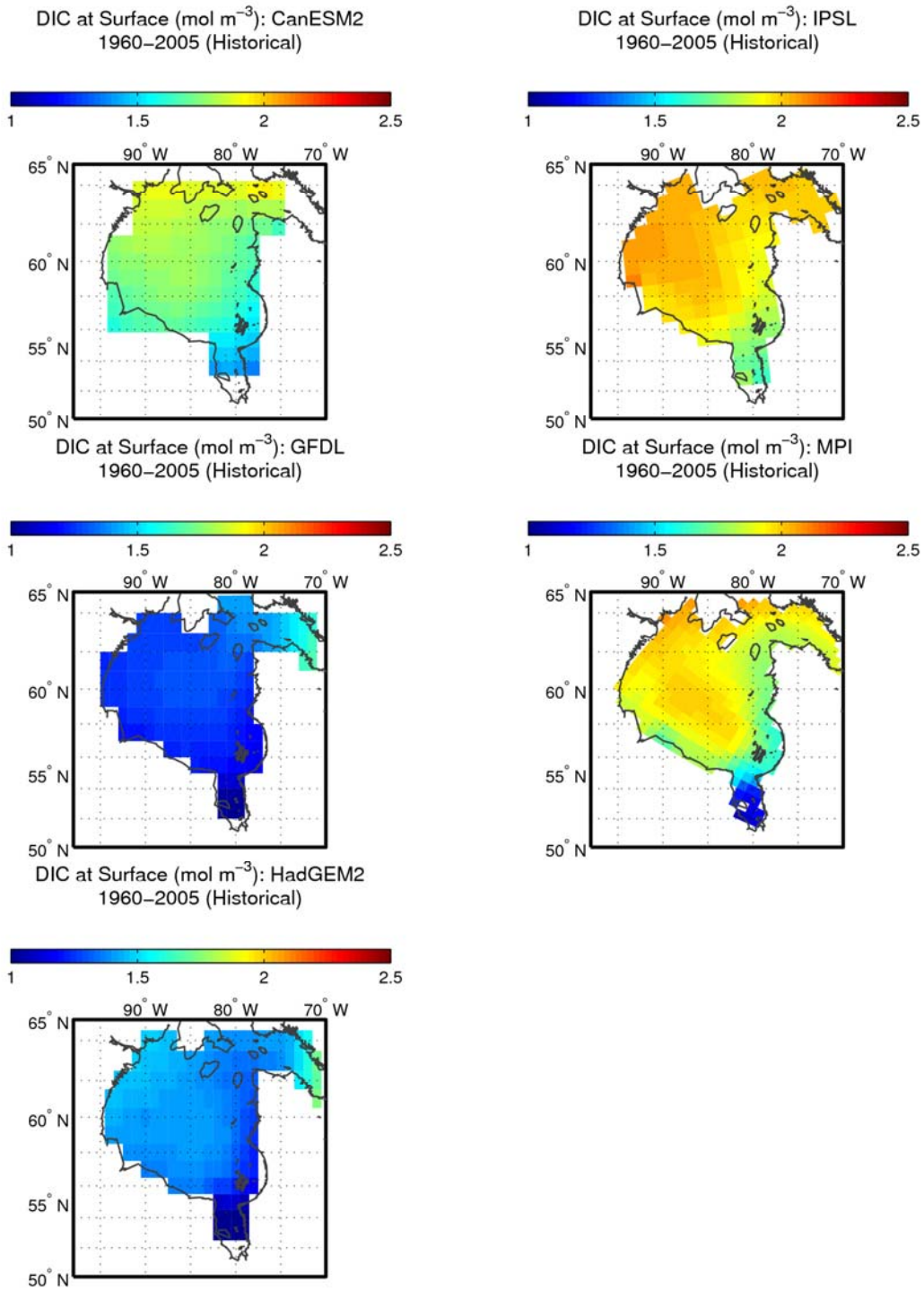

Figure 27. Mean simulated dissolved inorganic carbon concentration in Hudson Bay for the historical period (1960–2005).

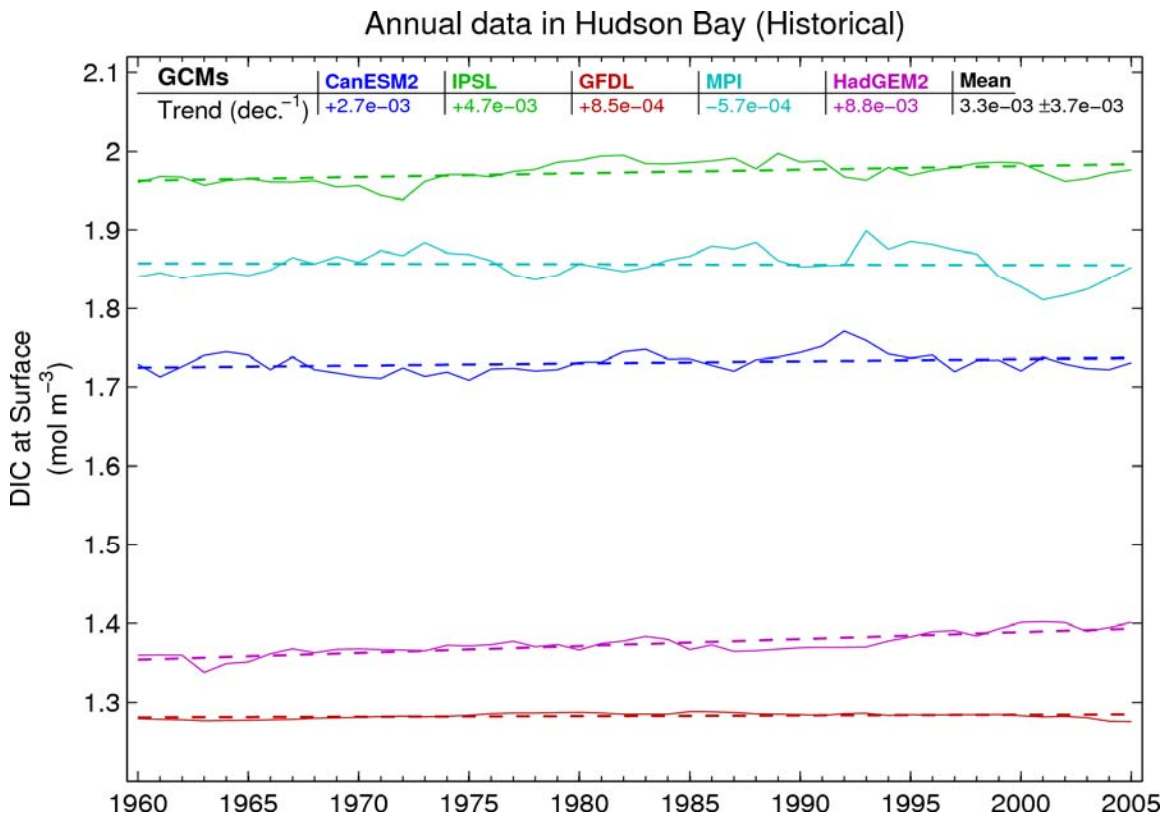

Figure 28. Simulated dissolved inorganic carbon concentration trends (mol m^{-3}/decade) at the surface in Hudson Bay for the historical period (1960–2005).

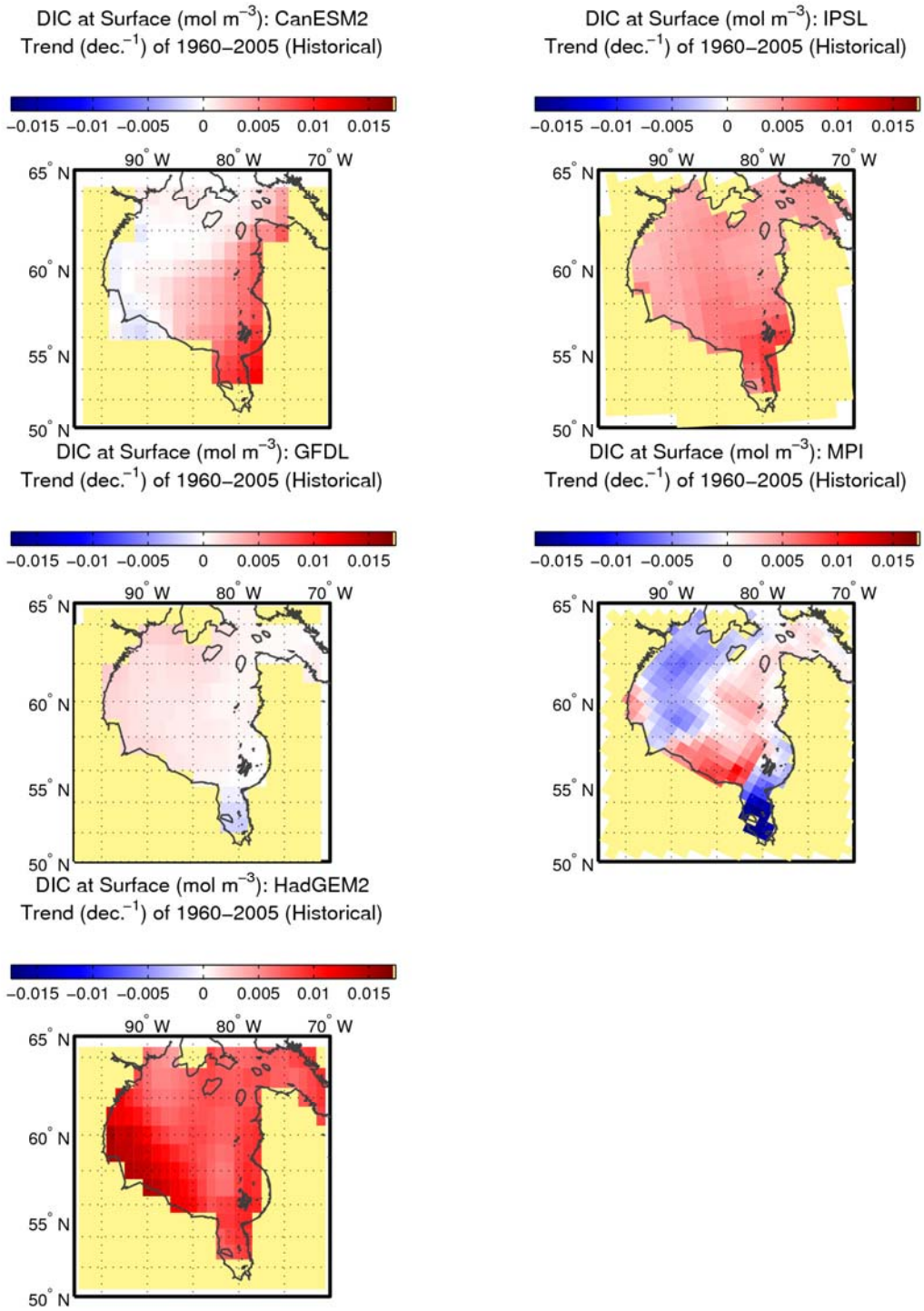

Figure 29. Dissolved inorganic carbon concentration trends (mol m^{-3}/decade) at the surface in each grid cell in Hudson Bay for the historical simulations (1960–2005).

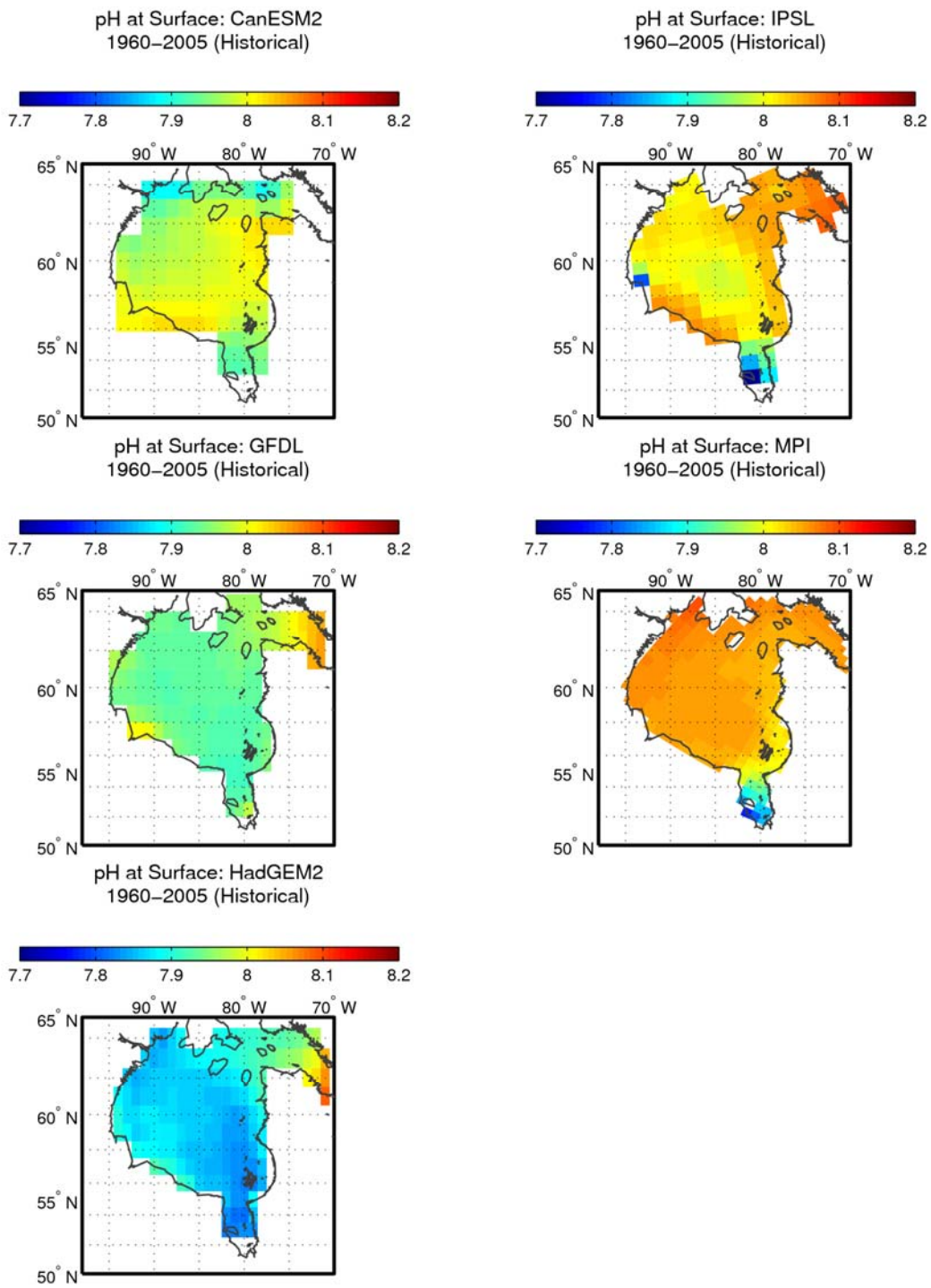

Figure 30. Mean simulated surface pH in Hudson Bay for the historical period (1960–2005).

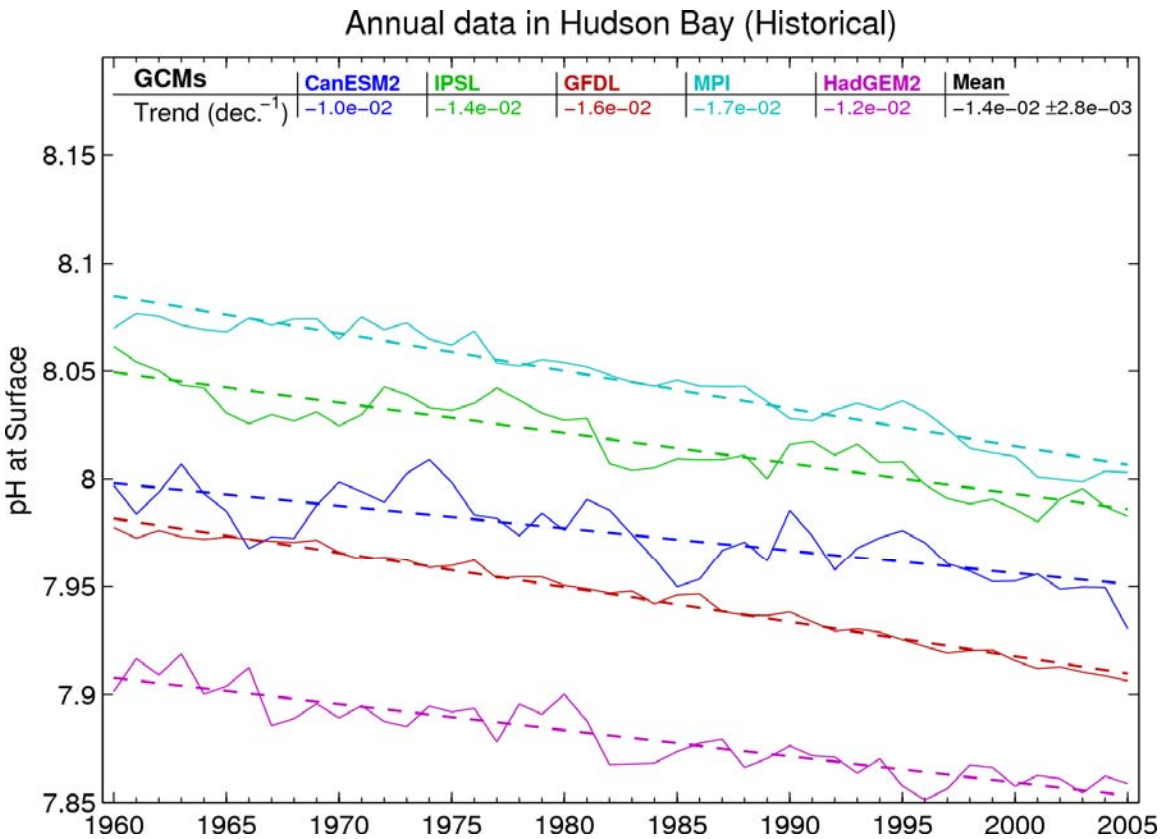

Figure 31. Simulated pH trends (per decade) at the surface in Hudson Bay for the historical period (1960–2005).

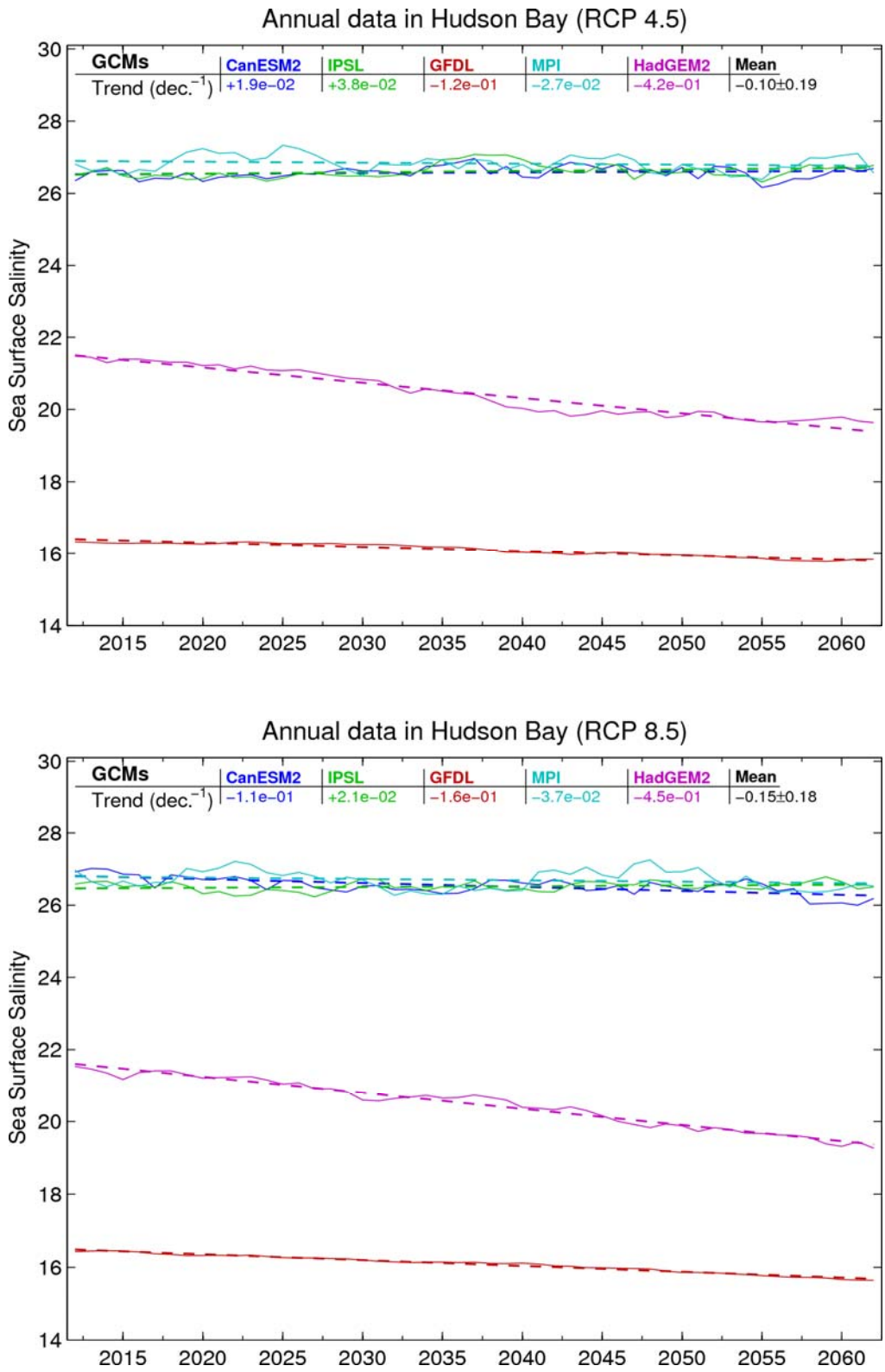

Figure 32. Future sea-surface salinity trends (per decade) in Hudson Bay for the 2012–2062 period for RCPs 4.5 and 8.5.

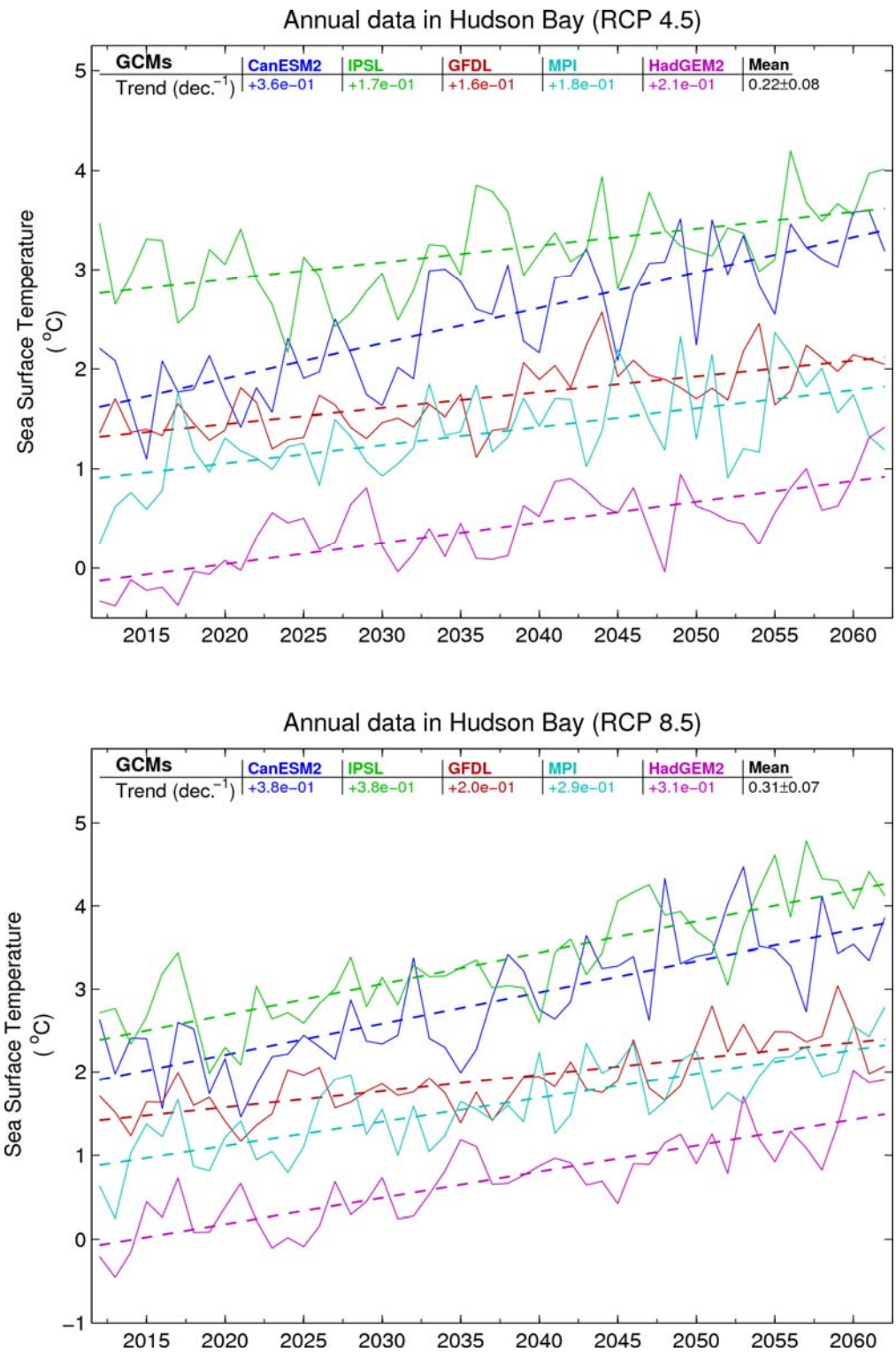

Figure 33. Future sea-surface temperature trends (°C/decade) in Hudson Bay for the 2012–2062 period for RCP 4.5 (upper panel) and RCP 8.5 (lower panel).

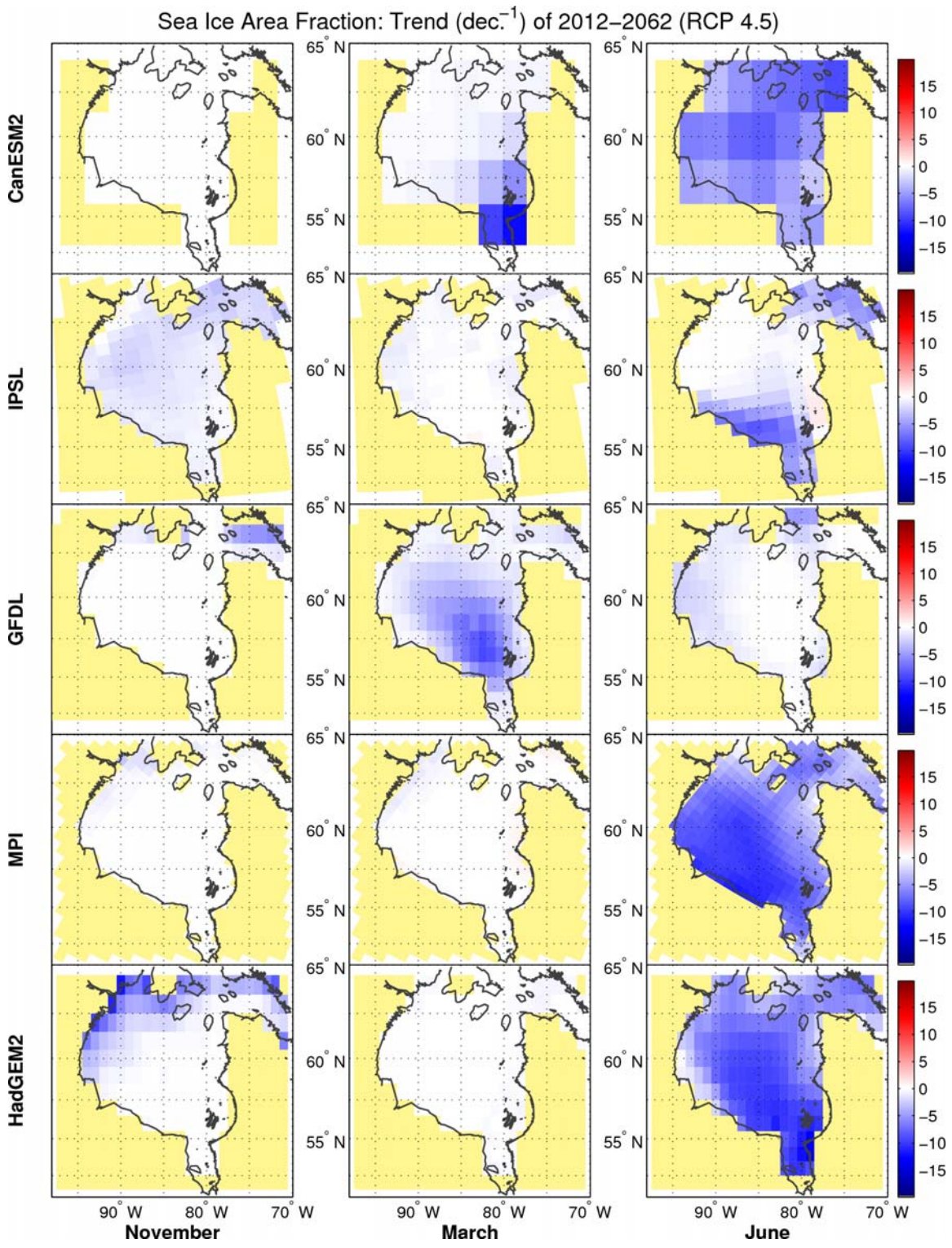

Figure 34. Future sea-ice concentration trends (%/decade) in Hudson Bay for the 2012–2062 period for RCP 4.5.

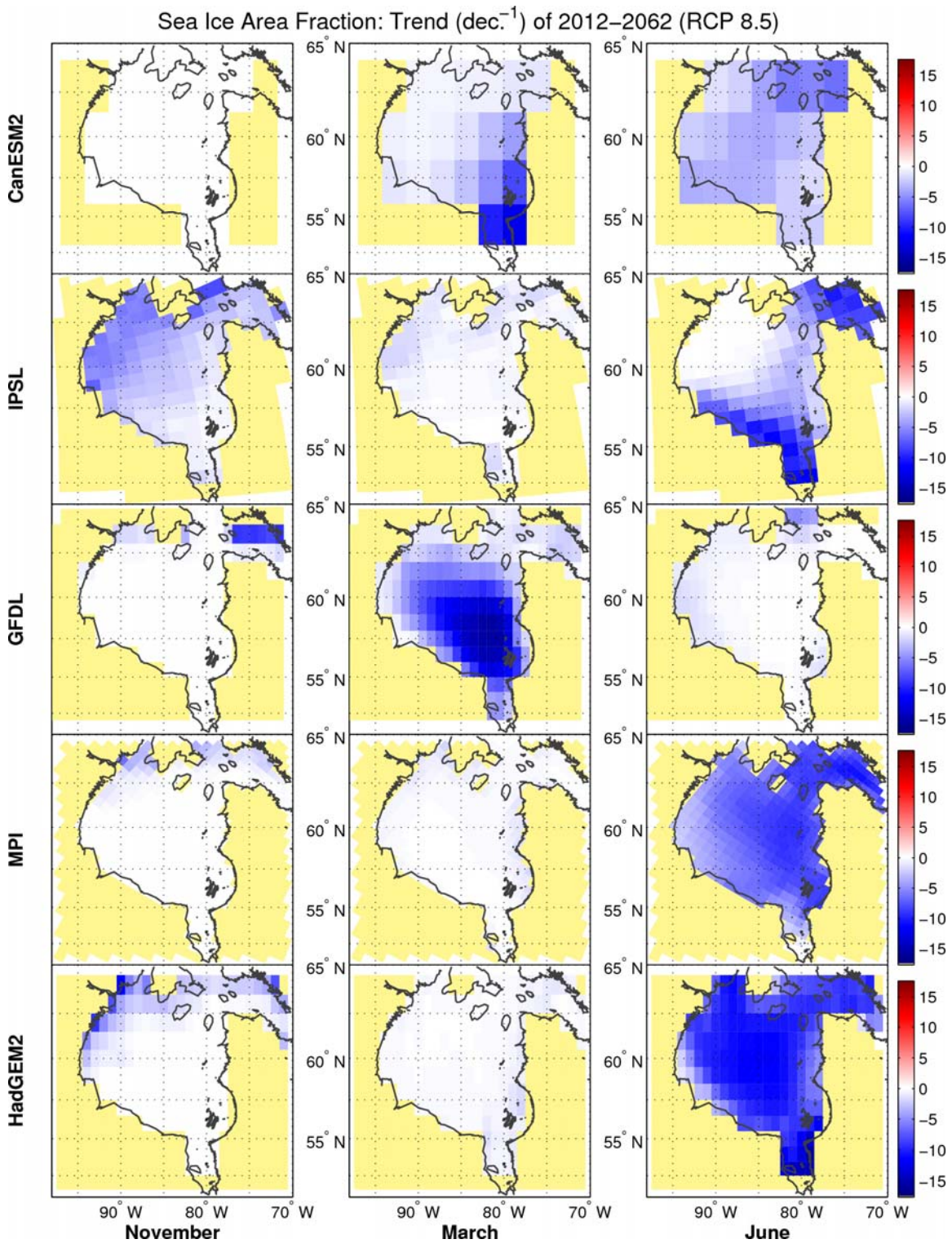

Figure 35. Future sea-ice concentration trends (%/decade) in Hudson Bay for the 2012–2062 period for RCP 8.5.

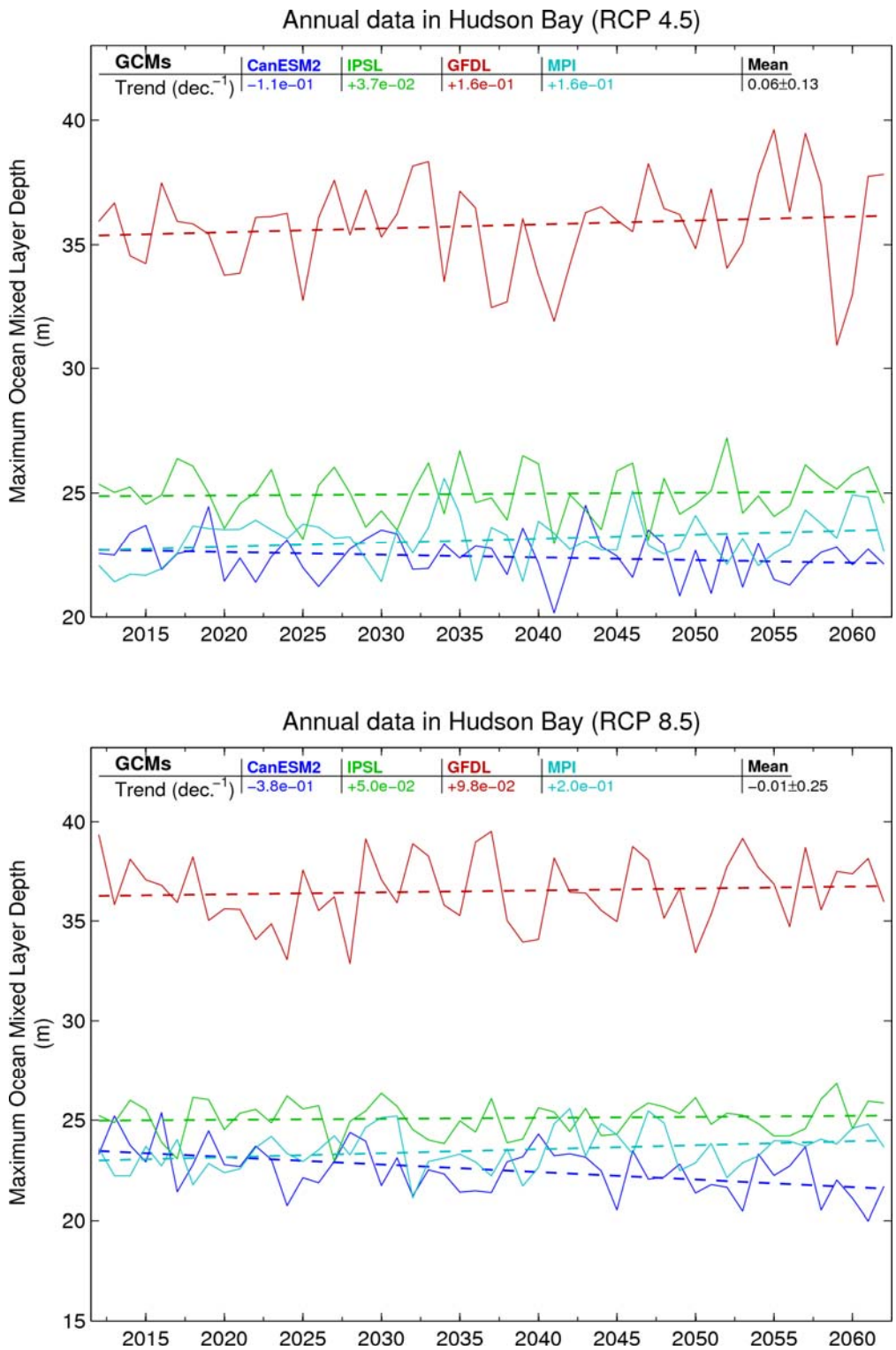

Figure 36. Future maximum ocean mixed layer depth trends (m/decade) in Hudson Bay for the 2012–2062 period for RCP 4.5 (upper panel) and RCP 8.5 (lower panel).

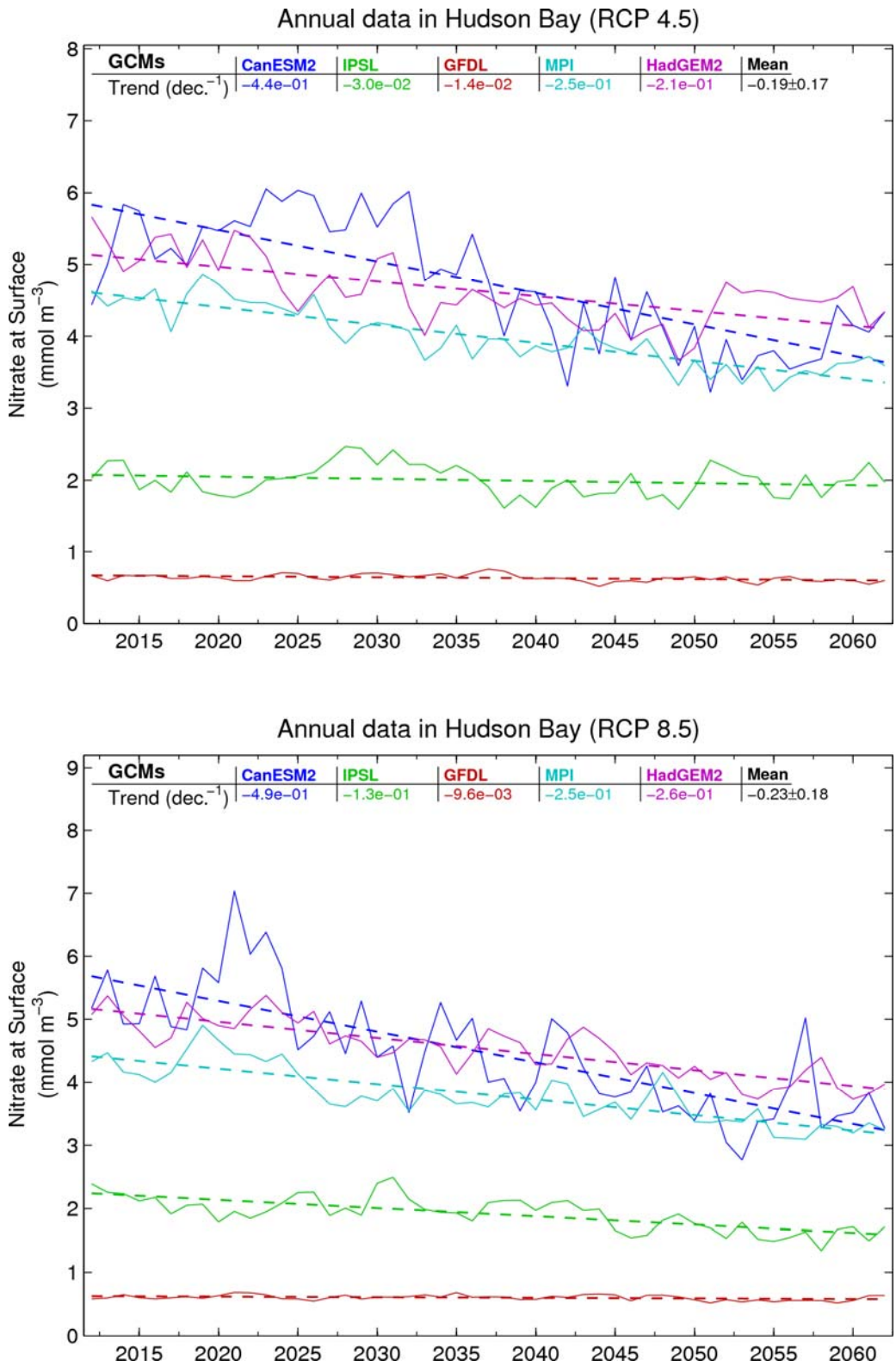

Figure 37. Future nitrate concentration trends (mmol m^{-3}/decade) at the surface in Hudson Bay for the 2012–2062 period for RCP 4.5 (upper panel) and RCP 8.5 (lower panel).

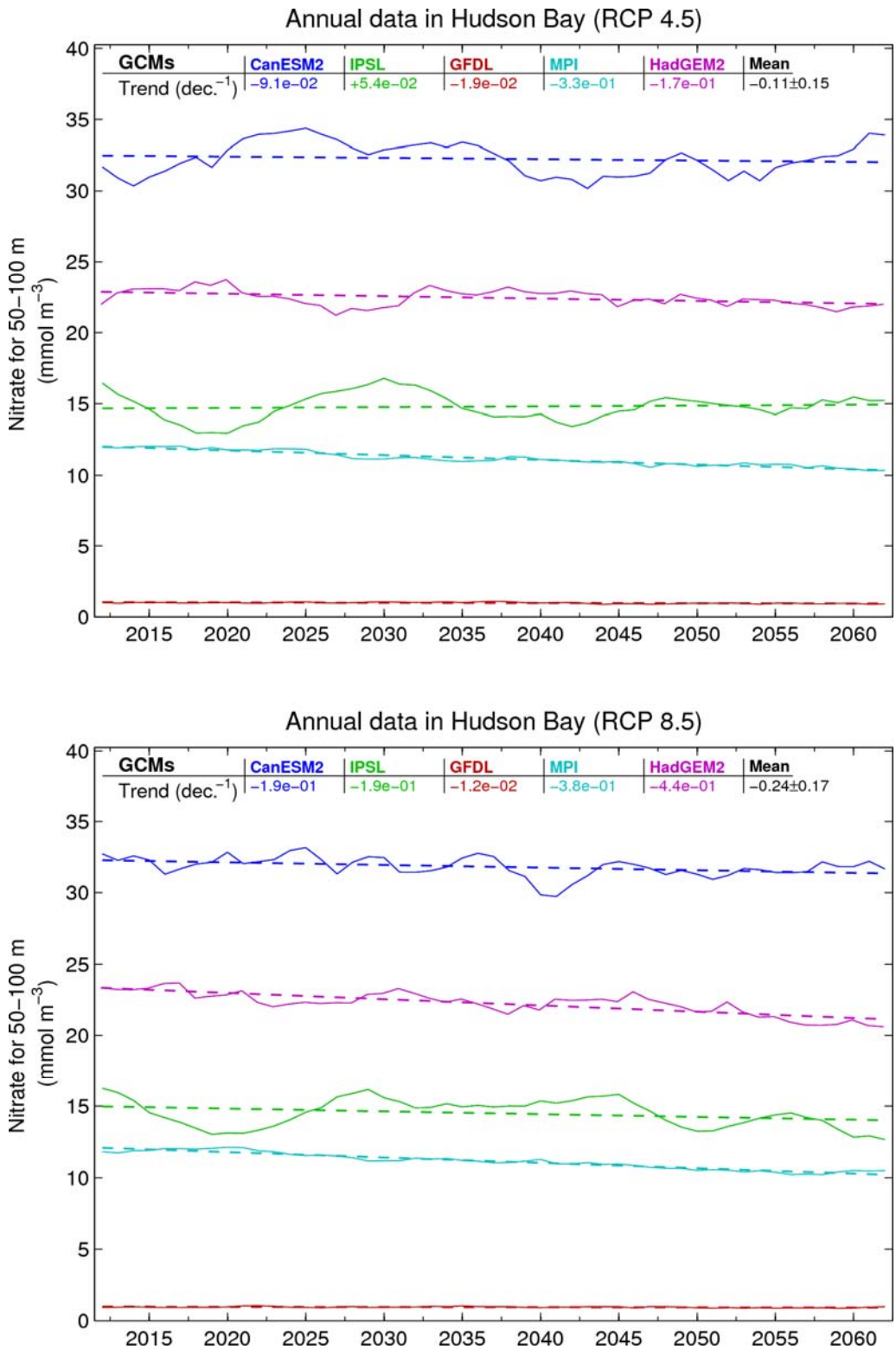

Figure 38. Future nitrate concentration trends (mmol m^{-3}/decade) at 50–100 m in Hudson Bay for the 2012–2062 period for RCP 4.5 (upper panel) and RCP 8.5 (lower panel).

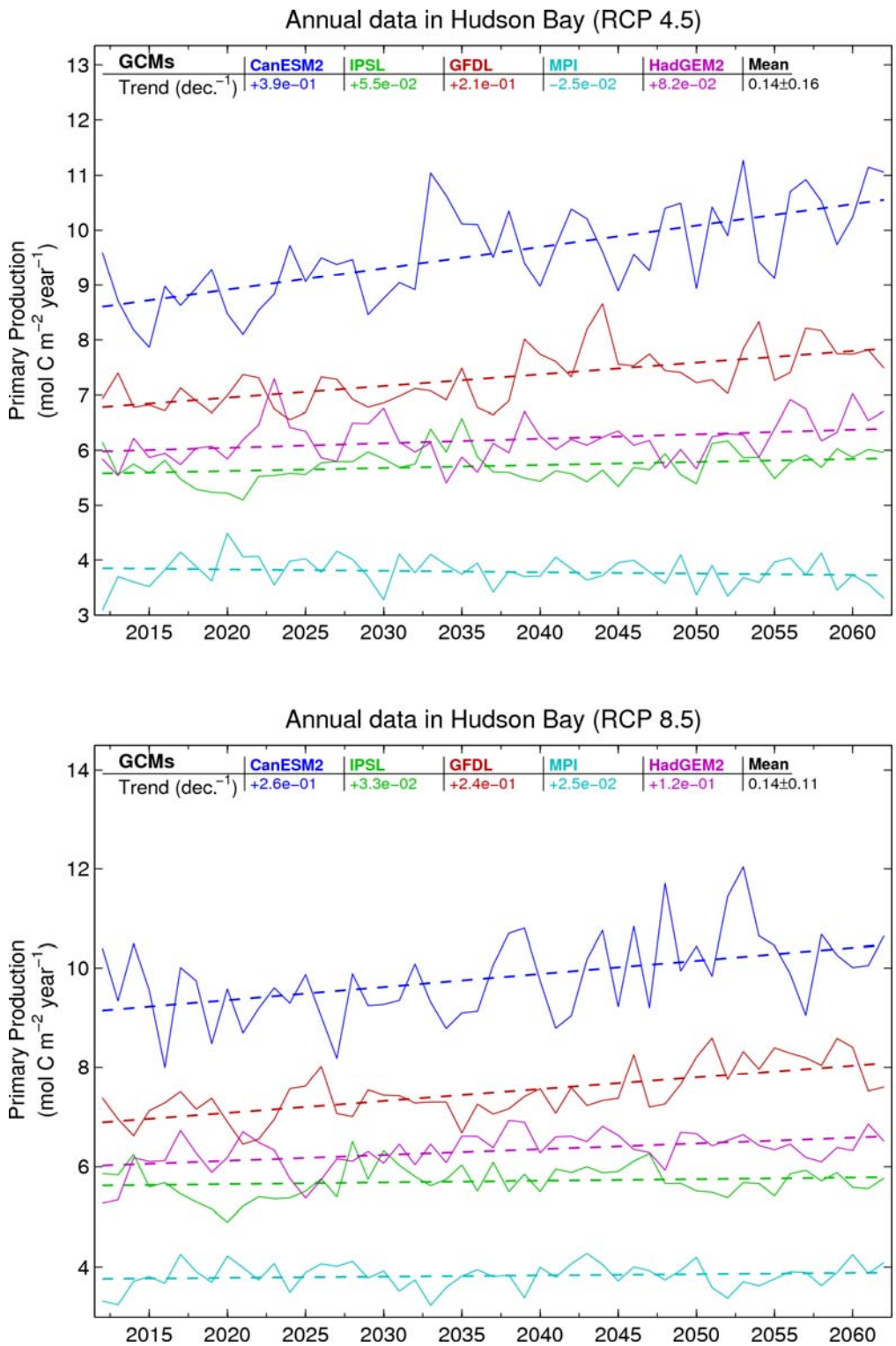

Figure 39. Future vertically integrated primary production trends (mol C m^{-2} year^{-1} per decade) in Hudson Bay for the 2012–2062 period for RCP 4.5 (upper panel) and RCP 8.5 (lower panel).

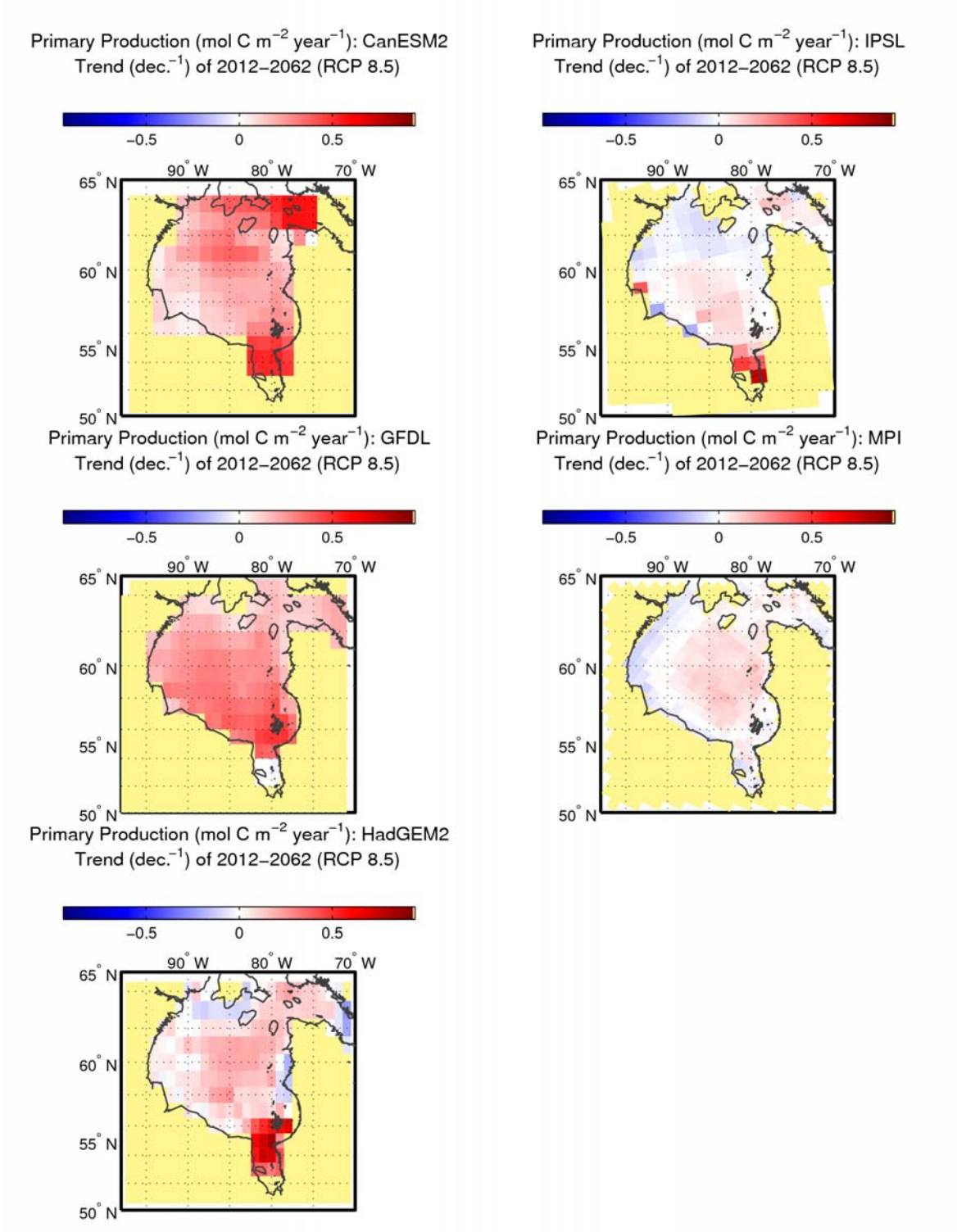

Figure 40. Future vertically integrated primary production trends (mol C m^{-2} year^{-1} per decade) in each grid cell in Hudson Bay for the 2012–2062 period for RCP 8.5.

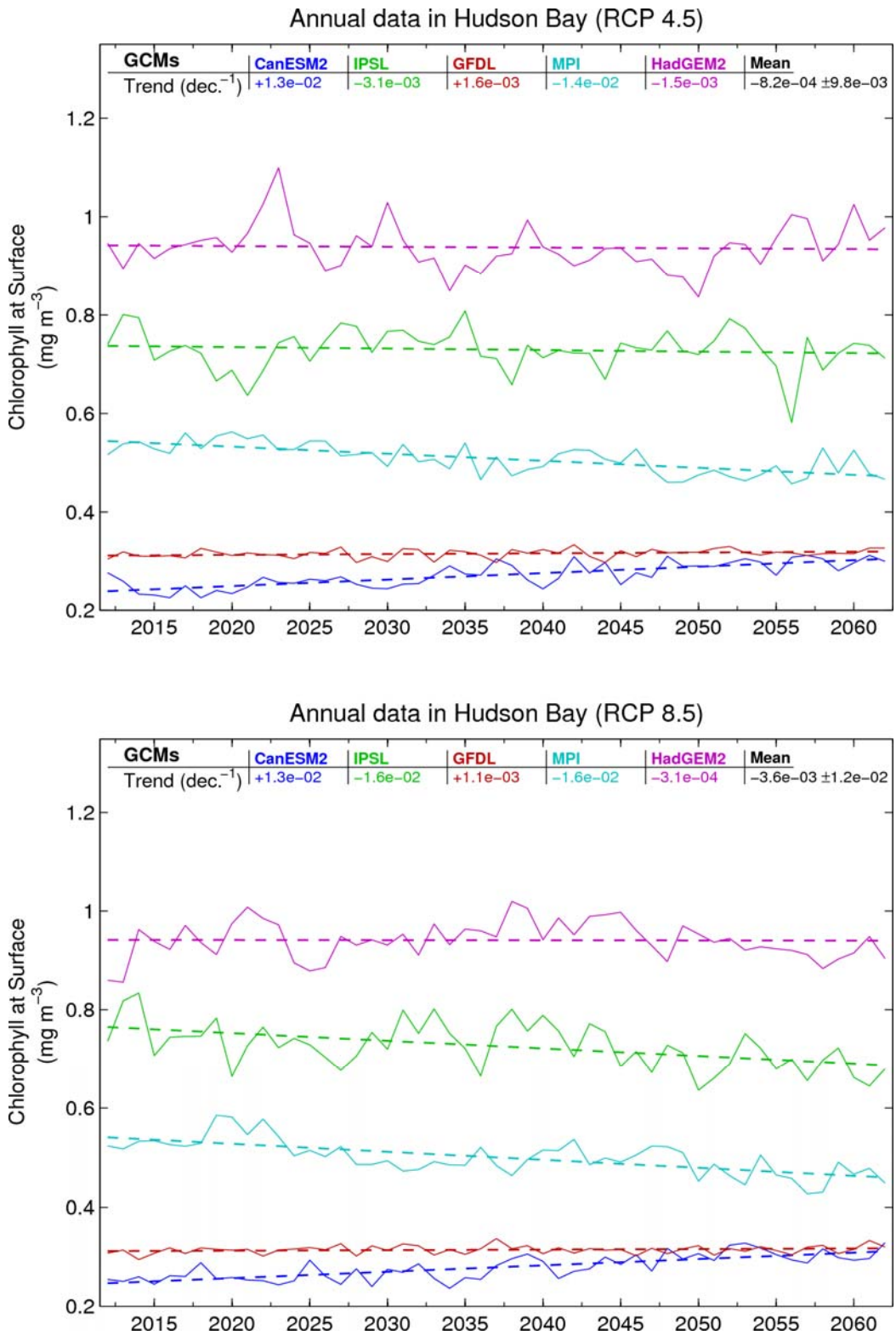

Figure 41. Future Chl *a* concentration trends (mg m^{-3}/decade) at the surface in Hudson Bay for the 2012–2062 period for RCP 4.5 (upper panel) and RCP 8.5 (lower panel).

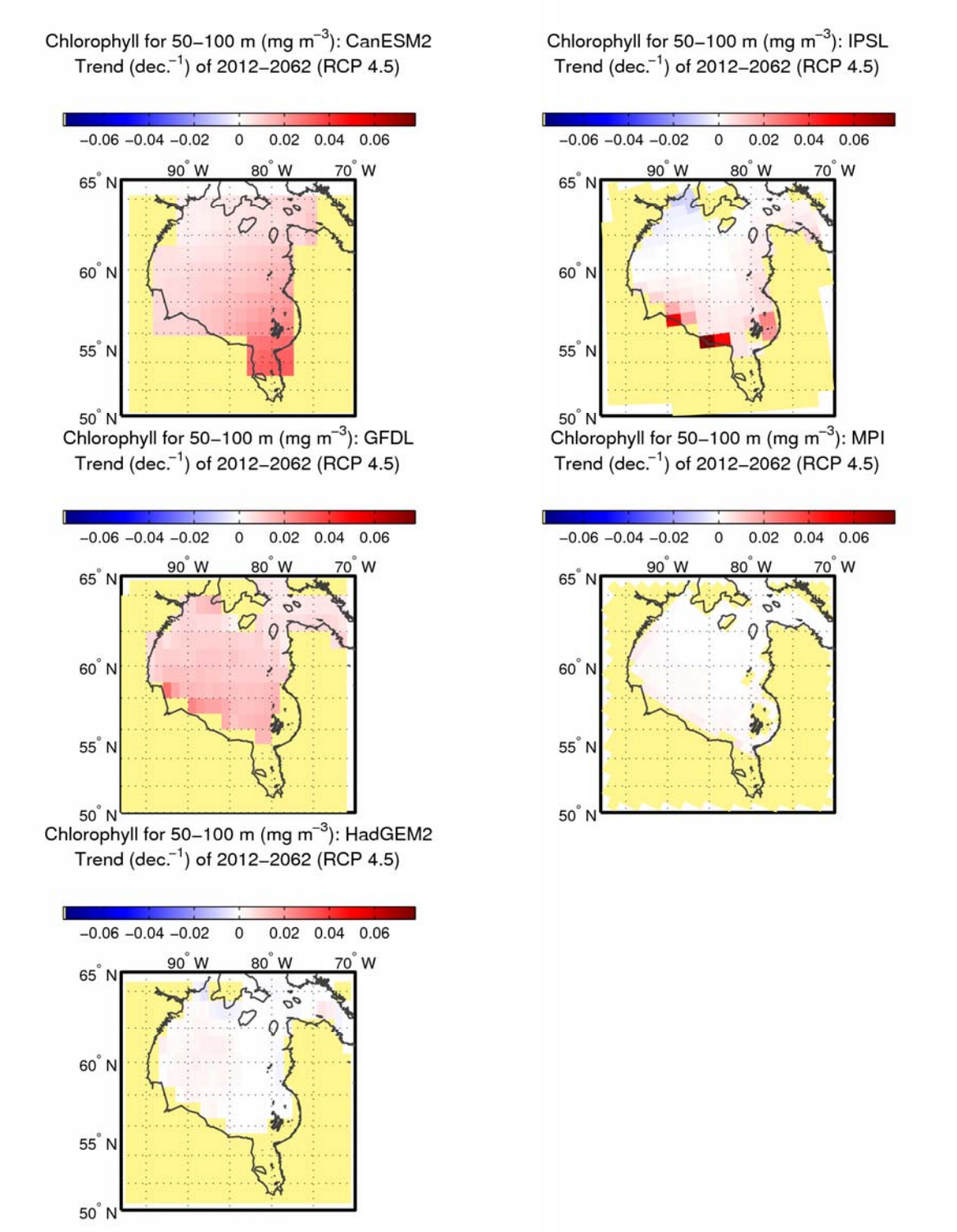

Figure 42. Future Chl *a* concentration trends (mg m^{-3}/decade) at 50–100 m in each grid cell in Hudson Bay for the 2012–2062 period for RCP 4.5.

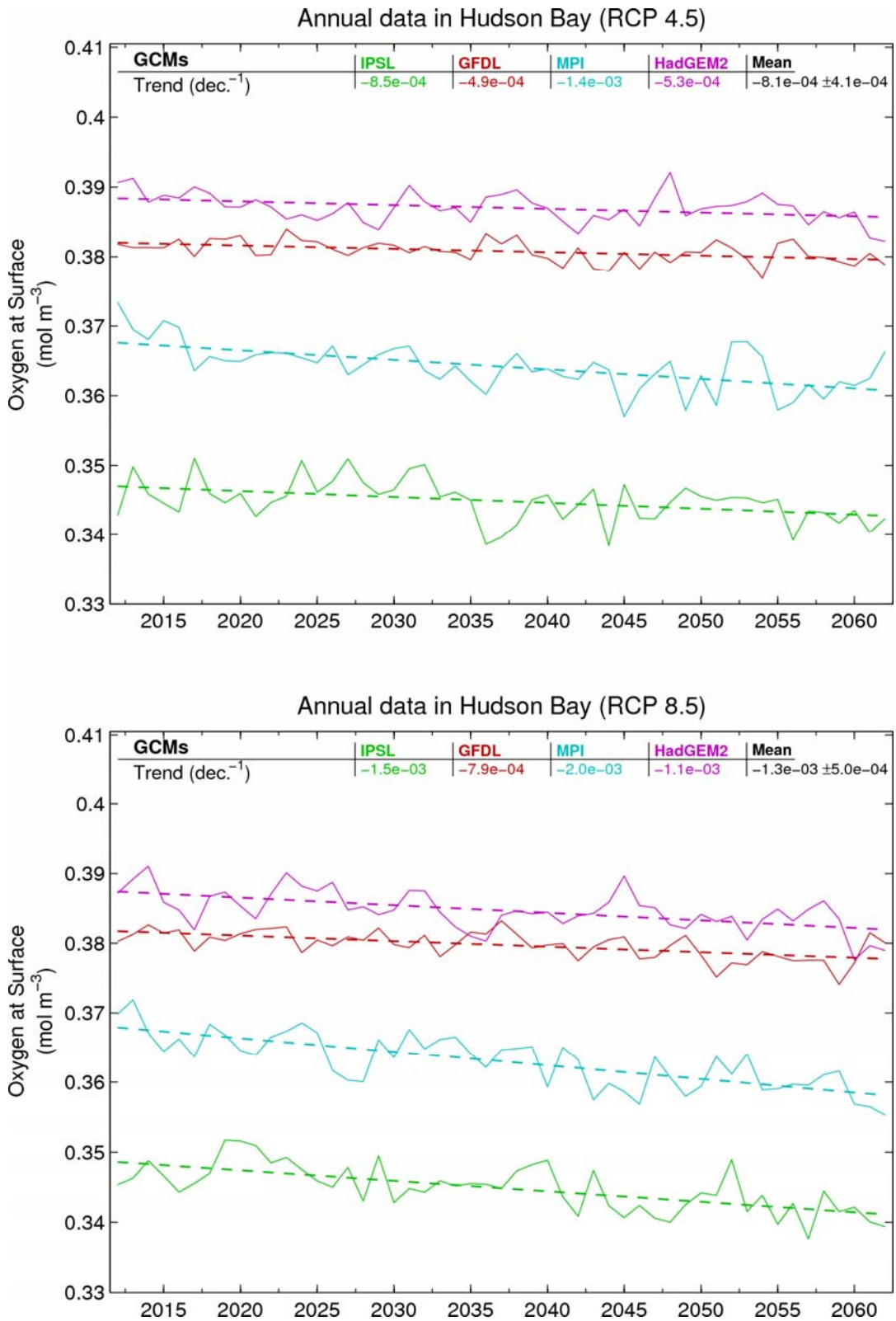

Figure 43. Future dissolved oxygen concentration trends (mol m^{-3}/decade) at the surface in Hudson Bay for the 2012–2062 period for RCP 4.5 (upper panel) and RCP 8.5 (lower panel).

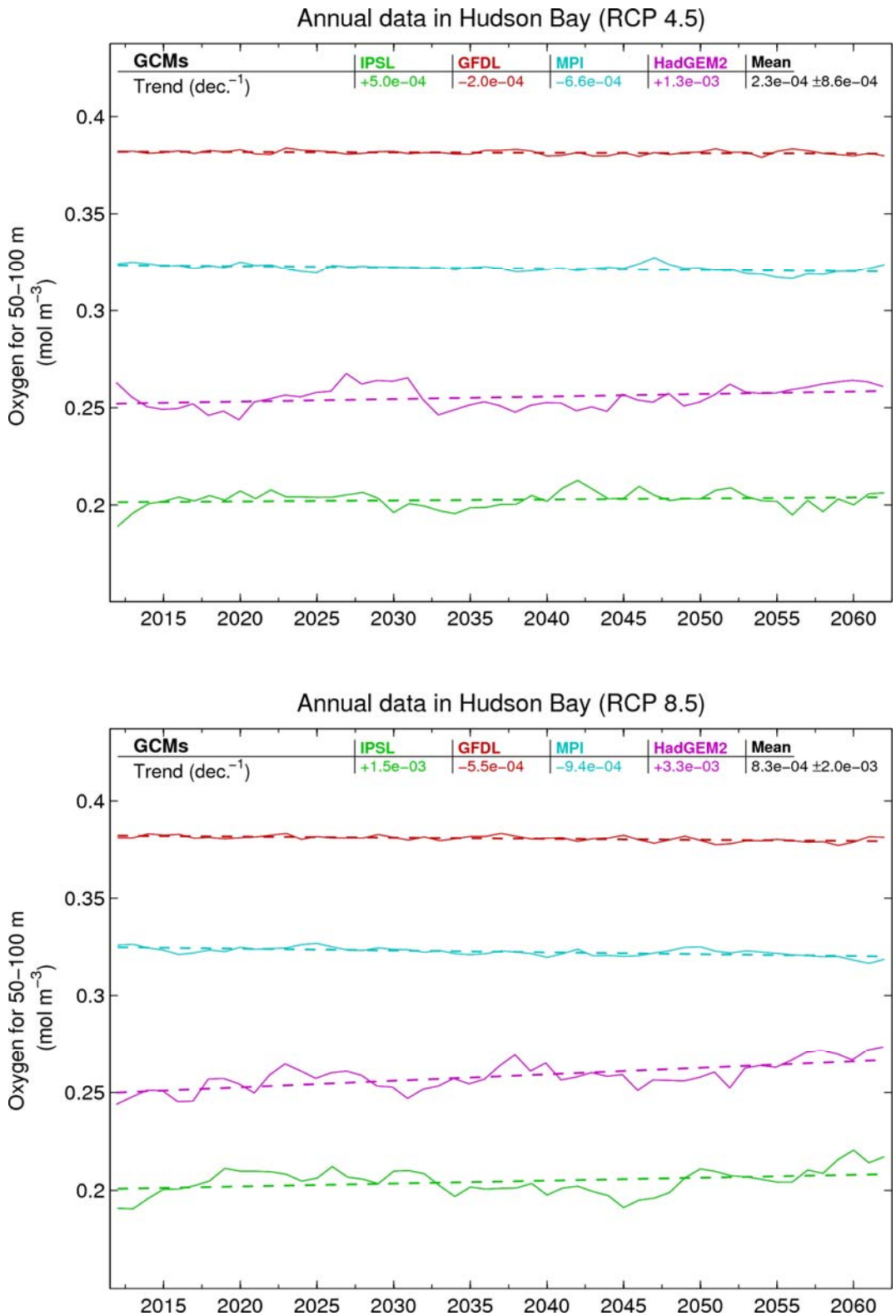

Figure 44. Future dissolved oxygen concentration trends (mol m^{-3}/decade) at 50–100 m in Hudson Bay for the 2012–2062 period for RCP 4.5 (upper panel) and RCP 8.5 (lower panel).

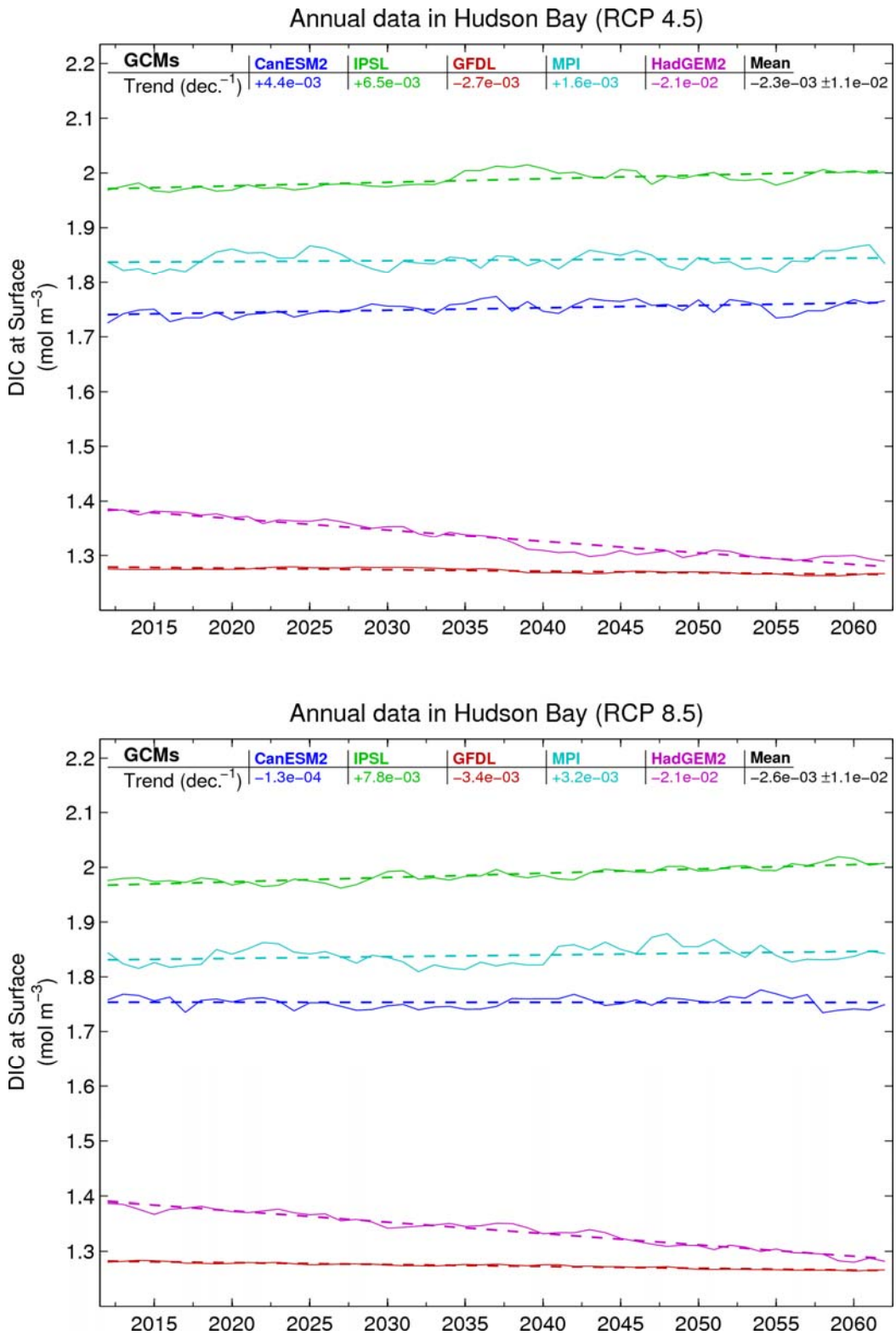

Figure 45. Future DIC concentration trends (mol m^{-3}/decade) at the surface in Hudson Bay for the 2012–2062 period for RCP 4.5 (upper panel) and RCP 8.5 (lower panel).

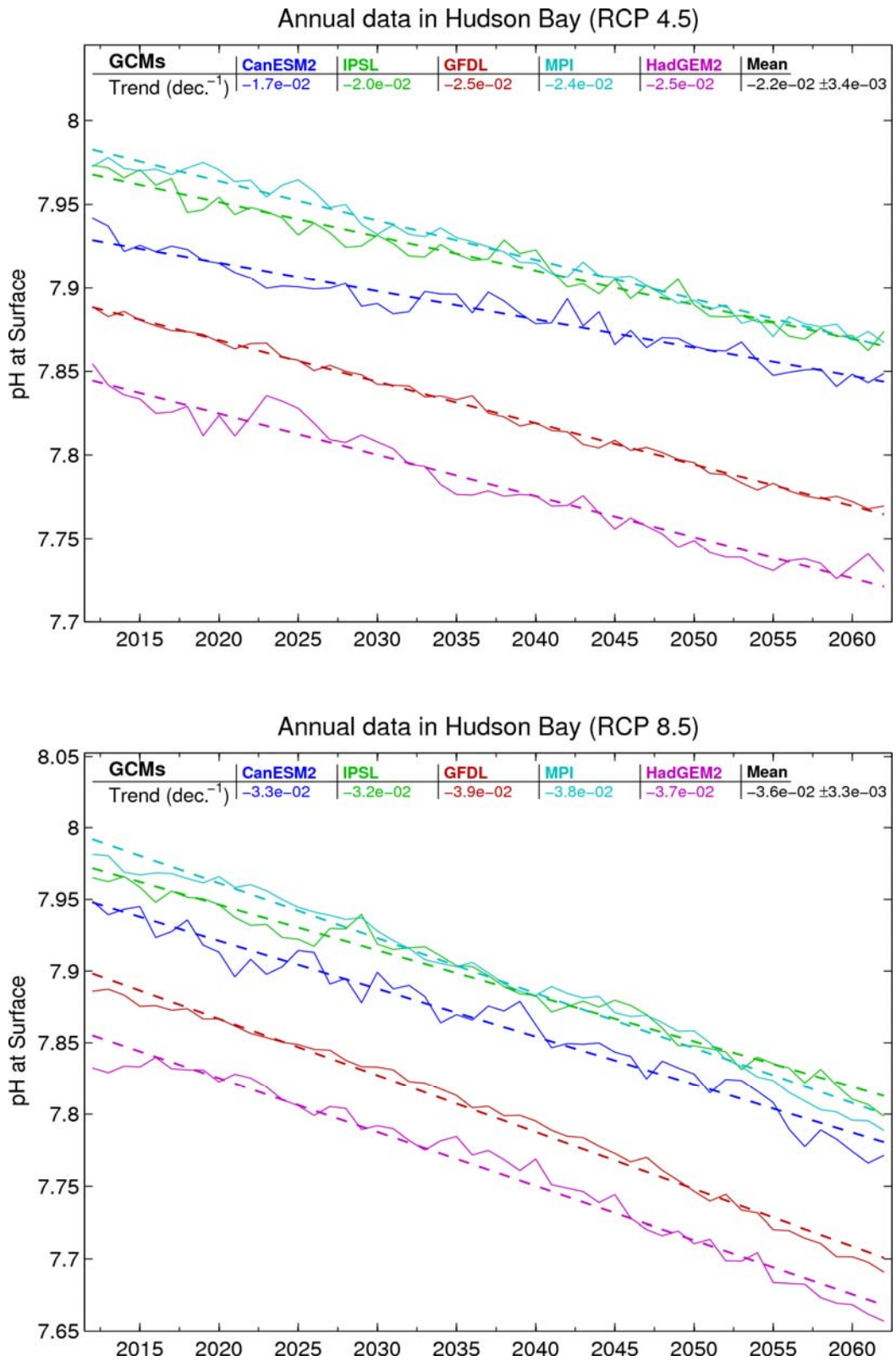

Figure 46. Future pH trends (per decade) at the surface in Hudson Bay for the 2012–2062 period for RCP 4.5 (upper panel) and RCP 8.5 (lower panel).

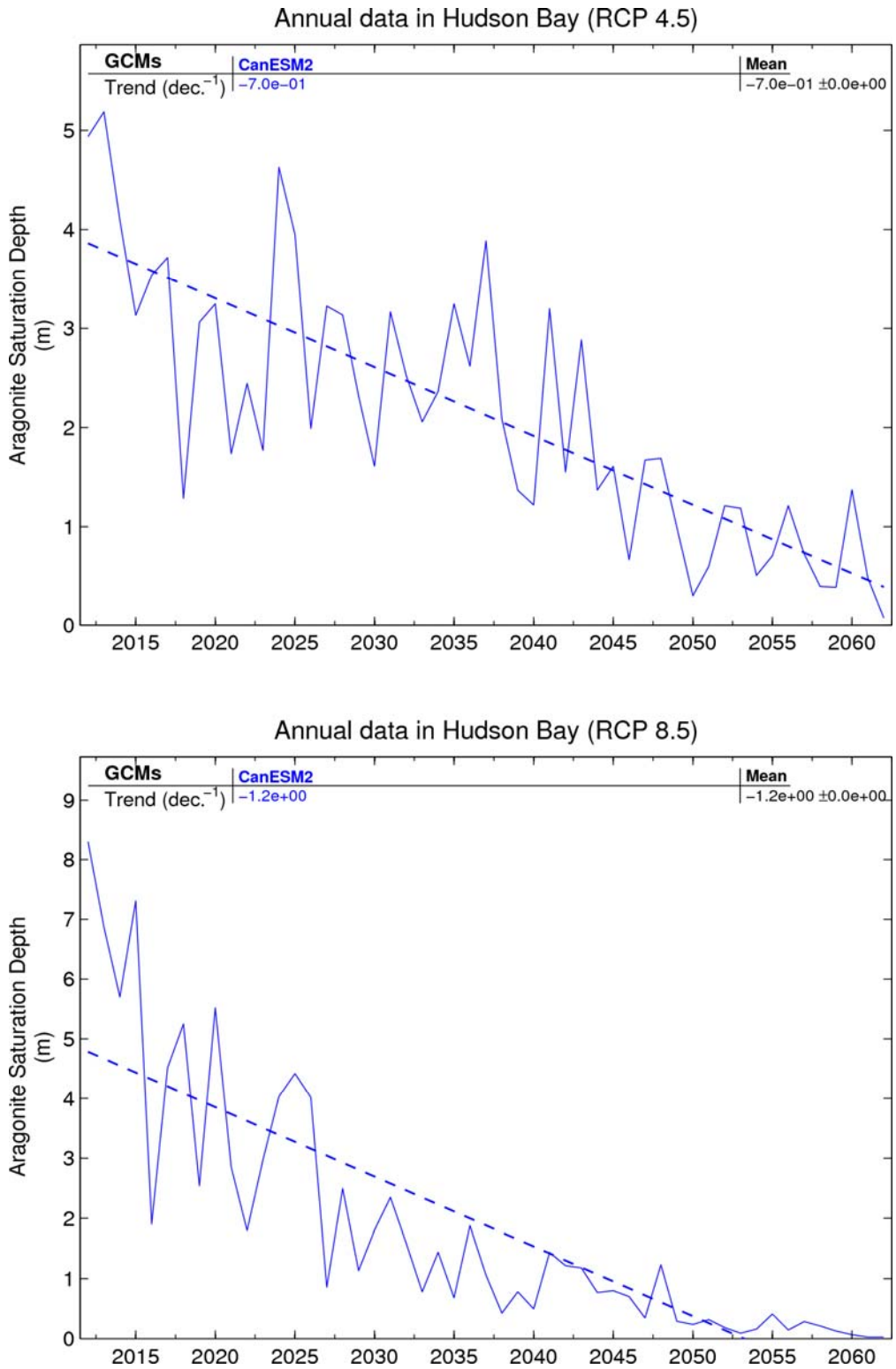

Figure 47. Future aragonite saturation horizon depth in Hudson Bay for the 2012–2062 period for RCPs 4.5 and 8.5.

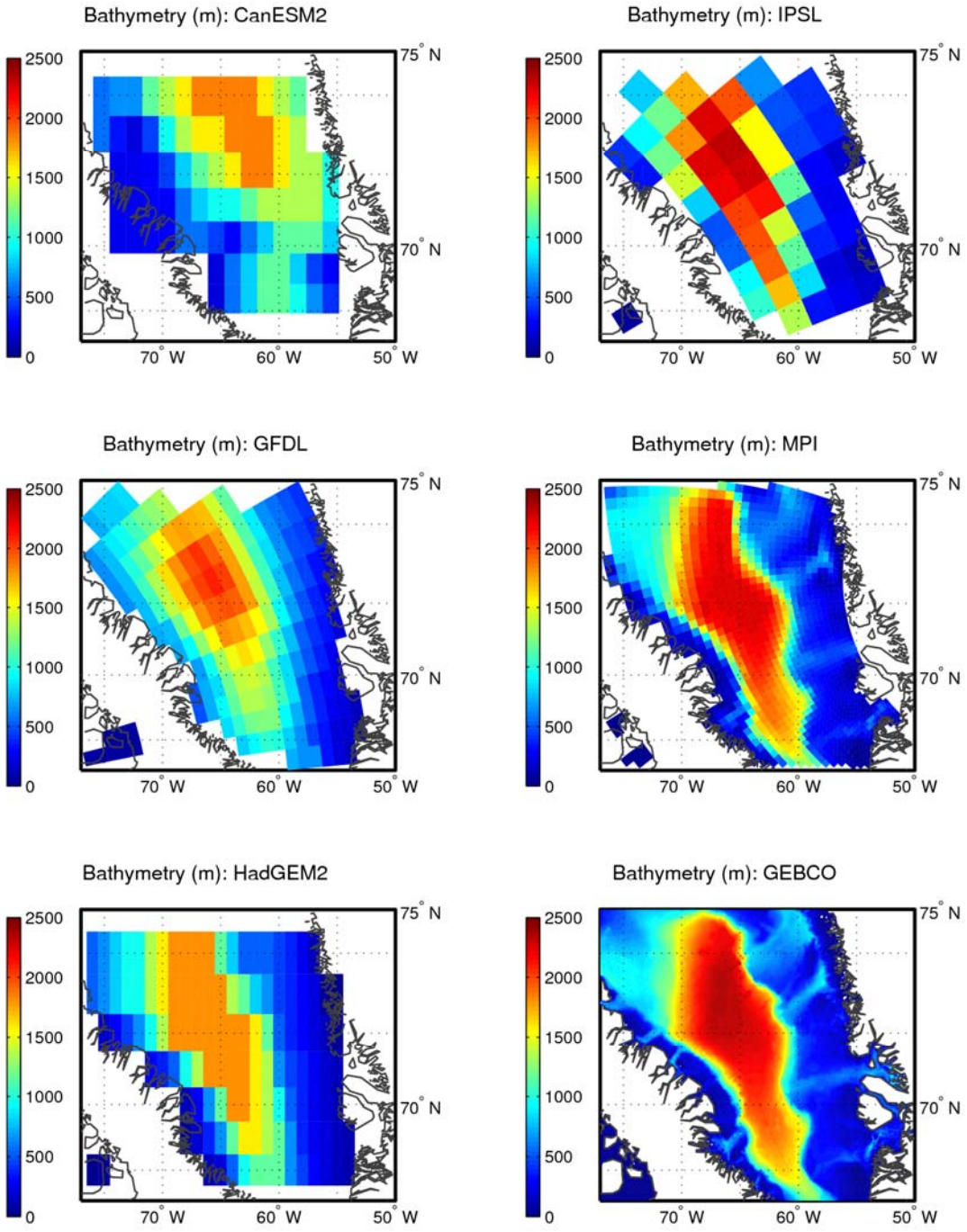

Figure 48. Bathymetry of Baffin Bay in the different models and from the General Bathymetric Chart of the Oceans (GEBCO).

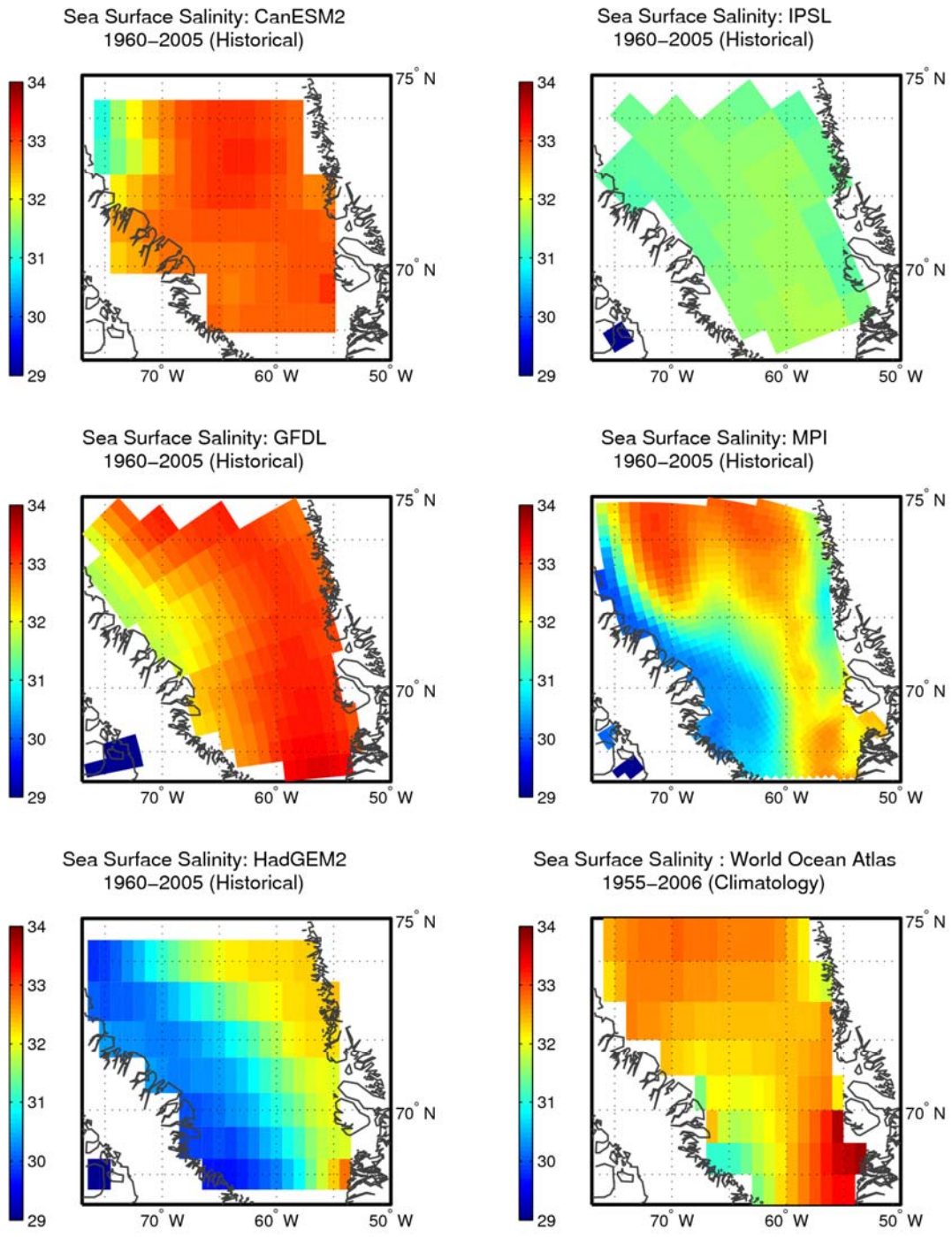

Figure 49. Mean simulated sea-surface salinity in Baffin Bay for the historical period (1960–2005) with sea-surface salinity from the World Ocean Atlas (Antonov et al., 2010).

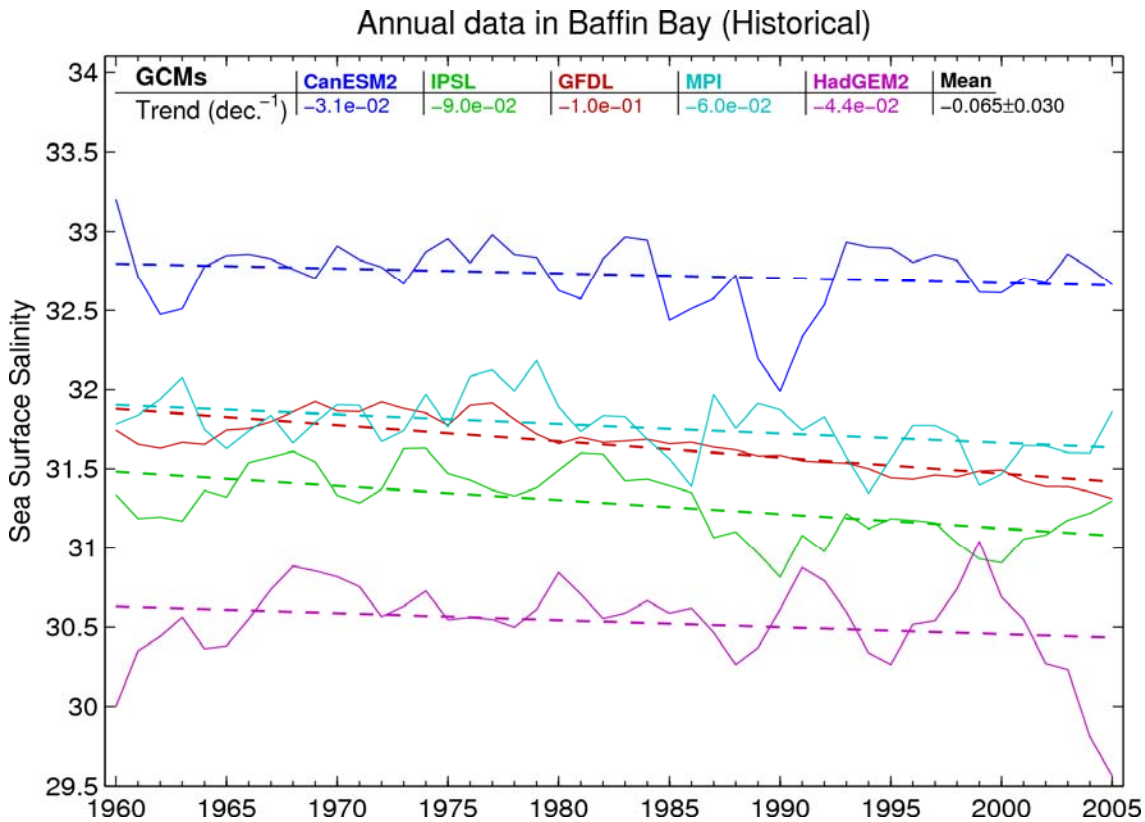

Figure 50. Average sea-surface salinity trends (per decade) over Baffin Bay (see Figure 1) for the historical period (1960–2005).

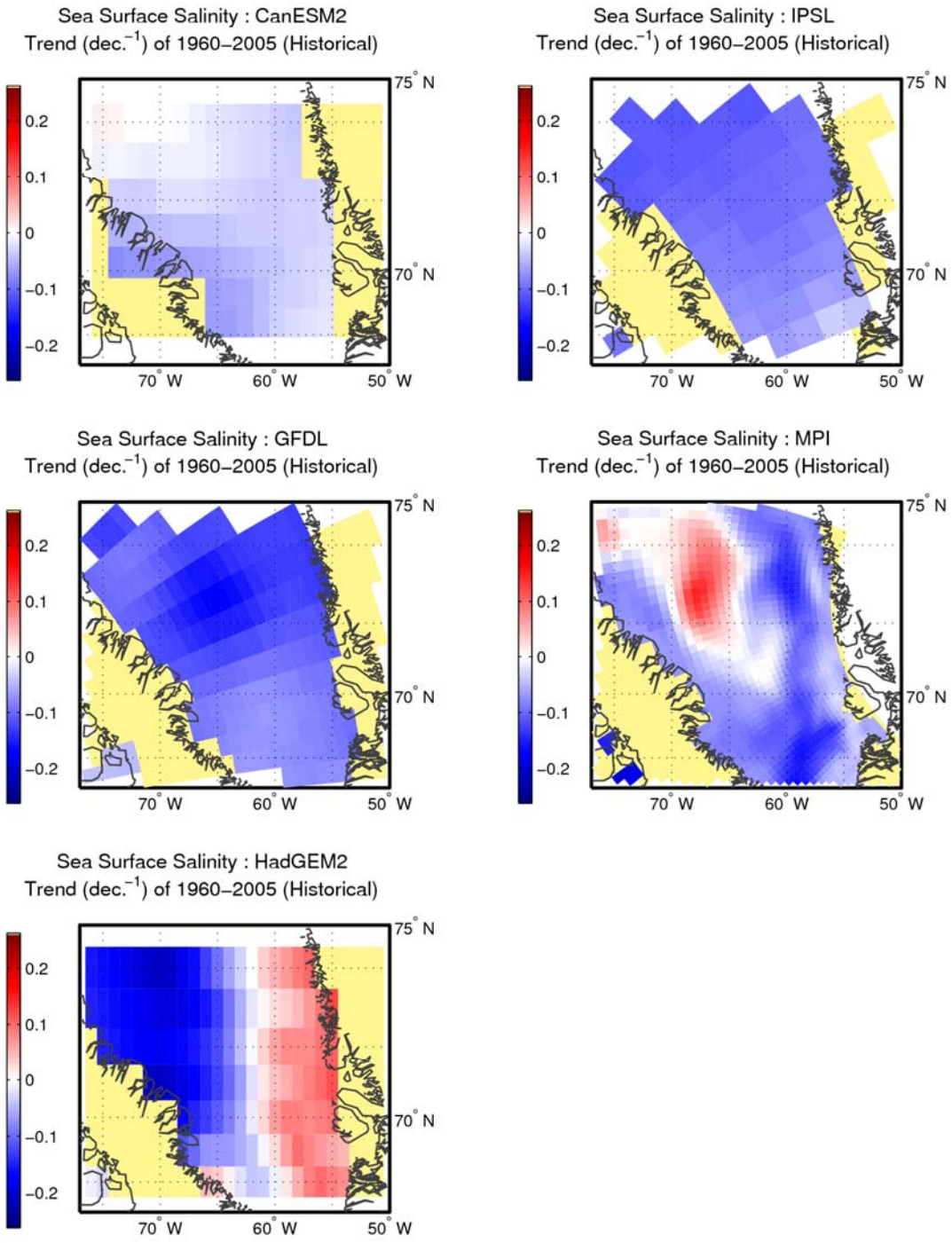

Figure 51. Sea-surface salinity trends (per decade) in each grid cell in Baffin Bay for the historical period (1960–2005).

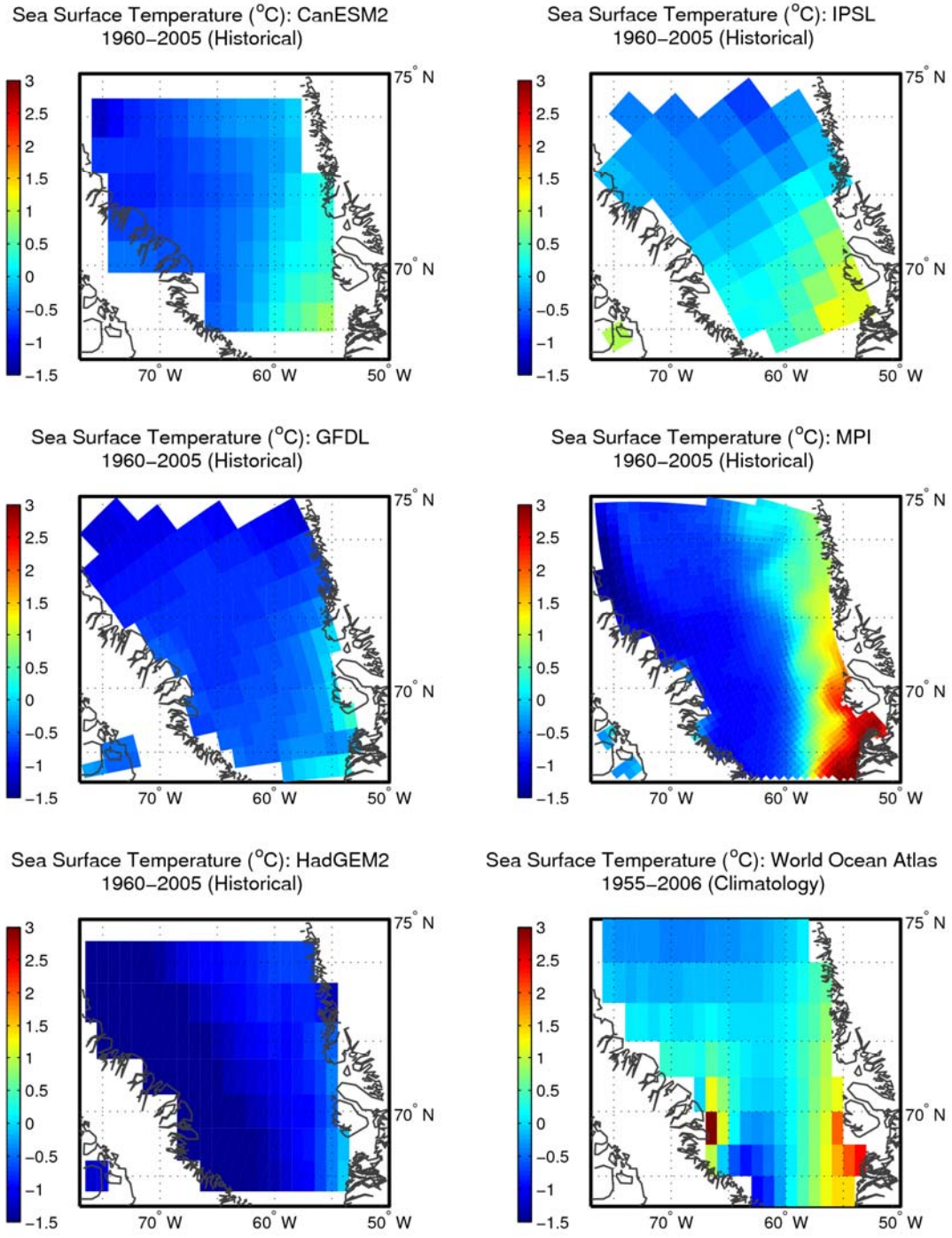

Figure 52. Mean simulated sea-surface temperature (°C) in Baffin Bay for the historical period (1960–2005) with sea-surface temperature from the World Ocean Atlas (Locarnini et al., 2010).

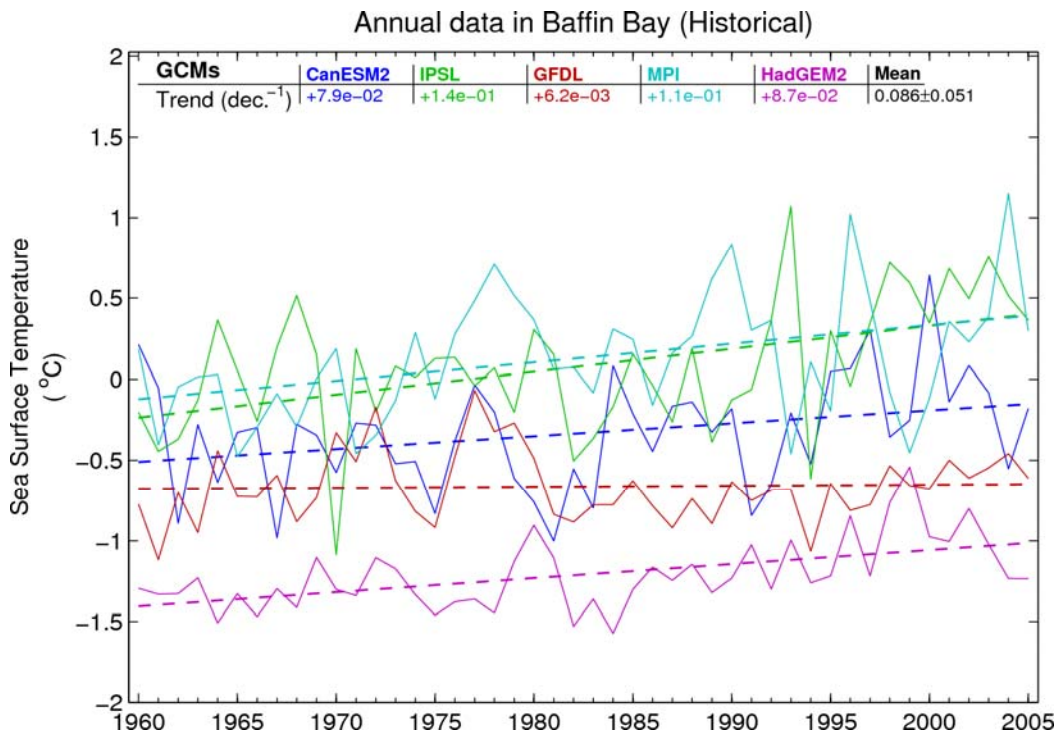

Figure 53. Average sea-surface temperature trends (°C/decade) over Baffin Bay for the historical period (1960–2005).

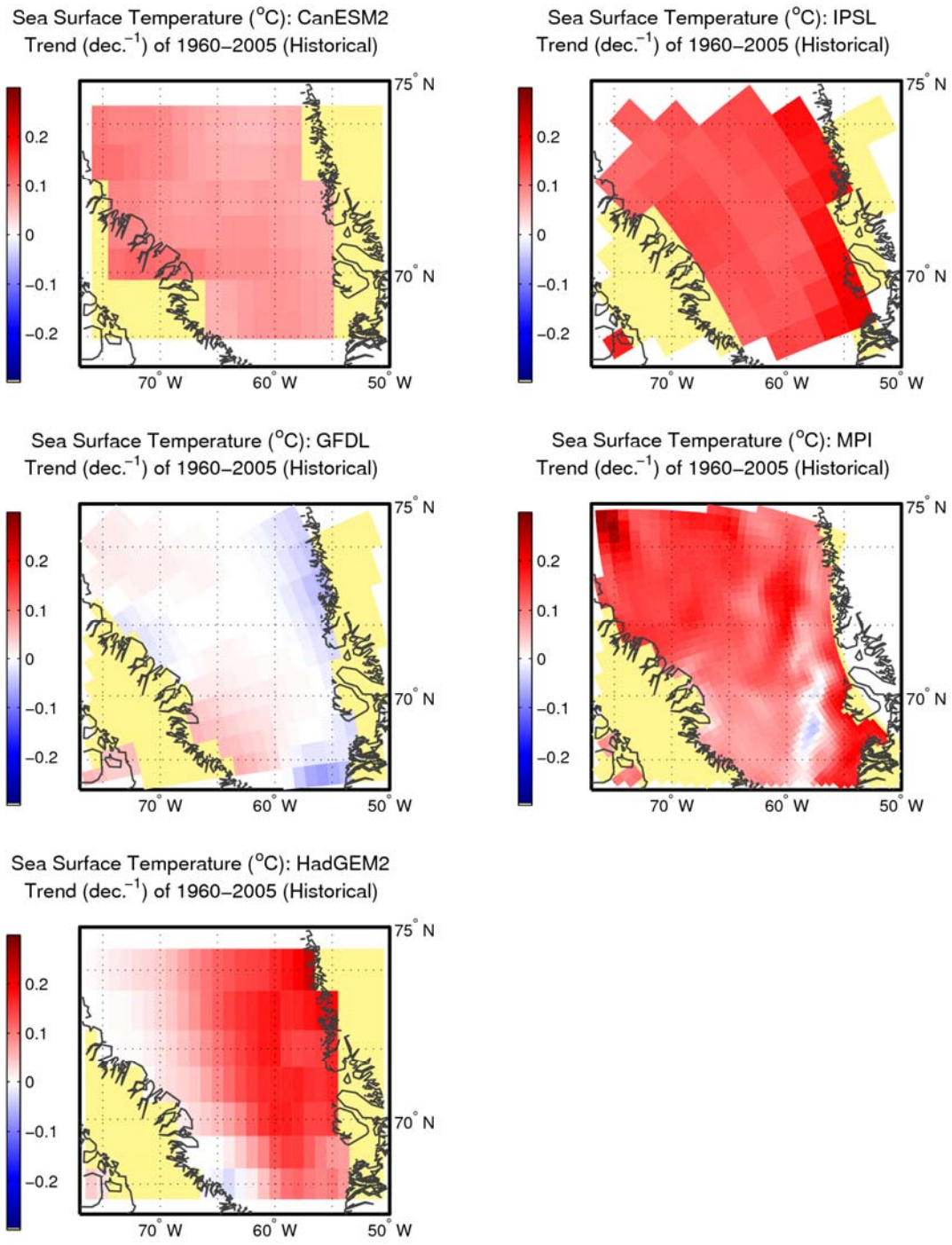

Figure 54. Sea-surface temperature trends (°C/decade) in each grid cell in Baffin Bay for the historical period (1960–2005).

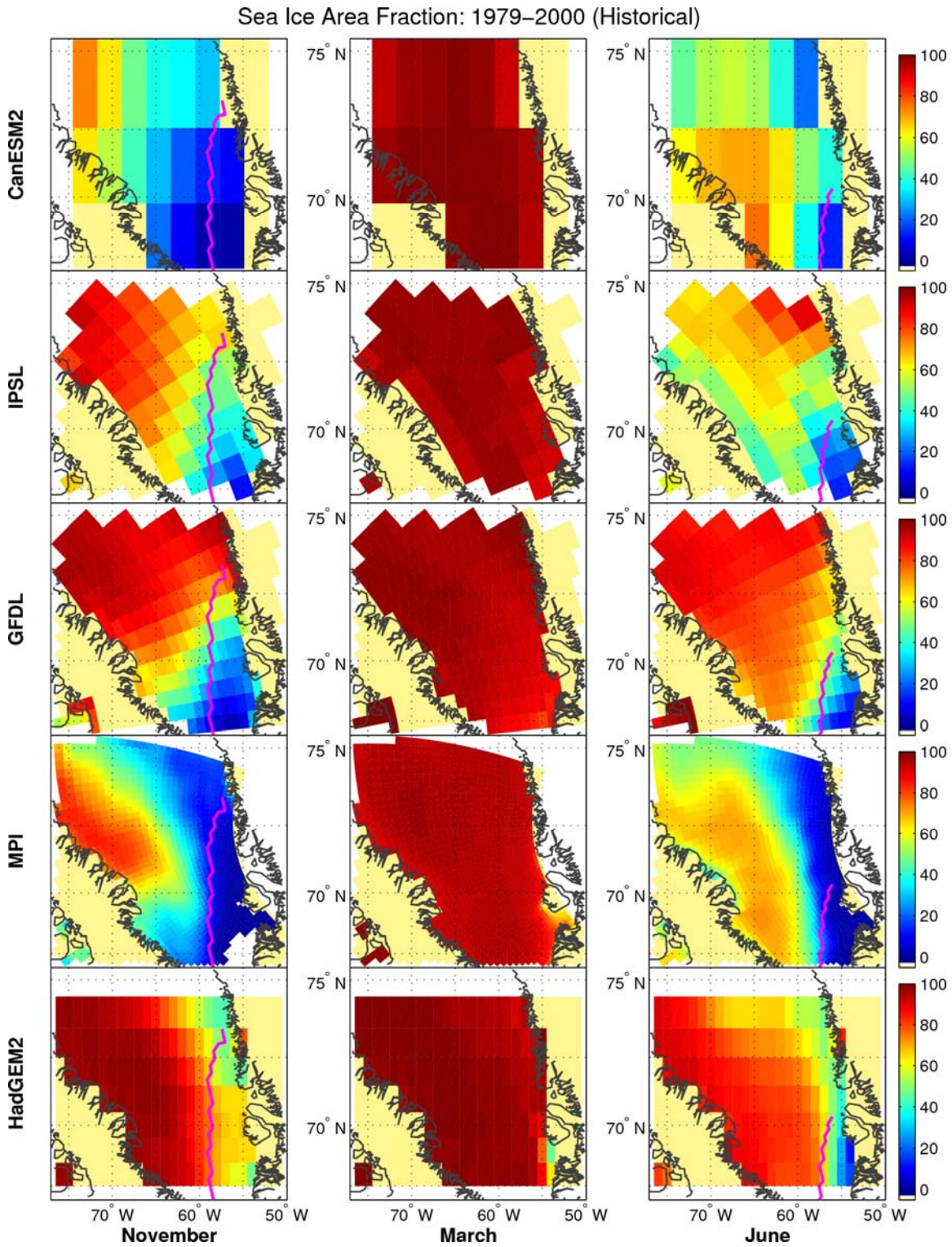

Figure 55. Average sea-ice concentration in the Baffin Bay for November, March, and June for the historical period (1979–2000) according to the 5 GCMs. The magenta lines represents the median extent (15% limit) measured by Fetterer et al. (2009) for the same period.

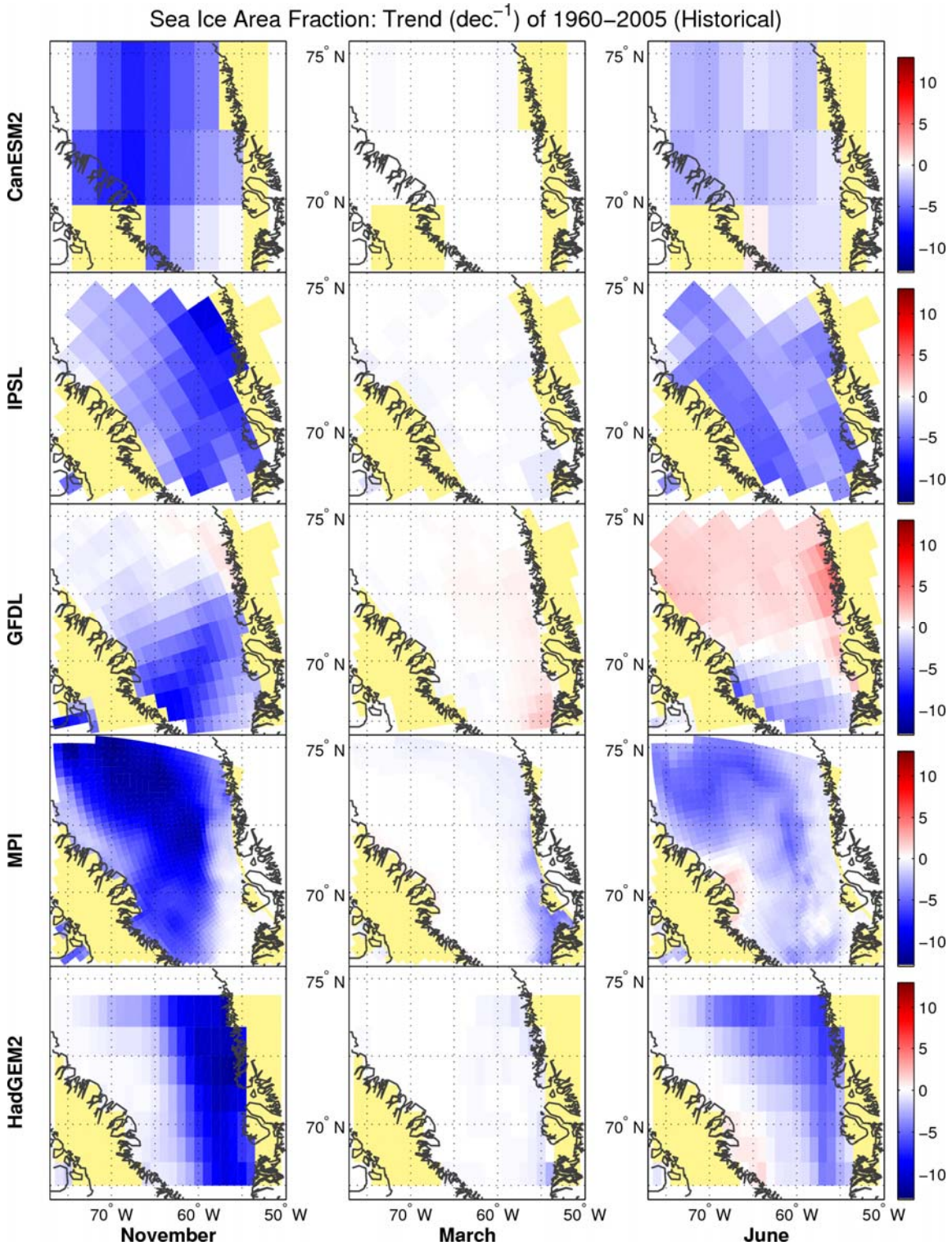

Figure 56. Sea-ice concentration trends (%/decade) in each grid cell in Hudson Bay for November, March, and June for the historical period (1960–2005) according to the 5 GCMs.

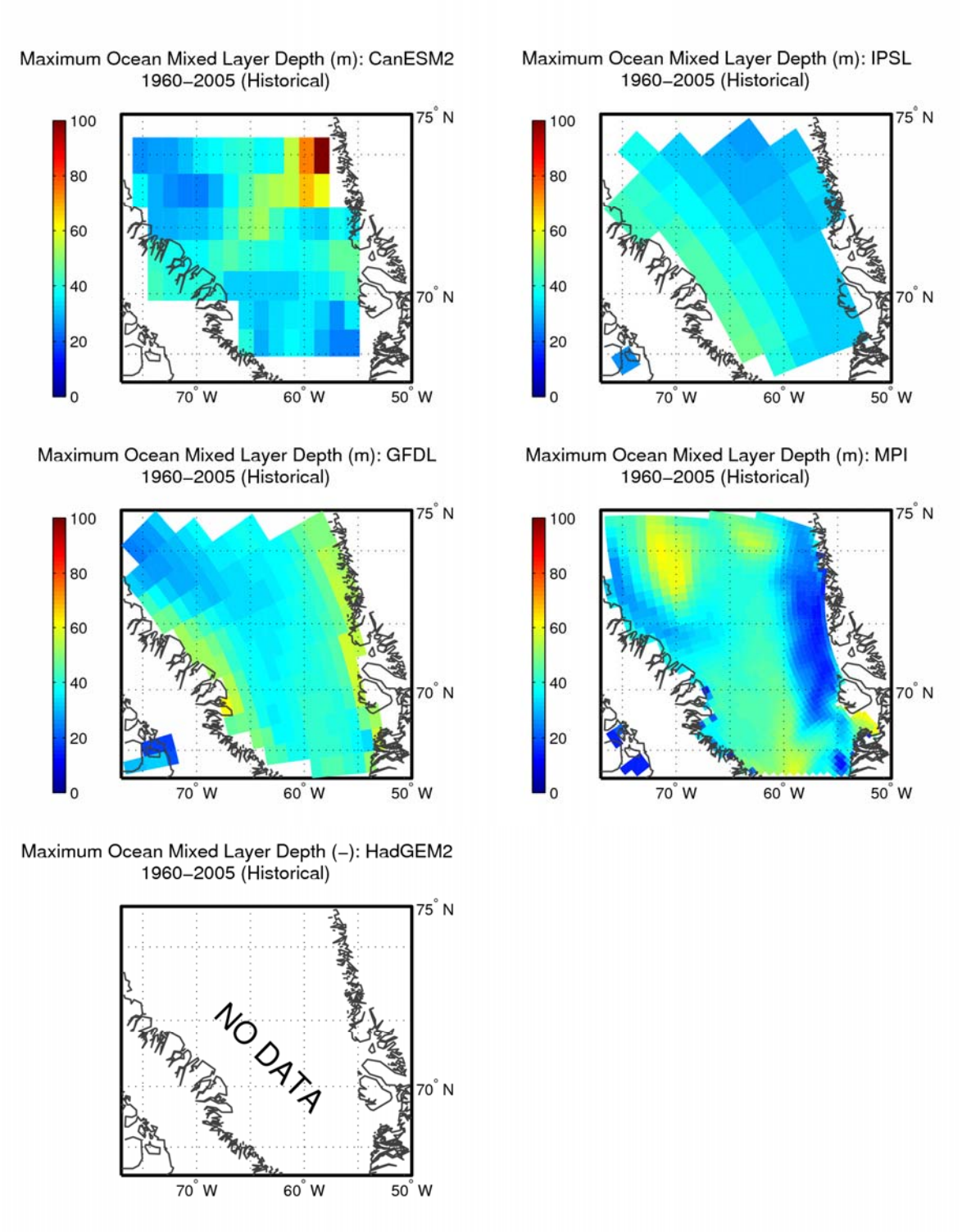

Figure 57. Average maximum mixed layer depth (m) in Baffin Bay for the historical period (1960–2005).

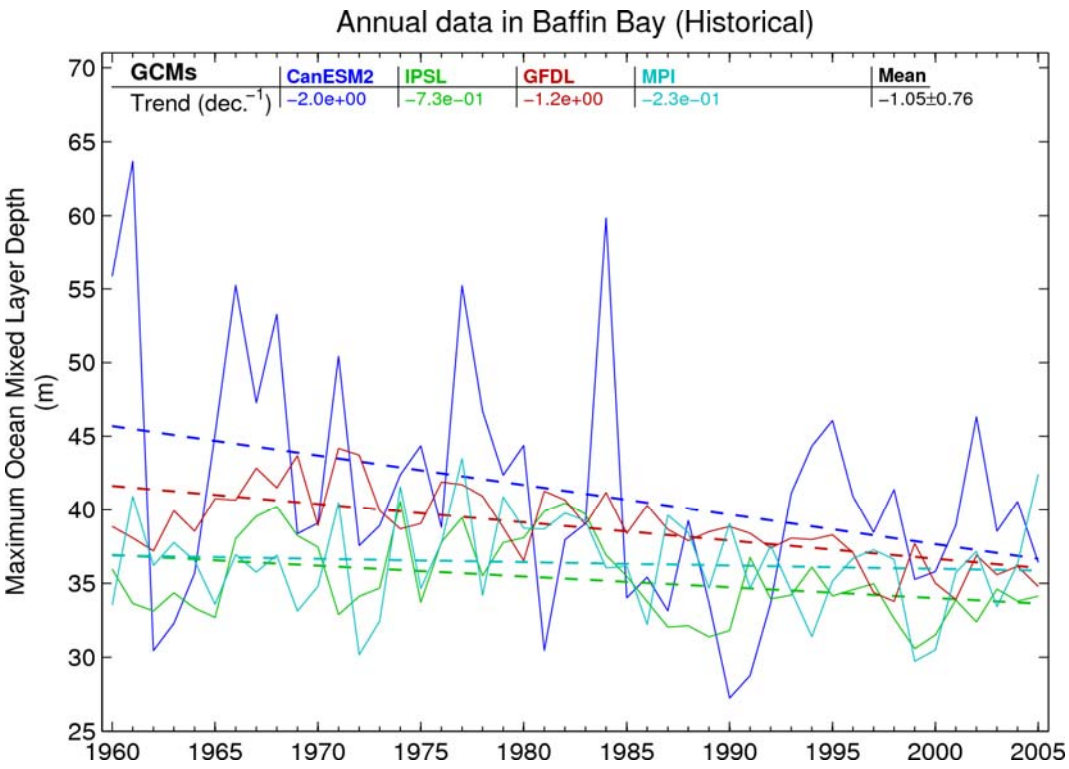

Figure 58. Maximum ocean mixed layer depth trends (m/decade) for the historical period (1960–2005) in Baffin Bay.

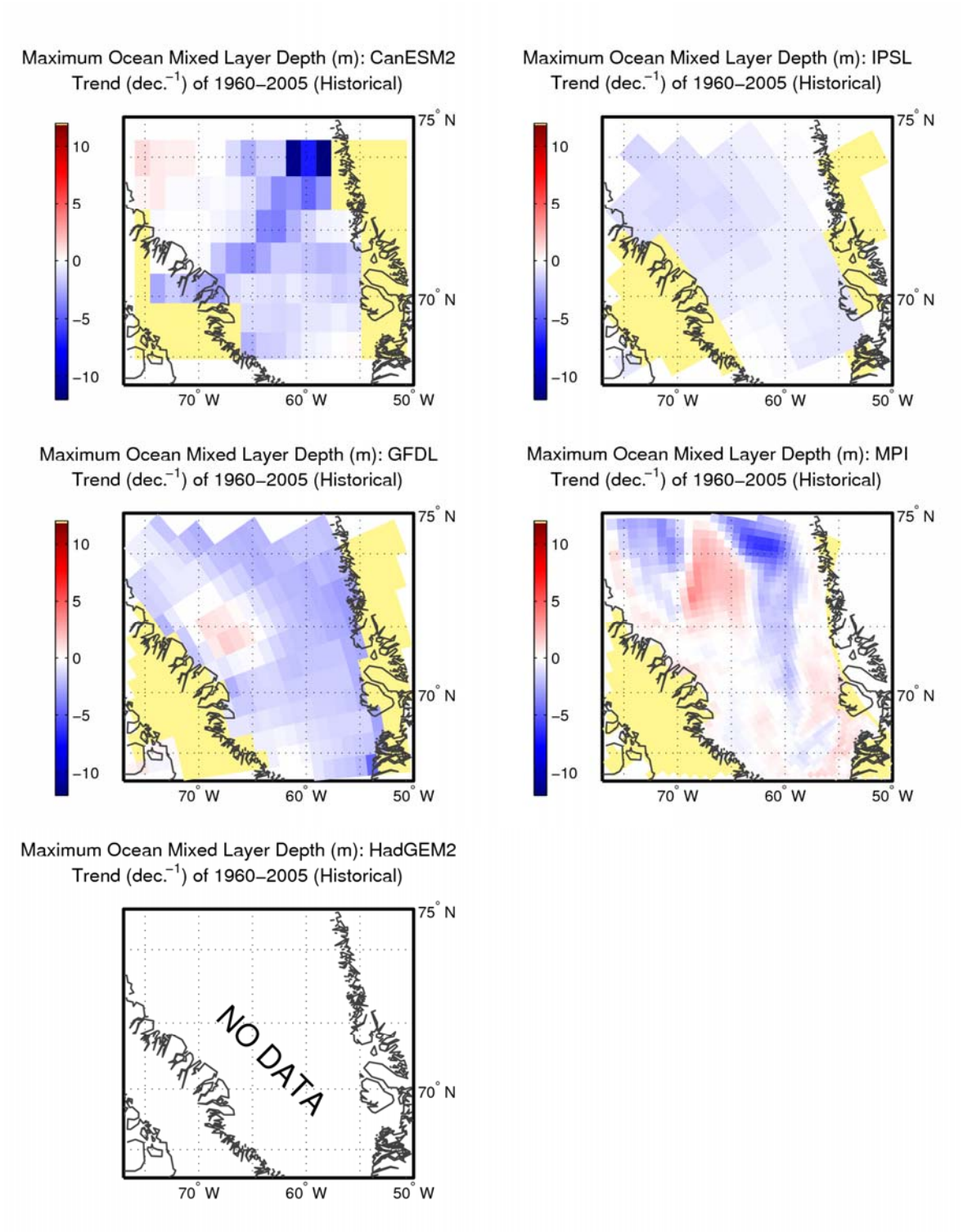

Figure 59. Maximum ocean mixed layer thickness trends (m/decade) in each grid cell for the historical period (1960–2005) in Baffin Bay.

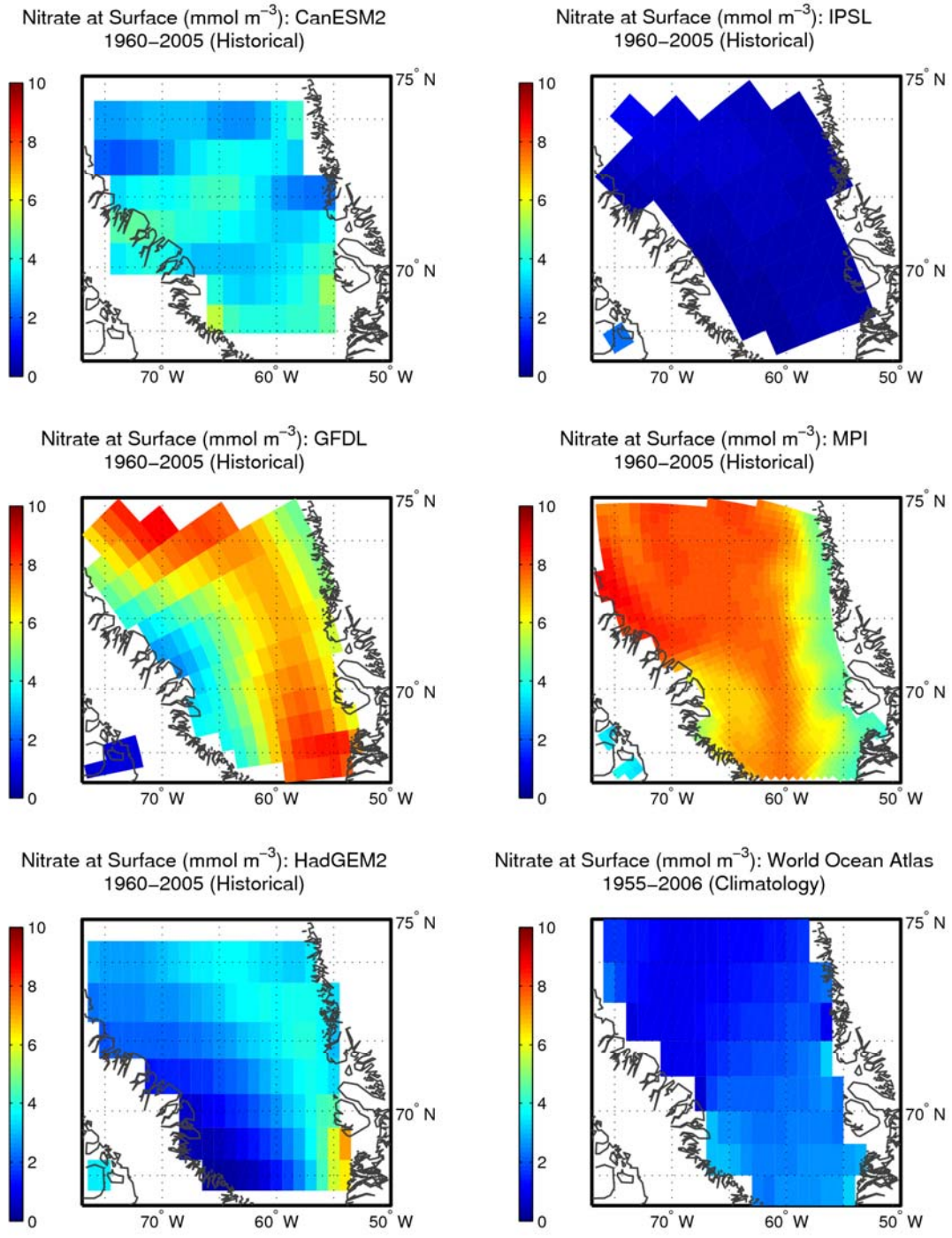

Figure 60. Mean simulated surface nitrate concentration (mmol m^{-3}) in Baffin Bay for the historical period (1960–2005) and nitrate concentration at the surface from the World Ocean Atlas (Garcia et al., 2010b).

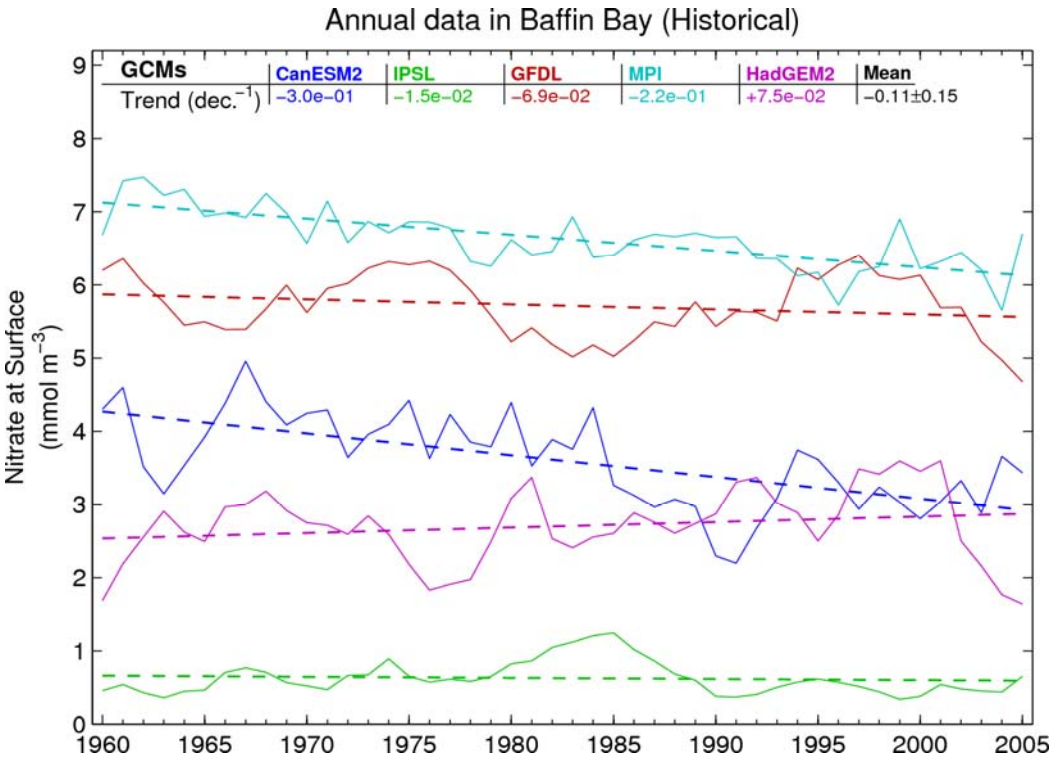

Figure 61. Surface nitrate concentration trends (mmol m^{-3}/decade) in Baffin Bay for the historical period (1960–2005).

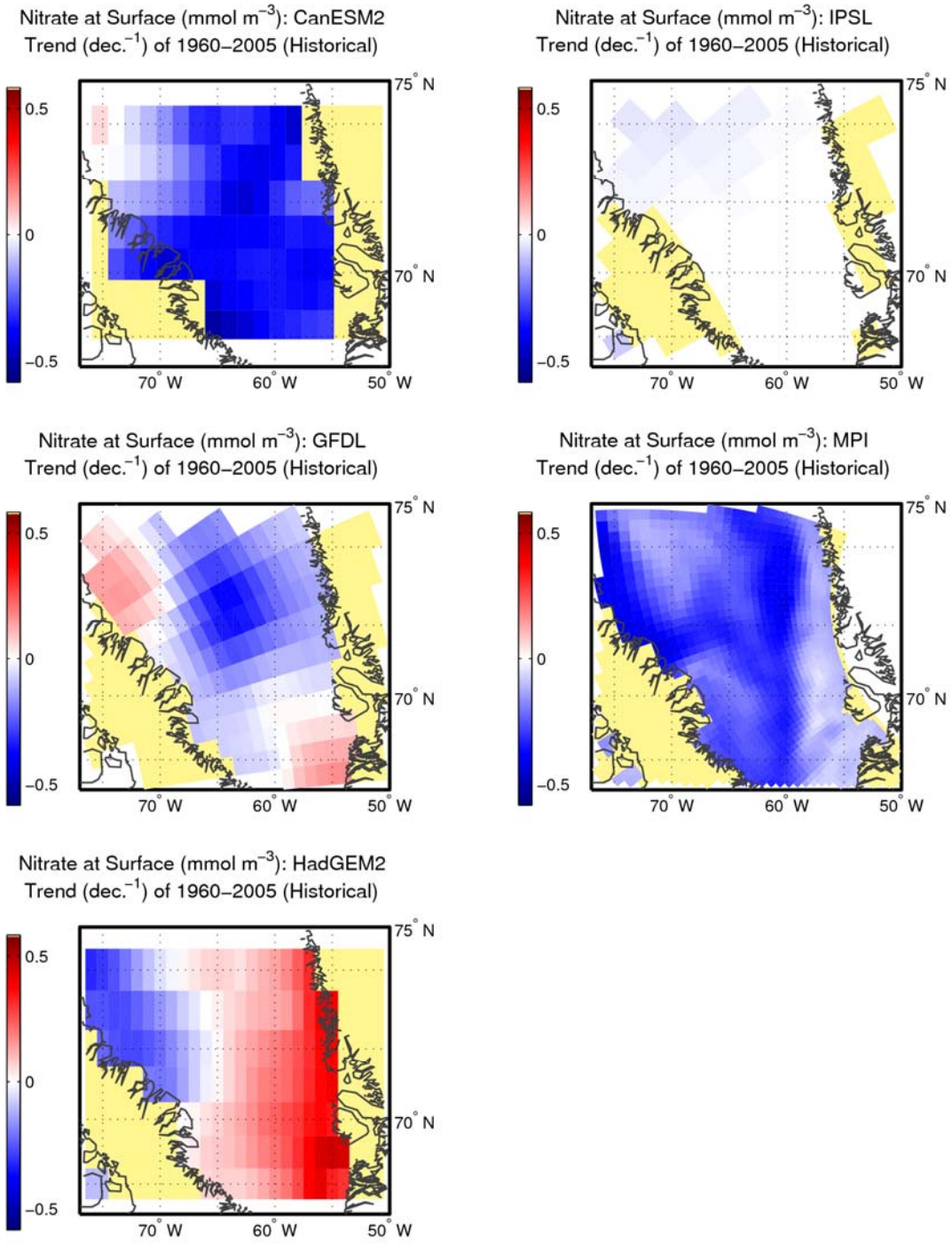

Figure 62. Nitrate concentration trends (mmol m^{-3}/decade) at the surface in each grid cell in Baffin Bay for the historical period (1960–2005).

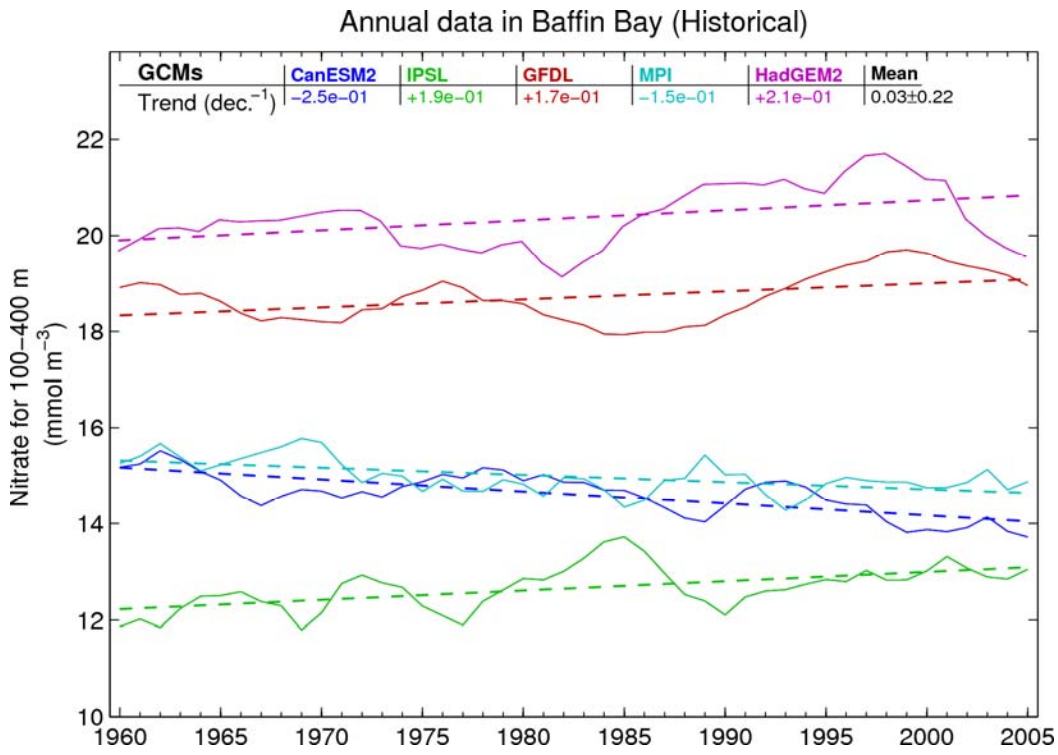

Figure 63. Nitrate concentration trends (mmol m^{-3}/decade) at 100–400 m in Baffin Bay for the historical period (1960–2005).

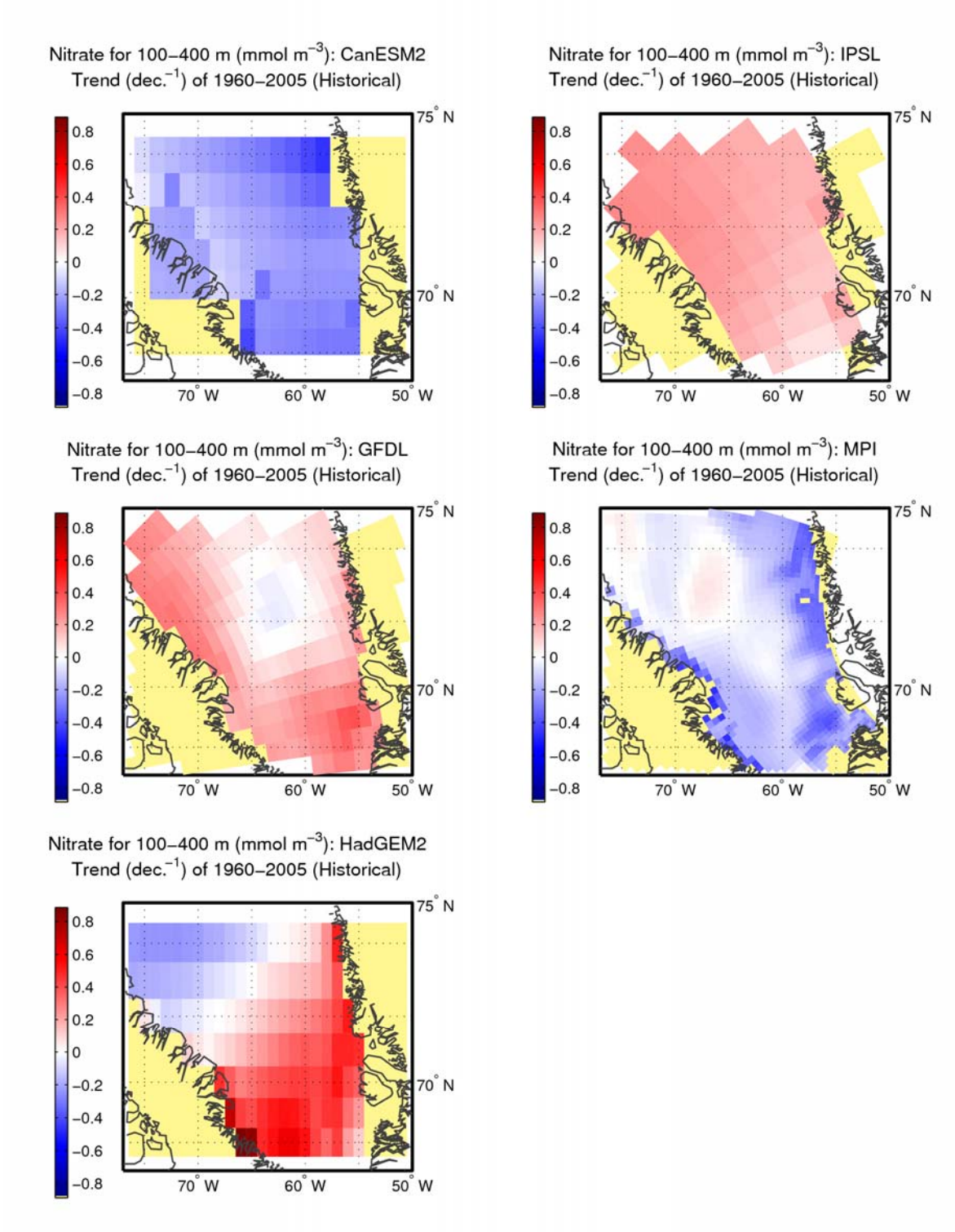

Figure 64. Nitrate concentration trends (mmol m^{-3}/decade) at 100–400 m in each grid cell in Baffin Bay for the historical simulations (1960–2005).

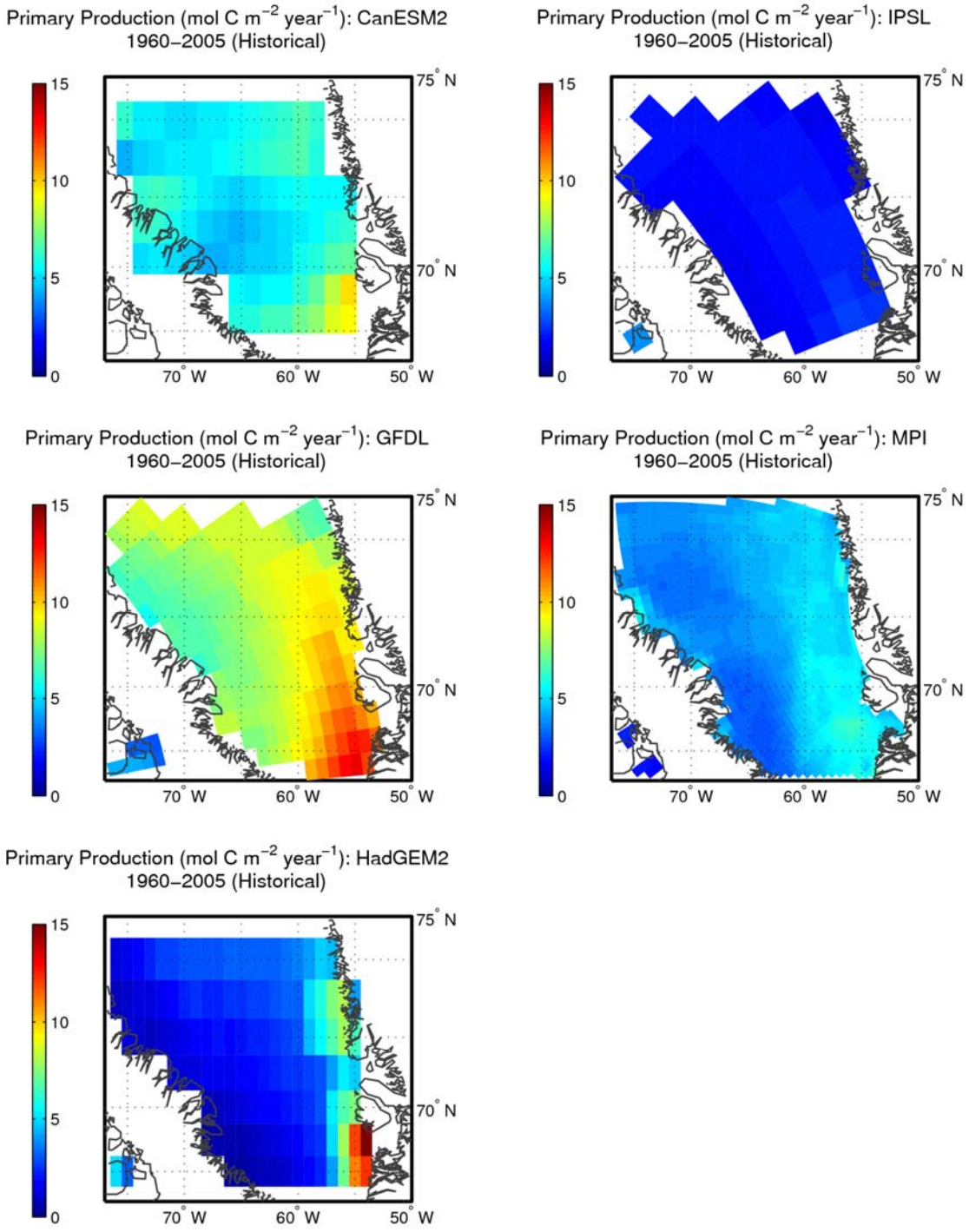

Figure 65. Mean simulated vertically integrated primary production (mol C m^{-2} year^{-1}) in Baffin Bay for the historical period (1960–2005).

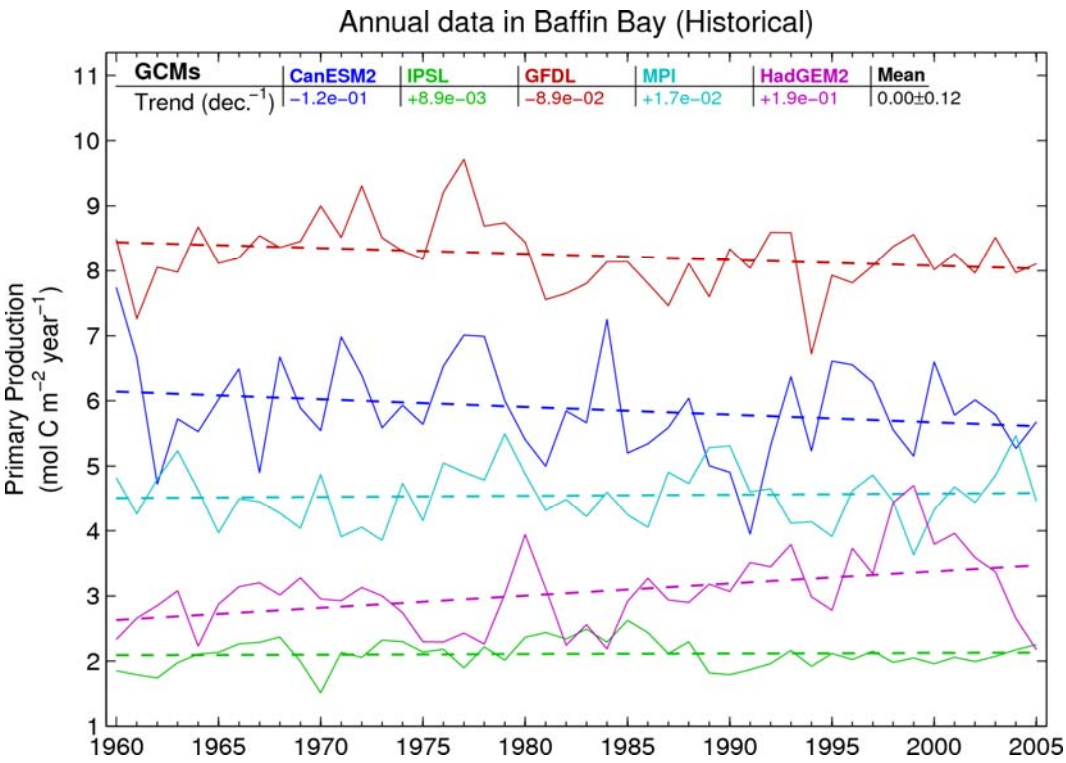

Figure 66. Simulated vertically integrated primary production trends (mol C m^{-2} year^{-1} per decade) in Baffin Bay for the historical period (1960–2005).

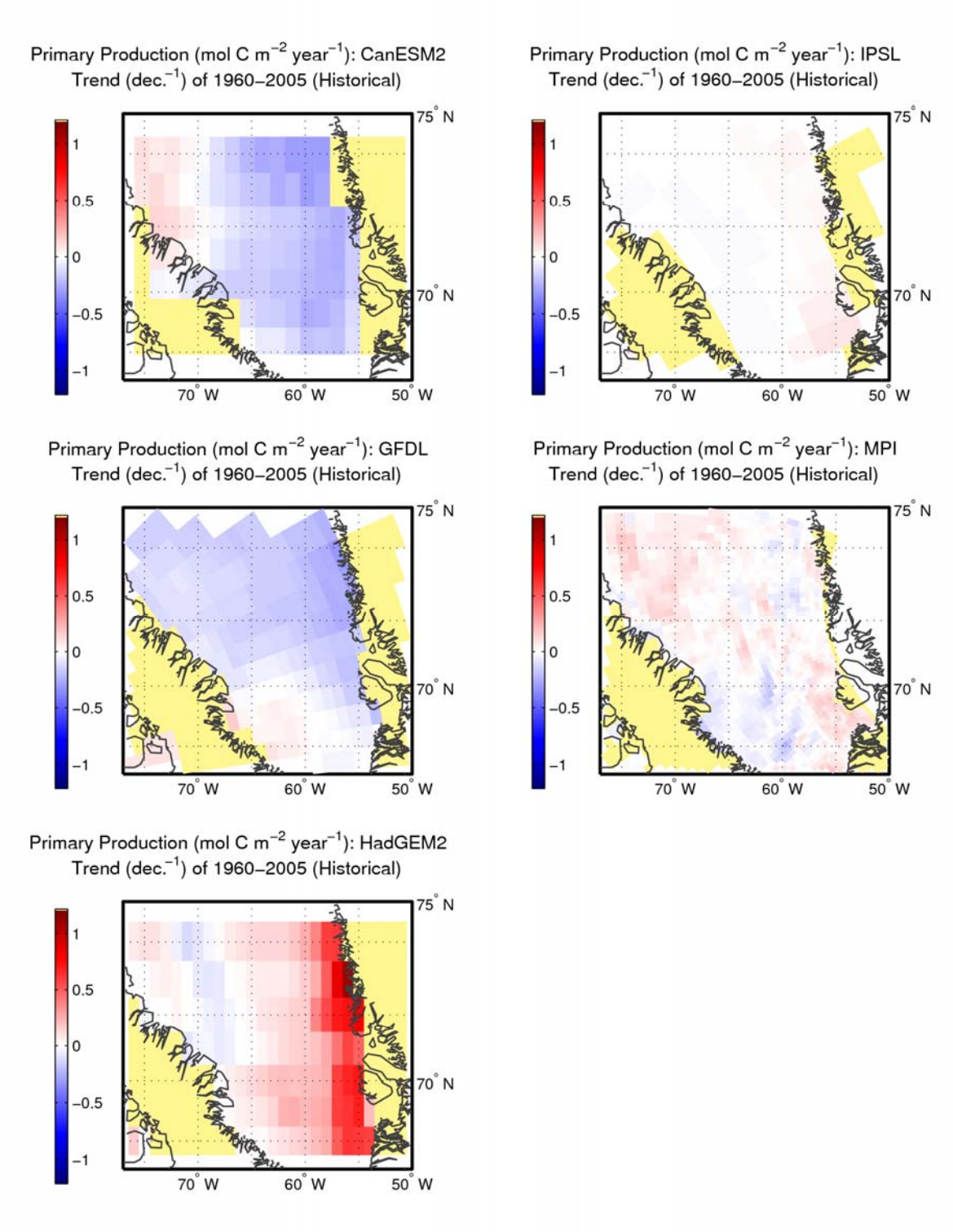

Figure 67. Vertically integrated primary production trends (mol C m^{-2} year^{-1} per decade) in each grid cell in Baffin Bay for the historical simulations (1960–2005).

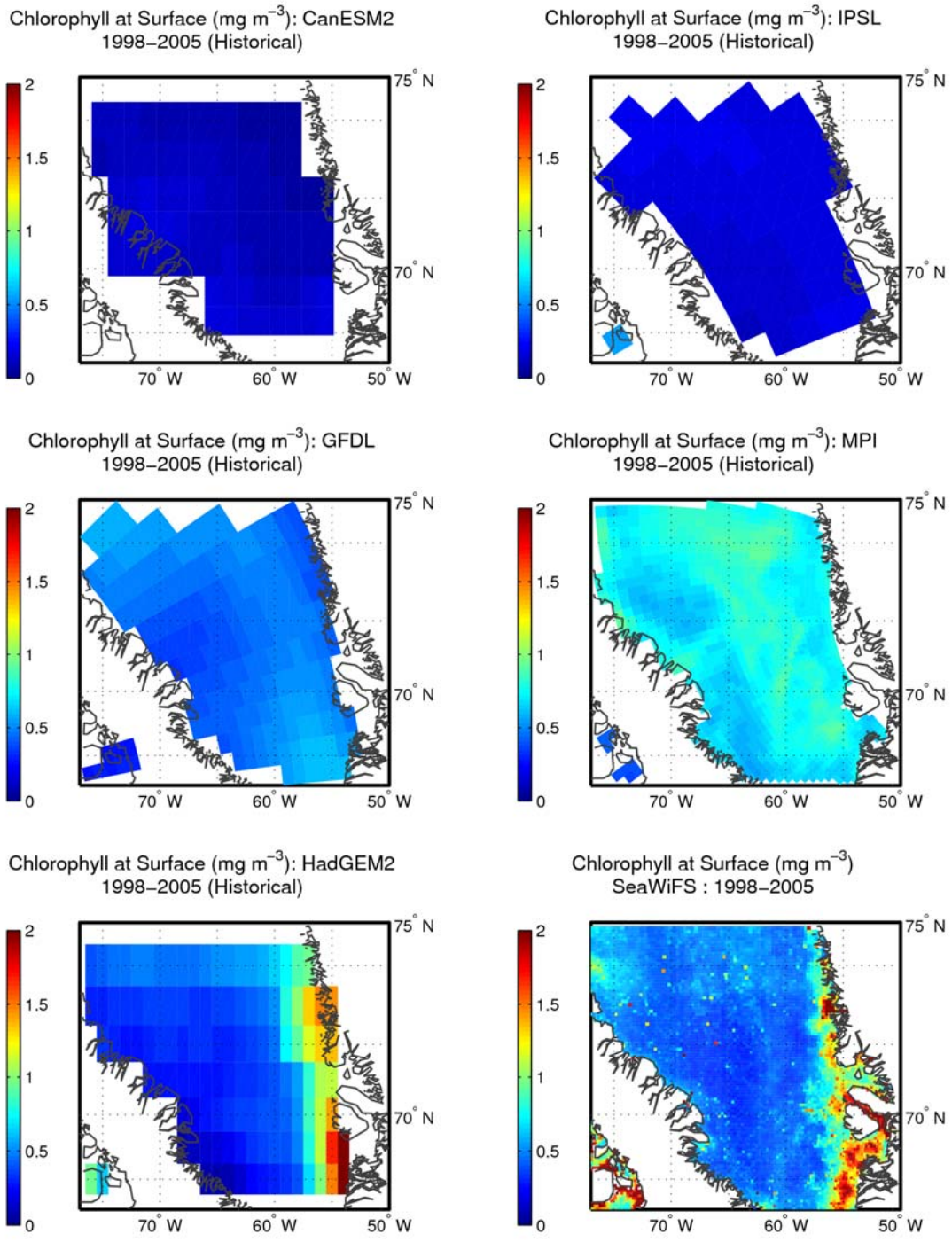

Figure 68. Annual mean simulated surface Chl *a* concentration (mg m^{-3}) and chlorophyll data from SeaWiFS in Baffin Bay for the 1998–2005 period.

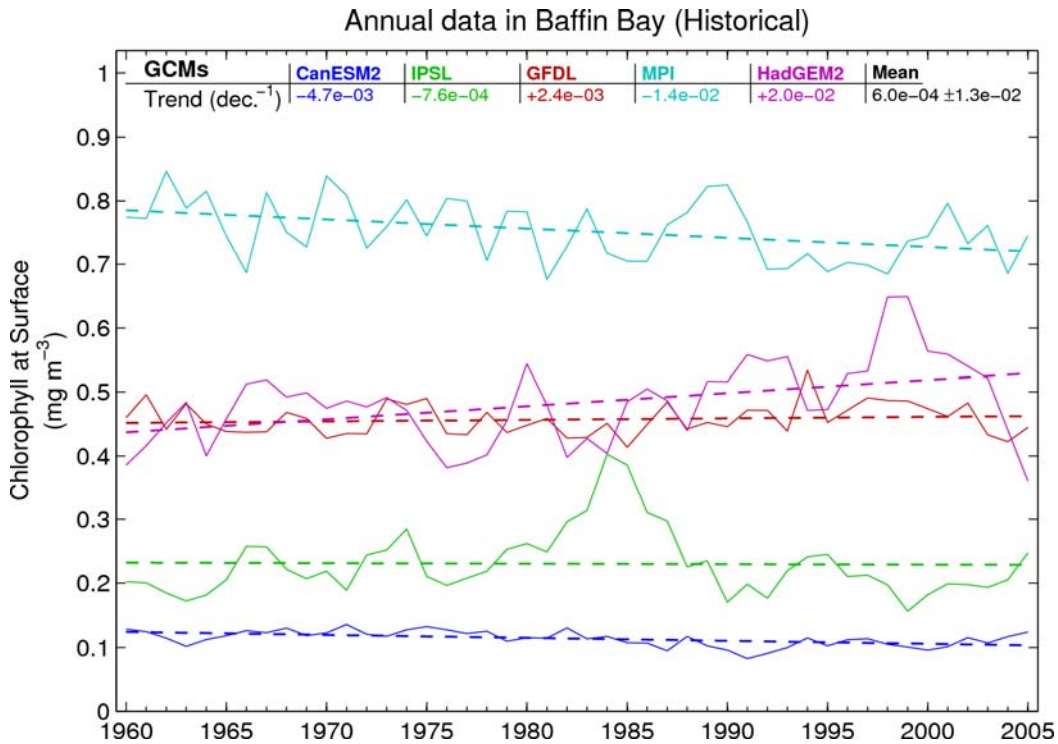

Figure 69. Average Chl *a* concentration trends (mg m^{-3}/decade) at the surface in Baffin Bay for the historical period (1960–2005).

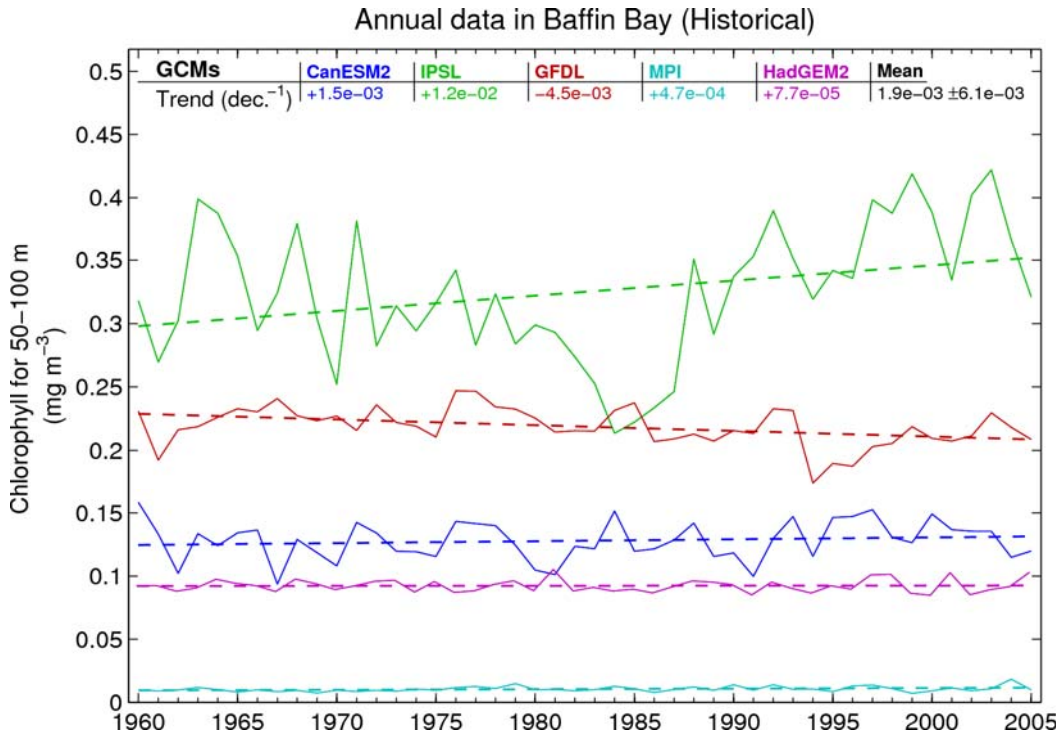

Figure 70. Average Chl *a* concentration trends (mg m^{-3}/decade) at 50–100 m in Baffin Bay for the historical period (1960–2005).

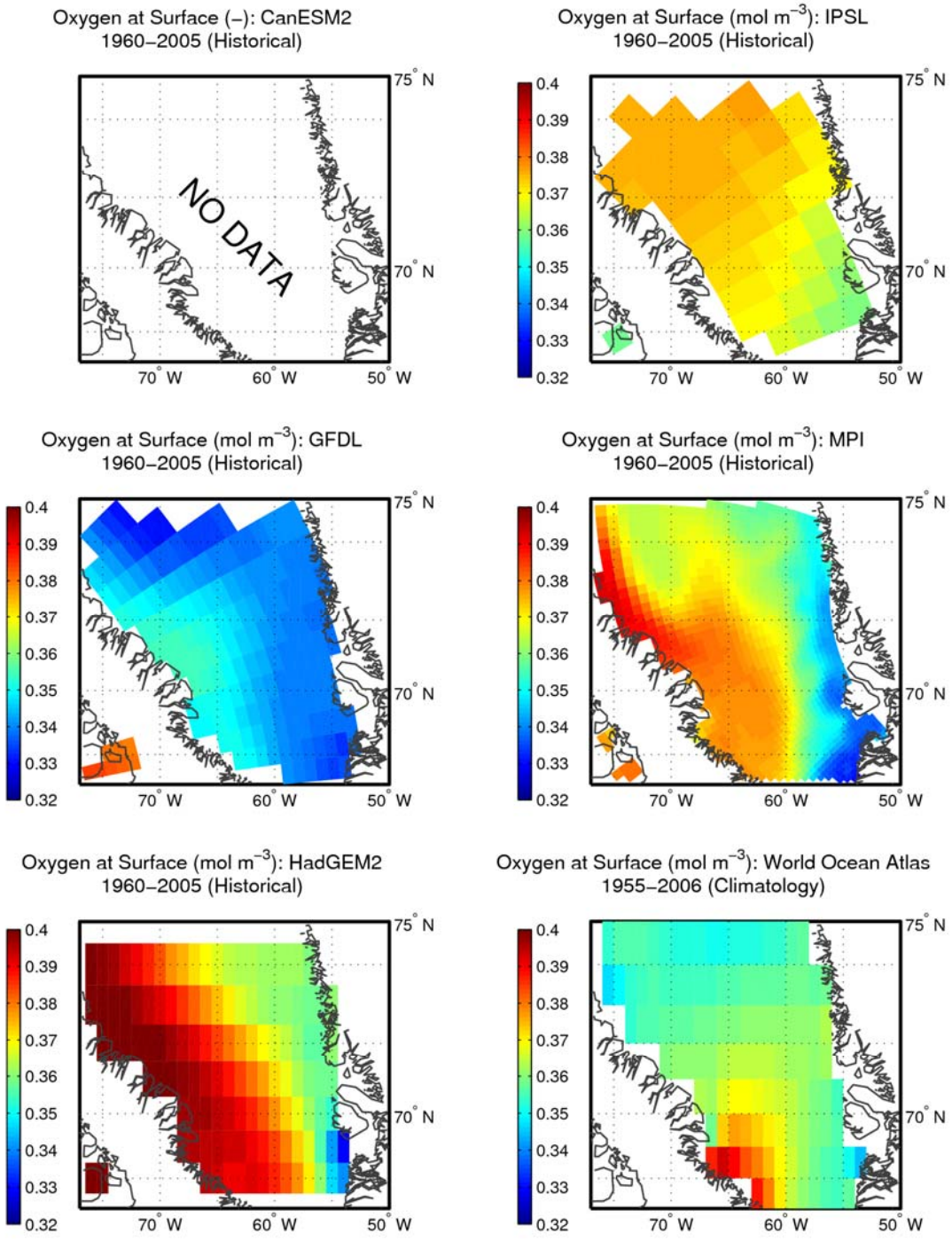

Figure 71. Mean simulated surface dissolved oxygen concentration (mol m^{-3}) in Baffin Bay for the historical period (1960–2005) and dissolved oxygen concentration at the surface from the World Ocean Atlas (Garcia et al., 2010a).

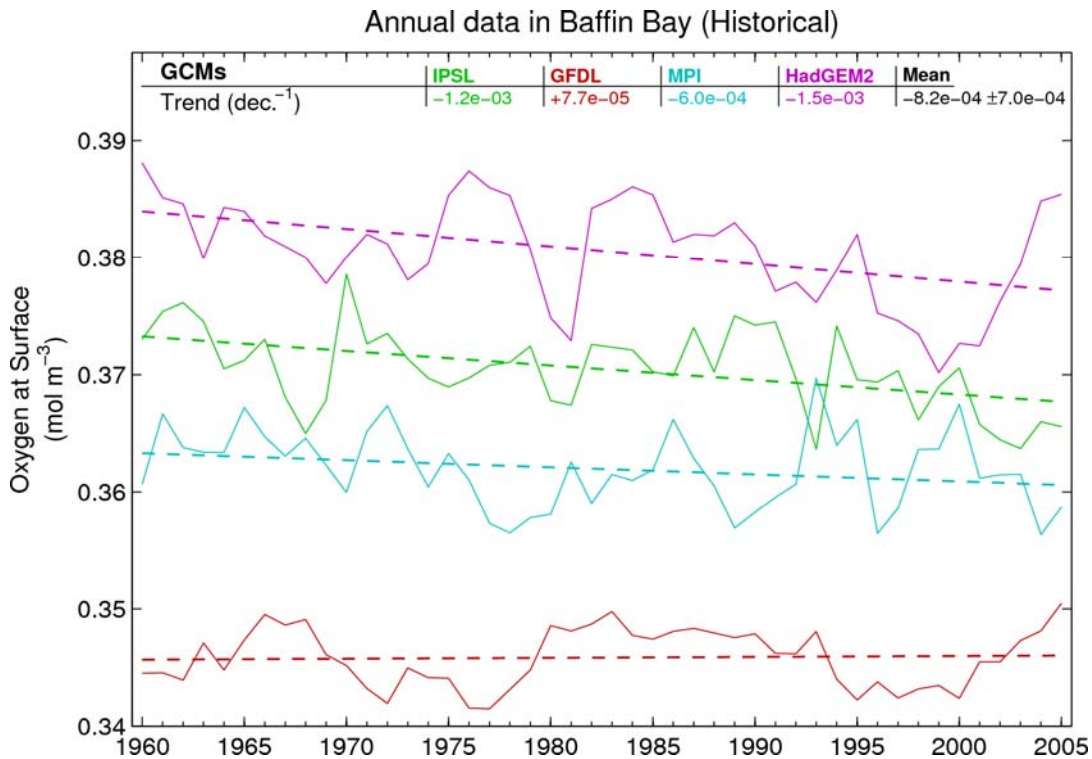

Figure 72. Simulated dissolved oxygen concentration trends (mol m^{-3}/decade) at the surface in Baffin Bay for the historical period (1960–2005).

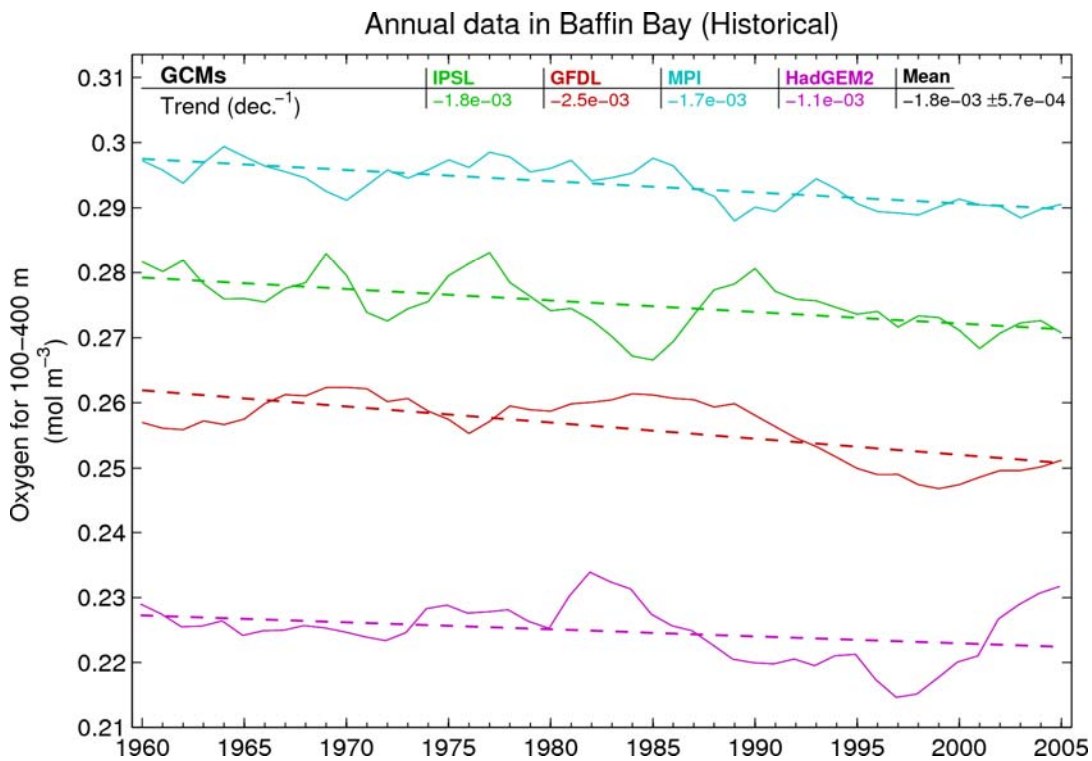

Figure 73. Simulated dissolved oxygen concentration trends (mol m^{-3}/decade) at 100–400 m in Baffin Bay for the historical period (1960–2005).

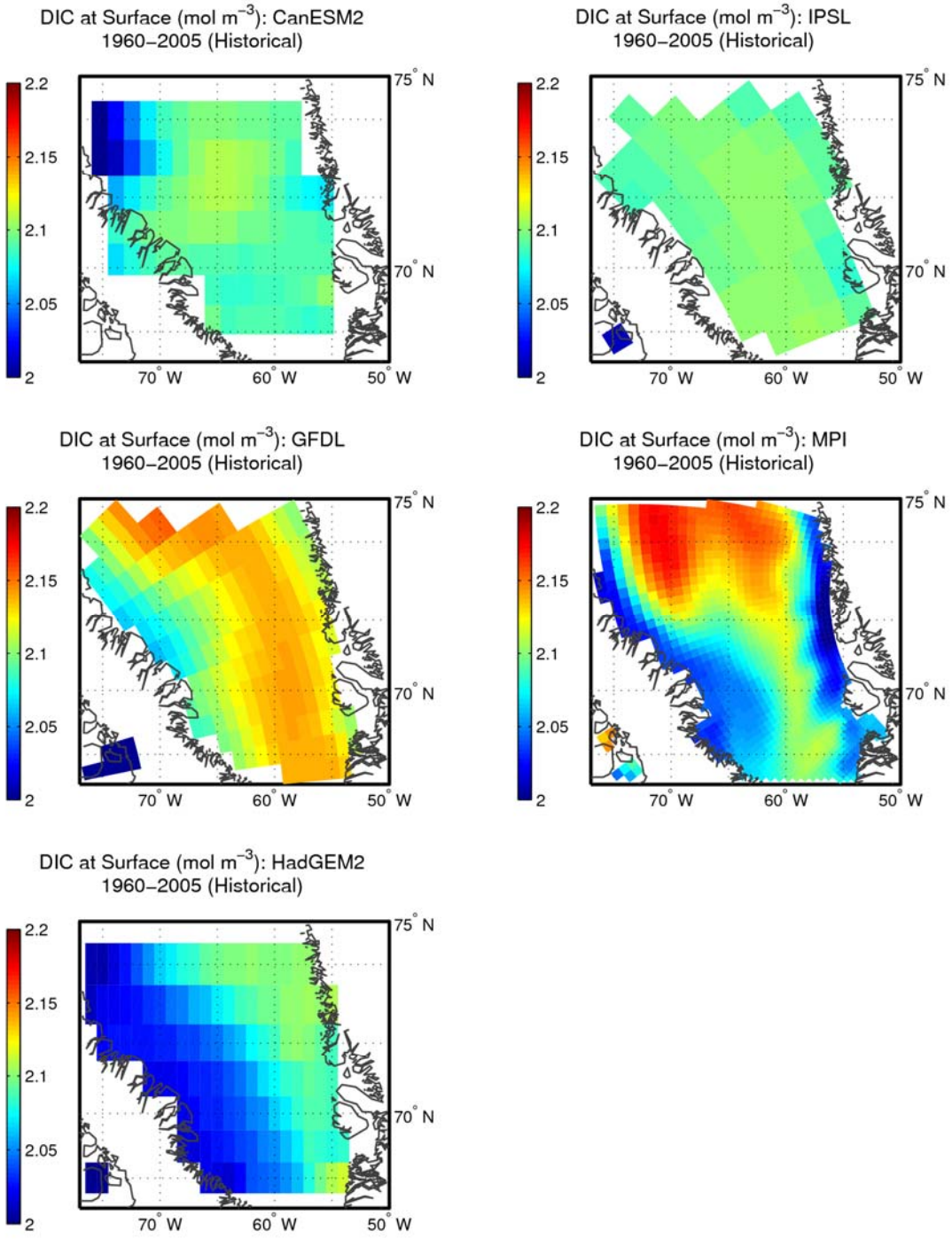

Figure 74. Mean simulated dissolved inorganic carbon concentration (mol m^{-3}) in Baffin Bay for the historical period (1960–2005).

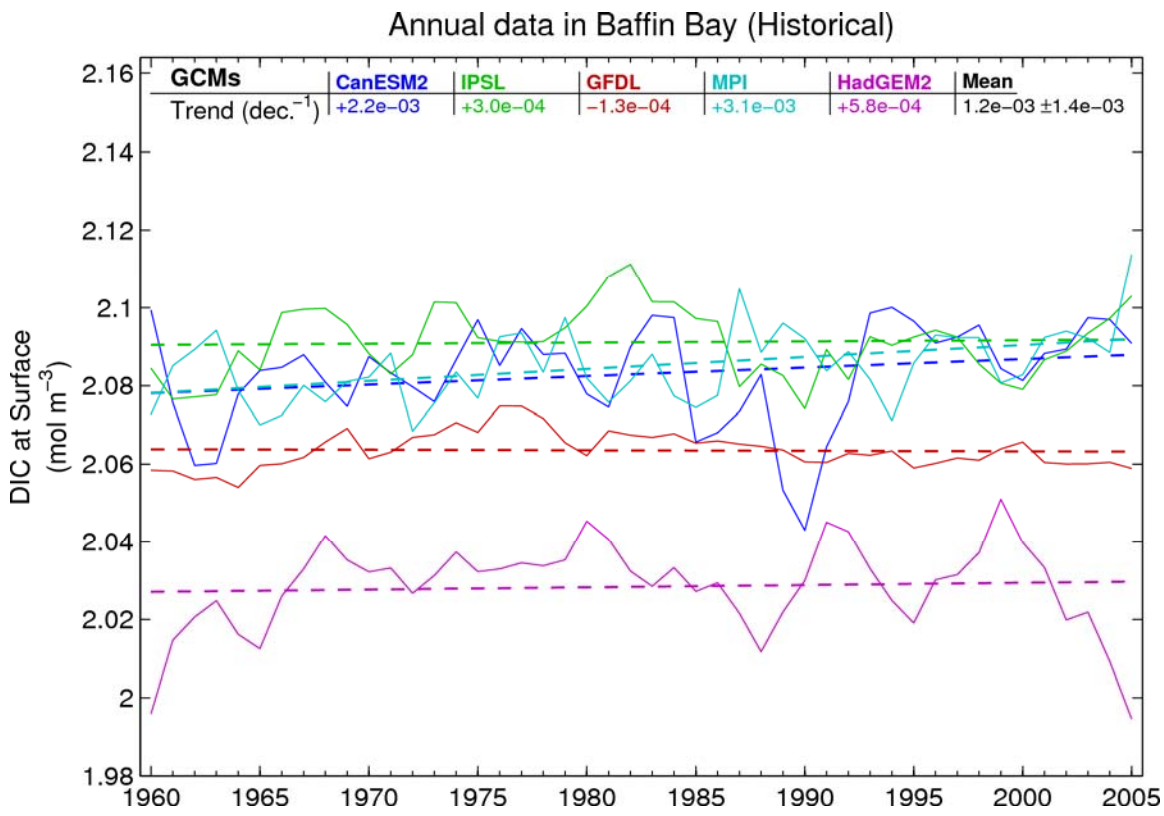

Figure 75. Simulated dissolved inorganic carbon concentration trends (mol m^{-3}/decade) at the surface in Baffin Bay for the historical period (1960–2005).

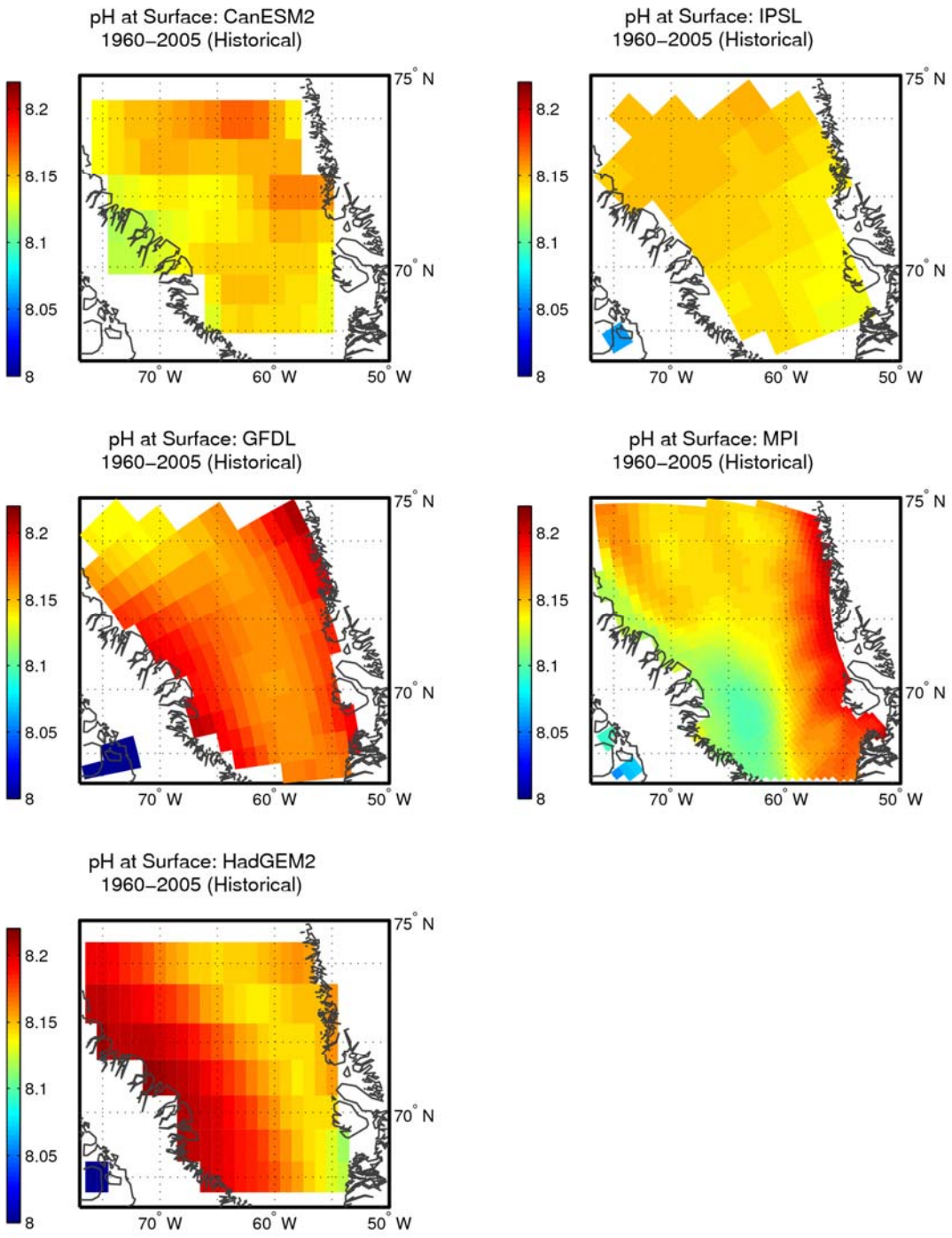

Figure 76. Mean simulated surface pH in Baffin Bay for the historical period (1960–2005).

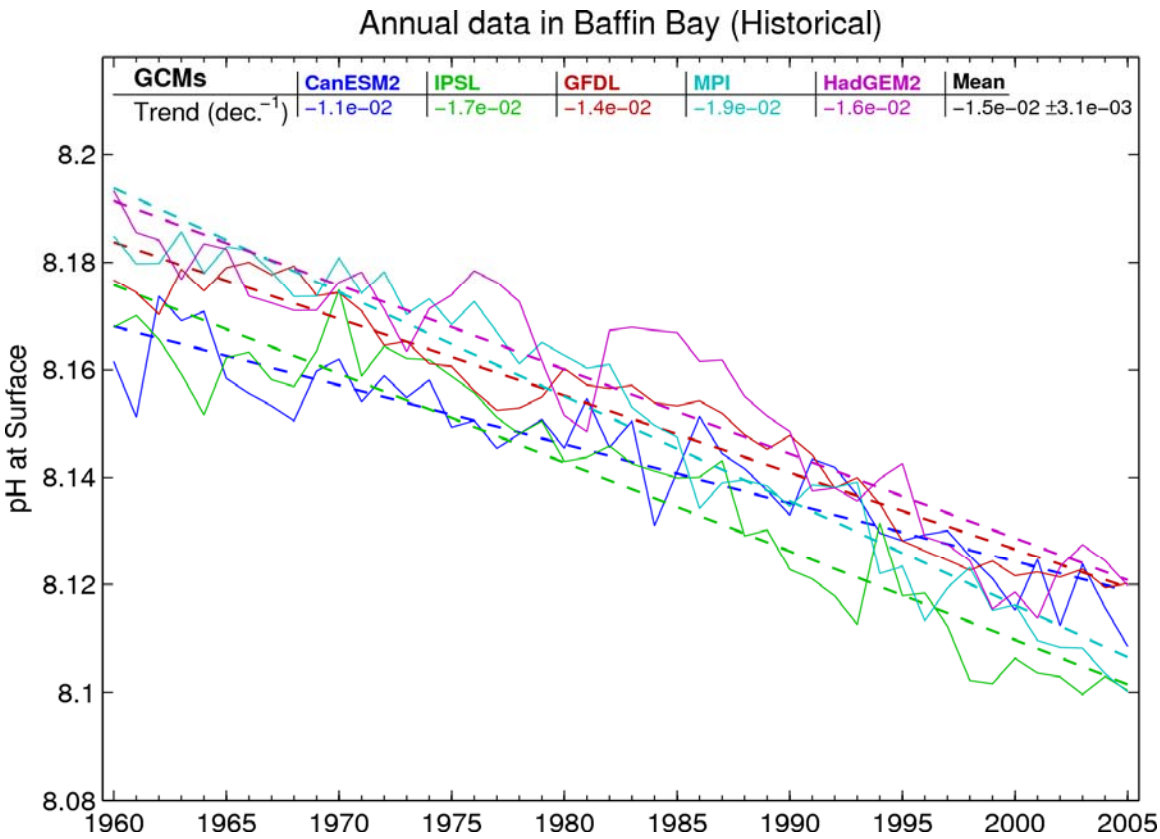

Figure 77. Simulated pH trends (per decade) at the surface in Baffin Bay for the historical period (1960–2005).

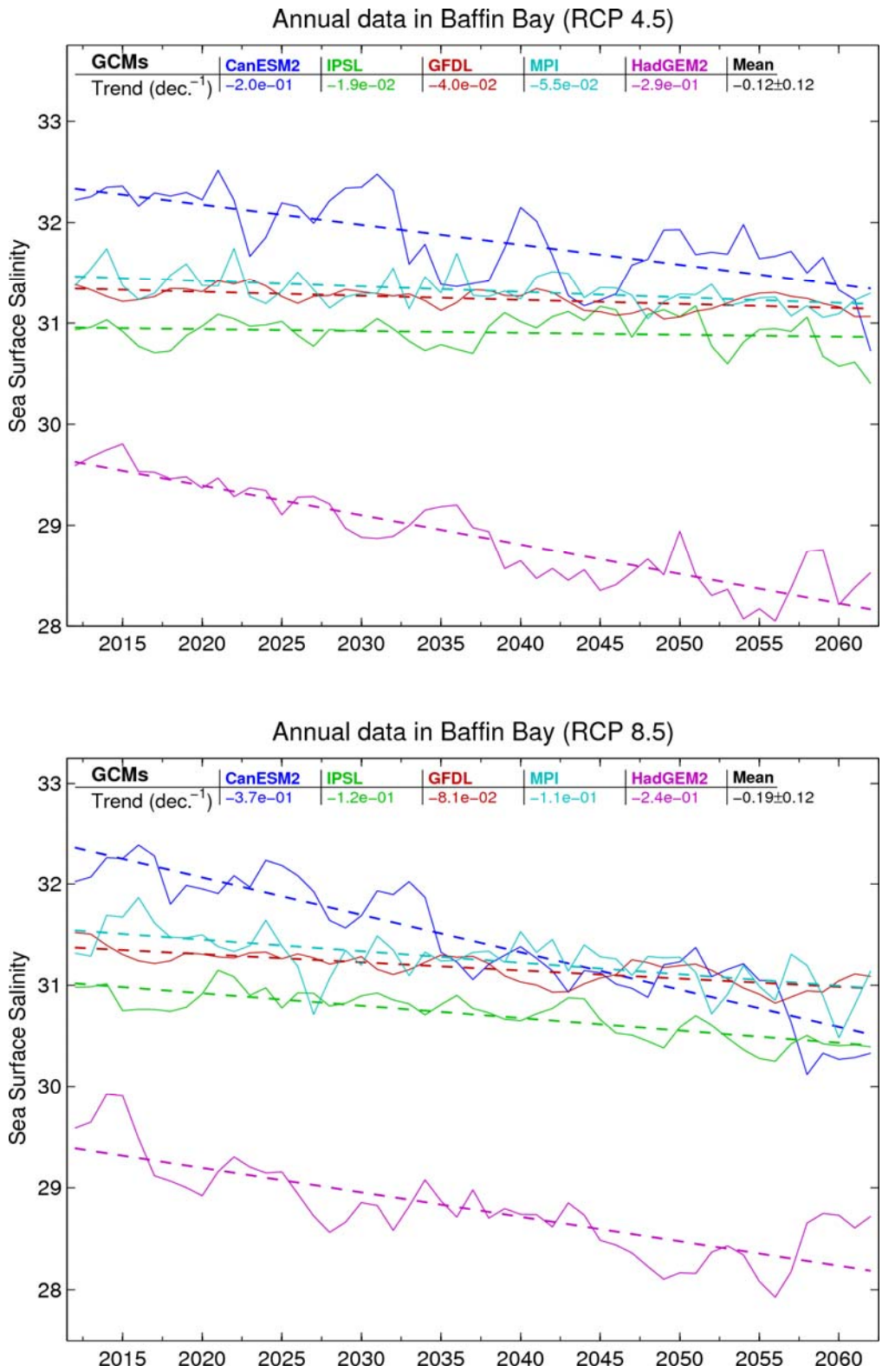

Figure 78. Future sea-surface salinity trends (per decade) in Baffin Bay for the 2012–2062 period for RCPs 4.5 and 8.5.

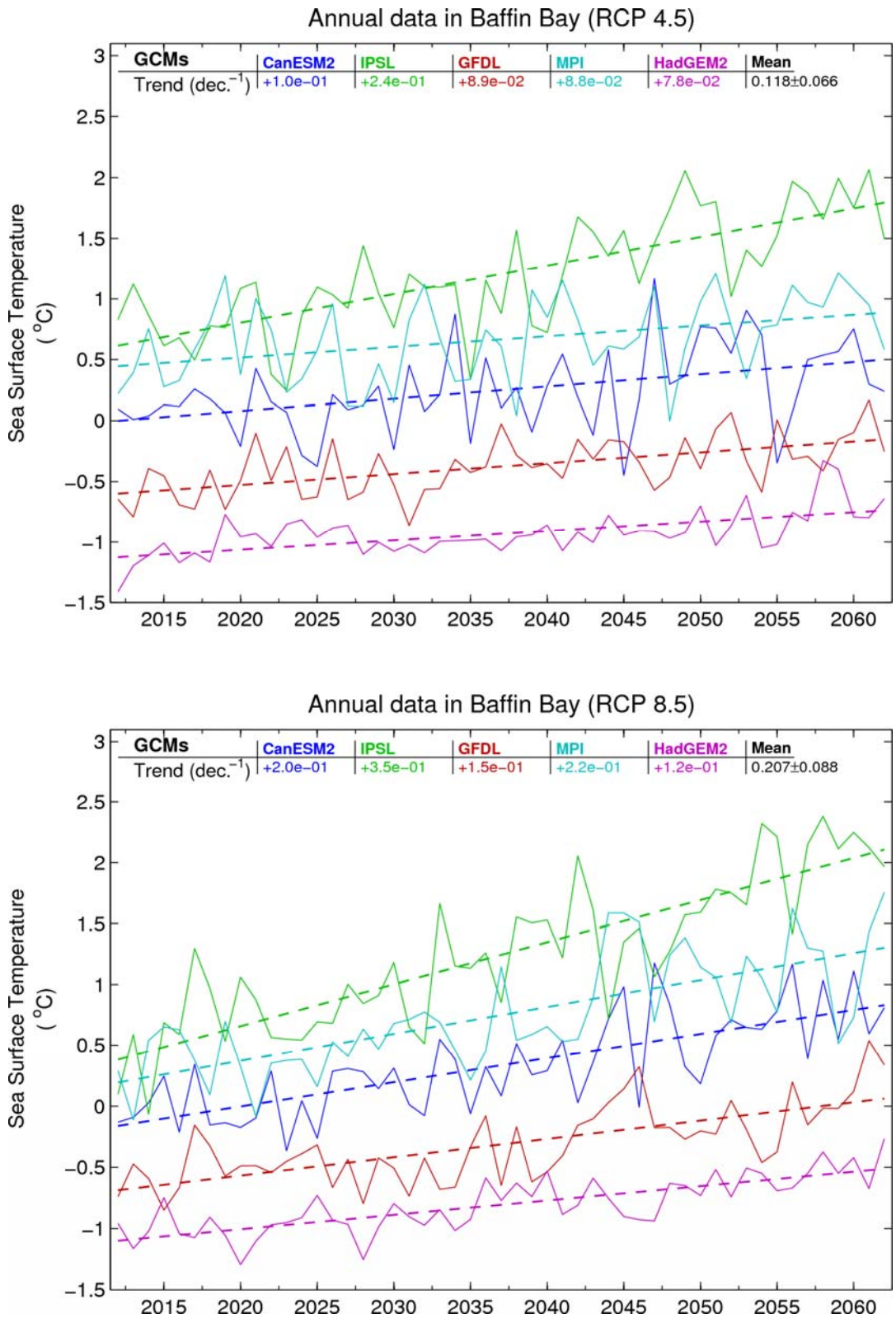

Figure 79. Future sea-surface temperature trends (°C/decade) in Baffin Bay for the 2012–2062 period for RCPs 4.5 and 8.5.

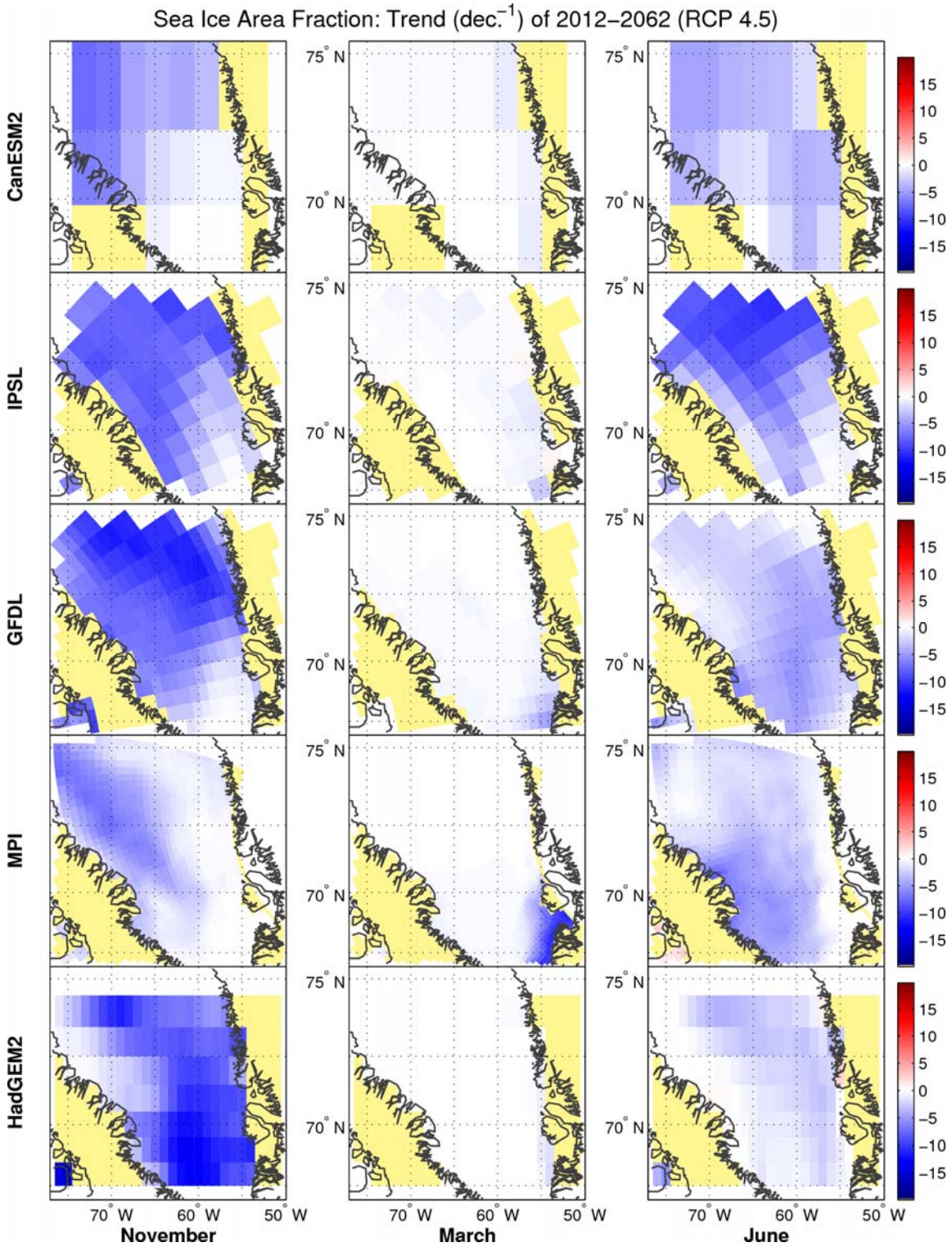

Figure 80. Future sea-ice concentration trends (%/decade) in Baffin Bay for the 2012–2062 period for RCP 4.5.

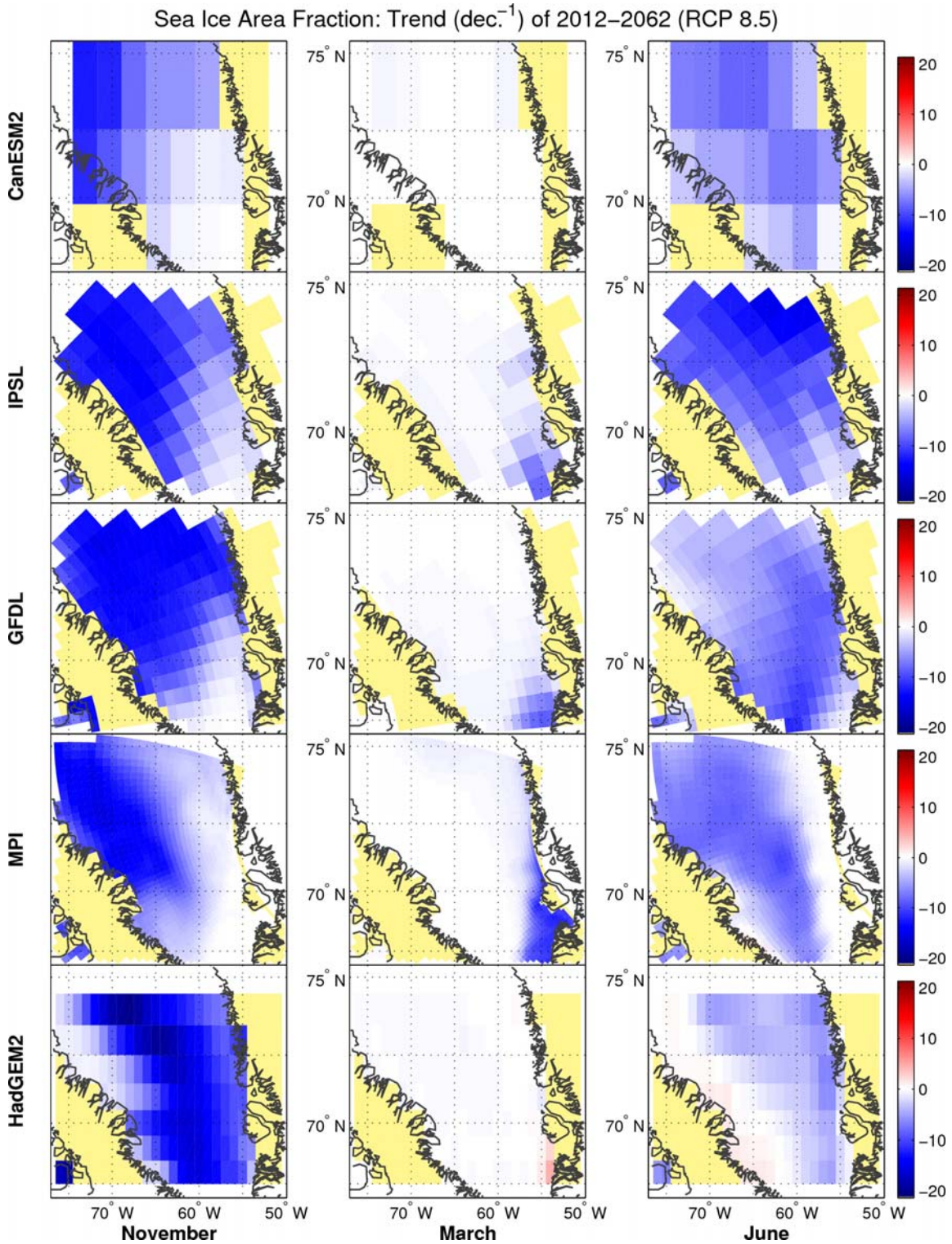

Figure 81. Future sea-ice concentration trends (%/decade) in Baffin Bay for the 2012–2062 period for RCP 8.5.

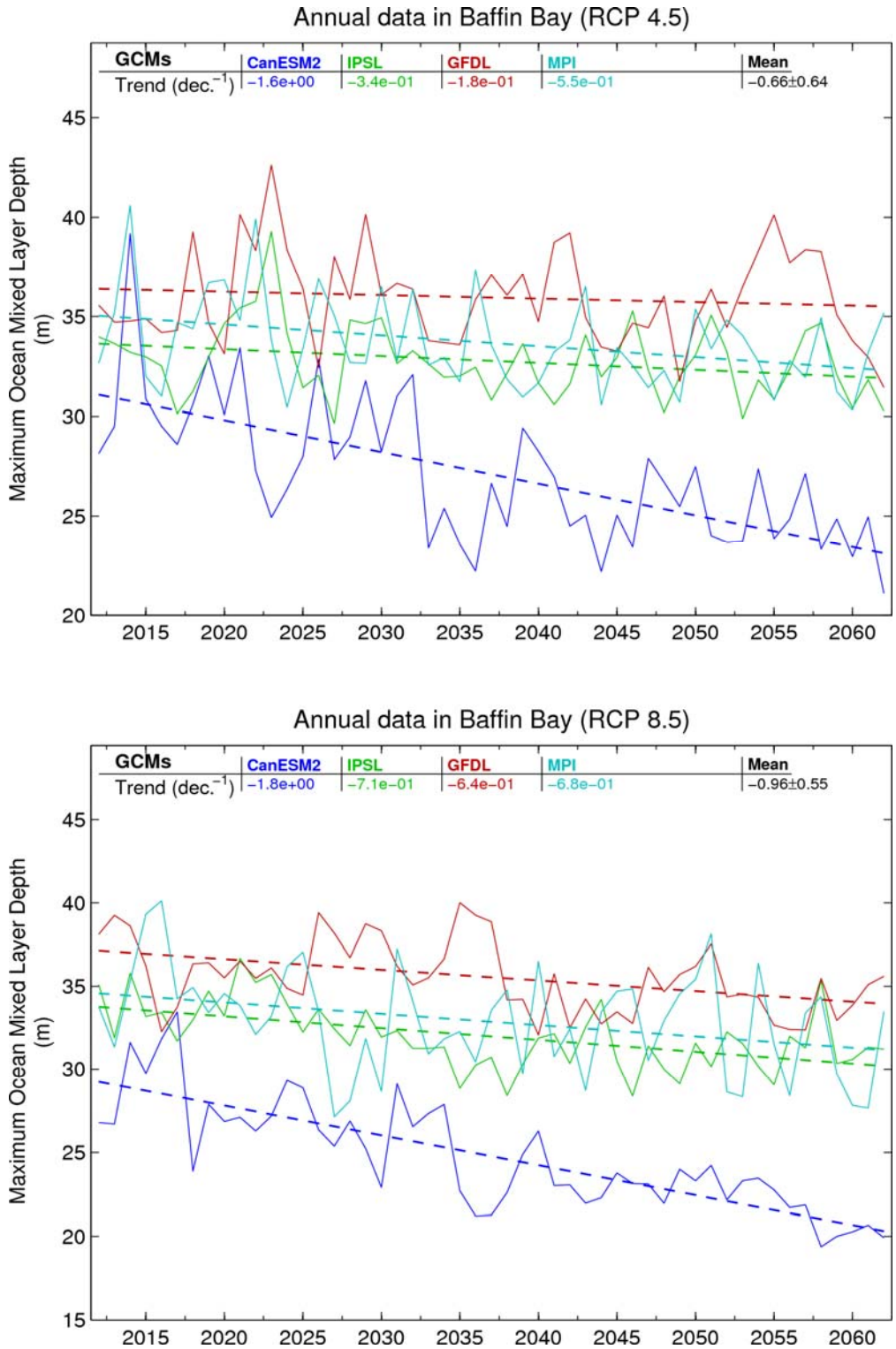

Figure 82. Future maximum mixed layer depth (m/decade) in Baffin Bay for the 2012–2062 period for RCPs 4.5 and 8.5.

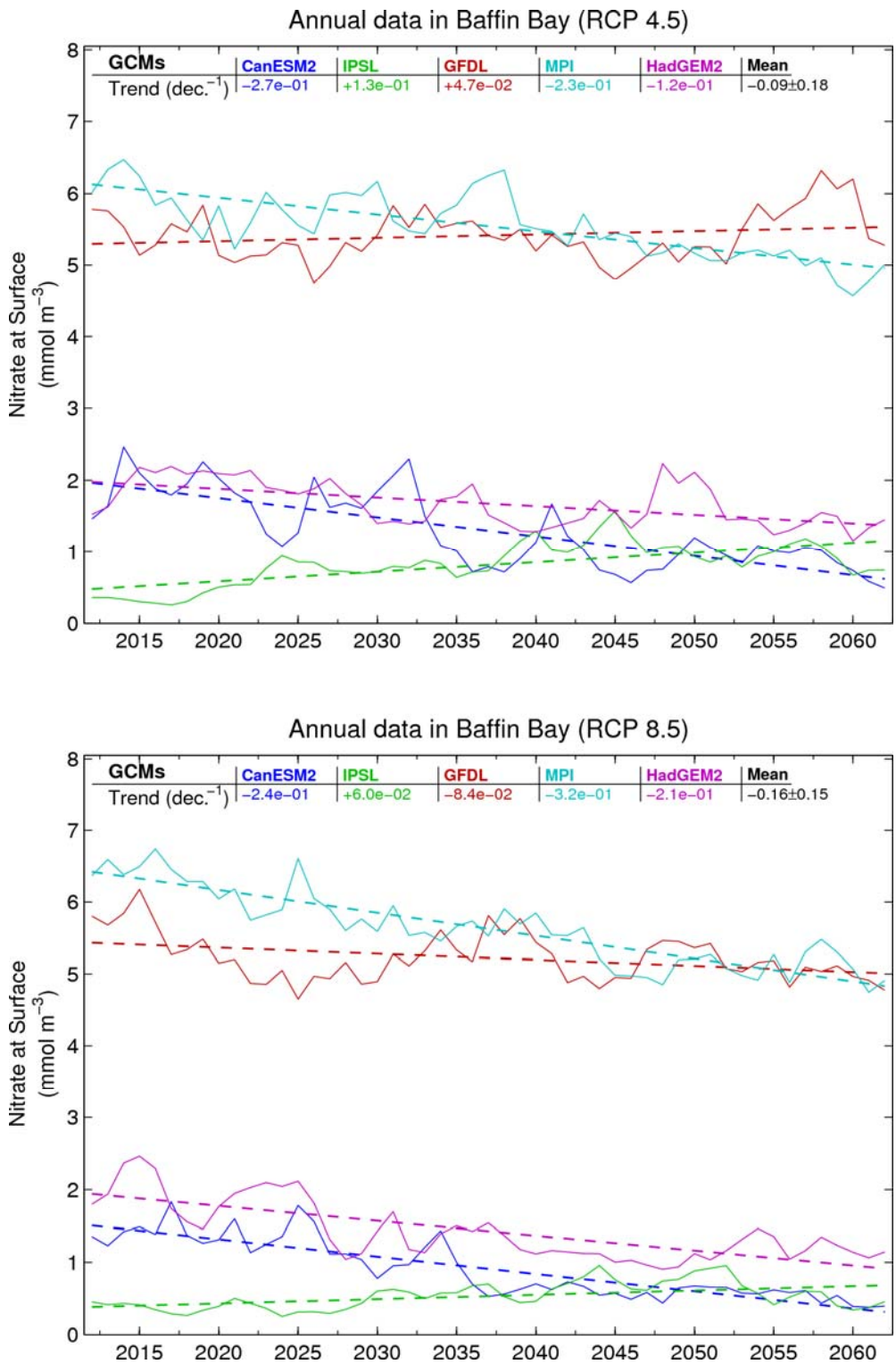

Figure 83. Future surface nitrate concentration trends (mmol m^{-3}/decade) in Baffin Bay for the 2012–2062 period for RCP 4.5 and 8.5.

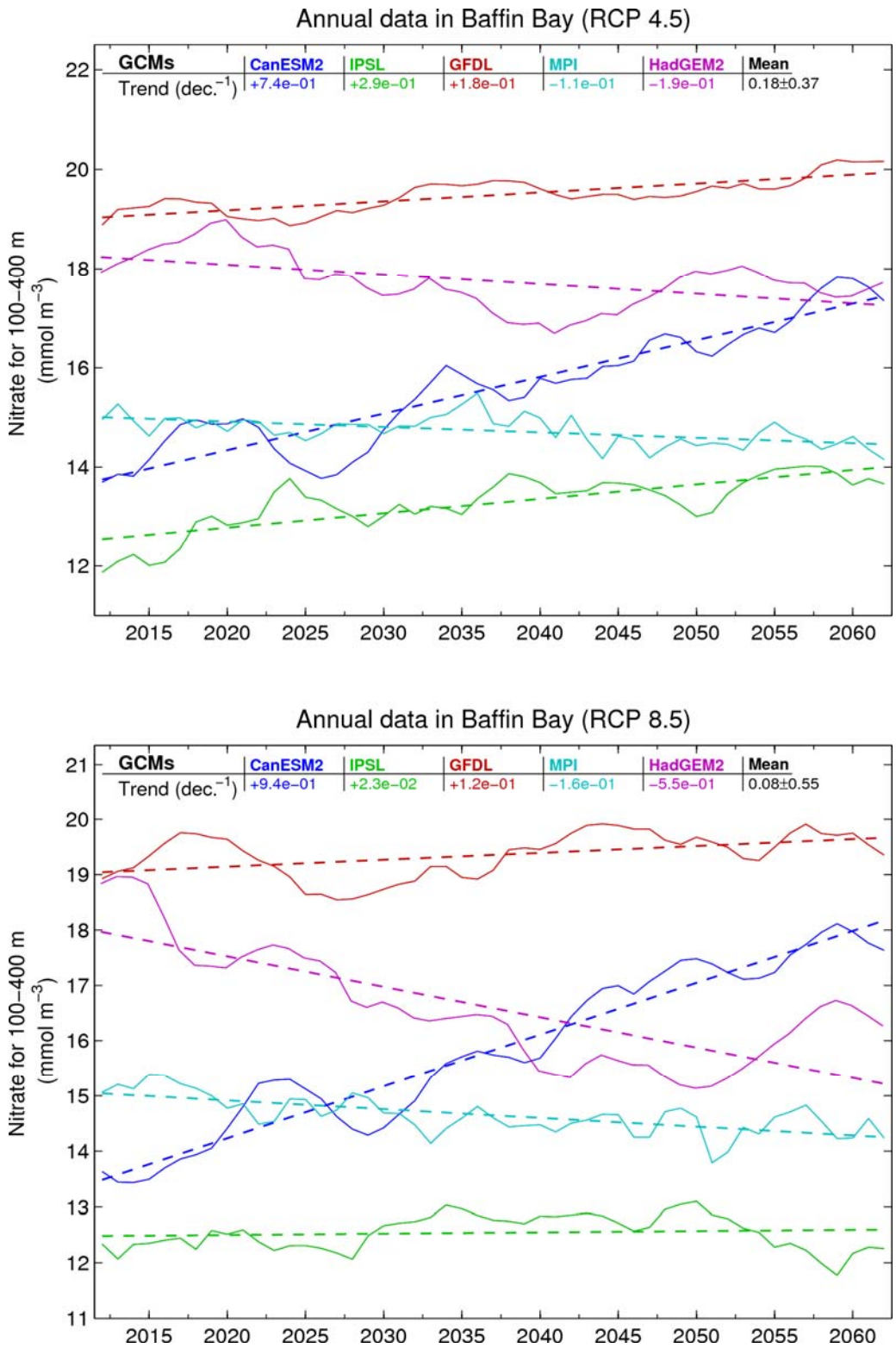

Figure 84. Future nitrate concentration trends (mmol m^{-3}/decade) at 100–400 m in Baffin Bay for the 2012–2062 period for RCPs 4.5 and 8.5.

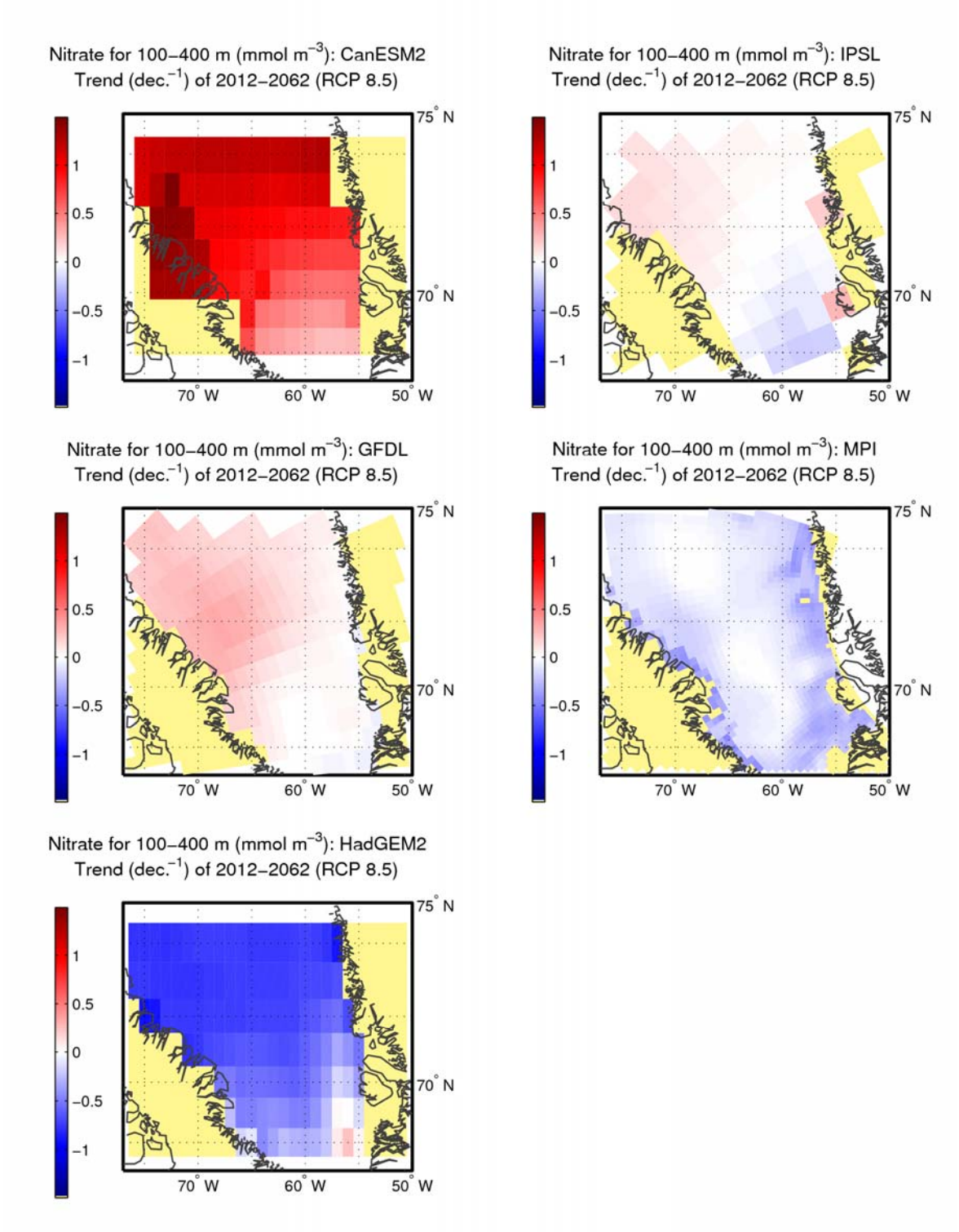

Figure 85. Future nitrate concentration trends (mmol m^{-3}/decade) in each grid cell at 100–400 m in Baffin Bay for the 2012–2062 period for RCP 8.5.

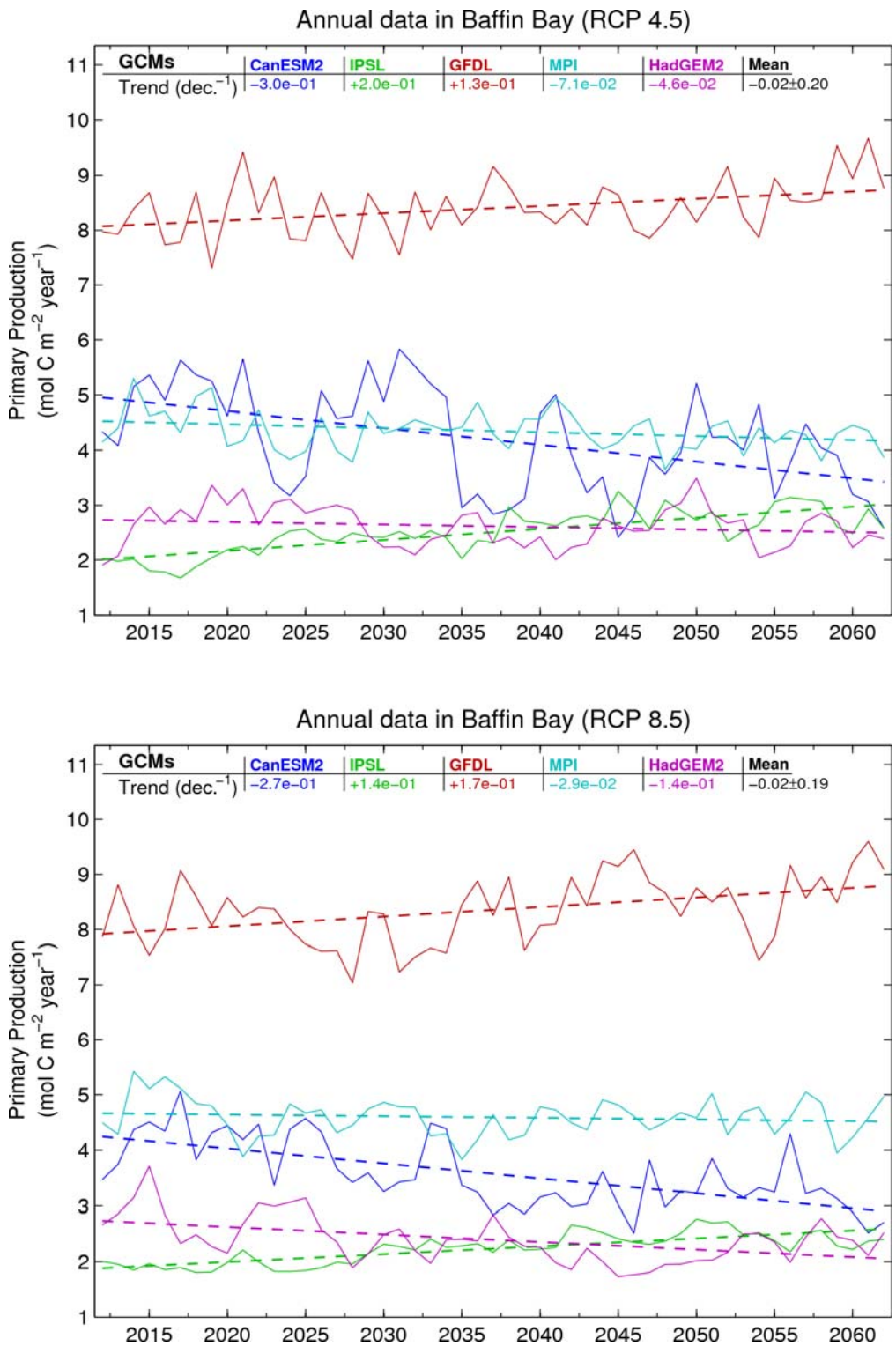

Figure 86. Future vertically integrated primary production trends (mol C m^{-2} year^{-1} per decade) in Baffin Bay for the 2012–2062 period for RCPs 4.5 and 8.5.

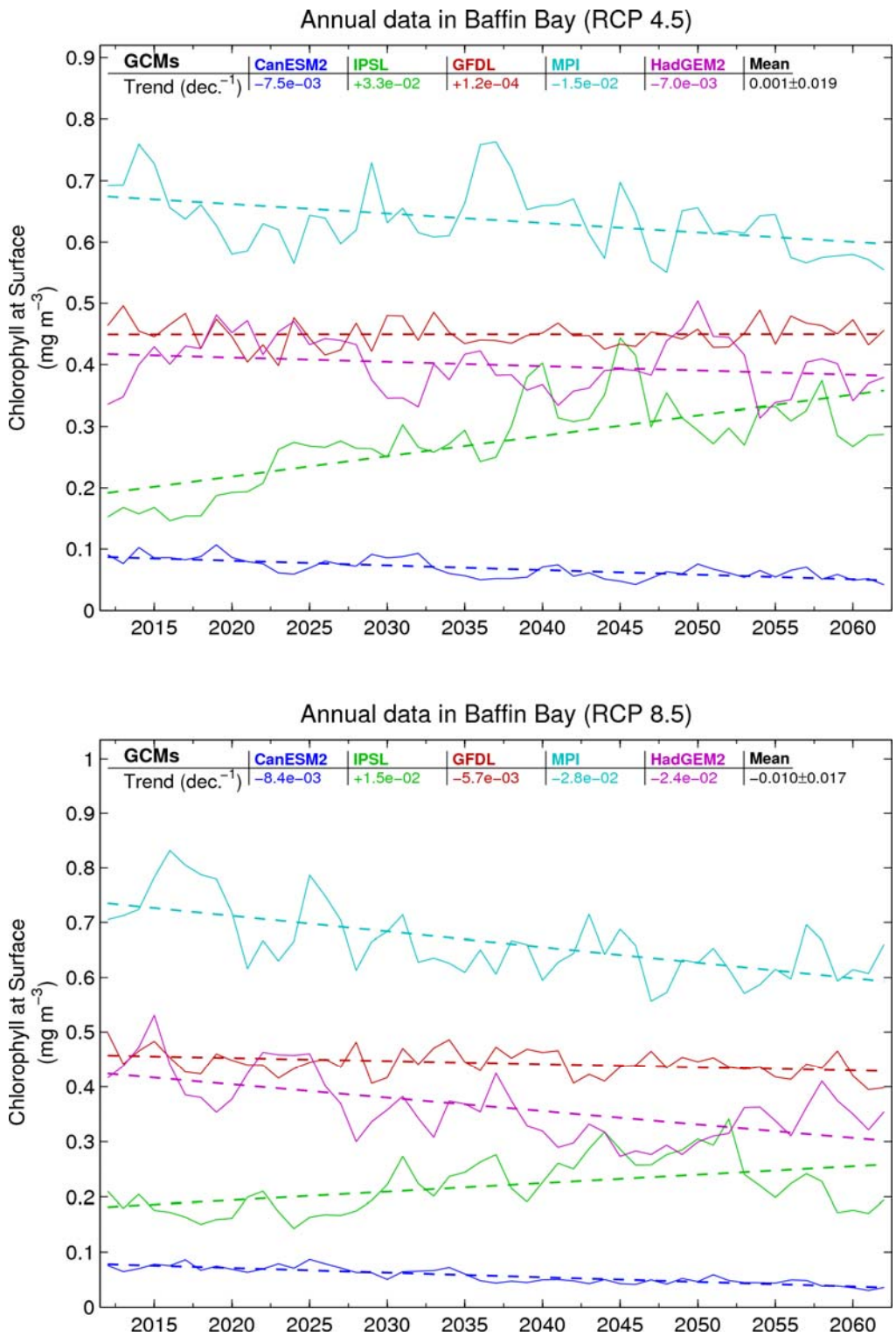

Figure 87. Future Chl *a* concentration trends (mg m^{-3}/decade) at the surface in Baffin Bay for the 2012–2062 period for RCPs 4.5 and 8.5.

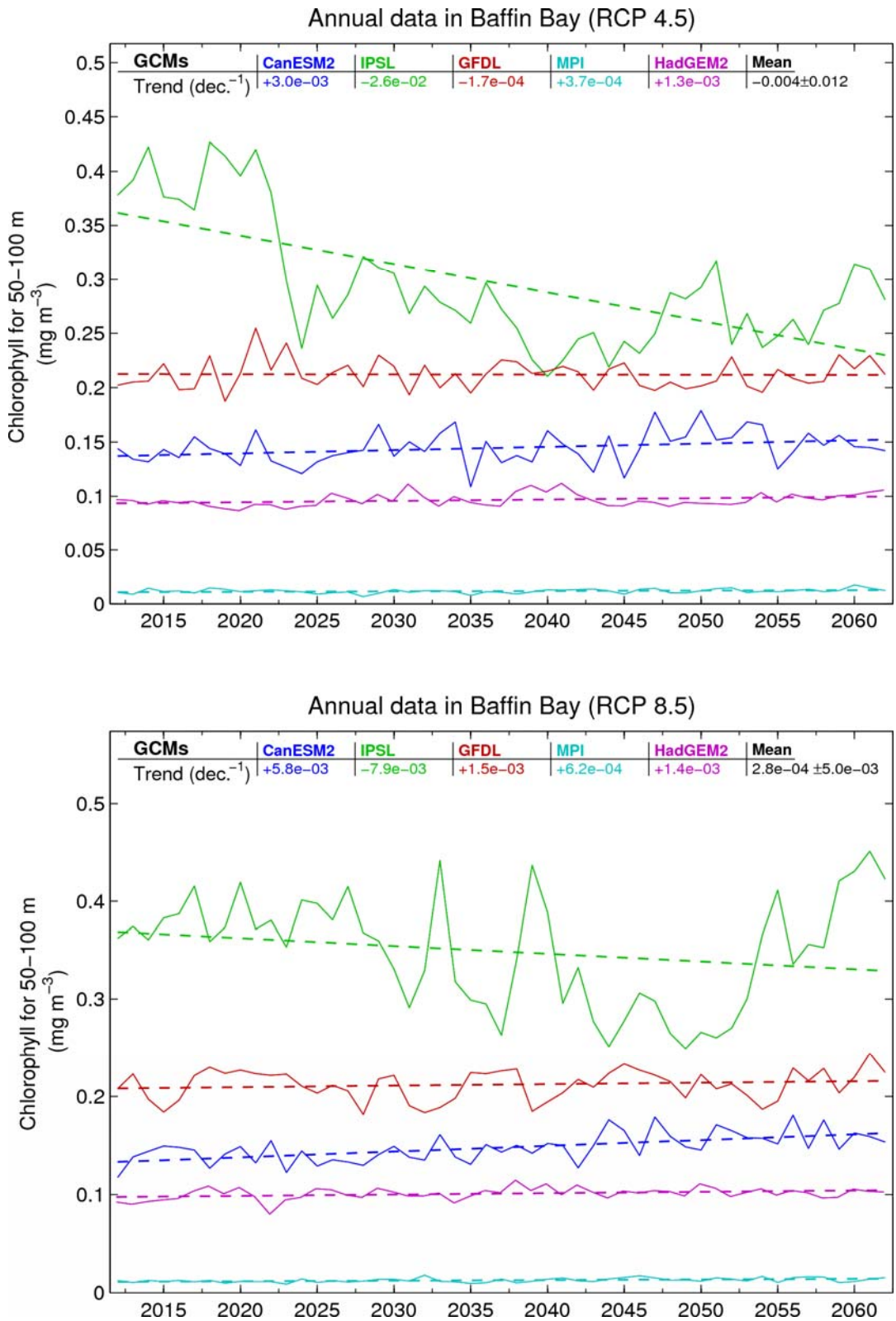

Figure 88. Future Chl *a* concentration trends (mg m^{-3}/decade) at 50–100 m in Baffin Bay for the 2012–2062 period for RCPs 4.5 and 8.5.

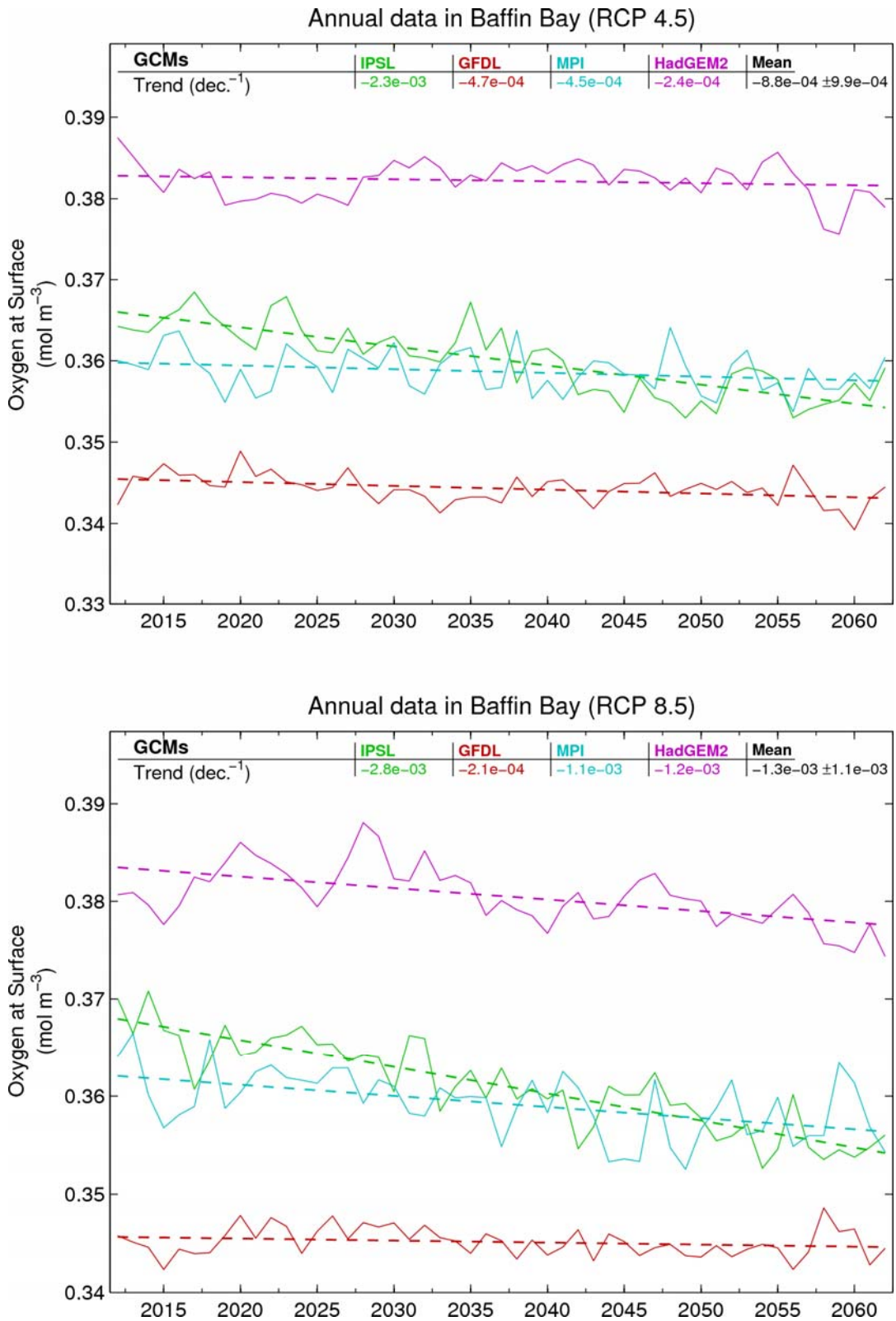

Figure 89. Future dissolved oxygen concentration trends (mol m^{-3}/decade) at the surface in Baffin Bay for the 2012–2062 period for RCPs 4.5 and 8.5.

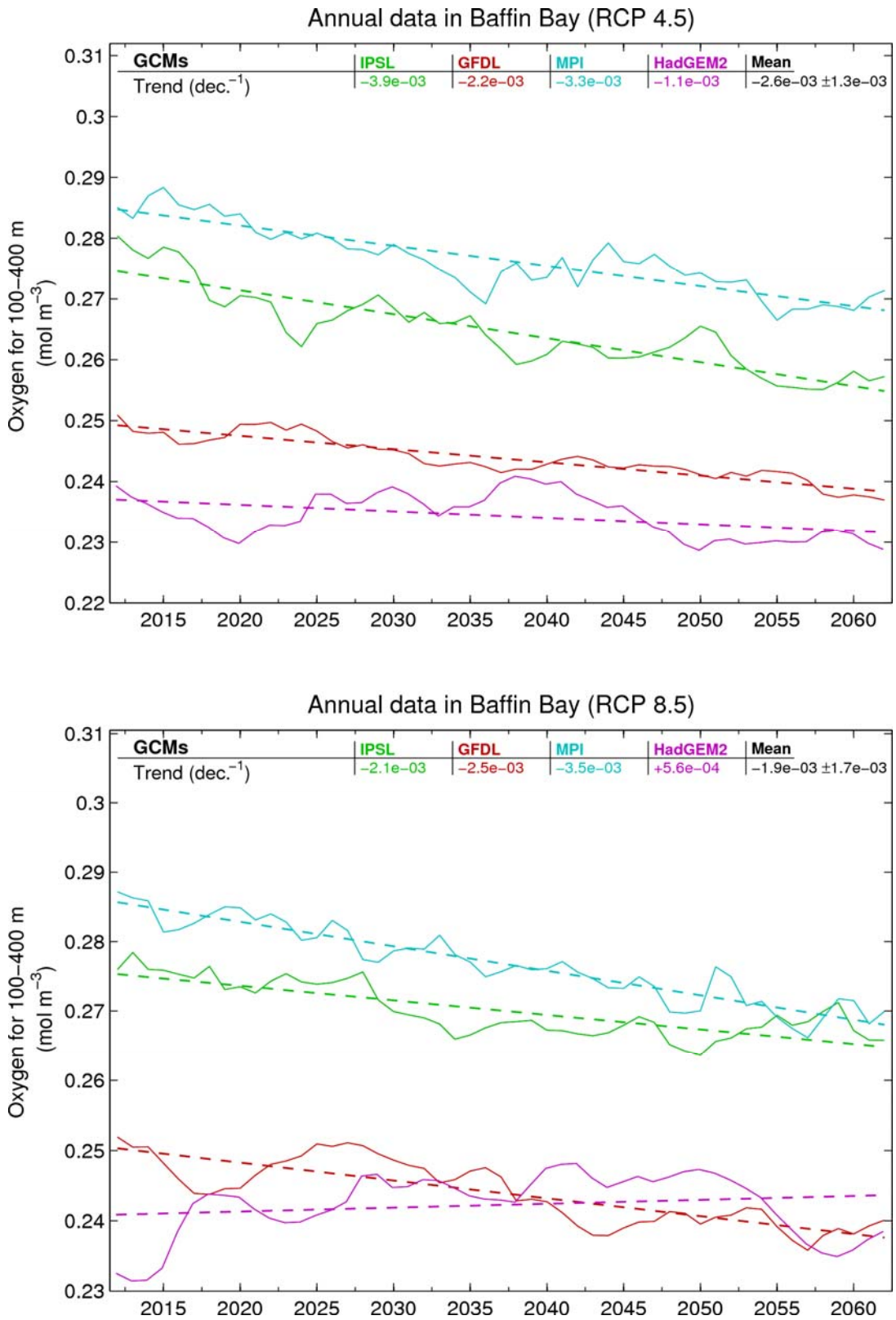

Figure 90. Future dissolved oxygen concentration trends (mol m^{-3}/decade) at 100–400 m in Baffin Bay for the 2012–2062 period for RCPs 4.5 and 8.5.

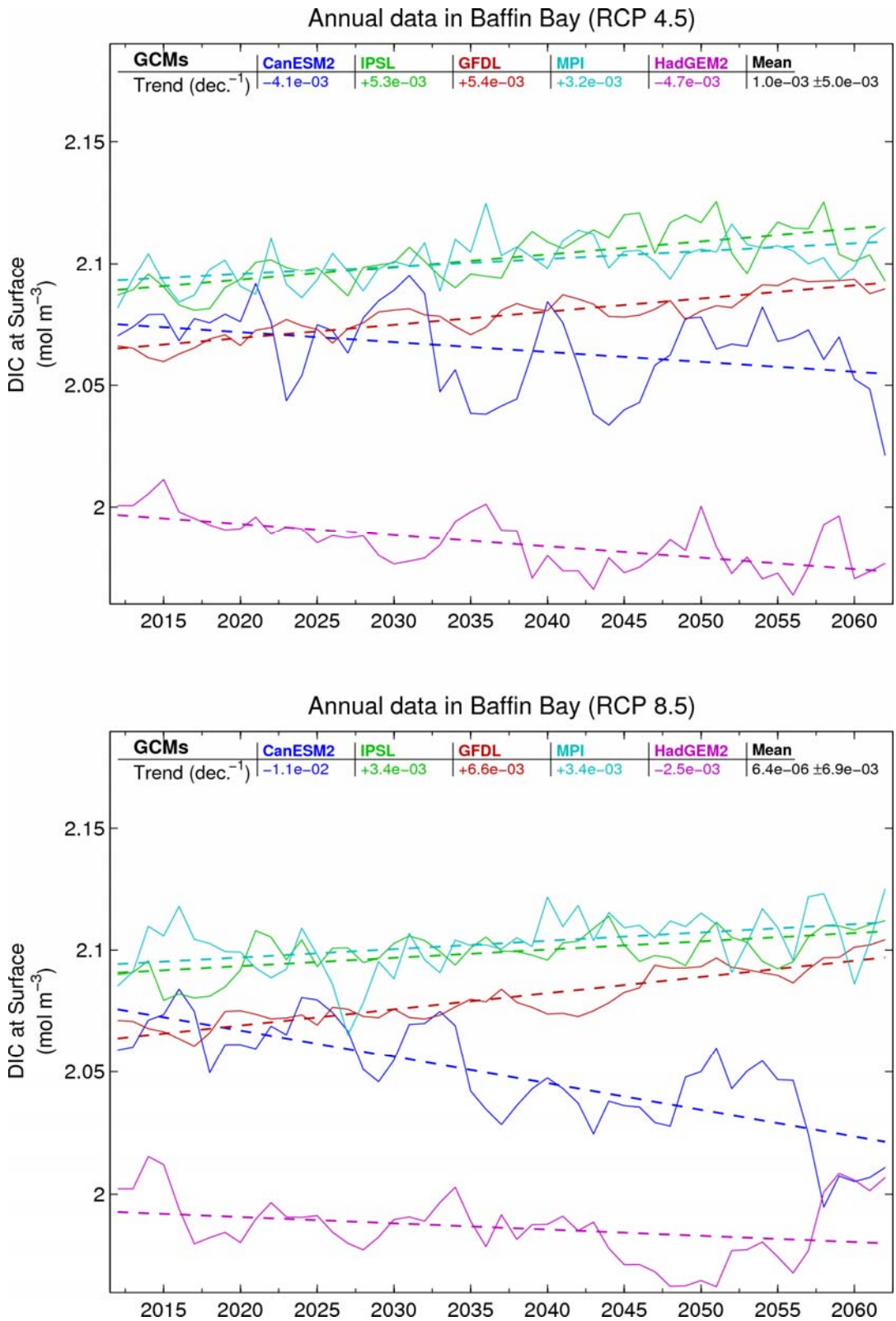

Figure 91. Future DIC concentration trends (mol m^{-3}/decade) at the surface in Baffin Bay for the 2012–2062 period for RCPs 4.5 and 8.5.

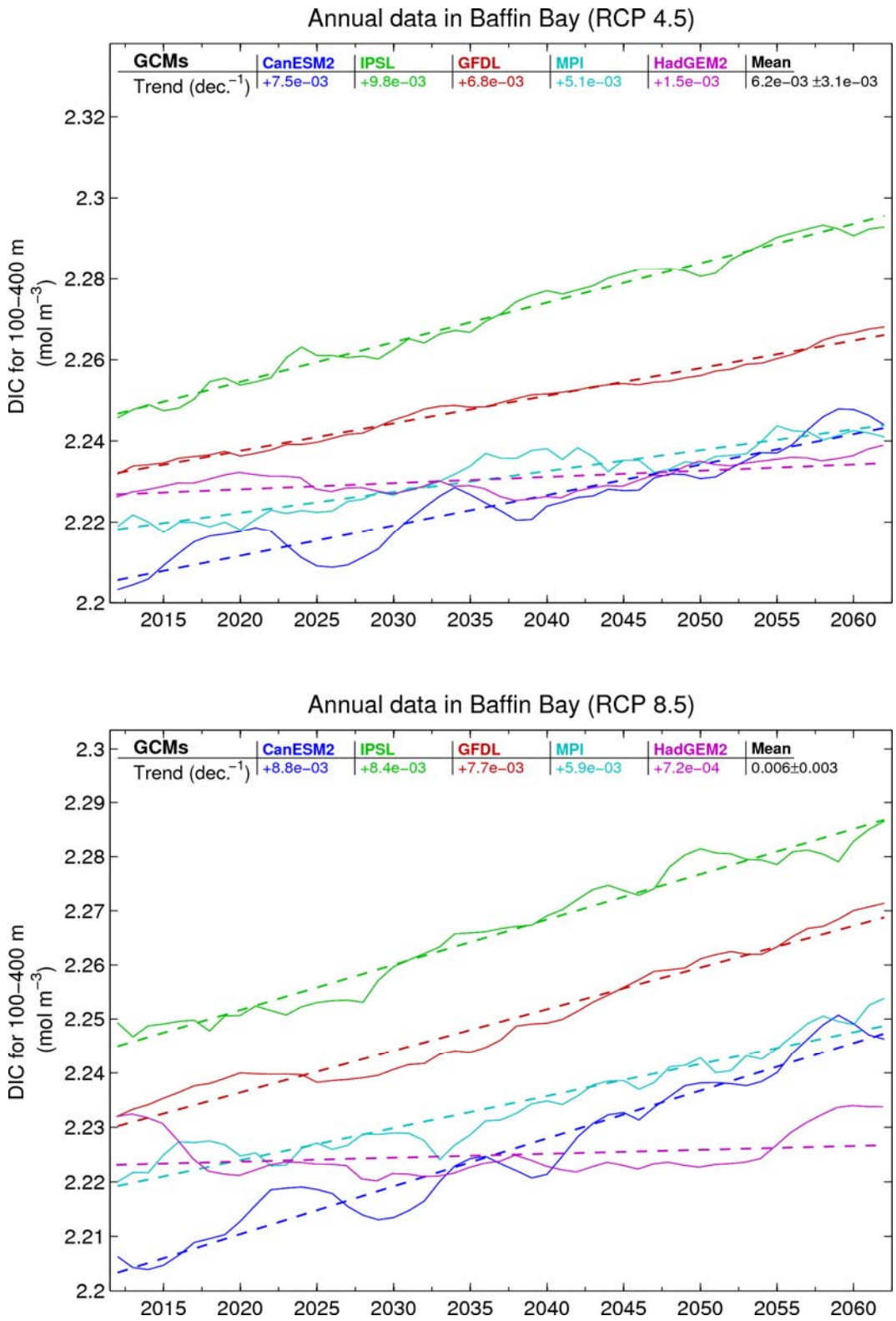

Figure 92. Future DIC concentration trends (mol m^{-3}/decade) at 100–400 m in Baffin Bay for the 2012–2062 period for RCPs 4.5 and 8.5

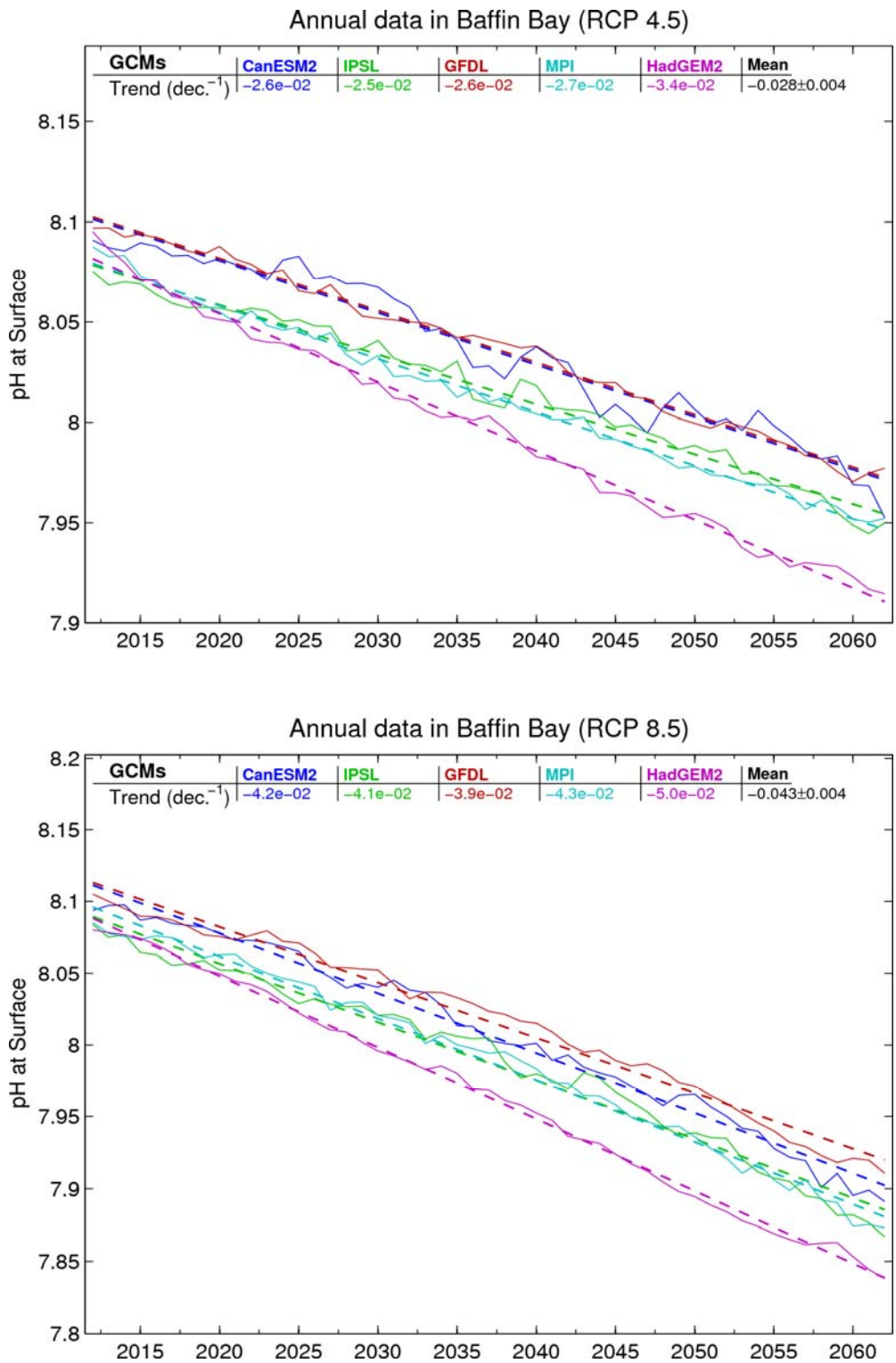

Figure 93. Future pH trends (per decade) at the surface in Baffin Bay for the 2012–2062 period for RCPs 4.5 and 8.5.

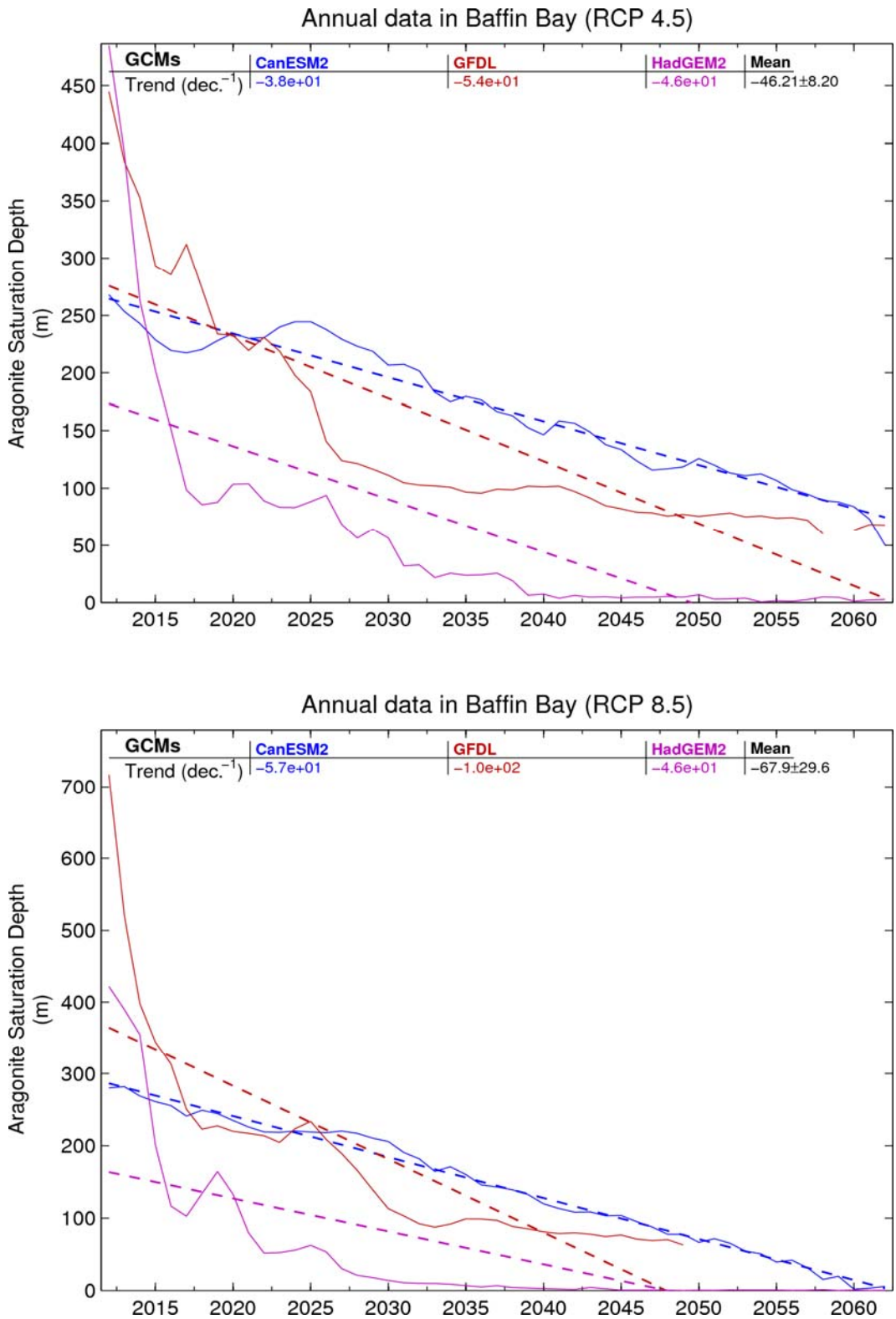

Figure 94. Future aragonite saturation depth trends (m/decade) in Baffin Bay for the 2012–2062 period for RCPs 4.5 and 8.5.

Appendix I

Appendix I-1 Multi-model ensemble mean trends (per decade) over the next 50 years for the different variables (sea-surface temperature [SST], sea-surface salinity [SSS], mixed layer depth [MLD], nitrate concentration [NO_3], vertically integrated primary production [PP], chlorophyll *a* concentration [Chl *a*], dissolved oxygen concentration [O_2], dissolved inorganic carbon concentration [DIC], and pH) at the surface, in the 50–100 m layer, and in the 100–400 m layer for the two scenarios (RCP 4.5 and RCP 8.5).

Region		Baffin Bay		Hudson Bay	
RCPs		RCP 4.5	RCP 8.5	RCP 4.5	RCP 8.5
SST (°C/dec.)	Surf.	0.12±0.07	0.21±0.09	0.22±0.08	0.31±0.07
	50-100m	0.17±0.10	0.23±0.17	0.13±0.06	0.16±0.06
	100-400m	0.28±0.21	0.33±0.28	0.14±0.05	0.19±0.08
SSS (/dec.)	Surf.	-0.12±0.12	-0.19±0.12	-0.10±0.19	-0.15±0.18
	50-100m	-0.06±0.05	-0.11±0.04	-0.13±0.17	-0.19±0.17
	100-400m	+0.004±0.035	-0.018±0.030	-0.12±0.17	-0.16±0.17
MLD (m/dec.)	mean	-1.8±2.4	-1.6±1.8	-0.02±0.17	-0.11±0.39
	max	-0.66±0.64	-0.96±0.55	0.06±0.13	-0.007±0.254
NO_3 (mmol m^{-3} /dec.)	Surf.	-0.09±0.18	-0.16±0.15	-0.19±0.17	-0.23±0.18
	50-100m	0.11±0.34	-0.06±0.39	-0.11±0.15	-0.24±0.17
	100-400m	0.18±0.37	0.08±0.55	0.11±0.32	0.07±0.37
PP (mol C m^{-2} $year^{-1}$ /dec.)	Integrated	-0.02±0.20	-0.02±0.19	0.14±0.16	0.14±0.11
Chl *a* (mg m^{-3}/dec.)	Surf.	7e-4±1.9e-2	-0.010±0.017	8e-4±9.8e-3	-0.004±0.0.12
	50-100m	-0.004±0.012	-0.0003±0.0050	0.005±0.005	0.007±0.006
	100-400m	-3e-4±8e-4	-0.3e-3±1.0e-3	1.7e-3±2.8e-3	1.5e-3±2.3e-3
O_2 (mol m^{-3} /dec.)	Surf.	-0.9e-3±1.0e-3	-1.3e-3±1.1e-3	-8.1e-4±4.1e-4	-1.3e-3±5e-4
	50-100m	-2.8e-3±2.4e-3	-1.9e-3±2.5e-3	2.3e-4±8.6e-4	8.3e-4±2.0e-3
	100-400m	-2.6e-3±1.3e-3	-1.9e-3±1.7e-3	4e-5±8.5e-4	-4e-4±1.1e-3
DIC (mol m^{-3} /dec.)	Surf.	0.001±0.005	6.3e-6±0.007	-0.0023±0.011	-0.0026±0.011
	50-100m	0.004±0.004	0.003±0.004	-0.004±0.013	-0.005±0.014
	100-400m	0.006±0.003	0.006±0.003	-0.0014±0.012	-0.0018±0.012
pH (/dec.)	Surf.	-0.028±0.004	-0.043±0.004	-0.022±0.003	-0.036±0.003
	50-100m	-0.028±0.004	-0.038±0.004	-0.022±0.003	-0.032±0.006
	100-400m	-0.028±0.005	-0.034±0.006	-0.022±0.004	-0.033±0.006

Appendix II: Figures of bidecadal changes

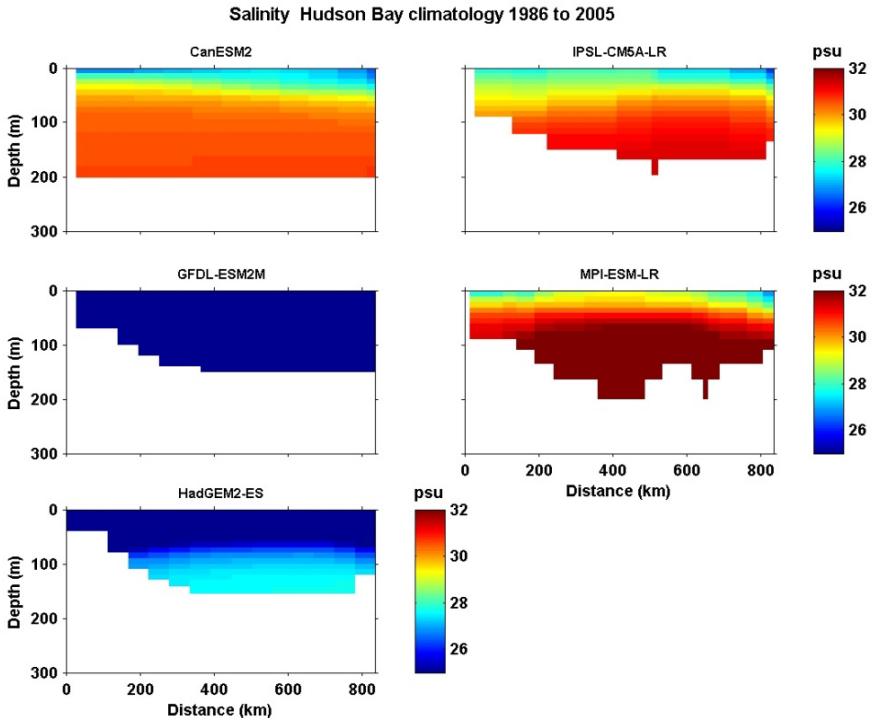

Figure II- 1. Mean simulated seawater salinity along the Hudson Bay longitudinal transect (see Figure 1) for the historical period (1986–2005).

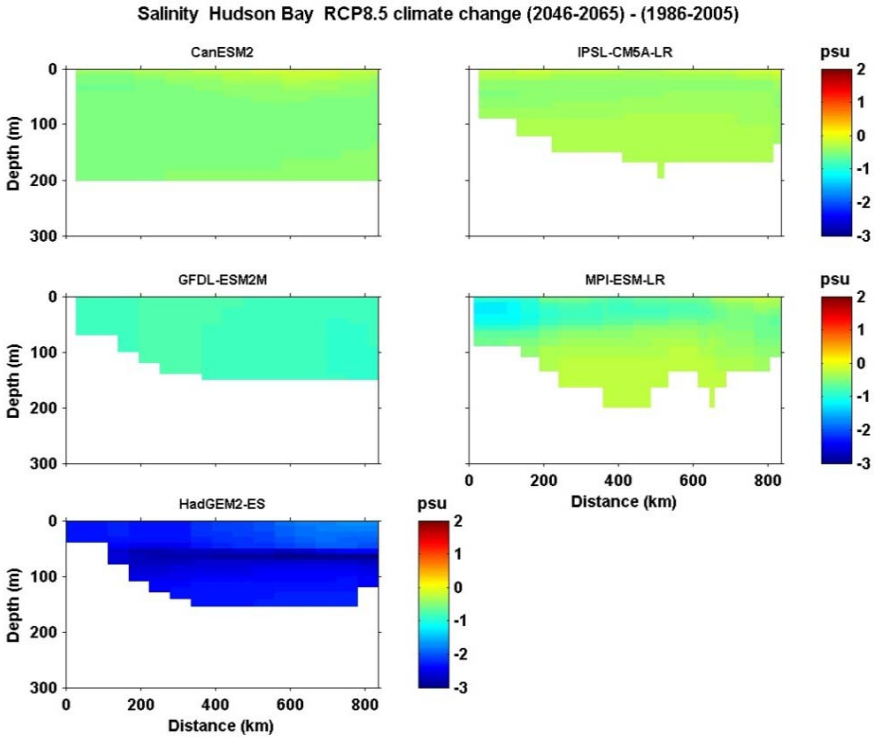

Figure II- 2. Bidecadal changes (2046-2065 average minus 1986-2005 average) in seawater salinity along the Hudson Bay transect for RCP 8.5.

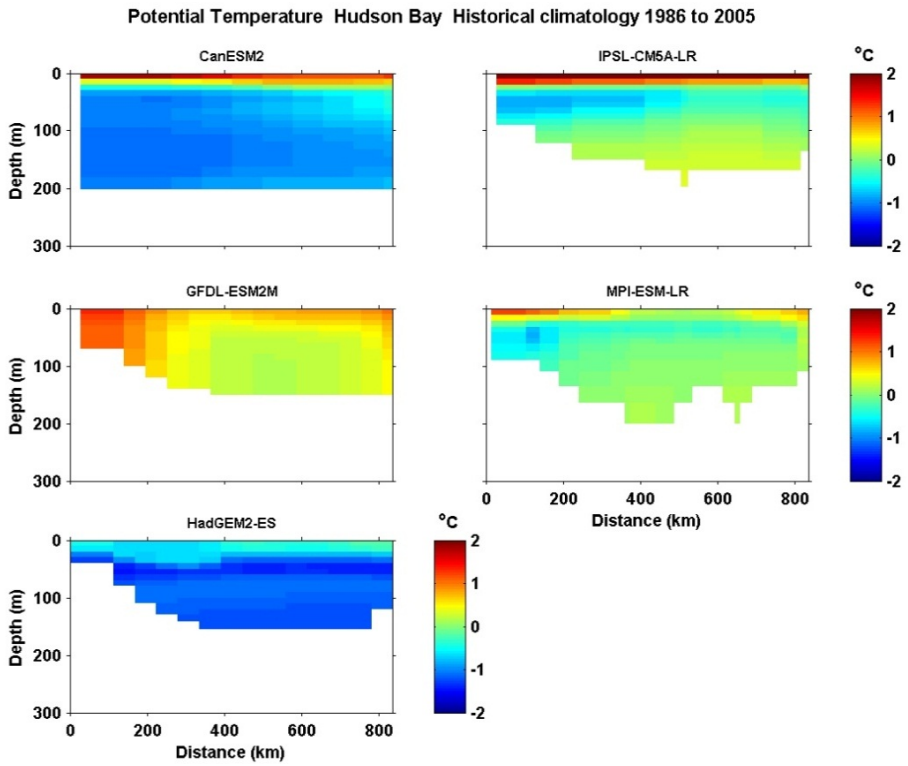

Figure II- 3. Mean simulated seawater temperature along the Hudson Bay longitudinal transect for the historical period (1986–2005).

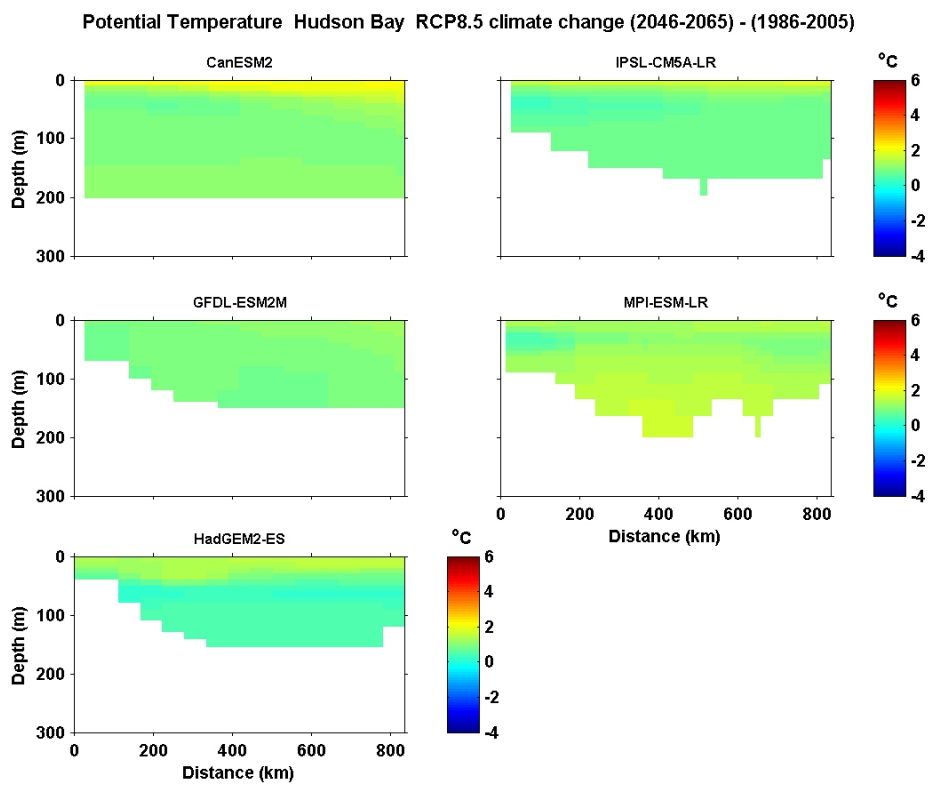

Figure II- 4. Bidecadal changes (2046-2065 average minus 1986-2005 average) in potential temperature along the Hudson Bay transect for RCP 8.5.

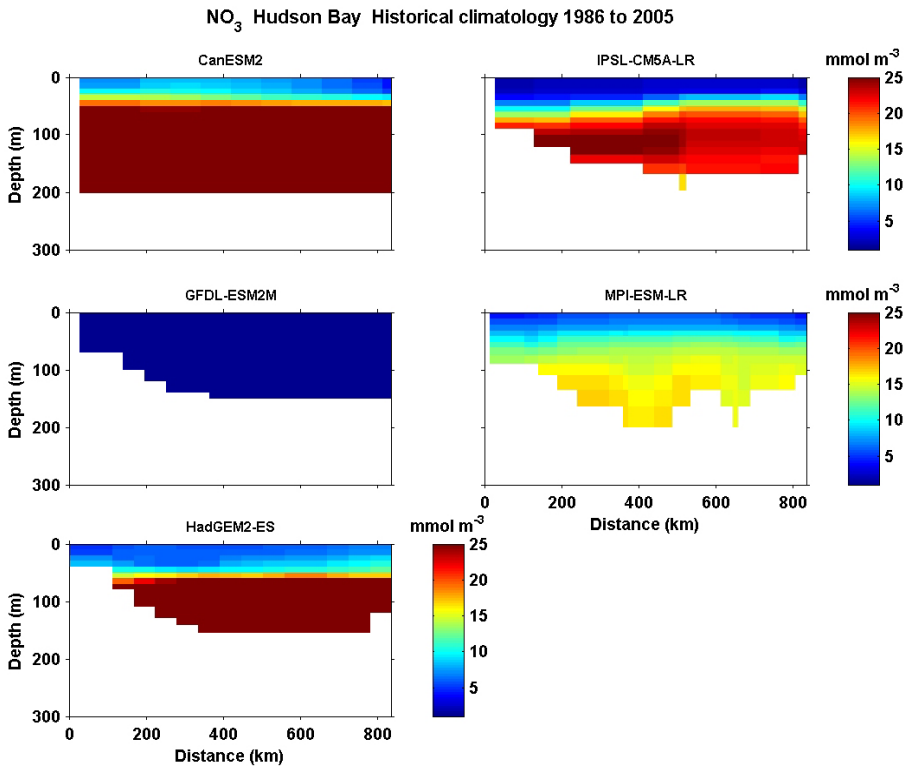

Figure II- 5. Mean simulated nitrate concentration along the Hudson Bay transect over the historical period (1986–2005). Values as high as 35 mmol m^{-3} are found in CanESM2 and HadGEM2.

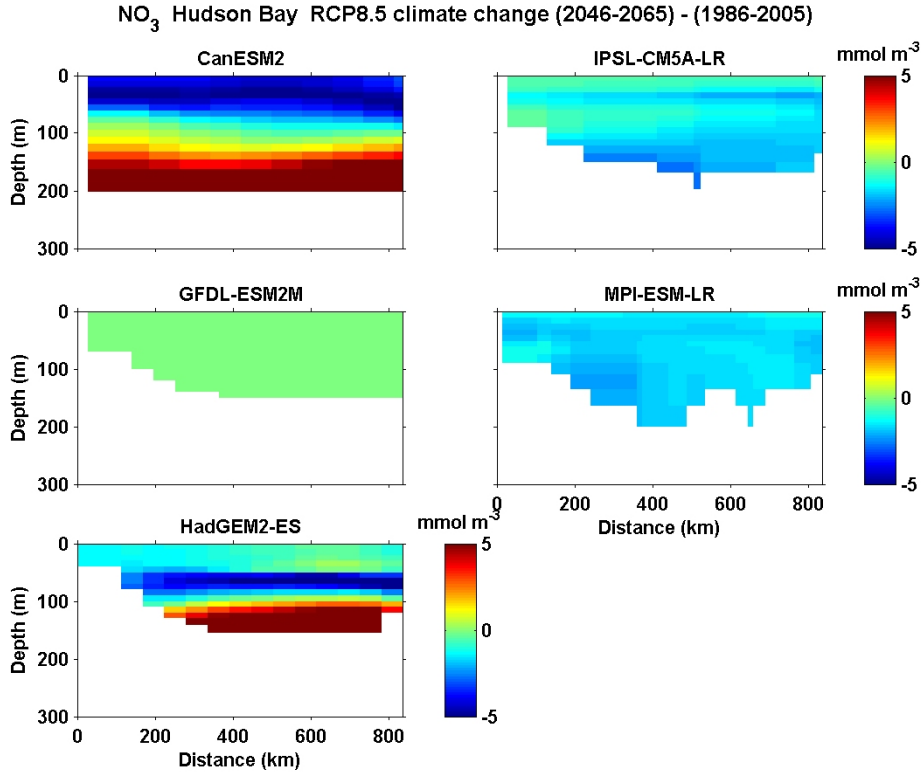

Figure II- 6. Bidecadal changes (2046-2065 average minus 1986-2005 average) in nitrate concentration along the Hudson Bay transect for RCP 8.5.

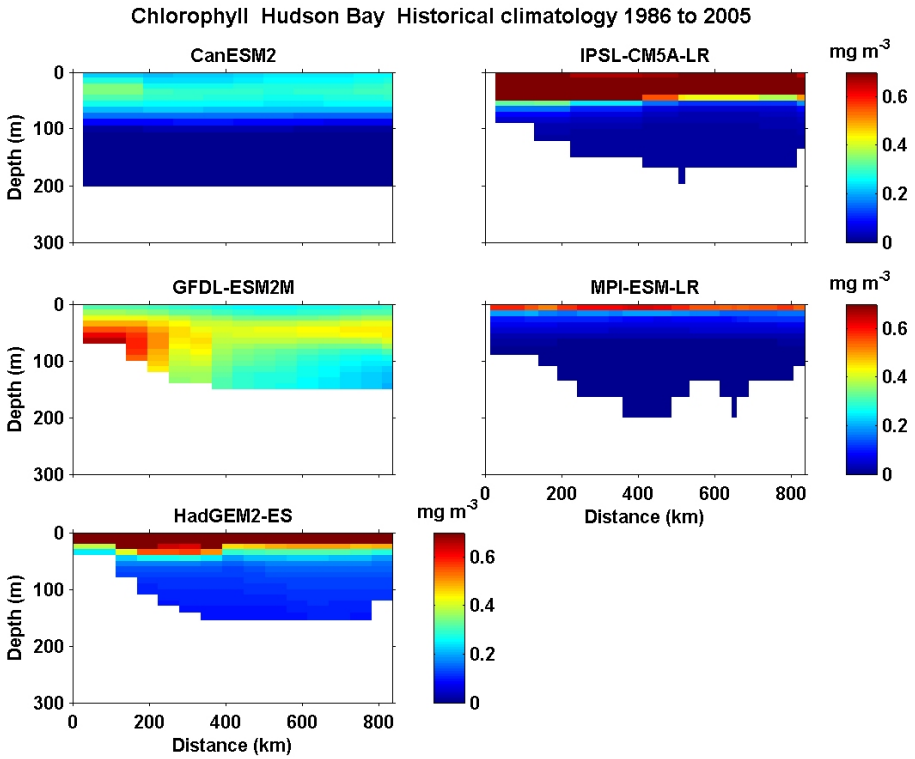

Figure II- 7. Mean simulated Chl *a* (mg m^{-3}) concentration along the Hudson Bay transect for the historical period (1986–2005).

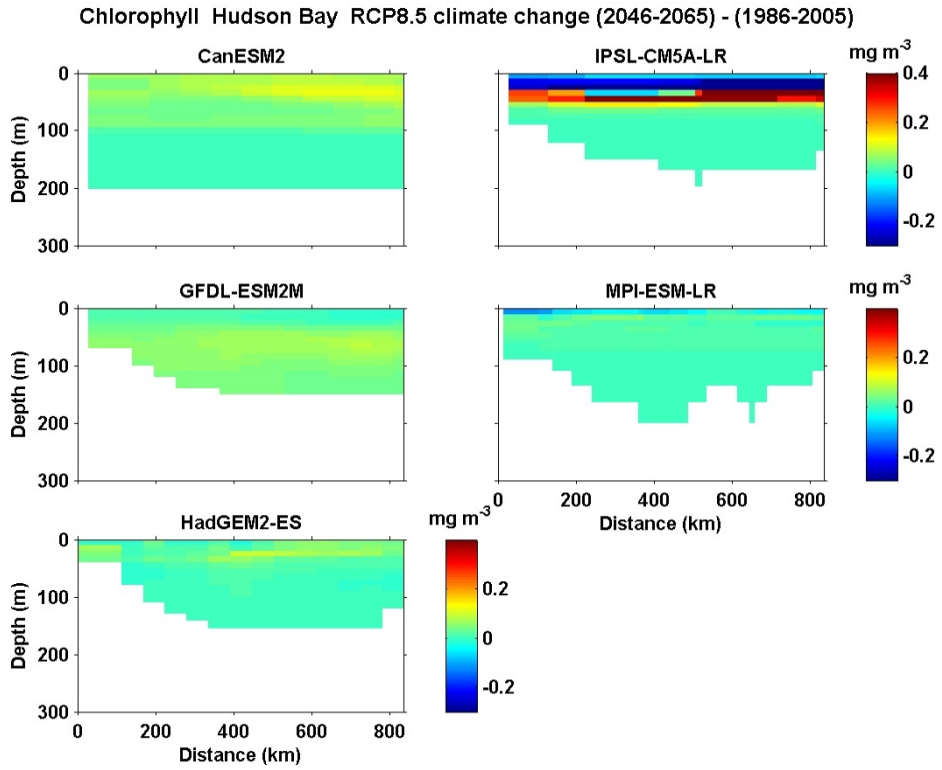

Figure II- 8. Bidecadal changes (2046-2065 average minus 1986-2005 average) in Chl *a* concentration along the Hudson Bay transect for RCP 8.5.

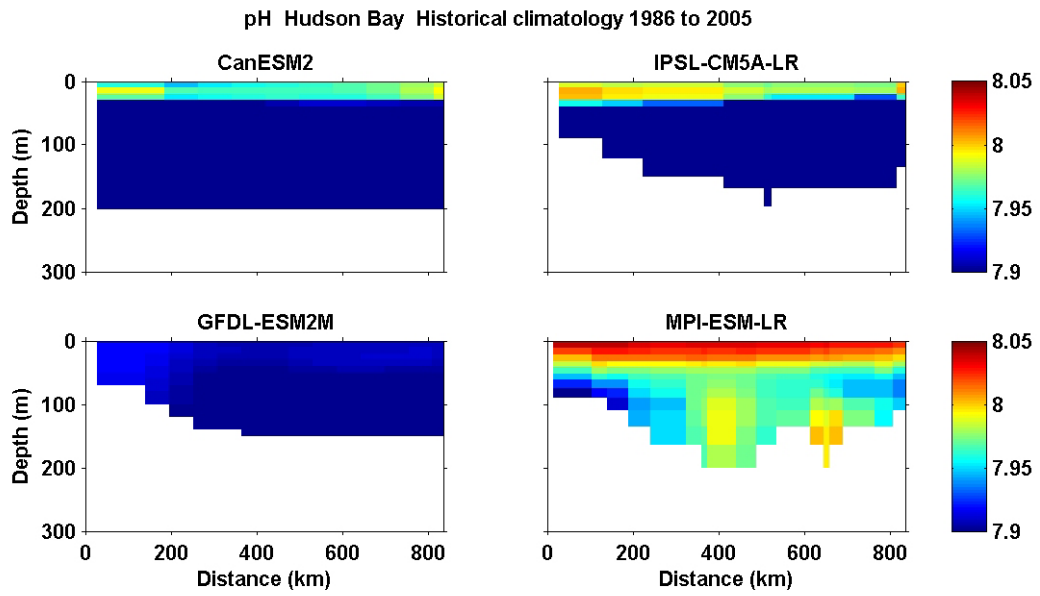

Figure II- 9. Mean simulated pH along the Hudson Bay transect for the historical period (1986–2005). pH values as low as 7.2 can be found at the bottom of the bay in CanESM2 and IPSL.

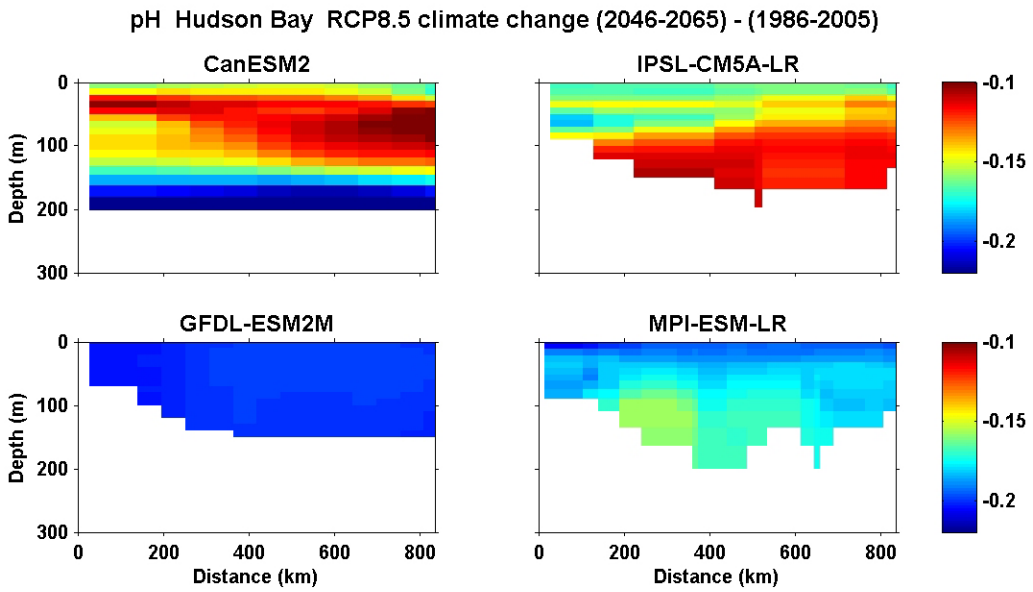

Figure II- 10. Bidecadal changes (2046-2065 average minus 1986-2005 average) in pH along the Hudson Bay transect for RCP 8.5.

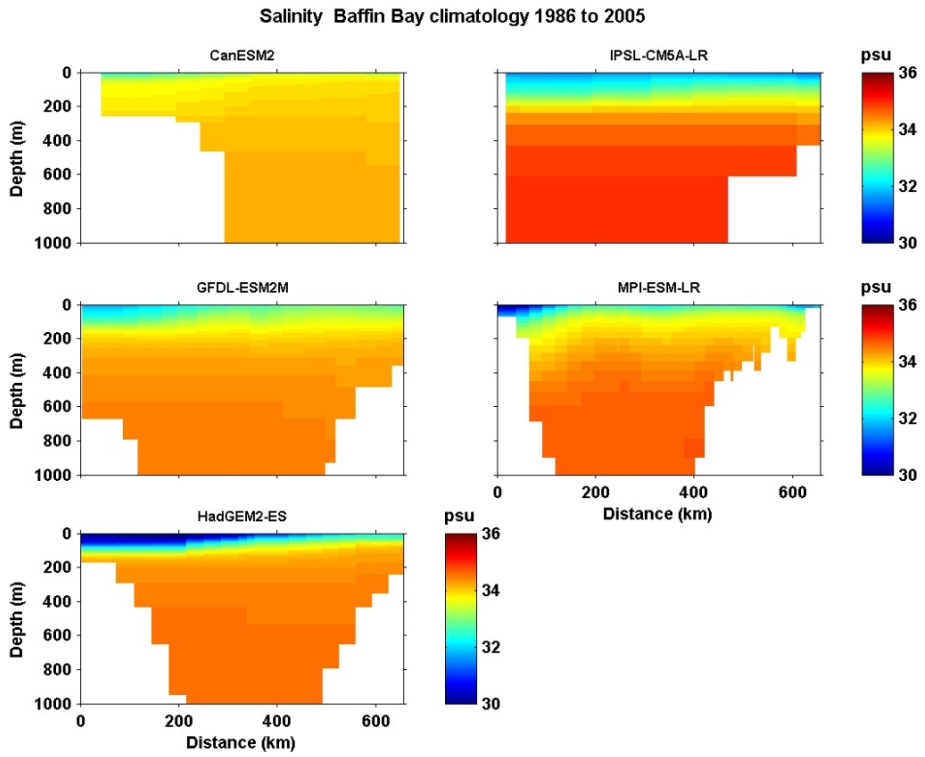

Figure II- 11. Mean simulated seawater salinity along the Baffin Bay longitudinal transect (see Figure 1) for the historical period (1986–2005).

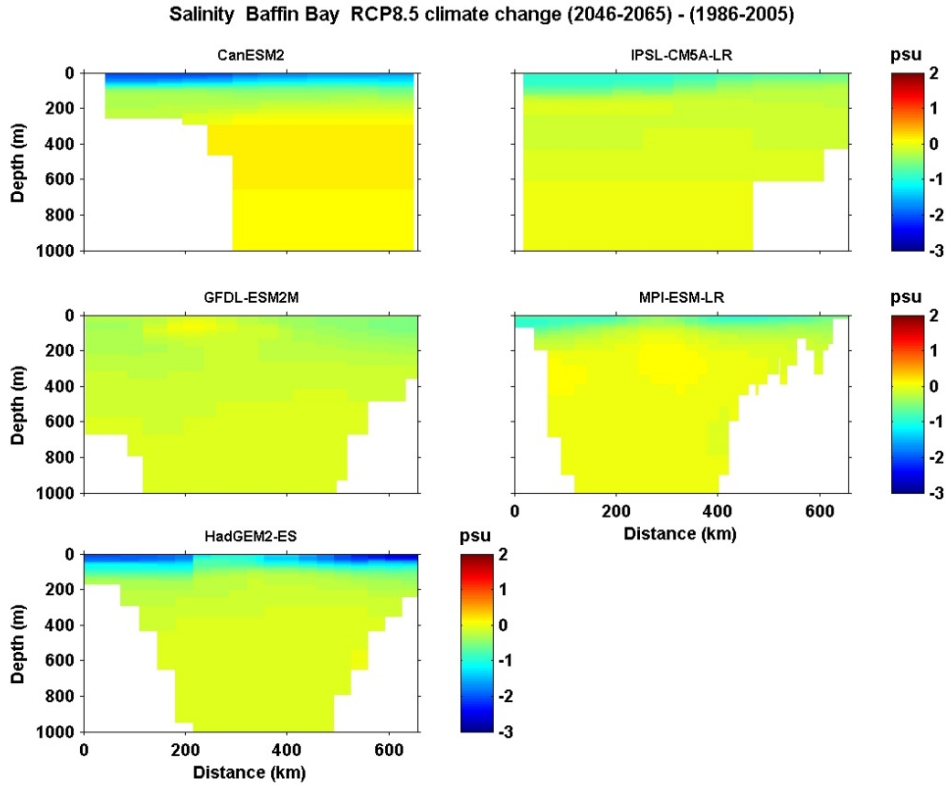

Figure II- 12. Bidecadal changes (2046-2065 average minus 1986-2005 average) in seawater salinity along the Baffin Bay transect for RCP 8.5.

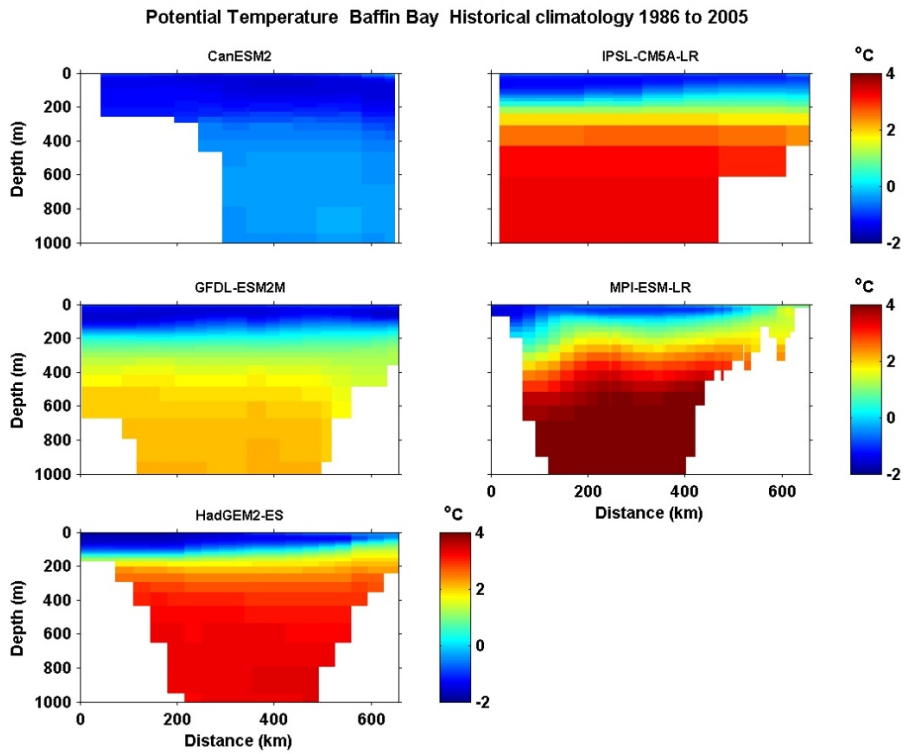

Figure II- 13. Mean simulated potential temperature in Baffin Bay along the longitudinal transect for the historical period (1986–2005).

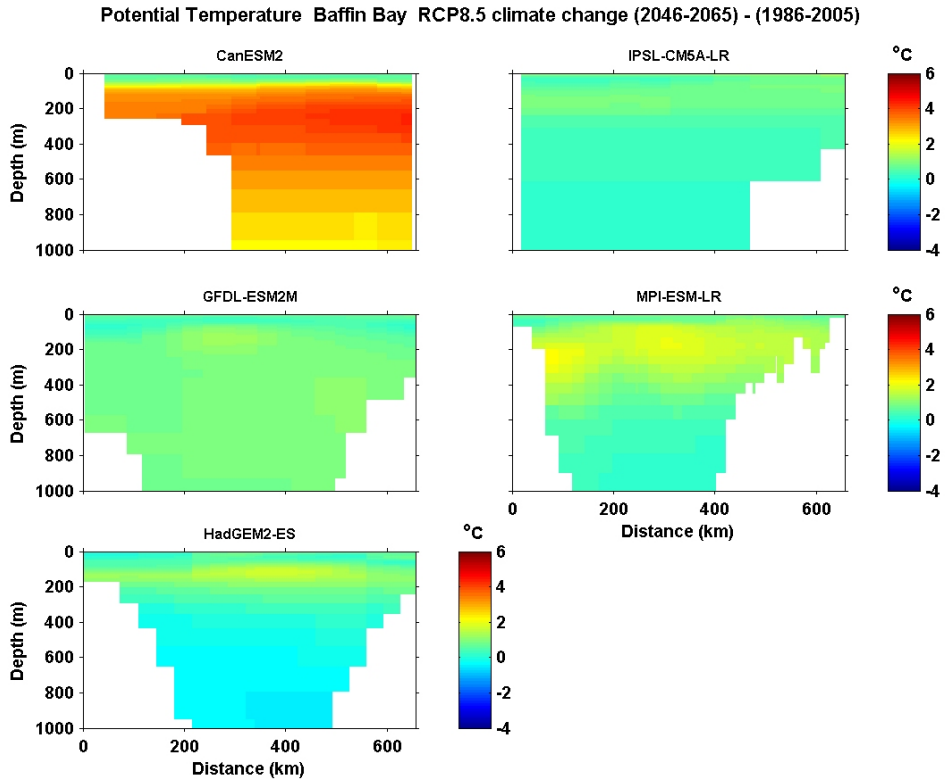

Figure II- 14. Bidecadal changes (2046-2065 average minus 1986-2005 average) in potential temperature along the Baffin Bay transect for RCP 8.5.

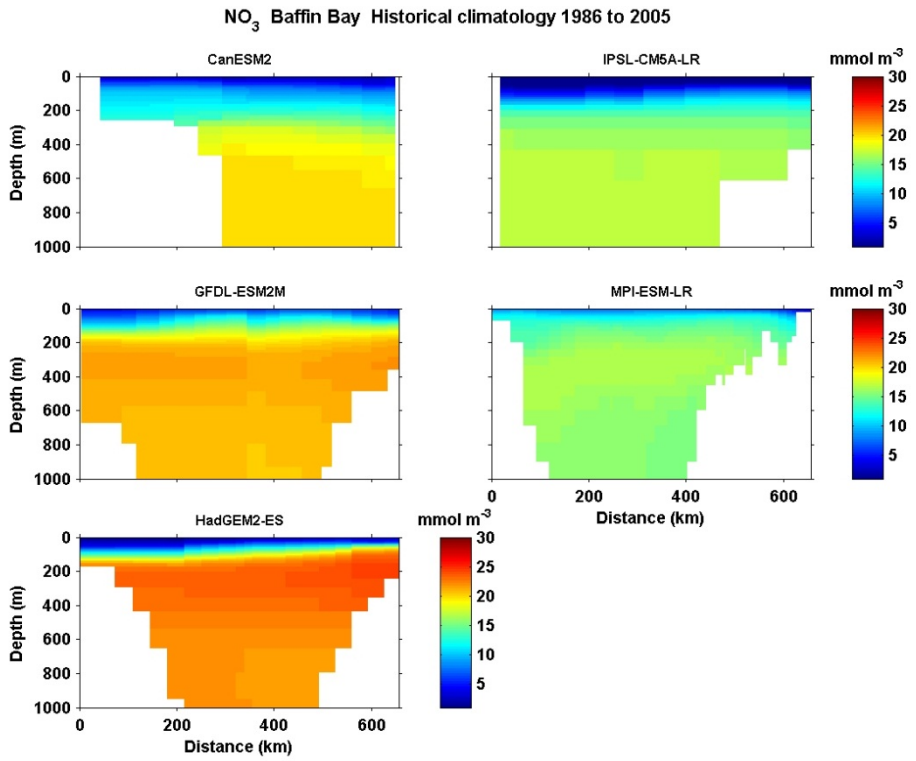

Figure II- 15. Mean simulated nitrate concentration along the Baffin Bay transect over the historical period (1986–2005).

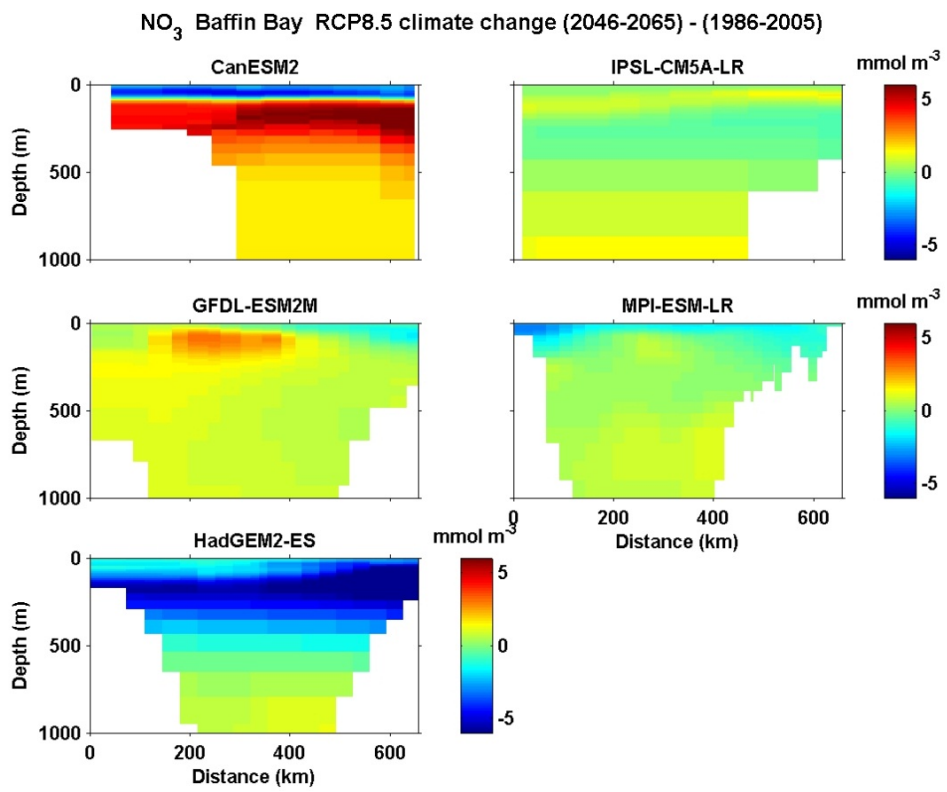

Figure II- 16. Bidecadal changes (2046-2065 average minus 1986-2005 average) in nitrate concentration along the Baffin Bay transect for RCP 8.5.

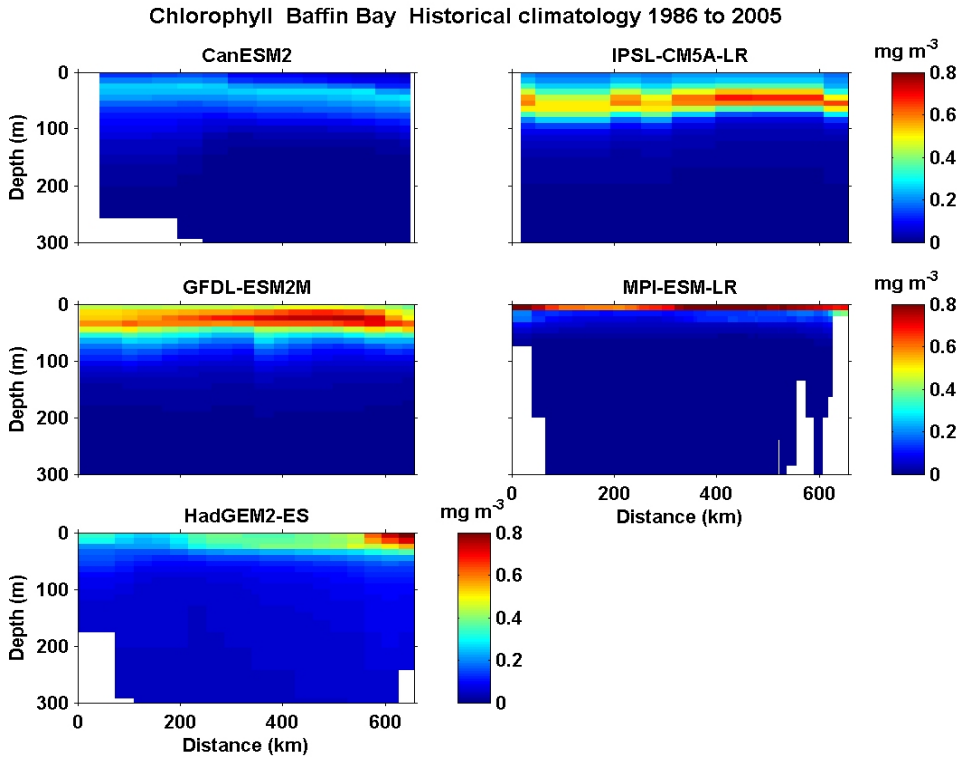

Figure II- 17. Mean simulated Chl *a* concentration (mg m^{-3}) along the Baffin Bay transect over the historical period (1986–2005).

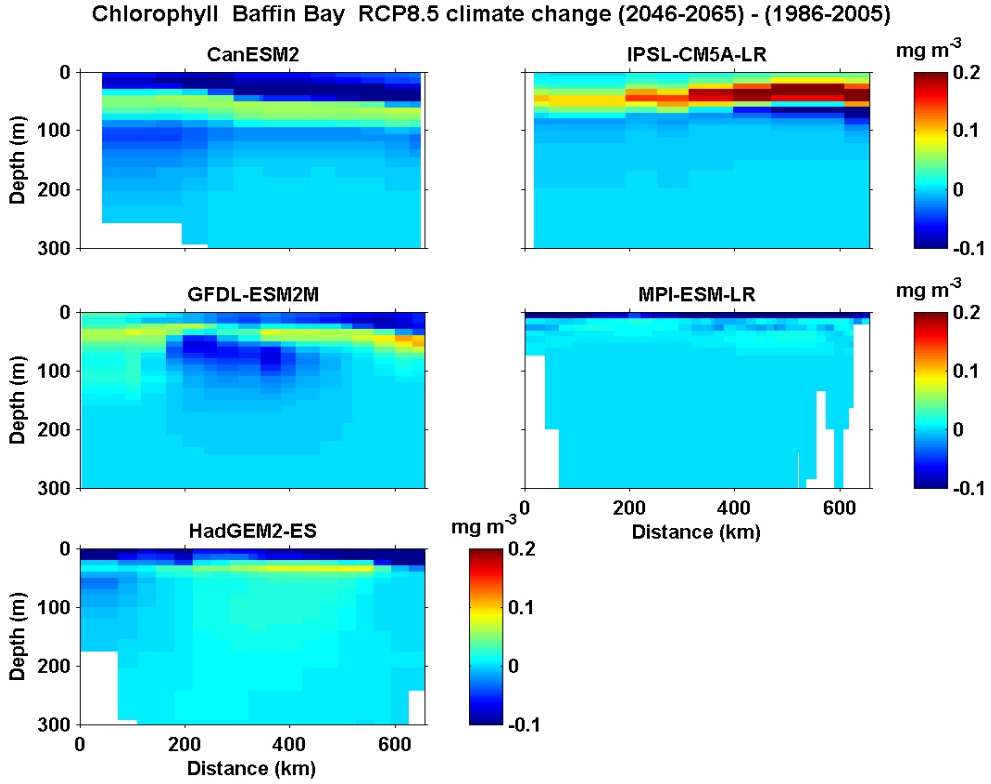

Figure II- 18. Bidecadal changes (2046-2065 average minus 1986-2005 average) in Chl *a* concentration along the Baffin Bay transect for RCP 8.5.

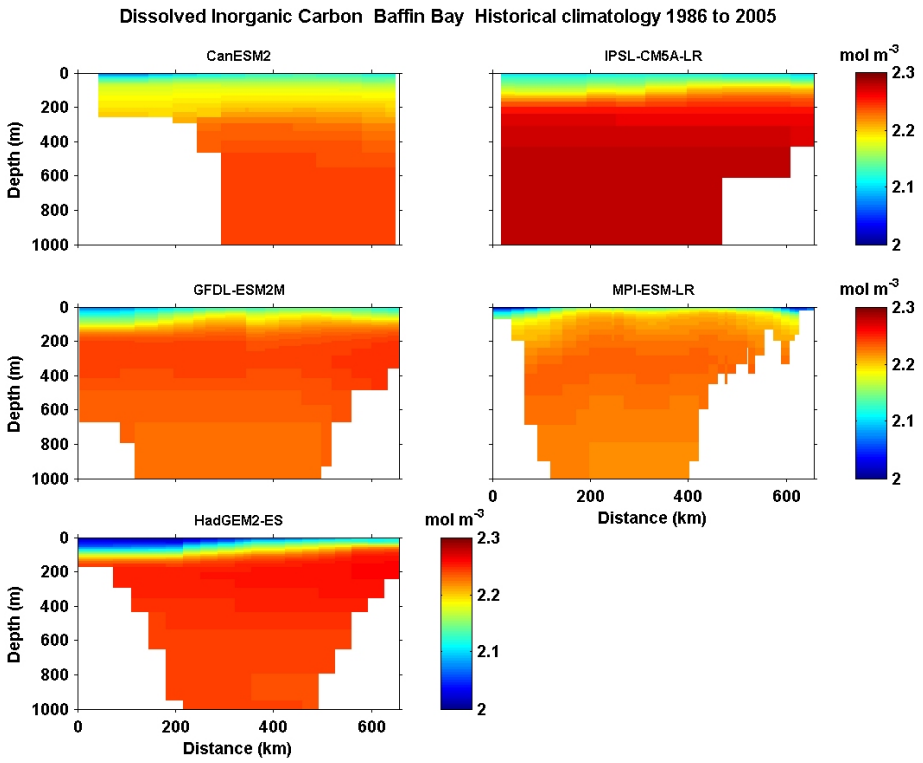

Figure II- 19. Mean simulated DIC concentration (mol m^{-3}) along the Baffin Bay transect over the historical period (1986–2005).

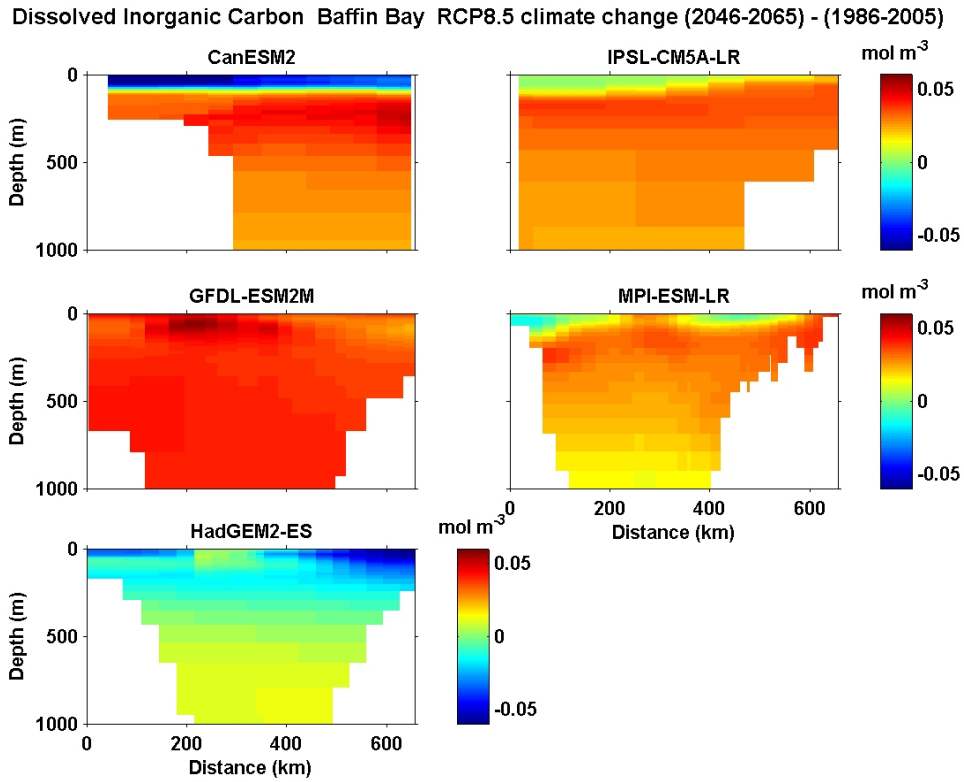

Figure II- 20. Bidecadal changes (2046-2065 average minus 1986-2005 average) in DIC concentration along the Baffin Bay transect for RCP 8.5.

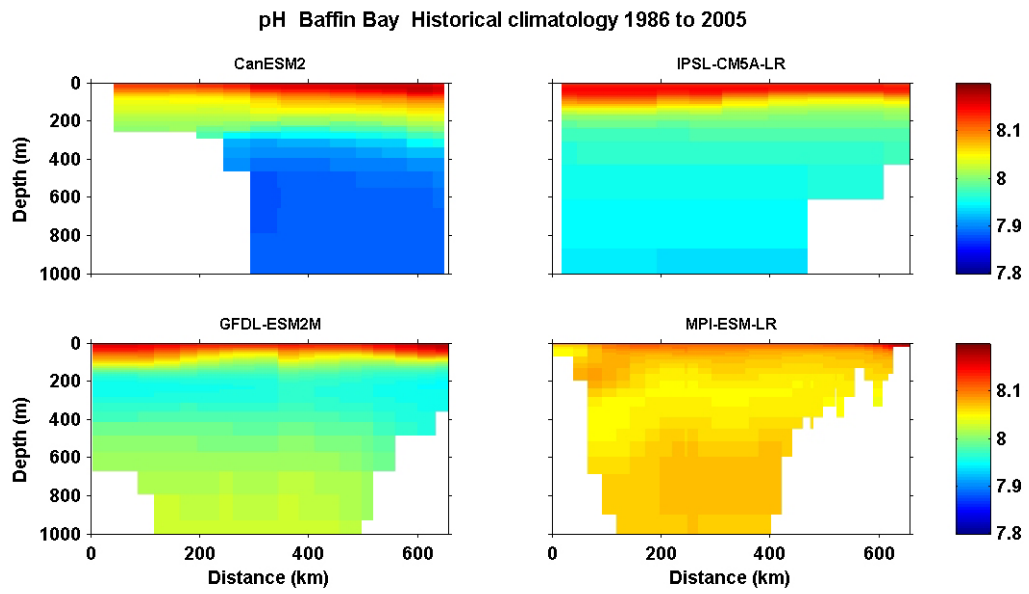

Figure II- 21. Mean simulated pH along the Baffin Bay transect for the historical period (1986–2005).

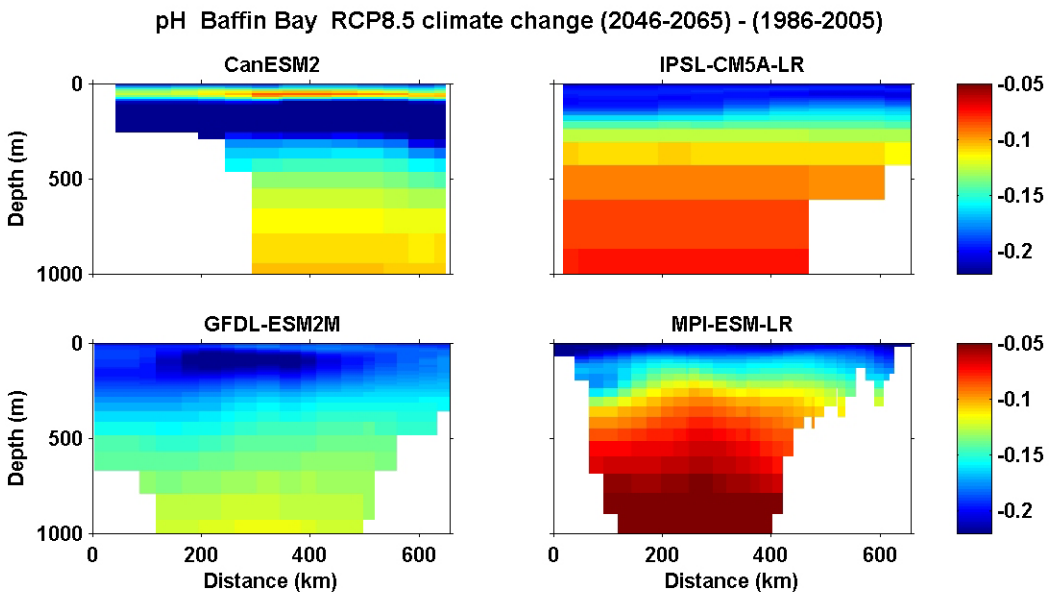

Figure II- 22. Bidecadal changes (2046-2065 average minus 1986-2005 average) in pH along the Baffin Bay transect for RCP 8.5.